Università degli Studi di Padova

Dipartimento di Fisica e Astronomia "Galileo Galilei"

Corso di Laurea Magistrale in Fisica

Tesi di Laurea Magistrale

Fast filtering of events for the Cherenkov Telescope Array

Relatore:
Prof. Denis Bastieri

Laureando:
Michele Urbani

Anno Accademico 2015/2016

To my Family

"L'amor che move il sole e l'altre stelle"

Dante, Paradiso XXXIII

Index

Thesis Summary

The aim of this thesis work is to test the feasibility of a first-level trigger based on GPU for the Cherenkov Telescope Array (CTA) project.

The CTA Consortium is building a new observatory for very high-energy (VHE) gamma rays. Supported by a wide international collaboration, its project consists into the realization of two arrays of the latest generation of Imaging Atmospheric Cherenkov telescopes (IACTs), one located in the northern hemisphere (Canary Islands), with an emphasis on the study of extragalactic objects, and one in southern hemisphere (Chile) dedicated to the galactic sources. Beside a wealth of high-energy astrophysics results, CTA will have a large discovery potential in key areas of astronomy and fundamental physics research. These include the study of the origin of cosmic rays and their role in the Universe, the investigation of the nature and varieties of black hole particle accelerators and the search for signals from dark matter and physics beyond the Standard Model. If signatures of dark matter will appear in direct-detection experiments, gamma-ray observation may provide complementary information to identify its property and mass. CTA has ambitious science goals, for which it is necessary to achieve full-sky coverage, to improve sensitivity by about an order of magnitude in a wide range of energy, from a few GeV to above 100 TeV with enhanced angular and energy resolutions over the existing VHE gamma ray observatories with the same detection technique, such as H.E.S.S, MAGIC and VERITAS.

To better understand the importance and the requirements of a trigger for CTA, we need to highlight the main features of the IACTs detection technique. When a primary cosmic ray interacts with atmosphere, it produces a cascade of ultra-relativistic charged particles which emit Cherenkov light at a characteristic angle. The first interaction with nuclei of the atmosphere takes place at about $10 - 20$ km above sea level and thus the Cherenkov light footprint on the ground is of the order of 10^5 m^2. This light may be collected by large segmented mirrors which focus it onto an array of photomultiplier tubes. The tubes are coupled to fast electronics which amplify and digitise the pattern or image of the shower and transmit a signal to the trigger system. In the GeV-TeV region, the background from charged particles is about three orders of magnitude larger than VHE gamma rays signal. Hadronic showers, however, have a different topology, being larger and more subject to fluctuations than electromagnetic showers, therefore it is possible to discriminate with good accuracy hadronic versus e.m. showers. VHE gamma ray events are quite rare, obviously depending upon the source intensity and the sensitivity of the instruments. To give an idea of the typical sensitivities of the existing observatories, sources as luminous as less than 1% of Crab (the standard candle in gamma-ray astronomy) can be detected at a 5σ significance in 50 hours of observation.

To improve resolution, sensitivity and background rejection, the CTA project aims at building tens of telescopes able to working together and pointing to the sky in the same direction, allowing the possibility to perform stereoscopic observations or working in subarray. This is one of the most remarkable differences with the others existing observatories: the great number of telescopes. But the deployment of about $50-100$ telescopes per site will produce a huge amount of data. The processing of CTA data will be a computational challenge, as all measurements made with CTA should undergo a rapid data analysis, including event selection and calibration

of instrumental and environmental effects. It will be necessary to reduce a volume of typically $10 - 20$ TB of raw data per night to a few MB of high-level data. In order to observe transient phenomena like Gamma-Ray Bursts (GRBs) and gamma ray flares, the filtering of events have to be rapid and efficient to allow a Real-Time Analysis (RTA).

The first-level trigger must be able to recognize from the whole telescopes array which signals belong to the same physical event by being stereoscopically detected. Knowing the positions of the telescopes and their pointing direction, it is possible to write an algorithm to compute the relative delays and compare them with the signals of each telescope. If the time correlation is acceptable, two or more signals from different telescopes are tagged as originating from the same physical event. The first-level trigger will be able to reject background events or events without the required resolution. In particular, if each signal from telescopes will contain the hadroness (the likelihood that the particle cascade originated from a hadronic shower) the trigger will be able to filter out hadronic events.

Summing up, the main goals of this thesis are: the study in depth about VHE gamma ray astronomy and the CTA project, the development of a first-level trigger for the CTA, testing its efficiency through a toy-MC simulations of several different setup and with MC simulations provided by the ASTRI collaboration and finally to deploy the algorithm on a GPU system in order to obtain the required performance.

Chapter 1

Introduction to Very High Energy Astrophysics

For several centuries, the study of the night sky and astronomical phenomena was conducted through observation of light from celestial bodies.

The human eye allows, in fact, sufficient resolution and sensitivity to be able to observe a few hundreds of light sources in the darkness of the sky.

This capability was improved by the invention of telescopes, optical devices able to collect light from distant sources increasing their apparent brightness and angular size.

Galileo Galilei was the first man who turned a telescope to the sky and opened the era of modern observational astronomy. The use of the telescope was a great step forward in the history of astronomy, since for the first time it was possible to "see the unseen".

Figure 1.1: a) The original Galileo telescopes, b) LST for the CTA-North project

Improving human senses through devices and tools, is a key element of the scientific progress because extends the idea of observation and opens horizons of research in every scientific field. The development of these tools, generally called detectors, go hand in hand with scientific discovery.

1.1 Cosmic Rays discovery

In 1785, Charles Augustin de Coulomb described, in his reports on electricity and magnetism, an experiment with a torsion balance, which showed that the device would spontaneously discharge due to the action of the air rather than defective insulation.

Similar observations were conducted by William Crookes, who observed in 1879 that the rate of spontaneous discharge decreased when the pressure of the air inside the electroscope was reduced. The discharge was then likely due to the ionization of the air. But what was the cause of ionization?

The explanation of this phenomenon came at the begining of 20th century and paved the way for the discovery of cosmic rays.

In 1909 Theodor Wulf, built a new type of electrometer more sensitive and more transportable than the gold leaf electroscopes. Wulf started measuring changes in radioactivity with respect to height to understand the origin of the radiation.

The hypothesis was simple: if the radioactivity was coming from the Earth, it should decrease with height. He took his electroscope to the top of the Eiffel Tower but he found a too small decrease to confirm his hypothesis.

The answer of the origin of atmospheric radiation came from two scientists, the Austrian Victor Hess and the italian Domenico Pacini, which developed two brilliant lines of research independently.

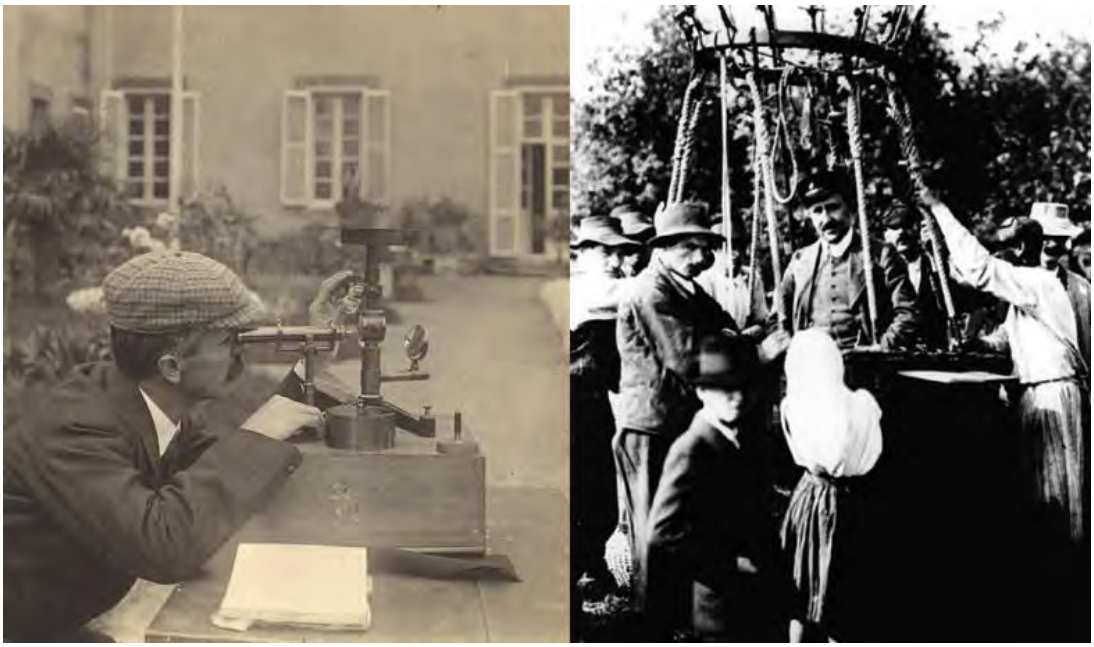

Figure 1.2: (*Left*) Pacini making a measurement in 1910. (*Right*) Hess during the balloon flight in 1912.

In 1911, Pacini took measurements with a Wulf-type electroscope in several settings. He observed a 30% reduction of radioactivity comparing ionization levels on a ship 300 m offshore from Livorno coast to measurements on land. This result suggested that a significant portion of the penetrating radiation must be independent from emissions of the upper layers of the Earth's surface. Pacini also measured the levels of radiation in the deep sea of the Genova gulf and then into Bracciano Lake. He noted that there was a 20% reduction of radioactivity 3 meters underwater compared to on the surface, concluding that ionizing radiation must come from the atmosphere.

In the same period Hess made a series of ascents aboard atmospheric balloon to take measurements of radiation at different heights. On 7April 1912, Hess made an ascent of 5300 meters during a near-total sun eclipse. He observed that ionization did not decrease during the eclipse, so the source of radiation could not be the Sun. But the most interesting fact was that radiation increased with height, and this was the final proof of the extraterrestrial origin of the observed radiation.

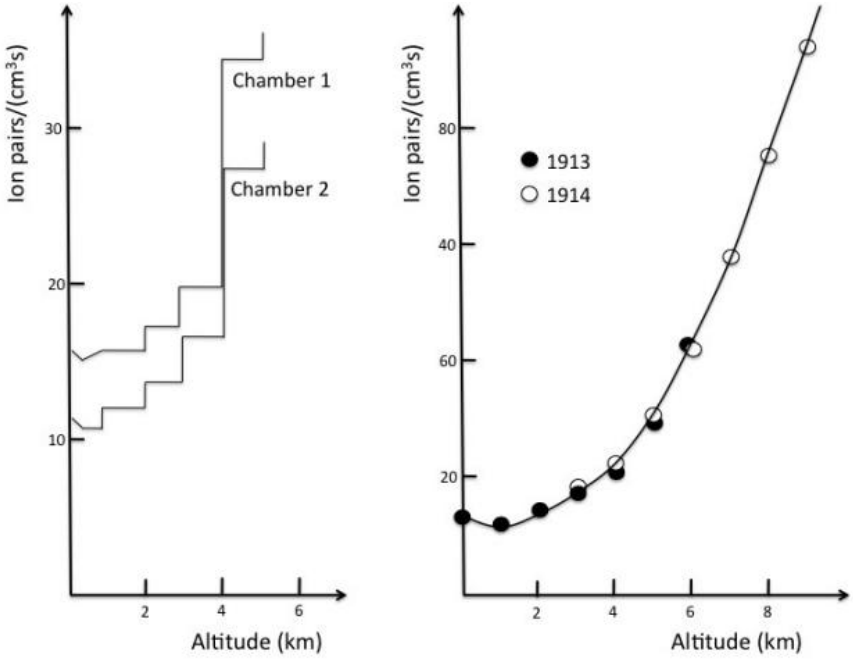

Figure 1.3: Increase in ionization with height measured by Hess and Kolhörster.

The results by Hess were later confirmed by Kolhörster in 1913 and 1914 for greater heights. Kolhörster took balloon measurements up to a height of 9300 m and observed that the intensity of the radiation was relatively constant, with no day-night or weather-dependent variations. The word Cosmic–Rays (CRs), coined by the American physicist Millikan in 1925, includes all the particles of extraterrestrial origin that constantly hit the Earth.

The idea of CRs, despite the experimental evidence, was not immediately accepted and the Nobel prize was assigned to Hess only in 1936. Since then the CRs has been intensely explored, giving rise to new scientific fields (elementary particle physics and astroparticle physics), new technologies (detectors and accelerators) and a new interaction mechanisms in astrophysics.

1.2 The Nature of Cosmic Rays

The Cosmic radiation was generally believed to be γ radiation because of its penetrating power. In 1928, the Geiger-Müller counter tube was introduced in measurement operations, and confirmation that cosmic radiation is indeed electrically charged came readily. A key experiment on the nature of cosmic rays was the measurement of the intensity variation with geomagnetic latitude.

In 1933, three independent experiments by Alvarez and Compton, Johnson, and Rossi, discovered that close to the equator there were more cosmic rays coming from West than from East. This effect, due to the interaction with the geomagnetic field, showed that cosmic rays are mostly positively charged and thus most probably protons, as it was possible to demonstrate some years later thanks to more powerful spectrometers.

It was already clear at that time that the particles observed with balloons were not the primary CRs but secondary particles initiated by the interaction of energetic CRs with the atmospheric nuclei. The study of the composition of these secondary particles cascade leading to the discovery of many previously unknown particles ($e+$, $\mu\pm$, $\pi\pm$, $K\pm$, ...).
When a primary CR interacts with atmosphere, it produces a cascade of ultra-relativistic charged particles, these cascades were called particle shower. There are two basic types of showers. Electromagnetic showers are produced by a particle that interacts primarily or exclusively via the electromagnetic force, usually photons or electrons and Hadronic showers produced by hadrons (i.e. protons, nucleons and other particles made of quarks). We study in depth Electromagnetic and Hadronic shower in chapter 4.

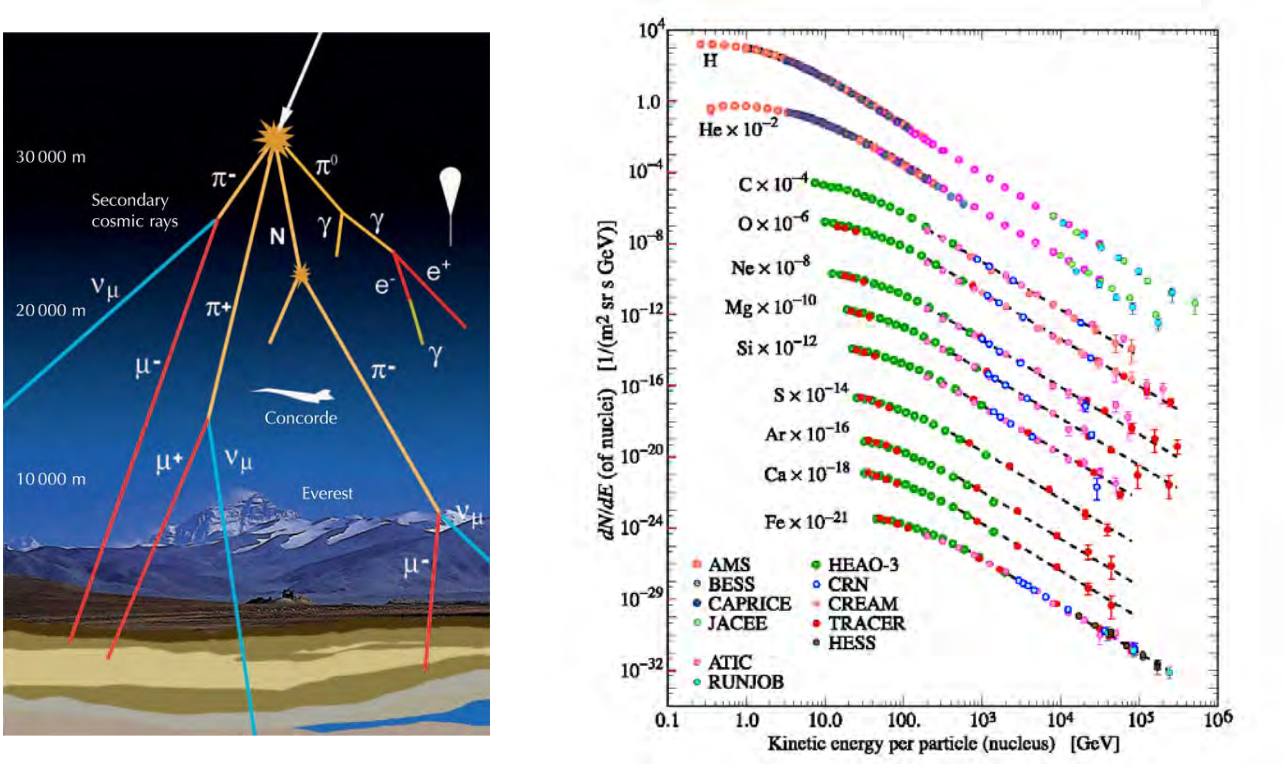

Figure 1.4:(*Left*) Sketch of primary and secondary CRs concepts. (*Right*) Differential energy spectra for primary cosmic ray nuclei.

Except for neutrinos, which are weakly interacting particles, primary CRs are made up for 99.9% of charged particles, mainly protons ($\sim$ 89%), α–particles ($\sim$ 10%), ionized nuclei of heavier elements ($\sim$ 10%), electrons/positrons ($\sim$ 1%), and only for a tiny fraction of photons of energy greater than 1 MeV.
The spectrum of the observed CRs covers 13 orders of energy magnitude, ranging from a few MeV to 10^{21} eV (below 100 GeV , the solar wind would cause their absorption) and to 32 orders of magnitude in the flux, from 1 particle/$(cm^2 s)$ at $\sim$ 100 MeV to less than 0.01 particles/$(km^2$ century) for the highest observed energies.
Where the energy spectrum is unaffected by the Earth's magnetic field, the differential flux of CRs follows a power-law:

$$I(E) \propto E^{-\alpha} \tag{1.2.1}$$

with at least two variations of spectral index α. The regions where there are changes in the slope are called:

- *knee* $\rightarrow$ $E \sim 10^{15.5}$ eV, from $\alpha \simeq 2.7$ to $\alpha \simeq 3$.
- *ankle* $\rightarrow$ $E \sim 10^{18}$ eV, from $\alpha \simeq 3$ to $\alpha \simeq 2.6$.

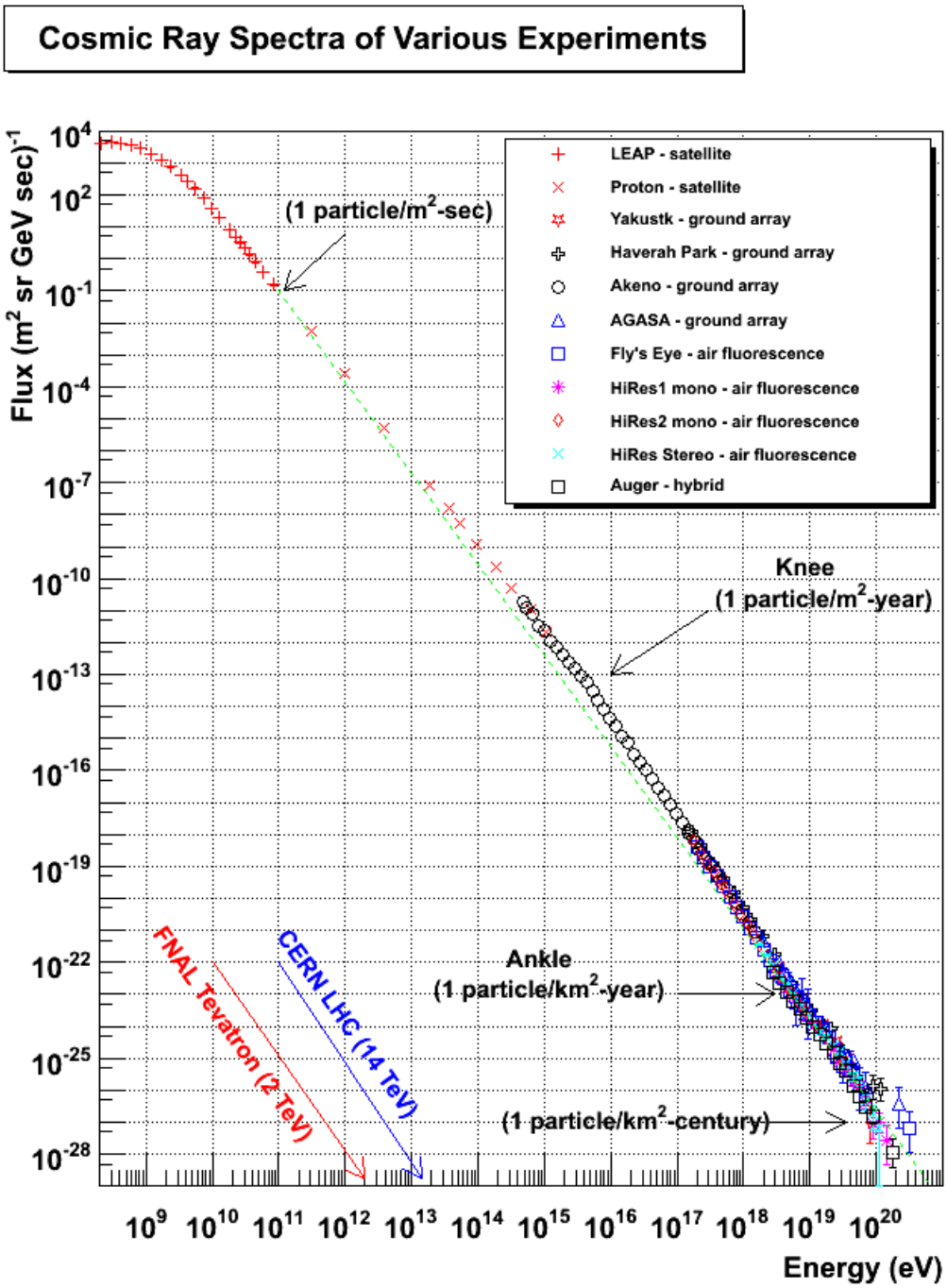

Figure 1.5: All particles CRs spectrum, taken from http://www.physics.utah.edu/∼whanlon/spectrum.html.

The knee is probably caused by a change in the composition of the primary particles. Instead the ankle is most probably caused by an interplay between CRs of galactic and extragalactic origin. CRs with energies above 10^{20} eV can interact with the Cosmic Microwave Background (CMB) radiation. This leads to a cutoff in the CR–spectrum, also known as the GZK–cutoff (Greisen, Zatsepind, Kuzmin).

It is generally believed that CRs below 10^{15} eV have a galactic origin and have been confined inside our galaxy for at least 10^7 yr. This is the reason why these particles have been completely isotropized before they arrive to the Earth. Particles above 10^{17} eV are believed to be mostly of extragalactic origin, since the galactic magnetic field is not able to trap them in our galaxy. CRs up to about 10^{18} eV are isotropic, while the explanation of the anisotropy at higher energies is still under debate.

1.3 Why photons ?

Even if charged particles are dominant in the composition of the cosmic rays, they are of little use in all those studies of astronomy and astrophysics because of the difficulty to associate the detected particles with the position of their sources in the sky. This difficulty is due to the presence in the Universe, on various scales, of magnetic fields that curve the trajectories of charged particles.

Only the neutral CRs retain the information about the incoming direction and allow the connection between the observed events and the emitter sources.

Among the neutral known particles: photons and neutrinos can be used to astrophysical observations, because neutrons decay too quickly, just ~ 15 minutes to be used in these studies. The neutrinos are potentially very interesting in VHE astrophysics but their small cross section represents an experimental limit today.

So photons are then the privileged vectors of information because, being electrically neutral, they travel across the Universe along straight lines, that can be traced back to the source of emission.

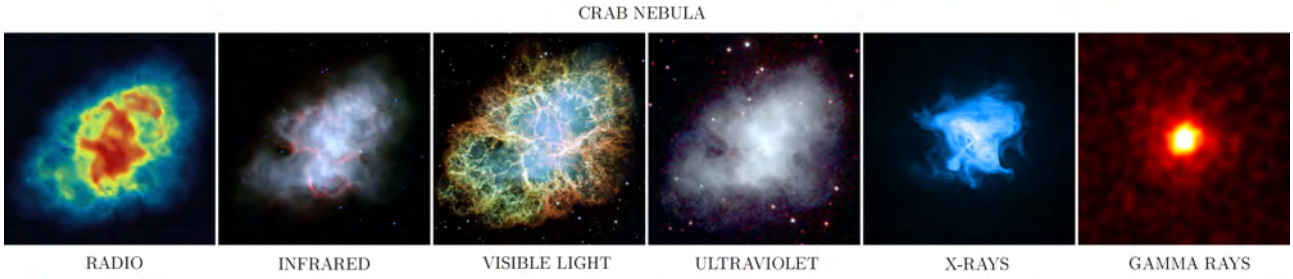

Figure 1.6: Images of the Crab Nebula at different wavelengths. Radio band (NRAO/ Very large Array) shows where free electrons are interacting with a magnetic field, infrared band (Spitzer) shows cloud of energetic electrons trapped within the star's magnetic field, optical band (HST) shows where hydrogen is in the nebula, ultraviolet band (Swift) shows cooler electrons, X-ray (Chandra) band shows where very hot electrons are and finally γ-ray band (Fermi LAT) shows the pulsar's emissions in very high energy.

Moreover, photon production involve the vast majority of celestial objects and provide us informations about in several different energy ranges.
Multiwavelength studies allow to appreciate the same object acquiring many informations about position, structure, dynamics and composition and to understand better the physical phenomena which involve nuclear reactions, magnetohydrodynamics, radiative processes, etc.

In this thesis, in particular, we focus on the most energetic photons, which consist of high energy (from 100 GeV to 100 TeV) gamma rays. Gamma-ray photons differs fundamentally from those detected at lower energies, in the sense that they carry non-thermal information from the Universe. In fact this kind of radiation cannot be generated by thermal processes from hot celestial objects. So gamma rays track back to those mechanisms where a large amounts of energy is concentrated onto single quantum emissions. This indeed is the environment where cosmic rays are produced.

Since the flux and energy spectrum of gamma rays reflects the flux and spectrum of the high energy particles then studying the gamma component of cosmic radiation it is possible to obtain information about the charged component, about its origins, production and acceleration mechanisms. Moreover the study of gamma rays provides a window on the discovery of the nature and constituents of dark matter.

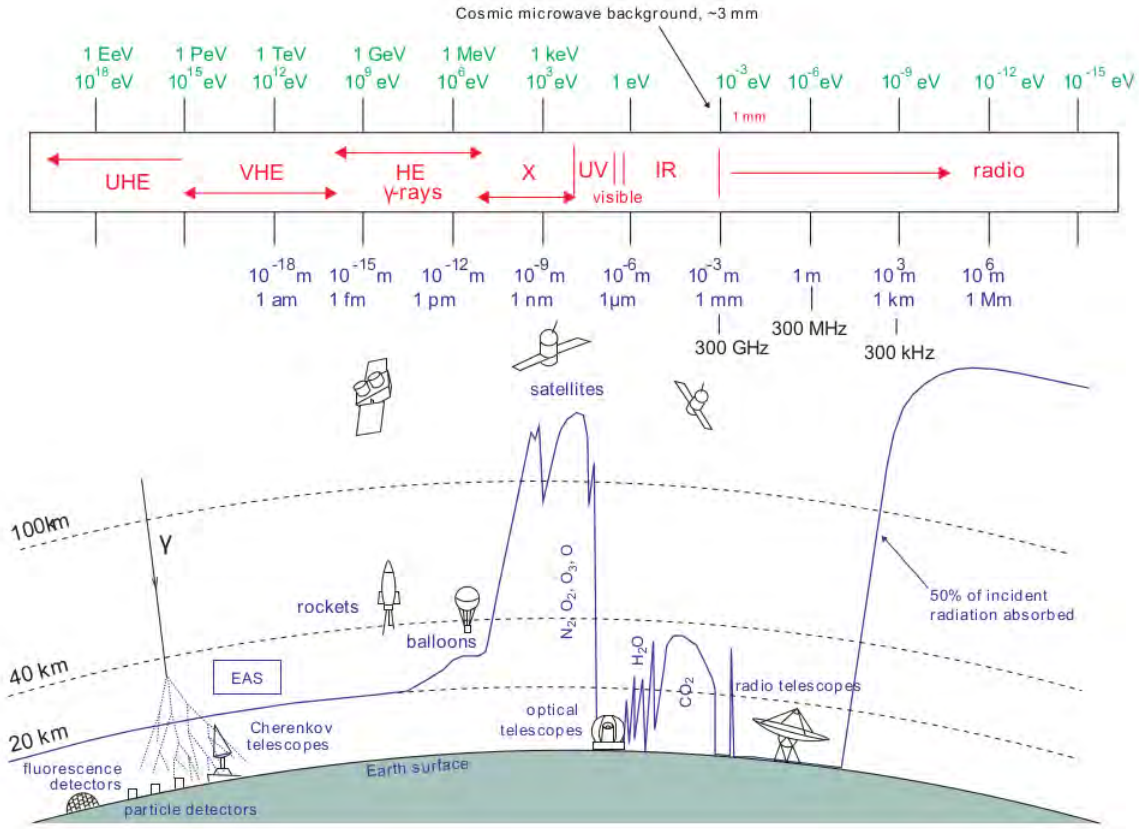

Figure 1.7 :The electromagnetic spectrum and its atmospheric windows for observation. For each wavelength the blue line marks the altitude at which 50% of the incident cosmic radiation is absorbed. A sketch of an extended air shower (EAS) and a Cherenkov telescope are shown in the lower left corner.

The energy bands can conventionally be divided (although definitions are not standard and depend by the thresholds of the instruments) in:

- **Medium Energy region (ME)**: energies below 30 MeV. Compton scattering is the main interaction process used for the detection. In this energy band cosmic γ–rays of this energy domain are completely absorbed in the atmosphere, therefore satellite telescopes are the principal detectors.

- **High Energy region (HE)**: energies between 30 MeV and 100 GeV. Pair production is the main process on the basis of the detection of those photons. The produced leptonic pairs can be detected with satellites but also by atmospheric balloons.

- **Very High Energy region (VHE)**: energies range between 100GeV and 100 TeV. When entering the Earth's atmosphere these photons are enough energetic to produce electromagnetic showers, which can be well detected by ground-based telescopes through secondary flashes of Cherenkov light.

- **Ultra High Energy (UHE)**: energies above 100 TeV. This is a rather unknown energy region. The experiments are placed on the ground and directly reveal the particles produced in the so-called extensive air showers (EAS). Until now, a good discrimination of the nature of the primary CR producing the shower is still difficult to achieve.

Chapter 2

VHE Gamma Ray Physics

To advance in our understanding of astrophysical phenomena, we need to discuss fundamental interaction processes able to produce or absorb high energy γ-rays.
Any interpretation of astrophysical data requires adequate knowledge of the principal radiation processes to be able to distinguish which processes are dominant and try to understand why. Therefore the physics of radiation and absorption mechanism is one of the central subject of astronomy.

Generally, in astronomy, each wavelength band is characterized by one or two basic radiation mechanism. However, this is not the case of γ-ray astronomy. Indeed we have to consider a large number of competing processes which makes the theoretical studies very interesting, but also challenging.

Indeed very often the same experimental observation data can be equally explained by more than one radiation mechanism. In these cases to obtain unambiguous identification of γ-ray production mechanism in celestial objects not only the analysis of experimental data about spectral, temporal and spatial properties of radiation is required, but also a clear understanding of features of the radiation processes and their relationship to each other, especially in the context of multiwavelength studies.
The most relevant non-thermal γ-ray production processes, which are expected to take place in celestial objects are: Synchrotron radiation, Inverse Compton scattering, Bremsstrahlung radiation and Neutral Pion decay.
In particular the hadronic process of Neutral Pion decay and Inverse Compton scattering are the most important mechanisms in the production of VHE γ-rays.

In this chapter, without claim for completeness, we discuss and summarize briefly the main radiation processes which are relevant in γ-ray astronomy with an emphasis on the mechanism that operate effectively in the HE and VHE regimes.
Nevertheless we tried to write a self-consistent presentation that allows the reader to appreciate the main results, understanding how they were obtained. In the appendices, missing parts and other topics useful for understanding are contained.

We follow several references, but in particular we want to cite the authors: F.Mandl and G.Shaw [38] for the QED treatments, J.D. Jackson [27] and L.D.Landau and E.M.Lifshitz [34] for the Electrodynamics topics. Moreover we consider the treatments of G.B. Rybicki and A.P. Lightman [47] and M.S.Longair [48] and G.R. Blumenthal and R.J. Gould [12] for radiative processes and F.A Aharonian [6] for pion decay and general conclusions.

2.1 Synchrotron Radiation

When a charged particle moves in the presence of a magnetic field $\boldsymbol{B}$, it experiences a force perpendicular to the field, called Lorentz force. Subjected to a radial acceleration, this particle continuously emits electromagnetic radiation (see A.2).

If the particle is non-relativistic, the radiation is named *Cyclotron emission* and the frequency of emission is roughly the particle gyration frequency. Instead when the particle is relativistic, the radiation is named *synchrotron emission* and the resulting spectrum is more complicated, because the frequency of emission extends over many higher order harmonics of the gyration frequency.[47]

Due to the large presence of magnetic fields near the celestial objects, synchrotron emission is one of the main radiation processes in astrophysics.

2.1.1 Total Emitted Power

The motion of a charged particle is subjected to by the general Lorentz equation of motion:

$$\boldsymbol{F} = \frac{d}{dt}(\gamma m \boldsymbol{v}) = q\big(\boldsymbol{E} + \boldsymbol{v} \times \boldsymbol{B}\big) \qquad \gamma = \frac{1}{\sqrt{1-\beta^2}} \tag{2.1.1}$$

where $\beta = v/c$. For sake of simplicity we assume conservation of energy and thus $\boldsymbol{v} \cdot \boldsymbol{E} = 0$, this imply that $|v| = \text{cost}$ and so $|\gamma| = \text{cost}$.

We can separate the components of the velocity vector: parallel and perpendicular to the magnetic field $\boldsymbol{B}$:

$$\frac{d\boldsymbol{v}_{/\!/}}{dt} = 0 \qquad \frac{d\boldsymbol{v}_{\perp}}{dt} = \frac{q}{\gamma m}\boldsymbol{v}_{\perp} \times \boldsymbol{B} \tag{2.1.2}$$

Thus $v_{/\!/} = \text{cost}$ with $|v| = \text{cost}$ imply also $v_{\perp} = \text{cost}$. This is a uniform circular motion in the plane orthogonal to $\boldsymbol{B}$ with the $\boldsymbol{a} \perp \boldsymbol{v}$ in this plane.

The combination of this circular motion $\perp$ to $\boldsymbol{B}$ and the uniform motion $/\!/$ to $\boldsymbol{B}$ results in helical motion (see figure). The magnitude of the acceleration is :

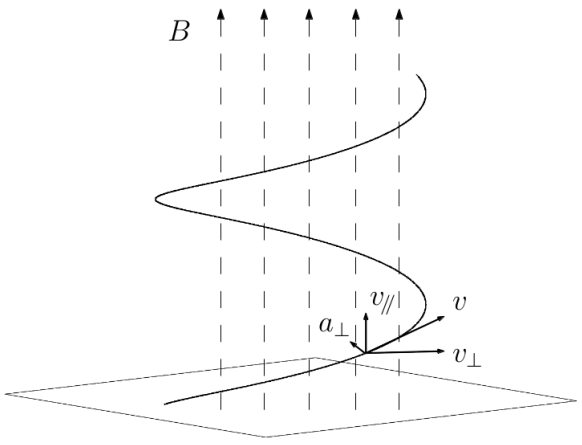

$$a_{\perp} = \frac{qB}{\gamma m} v_{\perp} = \Omega_c v_{\perp} \tag{2.1.3}$$

where Ω_c is the gyration frequency (or cyclotron frequency). We can substitute this result into the expression of the total power emitted by a relativistic particle with acceleration perpendicular to velocity (A.3.9).

$$P = \frac{q^2}{6\pi\varepsilon_0 c^3}\gamma^4(a_{\perp}^2) = \frac{q^2}{6\pi\varepsilon_0 c^3}\gamma^4\left(\frac{qB}{\gamma m}\right)^2 \tag{2.1.4}$$

Simplifying and substituting $v_{/\!/} = |v|\sin\alpha$ where α is the *pitch angle* between $\boldsymbol{v}$ and $\boldsymbol{B}$, we have:

$$P = \frac{1}{6\pi\varepsilon_0 c}\frac{q^4}{m^2}\gamma^2\beta^2 B^2 \sin^2\alpha \tag{2.1.5}$$

Note the dependence of the mass m: synchrotron emission is much more important for electrons than for protons since$m_e^2/m_p^2 \approx 3 \cdot 10^{-7}$.

To obtain the total emitted power for an isotropic distribution of velocities, it is necessary to averaged over all pitch angles for a given speed β:

$$\langle \beta_\perp^2 \rangle = \frac{\beta^2}{4\pi} \int sin^2\alpha d\Omega = \frac{\beta^2}{2} \int_{-1}^{+1} (1 - \cos^2\alpha) d\cos\alpha = \frac{2}{3}\beta^2 \tag{2.1.6}$$

Hence the total power emitted by an electron, average over all pitch angle is:

$$P = \frac{2}{3} \frac{1}{6\pi\varepsilon_0 c} \frac{q^4}{m^2} \gamma^2 \beta^2 B^2 \tag{2.1.7}$$

To compare this quantity with other emitted powers, (as we see in the next section 2.2) it is useful to express this formula in terms of the Thomson cross-section:

$$\sigma_T = \frac{8\pi}{3} r_e^2 = \frac{1}{6\pi\varepsilon_0^2 c^4} \frac{q^4}{m^2} \simeq 0.665 \cdot 10^{-28} m^2 \tag{2.1.8}$$

where r_e is the classical electron radius, obtain by equating the electrostatic potential energy with the rest mass energy. Therefore the Total emitted power, which represents also the total energy loss is:

$$P_{Synch} = \frac{2}{3} \frac{c}{\mu_0} \sigma_T \gamma^2 \beta^2 B^2 = \frac{4}{3} \sigma_T c \gamma^2 \beta^2 U_B \tag{2.1.9}$$

where $U_B = B^2/2\mu_0$ is the *magnetic energy density.*

2.1.2 Synchrotron Spectrum

The spectrum of the emitted photons can be calculated by considering the classical *Liénard-Wiechert potentials* and the radiation field (see A.2) in our case of a charge moving in a magnetic field. The radiation field due to a radial acceleration is:

$$\boldsymbol{E}_{rad}(\boldsymbol{r}, t) = \frac{q}{4\pi\varepsilon_0} \left[\frac{\hat{\boldsymbol{n}} \times \left((\hat{\boldsymbol{n}} - \boldsymbol{\beta}) \times \dot{\boldsymbol{\beta}} \right)}{c(1 - \hat{\boldsymbol{n}} \cdot \boldsymbol{\beta})^3 R} \right] \tag{2.1.10}$$

The Pointing vector gives the power emitted per unit of area A:

$$S = \frac{1}{\mu_0} \boldsymbol{E} \times \boldsymbol{B} = \frac{1}{\mu_0 c} |\boldsymbol{E}_{rad}(t)|^2 = \frac{dW}{dt dA} \tag{2.1.11}$$

Thus the energy emitted per unit of area is:

$$\frac{dW}{dA} = c\varepsilon_0 \int_{-\infty}^{+\infty} |\boldsymbol{E}_{rad}(t)|^2 dt \tag{2.1.12}$$

now we introduce the Fourier transform of the radiation field :

$$\begin{aligned} E_{rad}(t) &= \frac{1}{\sqrt{2\pi}} \int_{-\infty}^{+\infty} E_{rad}(\omega) \exp(-i\omega t) d\omega \\ E_{rad}(\omega) &= \frac{1}{\sqrt{2\pi}} \int_{-\infty}^{+\infty} E_{rad}(t) \exp(i\omega t) dt \end{aligned} \tag{2.1.13}$$

where $E_{rad}(t) = |\boldsymbol{E}_{rad}(t)|$. Using the Parseval's theorem we know that:

$$\int_{-\infty}^{+\infty} |\boldsymbol{E}_{rad}(t)|^2 dt = \int_{-\infty}^{+\infty} |E_{rad}(\omega)|^2 d\omega \tag{2.1.14}$$

Since $|E_{rad}(\omega)|^2$ is real and $E_{rad}(\omega)$ is symmetric, we have $\int_{-\infty}^{+\infty} |E^2{}_{rad}(\omega)|^2 d\omega = 2\int_0^{\infty} |E^2{}_{rad}(\omega)|^2 d\omega$ and so the energy emitted per unit of area is:

$$\frac{dW}{dA} = 2c\varepsilon_0 \int_0^{\infty} |E_{rad}(\omega)|^2 d\omega \tag{2.1.15}$$

This implies that the energy emitted per unit frequency and unit of solid angle is:

$$\frac{dW}{d\omega d\Omega} = 2c\varepsilon_0 R^2 |E_{rad}(\omega)|^2 \tag{2.1.16}$$

where we have substituted $dA = R^2 d\Omega$. Inverting the Fourier transform we obtain:

$$\frac{dW}{d\omega d\Omega} = 2c\varepsilon_0 R^2 |E_{rad}(\omega)|^2 = \frac{c\varepsilon_0}{\pi} \left| \int_{-\infty}^{+\infty} R E_{rad}(t) e^{i\omega t} dt \right|^2 \tag{2.1.17}$$

To simplify the notation, is useful evaluate the quantity $RE_{rad}(\omega)$:

$$RE_{rad}(\omega) = \frac{1}{\sqrt{2\pi}} \frac{q}{4\pi\varepsilon_0 c} \int_{-\infty}^{+\infty} \left[\frac{\hat{\boldsymbol{n}} \times \big((\hat{\boldsymbol{n}} - \boldsymbol{\beta}) \times \dot{\boldsymbol{\beta}}\big)}{(1 - \hat{\boldsymbol{n}} \cdot \boldsymbol{\beta})^3} \right] e^{i\omega t} dt \tag{2.1.18}$$

To solve this integral we make a change of variable, using the definition of retarded time $t' = t - R(t')/c$ with $R = |\boldsymbol{r} - \boldsymbol{r}_0|$:

$$dt = \left(\frac{\partial t}{\partial t'} \right) dt' = (1 - \hat{\boldsymbol{n}} \cdot \boldsymbol{\beta}) dt' \tag{2.1.19}$$

and express $e^{i\omega t}$ in terms of t' only: $e^{i\omega t} = \exp\big(i\omega(t' + R/c)\big)$.

We assume the radiation is being observed far enough away from the source, i.e. that $\boldsymbol{r}(t) \gg \boldsymbol{r}_0(t')$, so that $R \simeq r$. Then we expand r to first order in r_0, which gives $R(t') \simeq |\boldsymbol{r}| - \hat{\boldsymbol{n}} \cdot \boldsymbol{r}_0$. Thus we obtain:

$$RE_{rad}(\omega) \simeq \frac{1}{\sqrt{2\pi}} \frac{q}{4\pi\varepsilon_0 c} \int_{-\infty}^{+\infty} \left[\frac{\hat{\boldsymbol{n}} \times \big((\hat{\boldsymbol{n}} - \boldsymbol{\beta}) \times \dot{\boldsymbol{\beta}}\big)}{(1 - \hat{\boldsymbol{n}} \cdot \boldsymbol{\beta})^2} \right] \exp\big(i\omega(t' - \hat{\boldsymbol{n}} \cdot \boldsymbol{r}_0(t')/c)\big) dt' \tag{2.1.20}$$

Then we use the identity :

$$\frac{\hat{\boldsymbol{n}} \times \big((\hat{\boldsymbol{n}} - \boldsymbol{\beta}) \times \dot{\boldsymbol{\beta}}\big)}{(1 - \hat{\boldsymbol{n}} \cdot \boldsymbol{\beta})^2} = \frac{d}{dt'} \left(\frac{\hat{\boldsymbol{n}} \times \big(\hat{\boldsymbol{n}} \times \boldsymbol{\beta}\big)}{(1 - \hat{\boldsymbol{n}} \cdot \boldsymbol{\beta})} \right) \tag{2.1.21}$$

and integrate by parts. Replacing these terms into (2.1.17) we obtain the expression for the energy emitted per unit of frequency per solid angle:

$$\frac{dW}{d\omega d\Omega} = \frac{q^2\omega^2}{16\pi^3\varepsilon_0 c} \left| \int_{-\infty}^{+\infty} \big(\hat{\boldsymbol{n}} \times (\hat{\boldsymbol{n}} \times \boldsymbol{\beta})\big) \exp\big(i\omega(t' - \hat{\boldsymbol{n}} \cdot \boldsymbol{r}_0(t')/c)\big) dt' \right|^2 \tag{2.1.22}$$

This is now in a form that can be integrated. To simplify the integration, we need first to simplify the triple cross product. To do this we have to consider the geometrical meaning of the triple cross product.

Consider a charged particle moving along an orbital trajectory with radius of curvature a.
The coordinate system is set up so that the charge is moving in the xy-plane and passes through the origin at the retarded time $t' = 0$ with an instantaneous velocity in the x-direction.
The versor $\hat{\boldsymbol{e}}_\perp$ is direct along the y axis and $\hat{\boldsymbol{e}}_{/\!/} = \hat{\boldsymbol{n}} \times \hat{\boldsymbol{e}}_\perp$.
Thus, $\hat{\boldsymbol{e}}_{/\!/}$ and $\hat{\boldsymbol{e}}_\perp$ define a plane perpendicular to an observers line of sight defined by the direction $\hat{\boldsymbol{n}}$. This is the plane of propagation, defined by the triple cross product $\hat{\boldsymbol{n}}\times(\hat{\boldsymbol{n}}\times\boldsymbol{\beta})$ in the integral.

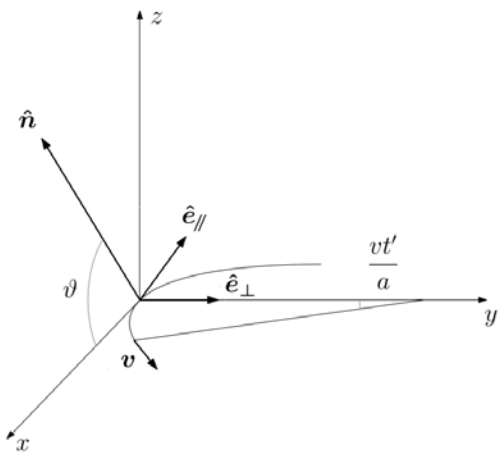

The magnetic field B must also be in the plane containing $\hat{\boldsymbol{n}}$ and β , so $\hat{\boldsymbol{e}}_{/\!/}$ and $\hat{\boldsymbol{e}}_\perp$ define directions parallel and perpendicular to the projection of the magnetic field on the propagation plane.

At any arbitrary retarded time t', for $|\beta| \simeq 1$, we have:

$$\hat{\boldsymbol{n}} \times (\hat{\boldsymbol{n}} \times \boldsymbol{\beta}) = \hat{\boldsymbol{e}}_{/\!/} \cos\left(\frac{vt'}{a}\right) \sin\vartheta - \hat{\boldsymbol{e}}_\perp \sin\left(\frac{vt'}{a}\right) \tag{2.1.23}$$

The exponential term in the integral (2.1.22) is simplified using a small angle expansion:

$$t' - \frac{\hat{\boldsymbol{n}} \cdot \boldsymbol{r}_0(t')}{c} = t' - \frac{a}{c}\cos\vartheta \sin\left(\frac{vt'}{a}\right) \simeq \frac{1}{2\gamma^2}\left[(1+\gamma^2\vartheta^2)t' + \frac{c^2\gamma^2 t'^3}{3a^2}\right] \tag{2.1.24}$$

where $1 - v/c \simeq 1/2\gamma^2$ and $v \simeq c$, ultra-relativistic regime. Now we calculate the spectrum in the two polarization states:

$$\frac{dW}{d\omega d\Omega} = \frac{dW_{/\!/}}{d\omega d\Omega} + \frac{dW_\perp}{d\omega d\Omega} \tag{2.1.25}$$

defined as:

$$\begin{aligned} \frac{dW_{/\!/}}{d\omega d\Omega} &= \frac{q^2\omega^2\vartheta^2}{16\pi^3\varepsilon_0 c}\left|\int \exp\left[\frac{i\omega}{2\gamma^2}\left(\vartheta_\gamma^2 t' + \frac{c^2\gamma^2 t'^3}{3a^2}\right)\right]dt'\right|^2 \\ \frac{dW_\perp}{d\omega d\Omega} &= \frac{q^2\omega^2}{16\pi^3\varepsilon_0 c}\left|\int \frac{ct'}{a}\exp\left[\frac{i\omega}{2\gamma^2}\left(\vartheta_\gamma^2 t' + \frac{c^2\gamma^2 t'^3}{3a^2}\right)\right]dt'\right|^2 \end{aligned} \tag{2.1.26}$$

where $\vartheta_\gamma^2 = 1 + \gamma^2\vartheta^2$, now we make another change of variables:

$$y \equiv \gamma\frac{ct'}{a\vartheta_\gamma} \qquad \eta \equiv \frac{\omega a \vartheta_\gamma^3}{3c\gamma^3} \tag{2.1.27}$$

$$\begin{aligned} \frac{dW_{/\!/}}{d\omega d\Omega} &= \frac{q^2\omega^2\vartheta^2}{16\pi^3\varepsilon_0 c}\left(\frac{a\theta_\gamma}{\gamma c}\right)^2\left|\int \exp\left[\frac{3}{2}i\eta\left(y + \frac{1}{3}y^3\right)\right]dy\right|^2 \\ \frac{dW_\perp}{d\omega d\Omega} &= \frac{q^2\omega^2\vartheta^2}{16\pi^3\varepsilon_0 c}\left(\frac{a\theta_\gamma^2}{\gamma^2 c}\right)^2\left|\int y\exp\left[\frac{3}{2}i\eta\left(y + \frac{1}{3}y^3\right)\right]dy\right|^2 \end{aligned} \tag{2.1.28}$$

These integrals can be expressed in terms of the modified Bessel function of 1/3-rd and 2/3-rd order:

$$\frac{dW_{/\!/}}{d\omega d\Omega} = \frac{q^2\omega^2\vartheta^2}{16\pi^3\varepsilon_0 c}\left(\frac{a\theta_\gamma}{\gamma c}\right)^2 K_{1/3}^2(\eta) \qquad \frac{dW_\perp}{d\omega d\Omega} = \frac{q^2\omega^2\vartheta^2}{16\pi^3\varepsilon_0 c}\left(\frac{a\theta_\gamma^2}{\gamma^2 c}\right)^2 K_{2/3}^2(\eta) \tag{2.1.29}$$

We next integrate over the solid angle to give the energy per frequency per orbit, emitted by the charge in the plane of propagation. Along one orbit, the emission is almost completely confined within an angle $1/\gamma$ around a cone of half-angle α (the pitch angle). So we use $d\Omega \simeq 2\pi sin\alpha d\vartheta$. Thus,

$$\begin{aligned} \frac{dW_{/\!/}}{d\omega d\Omega} &\simeq \frac{q^2\omega^2 a^2 \sin\alpha}{6\pi^2\varepsilon_0 c^3\gamma^2} \int \vartheta_\gamma^2 \vartheta^2 K_{1/3}^2(\eta) \\ \frac{dW_\perp}{d\omega d\Omega} &= \frac{q^2\omega^2 a^2 \sin\alpha}{6\pi^2\varepsilon_0 c^3\gamma^4} \int \vartheta_\gamma^4 K_{2/3}^2(\eta) \end{aligned} \tag{2.1.30}$$

These integrals were first solved by Westfold [51] and the results are:

$$\begin{aligned} \frac{dW_{/\!/}}{d\omega d\Omega} &\simeq \frac{\sqrt{3}q^2\gamma \sin\alpha}{8\pi^2\varepsilon_0 c}[F(x) - G(x)] \\ \frac{dW_\perp}{d\omega d\Omega} &= \frac{\sqrt{3}q^2\gamma \sin\alpha}{8\pi^2\varepsilon_0 c}[F(x) + G(x)] \end{aligned} \tag{2.1.31}$$

where

$$F(x) \equiv x \int_x^\infty K_{5/3}(\zeta) d\zeta \qquad G(x) \equiv x K_{5/3}(x) \tag{2.1.32}$$

and $x = \omega/\omega_c$, where $\omega_c = \frac{3}{2}\frac{qB}{m}\gamma^2 \sin\alpha$ is the critical frequency, above this frequency the spectrum results significantly suppressed.

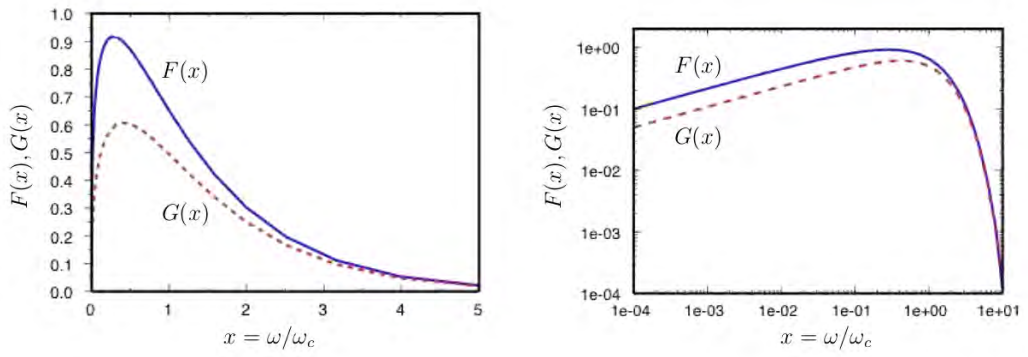

Figure 2.1: The functions $F(x)$ and $G(x)$ that appear in the synchrotron power spectrum are plotted in linear and logarithmic scales. .

To obtain from these equations the power per unit of frequency, we divide by the orbital period $T = \frac{2\pi\gamma m}{qB}$, and this gives:

$$\begin{aligned} P_{/\!/}(\omega) &= \frac{\sqrt{3}q^3 B \sin\alpha}{16\pi^2\varepsilon_0 mc}[F(x) - G(x)] \\ P_\perp(\omega) &= \frac{\sqrt{3}q^3 B \sin\alpha}{16\pi^2\varepsilon_0 mc}[F(x) + G(x)] \end{aligned} \tag{2.1.33}$$

These are the components of the power per unit of frequency emits by a single charge corresponding to polarisation modes $/\!/$ and $\perp$ to $\boldsymbol{B}$. The total synchrotron power per unit of frequency is then:

$$P(\omega) = P_{/\!/}(\omega) + P_\perp(\omega) = \frac{\sqrt{3}q^3 B \sin\alpha}{8\pi^2\varepsilon_0 mc} F(x) \tag{2.1.34}$$

The main implications of the synchroton spectrum are that the emission is broadband ($\Delta\omega/\omega \sim 1$), the spectrum is a power-law at small x and the emission peak is near $x \simeq 0.3$.

2.2 Compton Scattering

Compton scattering occurs when a photon is scattered by an electron (or positron).
In this process $\gamma + e^- \to \gamma + e^-$ we have an electron and a photon in the initial and final state.
We discuss Compton scattering in the general case, but we are more interested in high energies processes. For low photon energies, it reduce to the classical case of Thomson scattering. For relativistic electrons, low energy photons can be efficiently upscattered to high energy photons. This process is called Inverse Compton scattering and it is probably the main mechanism of VHE γ-rays production.

2.2.1 Relativistic Kinematics in Compton Scattering

Consider a photon of energy E_γ scattering on an electron of energy E. In the observer 's reference frame they can be represented by the four-momenta $k = (E_\gamma, \boldsymbol{k}c)$ and $p = (E, \boldsymbol{p}c)$.
Now for the sake of simplicity we assume that they collide head on along the z-axis, and that the photon is moving forward. Later we will face with a more general setup.
To study this process is useful switch to the reference frame where the electron is at the rest. This is the Rest Frame of the system and all quantities are denoted by 0 as subscript.

$$\begin{aligned} k_0 &= \big(E_{\gamma,0}, 0, 0, |k_0|c\big) \qquad & k_0' &= \big(E'_{\gamma,0}, |k_0'|c\sin\theta_0, 0, |k_0'|c\cos\theta_0\big) \\ p_0 &= \big(m_e c^2, 0, 0, 0\big) & p_0' &= \big(E_0', -|p_0|c\sin\phi_0, 0, -|p_0|c\cos\phi_0\big) \end{aligned} \tag{2.2.1}$$

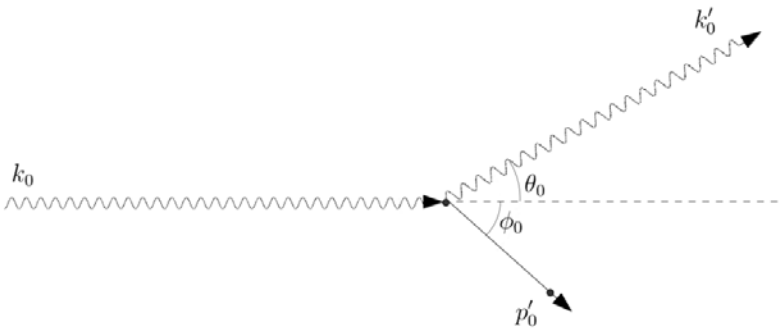

Figure 2.2: Compton Scattering in the Rest Frame.

The conservation of four-momenta is written as $k_0 + p_0 = k_0' + p_0'$, or, in components:
• Energy conservation $E_{\gamma,0} + m_e c^2 = E'_{\gamma,0} + E_0'$
• Tri-momenta conservation $|p_0'|^2 = |k_0|^2 + |k_0'|^2 - 2|k_0||k_0'|\cos\theta_0$
Equating conservation laws we obtain:

$$(E_{\gamma,0} - E'_{\gamma,0} + m_e c^2)^2 - m_e^2 c^4 = E_{\gamma,0}^2 + E'^{\,2}_{\gamma,0} - 2E_{\gamma,0}E'_{\gamma,0}\cos\theta_0 \tag{2.2.2}$$

the energy of scattered photon $E'_{\gamma,0}$ in the rest frame is :

$$E'_{\gamma,0} = \frac{m_e c^2 E_{\gamma,0}}{m_e c^2 + E_{\gamma,0}(1-\cos\theta_0)} \quad \to \quad E'_{\gamma,0} = \frac{E_{\gamma,0}}{1 + x(1-\cos\theta_0)} \qquad x = \frac{E_{\gamma,0}}{m_e c^2} \tag{2.2.3}$$

We can note that in the rest frame $E'_{\gamma,0} \leq E_{\gamma,0}$ but we have to boost this result in the observer 's reference frame. We are able to distinguish two different regimes: Thomson limit $x \ll 1$ and extreme Klein-Nishina limit $x \gg 1$.

To describe the photon scattered in the observer 's reference frame we have to apply the boost matrix $\mathcal{B}_z$ along z-axis to k'_0 and k_0 four-vectors, where $\beta = \frac{pc}{E}$ and $\gamma = \frac{1}{\sqrt{1-\beta^2}} = \frac{E}{m_e c^2}$.

$$k' = \mathcal{B}_z(-\beta)k'_0 = \begin{pmatrix} E'_\gamma \\ |k'|c\sin\theta \\ 0 \\ |k'|c\cos\theta \end{pmatrix} = \begin{pmatrix} \gamma & 0 & 0 & -\beta\gamma \\ 0 & 1 & 0 & 0 \\ 0 & 0 & 1 & 0 \\ -\beta\gamma & 0 & 0 & \gamma \end{pmatrix} \begin{pmatrix} E'_{\gamma,0} \\ |k'_0|c\sin\theta_0 \\ 0 \\ |k'_0|c\cos\theta_0 \end{pmatrix} \tag{2.2.4}$$

From the first component of the four-vector k'_0 we obtain the relativistic Doppler shift formula for the scattered photon:

$$E'_\gamma = \gamma E'_{\gamma,0}(1 - \beta\cos\theta_0) \tag{2.2.5}$$

With the same boost applied to the four-vector of the incoming photon $k = \mathcal{B}_z(-\beta)k_0$ we obtain the respective energy relation $E_\gamma = \gamma(1-\beta)E_{\gamma,0}$. To simplify our steps is more comfortable to multiply both member of the last equation for $\gamma(1+\beta)$ and get $E_{\gamma,0} = \gamma(1+\beta)E_\gamma = E_\gamma\frac{E+pc}{m_e c^2}$. Substituing we obtain:

$$E'_\gamma = \frac{\gamma^2 m_e c^2 E_\gamma(1+\beta)(1-\beta\cos\theta_0)}{m_e c^2 + \gamma E_\gamma(1+\beta)(1-\cos\theta_0)} = \frac{E E_\gamma(E+pc)(1-\beta\cos\theta_0)}{m_e^2 c^4 + E_\gamma(E+pc)(1-\cos\theta_0)} \tag{2.2.6}$$

Let us discuss the two regimes, function of x parameter:

• Thomson limit $x \ll 1$
In this condition we have that $E'_\gamma \simeq E_{\gamma,0}$ and so we obtain:

$$E'_\gamma \simeq \gamma^2 E_\gamma(1+\beta)(1-\beta\cos\theta_0) \tag{2.2.7}$$

If $\beta \to 1$ we have $E'_{\gamma,min} \approx E'_\gamma$ for $\theta_0 = 0$ and $E'_{\gamma,max} \approx 4\gamma^2 E_\gamma$ for $\theta_0 = \pi$.
In this case a low energy photon have a light interaction with relativistic electron.

• Extreme Klein-Nishina limit $x \gg 1$
In this case is useful to rescale the energy in units of $m_e c^2$, so we write $\tilde{E}_\gamma = E_\gamma/m_e c^2$.

$$E'_\gamma = E\frac{\gamma\tilde{E}_\gamma(1+\beta)(1-\beta\cos\theta_0)}{1+\gamma\tilde{E}_\gamma(1+\beta)(1-\cos\theta_0)} \tag{2.2.8}$$

with $\beta \to 1$ we obtain:

$$E'_\gamma = E\frac{b}{1+b} \qquad b = 4\gamma\tilde{E}_\gamma \tag{2.2.9}$$

In the high energy limit $b \gg 1$ therefore $E'_\gamma \to E$. This means that the relativistic electron has an hard interaction with the photon and it transfers all its kinetic energy to the photon.

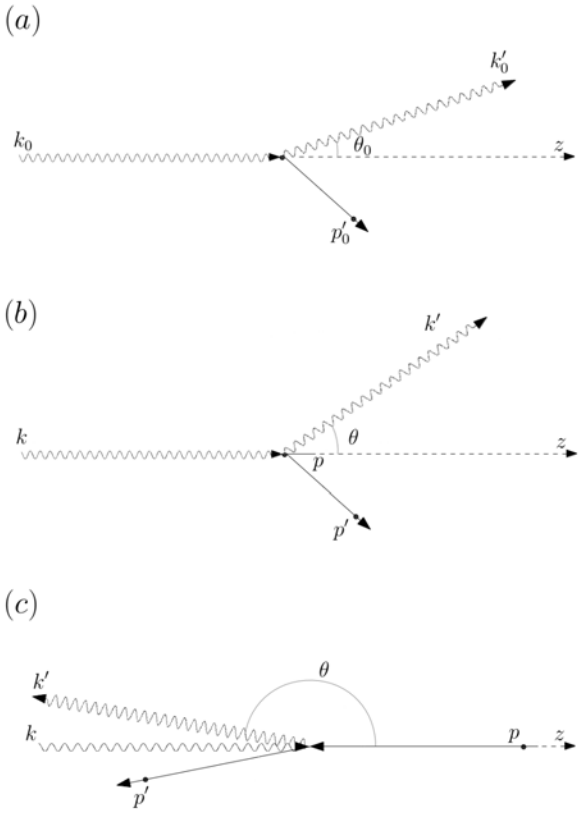

Figure 2.3: The same scattering event in the rest frame (a) and in the observer's reference frame in two different regimes: (b) Thomson limit and (c) Extreme K-N limit.

The emission angle in the two reference frames could be related dividing the second component of k' for the fourth obtaining the following relation:

$$\tan\theta = \frac{\sin\theta_0}{\gamma(\cos\theta_0 - \beta)} \tag{2.2.10}$$

If $\beta \approx 0$ we find again the rest frame description of the process, instead in the ultra-relativistic limit $\beta \to 1$ the photon is scattered backward with $\tan\theta \approx -\gamma^{-1}\cot\theta_0/2$.

Now we consider a more general situation. We assume that electron is moving backward along the z-axis and that the scattering process takes place in the same xy-plane for the sake of semplicity.

The initial and final states of the photon and the electron could be represented by the following four-momenta:

$$\begin{array}{ll} k = \big(E_\gamma, \boldsymbol{k}c\big) & k' = \big(E'_\gamma, \boldsymbol{k}'c\big) \\ p = \big(E, \boldsymbol{p}c\big) & p' = \big(E', \boldsymbol{p}'c\big) \end{array} \tag{2.2.11}$$

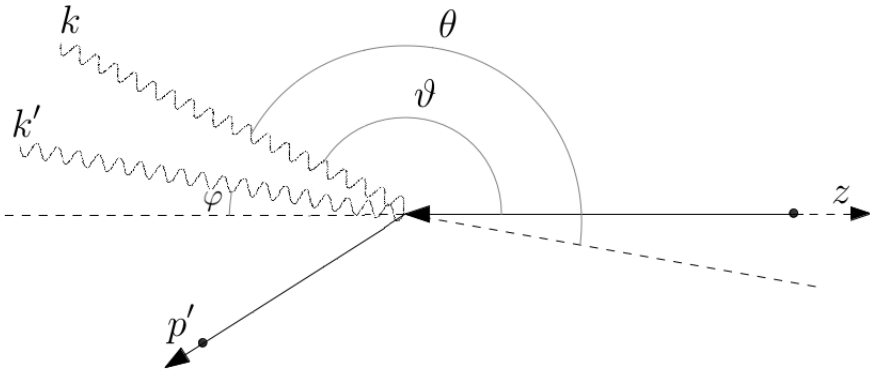

Figure 2.3: Compton Scattering in the observer 's reference frame.

Where:
ϑ the angle between the direction of the incoming electron and the incoming photon,
φ the angle between the direction of the incoming electron and the scattered photon,
θ the angle between the direction of the incoming photon and the scattered photon.

The four-momentum conservation $p + k = p' + k'$ implies that:

$$(pk) = (p'k') = (p + k - k')k' = (pk') + (kk') \tag{2.2.12}$$

expliciting the four-vectors we have:

$$EE_\gamma - \boldsymbol{pk}c^2 = E'_\gamma - \boldsymbol{pk}'c^2 + E_\gamma E'_\gamma(1 - \cos\theta) \tag{2.2.13}$$

and substituting we obtain

$$E_\gamma(1 - \beta\cos\vartheta) = E'_\gamma(1 - \beta\cos\varphi) + \frac{E_\gamma E'_\gamma}{E}(1 - \cos\theta) \tag{2.2.14}$$

the energy of scattered photon E'_γ in the observer 's reference frame, where $\beta = \dfrac{|\boldsymbol{p}|c}{E}$, is then

$$E'_\gamma = E_\gamma \frac{1 - \beta\cos\vartheta}{1 - \beta\cos\varphi + \frac{E_\gamma}{E}(1 - \cos\theta)} \tag{2.2.15}$$

If $\beta \approx 0$ we find again the result obtained in the rest reference frame. In the Extreme Klein-Nishina limit we have $\vartheta \approx \theta \approx \pi$ and $\varphi \approx 0$, hence in the ultra relativistic limit $\beta \to 1$ we obtain again $E'_\gamma \to E$.

2.2.2 Compton Scattering in Quantum Electrodynamics

We are interested in high-energy processes so we have to consider quantum effects. Now we derive the differential cross section for unpolarized Compton scattering describing the lower order interaction in perturbative Quantum Electrodynamics. In this section we use natural units where $c = \hbar = 1$ and the Feynman slash notation.

In the initial state we have an electron with momentum $p = (E, \boldsymbol{p})$ in the spin state $u = u_s(\boldsymbol{p})$, and a photon with momentum $k = (\omega, \boldsymbol{k})$ and polarization vector $\varepsilon = \varepsilon_r(\boldsymbol{k})$. In the final state we have the corresponding quantities $p' = (E', \boldsymbol{p}')$ $u' = u'_{s'}(\boldsymbol{p}')$ and $k' = (\omega', \boldsymbol{k}')$ $\varepsilon = \varepsilon'_{r\ '}(\boldsymbol{k}')$.

This process is described by two independent Feynman diagrams showed in Figure 2.4.

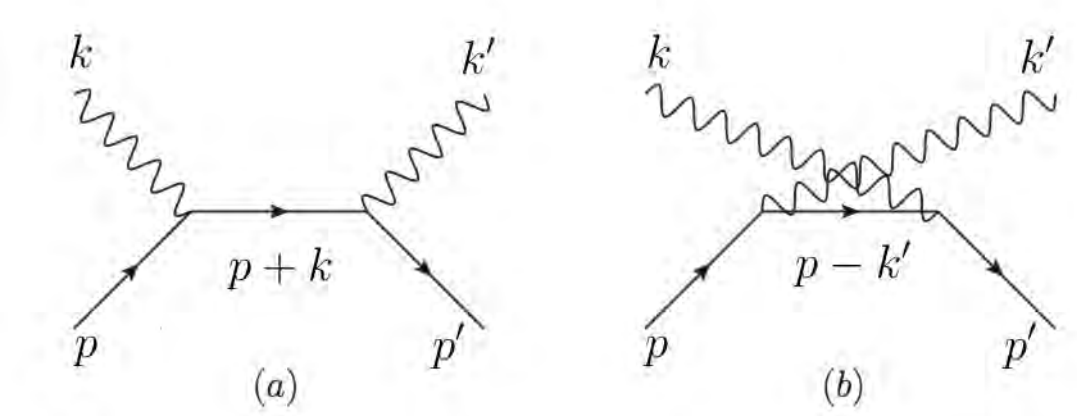

Figure 2.4: Feynman Diagrams for $\gamma + e^- \to \gamma + e^-$.

With Feynman rules for QED we can obtain the Feynman amplitudes from diagrams:

$$\begin{aligned} (a) \qquad & \mathcal{M}_a = \bar{u}'\varepsilon'^*_\mu (iq\gamma^\mu)\frac{i(\not{p} + \not{k} + m)}{(p+k)^2 - m^2}(iq\gamma^\nu)\varepsilon_\nu u \\ (b) \qquad & \mathcal{M}_b = \bar{u}'\varepsilon^*_\mu (iq\gamma^\mu)\frac{i(\not{p} - \not{k}' + m)}{(p-k')^2 - m^2}(iq\gamma^\nu)\varepsilon'_\nu u \end{aligned} \tag{2.2.16}$$

To obtain unpolarized Feynman amplitude we have to average over initial polarization and sum over the final polarization.

$$\overline{|\mathcal{M}|^2} = \frac{1}{4}\sum_{r,s}\sum_{r\ ',s'}|\mathcal{M}|^2 = \frac{1}{4}\sum_{r,s}\sum_{r\ ',s'}\mathcal{M}^*\mathcal{M} \tag{2.2.17}$$

We are interested in calculating the differential cross section for the process and we know that it is proportional to the squared Feynman amplitude:

$$\frac{d\sigma}{d\Omega} \propto \overline{|\mathcal{M}_a + \mathcal{M}_b|^2} = \overline{|\mathcal{M}_a|^2} + \overline{|\mathcal{M}_b|^2} + \overline{\mathcal{M}_a^*\mathcal{M}_b} + \overline{\mathcal{M}_a\mathcal{M}_b^*} \tag{2.2.18}$$

so we start to calculate the first term using relations (2.2.16) and (2.2.17);

$$\overline{|\mathcal{M}_a|^2} = \frac{1}{4}\frac{q^4}{((p+k)^2 - m^2)^2}\sum_{r,s}\sum_{r\ ',s'}\bar{u}'\varepsilon'^*_\mu\gamma^\mu(\not{p} + \not{k} + m)\gamma^\nu\varepsilon_\nu u\bar{u}'\varepsilon^*_\sigma\gamma^\sigma(\not{p} + \not{k} + m)\gamma^\rho\varepsilon'_\rho u \tag{2.2.19}$$

where the spin summation for the electron states can be performed using relations [1]

$$\sum_{s=1}^{2} u(p)\bar{u}(p) = \not{p} + m \qquad \sum_{s'=1}^{2} u(p')\bar{u}(p') = \not{p}' + m \tag{2.2.20}$$

and the summation for the photon polarization can be perfomed using the relations for real photons:

$$\sum_{r=1}^{2} \varepsilon_\sigma^* \varepsilon_\nu = -\eta_{\sigma\nu} \qquad \sum_{r\,'=1}^{2} \varepsilon_\mu'^* \varepsilon_\rho' = -\eta_{\mu\rho} \tag{2.2.21}$$

Expliciting spinorial indexes we can note that these summations can be written as a trace of γ-matrices products.

$$\overline{|\mathcal{M}_a|^2} = \frac{1}{4}\frac{q^4}{((p+k)^2-m^2)^2} Tr\left[\gamma_\mu(\not{p}'+m)\gamma^\mu(\not{p}+\not{k}+m)\gamma_\nu(\not{p}+m)\gamma^\nu(\not{p}+\not{k}+m)\right] \tag{2.2.22}$$

It is useful to introduce the Lorentz invariant Mandelstam variables s, t, u, according to four-momentum conservation. From these, we obtain useful conditions to calculate the traces.

$$\begin{aligned}
&s = (p+k)^2 = (p'+k')^2 = 2pk + m^2 = 2p'k' + m^2 && pk = p'k' \\
&t = (p-p')^2 = (k-k')^2 = -2pp' + 2m^2 = -2k'k' && kk' = pp' - m^2 \\
&u = (p-k')^2 = (p'-k)^2 = -2pk' + m^2 = -2p'k + m^2 && pk' = p'k \\
&s+t+u = 2m^2 \qquad pp = p'p' = m^2 \qquad kk = k'k' = 0
\end{aligned} \tag{2.2.23}$$

The calculation of the trace is just a mechanical procedure and is given in Appendix B.
The result is:

$$\overline{|\mathcal{M}_a|^2} = \frac{2q^4}{(s-m^2)^2}\left[4m^4 - (s-m^2)(u-m^2) + 2m^2(s-m^2)\right] \tag{2.2.24}$$

Note that the effect of the substitution $k \to -k'$ and $s \rightleftharpoons u$ allows to obtain:

$$\overline{|\mathcal{M}_b|^2} = \frac{2q^4}{(u-m^2)^2}\left[4m^4 - (u-m^2)(s-m^2) + 2m^2(u-m^2)\right] \tag{2.2.25}$$

The interference terms can be obtained in the same way calculating the traces. The evaluation can be semplified if we realize that $\mathcal{M}_a{}^*\mathcal{M}_b = \mathcal{M}_a\mathcal{M}_b{}^*$.

$$\overline{\mathcal{M}_a{}^*\mathcal{M}_b} + \overline{\mathcal{M}_a\mathcal{M}_b{}^*} = \frac{4q^4}{(s-m^2)(u-m^2)}\left[4m^4 + m^2(s-m^2) + m^2(u-m^2)\right] \tag{2.2.26}$$

Finally we obtain the Feynman amplitude for Compton scattering:

$$\overline{|\mathcal{M}_a + \mathcal{M}_b|^2} = 2q^4\left[4m^4\left(\frac{1}{s-m^2}+\frac{1}{u-m^2}\right)^2 + 4m^2\left(\frac{1}{s-m^2}+\frac{1}{u-m^2}\right) - \left(\frac{u-m^2}{s-m^2}+\frac{s-m^2}{u-m^2}\right)\right] \tag{2.2.27}$$

[1] N.B. There is another common normalization $\sum_{s=1}^{2} u(p)\bar{u}(p) = \frac{\not{p}+m}{2m}$ used in several books.

2.2.3 The Klein-Nishina formula

The Feynman amplitude $\overline{|\mathcal{M}_a + \mathcal{M}_b|^2}$ is an invariant quantity and it could be used to evaluate differential cross section in any reference frame.

In this section we calculate the differential cross section in the rest frame, using Mandelstam variables and the results obtained in 2.2.1.

$$\begin{aligned} &s = (p+k)^2 = m^2 + 2m\omega \qquad u = (p-k')^2 = m^2 - 2m\omega' \\ &\omega' = \frac{\omega}{1 + \frac{\omega}{m}(1-\cos\theta)} \quad \rightarrow \quad \left(\frac{1}{\omega} - \frac{1}{\omega'}\right) = \frac{(\cos\theta - 1)}{m} \end{aligned} \tag{2.2.28}$$

So the Feynman amplitude in the rest frame is:

$$\begin{aligned} \overline{|\mathcal{M}_a + \mathcal{M}_b|^2}_{RF} &= 2q^4\left[4m^4\left(\frac{\cos\theta - 1}{2m^2}\right)^2 + 4m^2\left(\frac{\cos\theta - 1}{2m^2}\right) + \frac{\omega'}{\omega} + \frac{\omega}{\omega'}\right] \\ &= 2q^4\left[\frac{\omega'}{\omega} + \frac{\omega}{\omega'} - \sin^2\theta\right] \end{aligned} \tag{2.2.29}$$

The differential cross section in the rest frame is called Klein-Nishina formula and could be written using the equation obtained in B.2.1 where $E = \omega$ and the dimensionless fine structure constant is $\alpha = \frac{q^2}{4\pi}$.

$$\left(\frac{d\sigma_{KN}}{d\Omega'}\right)_{RF} = \frac{\alpha^2}{2m^2}\left(\frac{\omega'}{\omega}\right)^2\left[\frac{\omega'}{\omega} + \frac{\omega}{\omega'} - \sin^2\theta\right] \tag{2.2.30}$$

• In the low-energy limit $\omega \ll m$, we have $\omega' \approx \omega$ and the differential cross section reduces to:

$$\left(\frac{d\sigma}{d\Omega'}\right)_{RF} = \frac{\alpha^2}{2m^2}\left[1 + \cos^2\theta\right] \tag{2.2.31}$$

The total cross section could be easily evaluated integrating in $d\cos\theta$:

$$\sigma = \int \frac{d\sigma}{d\Omega'} = 2\pi\frac{\alpha^2}{2m^2}\int_{-1}^{1} d\cos\theta(1 + \cos^2\theta) = \frac{8\pi}{3}\frac{\alpha^2}{m^2} \qquad \sigma_T = \frac{8\pi}{3}r_e^2 \simeq 0.665 \cdot 10^{-28} m^2 \tag{2.2.32}$$

where σ_T is the Thomson cross section classically derivable from interaction between an electron and classical electromagnetic field, where $r_e = \frac{\alpha}{m}$ is the classical electron radius.

• In the high-energy limit $\omega \gg m$. We work in CoM frame, more comfortable in this case.
The Mandelstam variables are: $s \approx 4\omega^2$ and $u \approx 2\omega^2(1 + \cos\theta)$.

With the condition $m \approx 0$:

$$\overline{|\mathcal{M}_a + \mathcal{M}_b|^2} \simeq 2q^4\left[\frac{u}{s} + \frac{s}{u}\right] = 2q^4\left[1 + \cos\theta + \frac{1}{1 + \cos\theta}\right] \tag{2.2.33}$$

So that the differential cross section in the CoM results:

$$\left(\frac{d\sigma}{d\Omega'}\right)_{CoM} = \frac{\alpha^2}{2s}\left[1 + \cos\theta + \frac{1}{1 + \cos\theta}\right] \tag{2.2.34}$$

In the international system of units $E_{\gamma,0} = \hbar\omega_0 = h\nu_0$ and $r_e = \dfrac{1}{4\pi\varepsilon_0}\dfrac{q^2}{m_e c^2}$, we define an auxiliary variable $x = E_{\gamma,0}/m_e c^2$ and rewrite the Klein Nishina differential cross section:

$$\left(\frac{d\sigma_{KN}}{d\Omega'}\right)_{RF} = \frac{r_e^2}{2}\left(\frac{1}{1+x(1-\cos\theta)}\right)^2\left[1+\cos^2\theta+\frac{x^2(1-\cos\theta)^2}{1+x(1-\cos\theta)}\right] \tag{2.2.35}$$

The total cross section can be found integrating in the solid angle Ω'.

$$\sigma_{KN} = 2\pi r_e^2\left[\frac{1+x}{x^3}\left(\frac{2x(1+x)}{1+2x}-\ln(1+2x)\right)+\frac{\ln(1+2x)}{2x}-\frac{1+3x}{(1+2x)^2}\right] \tag{2.2.36}$$

- Thomson limit $\quad x \ll 1$

$$\sigma \simeq \sigma_T\left[1-2x+\frac{26x^2}{5}+\cdots\right]$$

- Extreme K-N limit $\quad x \gg 1$

$$\sigma \simeq \frac{3}{8}\frac{\sigma_T}{x}\left[\ln(2x)+\frac{1}{2}\right]$$

where: $\sigma_T \simeq 0.665\ b$ (2.2.37)

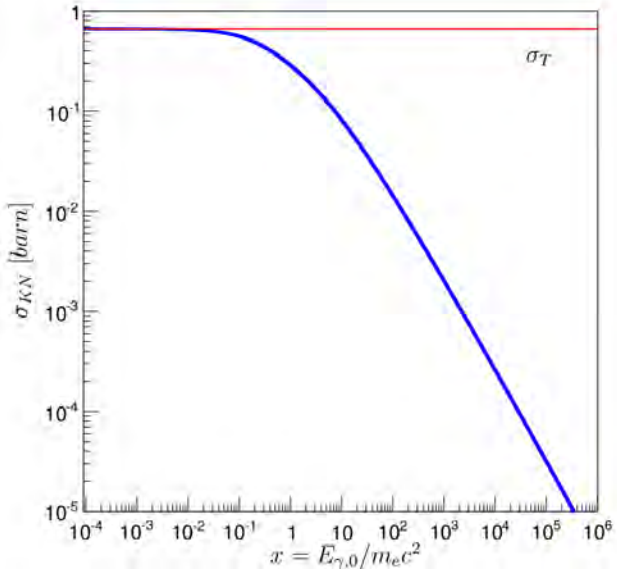

Figure 2.5: Klein Nishina Cross Section.

The angular distribution of the differential cross section showed in Fig.2.5 give us relevant information about the Inverse Compton scattering for several values of x.

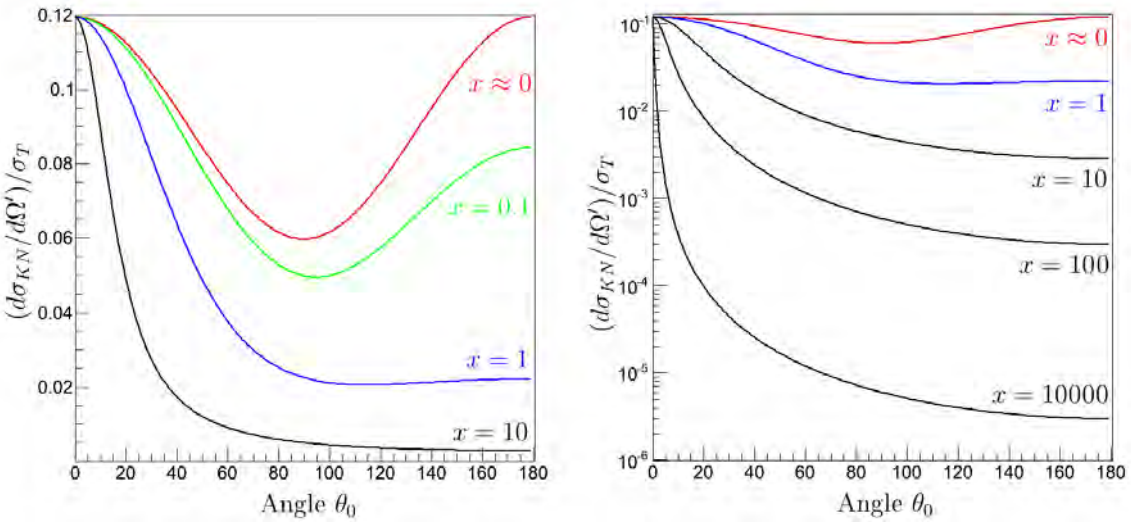

Figure 2.6: Angular distribution in linear and logarithmic scale for different values of x.

Note that at high photon energies we find preferentially forward scattering.

2.2.4 Energy loss rate and Spectrum for single scattering

We want to obtain an expression of the average electron energy loss rate due to inverse Compton scattering into photons with distribution $n(E_\gamma)$.

In the general case the total loss rate per electron could be computed from:

$$\frac{dE}{dt} = \int (E'_\gamma - E_\gamma)\left(\frac{dN_\gamma}{dtdE'_\gamma}\right)dE'_\gamma = \frac{dE'_\gamma}{dt} - \frac{dE_\gamma}{dt} \tag{2.2.38}$$

where $\dfrac{dN_\gamma}{dtdE'_\gamma}$ is the *Compton Spectrum of scattered photons* for a single relativistic electron and it can be written in the most general way as:

$$\frac{dN_\gamma}{dtdE'_\gamma} = n(E'_\gamma, E_\gamma)c\left(\frac{d\sigma_{KN}}{d\Omega dE'_\gamma}\right)d\Omega dE'_\gamma dE_\gamma \tag{2.2.39}$$

The electron energy loss rate and scattering rate are invariant quantities and usually were calculated in the rest frame. Now for the sake of simplicity we calculate the electron energy loss in the Thomson limit and then we quote the general results from several authors.

• Thomson limit

In this regime we can simply calculate the electron energy loss assuming an isotropic distribution of photons. In the rest frame the scattering rate is:

$$\frac{dN_\gamma}{dt} = \sigma_T c \int n(E_{\gamma,0})dE_{\gamma,0} \tag{2.2.40}$$

where $n(E_{\gamma,0})$ is the numerical density of photons at some given energy $E_{\gamma,0}$. Considering the invariant quantities and knowing that also $n(E_{\gamma,0})dE_{\gamma,0}/E_{\gamma,0}$ is invariant, we obtain:

$$\begin{aligned} \frac{dE_\gamma}{dt} &= \sigma_T c \int E_\gamma n(E_\gamma)dE_\gamma \\ \frac{dE'_\gamma}{dt} &= \frac{dE'_{\gamma,0}}{dt} = \sigma_T c \int E'_{\gamma,0} n(E_{\gamma,0})dE_{\gamma,0} = \sigma_T c \int {E'}^2_{\gamma,0}\frac{n(E_{\gamma,0})}{E_{\gamma,0}}dE_{\gamma,0} \end{aligned} \tag{2.2.41}$$

in the Thomson limit $E'_{\gamma,0} \simeq E_{\gamma,0}$ therefore we obtain:

$$\frac{dE'_\gamma}{dt} = \sigma_T c \int {E^2}_{\gamma,0}\frac{n(E_\gamma)}{E_\gamma}dE_\gamma \tag{2.2.42}$$

substituing with $E_{\gamma,0} = \gamma E_\gamma(1 - \beta\cos\vartheta)$ where ϑ is the angle between the electron velocity and the incoming photon

$$\frac{dE'_\gamma}{dt} = \sigma_T c\gamma^2 \int (1 - \beta\cos\vartheta)^2 E_\gamma n(E_\gamma)dE_\gamma \tag{2.2.43}$$

For an isotropic distribution of photons, we have $\langle(1 - \beta\cos\vartheta)^2\rangle_{iso} = 1 + \dfrac{1}{3}\beta^2$ giving:

$$\frac{dE'_\gamma}{dt} = \sigma_T c\gamma^2\left(1 + \frac{1}{3}\beta^2\right)U_\gamma \tag{2.2.44}$$

where $U_\gamma = \int E_\gamma n(E_\gamma)dE_\gamma$ is the initial photon energy density.

The net power converted into increased radiation from Inverse Compton scattering P_{IC} is this quantity minus the rate of the initial photon energy distribution and corresponds to the electron energy loss rate. Remembering that $\gamma^2 - 1 = \gamma^2\beta^2$ we finally obtain

$$\frac{dE}{dt} = \frac{dE'_\gamma}{dt} - \frac{dE_\gamma}{dt} = P_{IC} = \frac{4}{3}\sigma_T c\gamma^2\beta^2 U_\gamma \tag{2.2.45}$$

This expression is identical to the synchroton energy loss, once the radiation energy density U_γ is replaced by the magnetic energy density U_B.

$$\frac{P_{IC}}{P_{Sync}} = \frac{U_\gamma}{U_B} \tag{2.2.46}$$

The reasons of this remarkable similarity is that synchroton radiation can be viewed as Compton scattering of the virtual photons of the static magnetic field. This similarity can be observed also in the spectrum as we will see in the SSC model.

• General case and Klein-Nishina regime

The Spectrum of photons scattered by a high-energy electron in the general case can be analytically calculated from (2.2.39) using the differential Klein Nishina cross section ad the result is the following (Jones, Blumenthal and Gould):

$$\frac{dN_\gamma}{dtdE'_\gamma} = \frac{3}{4}\frac{\sigma_T c}{\gamma^2}\int \frac{n(E_\gamma)}{E_\gamma}\left(2q\ln q + (1+2q)(1-q) + \frac{1}{2}\frac{(4\gamma E_\gamma q)^2}{(1+4\gamma E_\gamma q)}(1-q)\right)dE_\gamma \tag{2.2.47}$$

where for sake of semplicity we define $q = \dfrac{E'_\gamma}{4\gamma^2 E_\gamma(1-z)} = \dfrac{z}{b(1-z)}$ and $z = \dfrac{E'_\gamma}{E}$.

The energy-loss rate of an electron with energy E, due to Inverse Compton scattering in isotropic field of photons E_γ is given by the equation (2.2.38) where using (2.2.47) we obtain:

$$\begin{aligned}\frac{dE}{dt} = \frac{3}{4}\sigma_T c\int \frac{n(E_\gamma)}{E_\gamma}\Bigg[&\left(6 + \frac{b}{2} + \frac{6}{b}\right)\ln(1+b) - \ln^2(1+b) + \\ &-2Li\left(\tfrac{1}{1+b}\right) - \tfrac{(11/12)b^3+8b^2+13b+6}{(1+b)^2}\Bigg]dE_\gamma\end{aligned} \tag{2.2.48}$$

where $Li(x) = \int_x^1 (1-y)^{-1}\ln(y)dy$.

In the Thomson and Klein-Nisihina regimes (2.2.48) reduce to the well known expressions:

$$\begin{aligned}\frac{dE}{dt} &= \frac{4}{3}\sigma_T c\gamma^2\int E_\gamma n(E_\gamma)dE_\gamma \qquad &\text{at } b \ll 1 \\ \frac{dE}{dt} &= \frac{3}{8}\sigma_T c\int \frac{n(E_\gamma)}{E_\gamma}\left(\ln b - \frac{11}{6}\right)dE_\gamma \qquad &\text{at } b \gg 1\end{aligned} \tag{2.2.49}$$

The different form of those energy loss rates has implications on the shape of electron spectrum, and consequently in the γ-rays spectrum.

If we consider the spectrum of scattered photons due to a power-law distribution of relativistic electrons $n_e(E_e) \propto E_e^{-p}$ we obtain:

$$\begin{aligned} \frac{dN_\gamma}{dE_\gamma} &\propto E_\gamma^{-(p+1)/2} \quad \rightarrow \quad \text{Thomson regime} \\ \frac{dN_\gamma}{dE_\gamma} &\propto E_\gamma^{-(p+1)} \log E_\gamma \quad \rightarrow \quad \text{KN regime} \end{aligned} \tag{2.2.50}$$

The same spectral index [2] describes the shape of synchrotron radiation, which is:

$$\frac{dN_\gamma}{dE_\gamma} \propto E_\gamma^{-(p+1)/2} \quad \rightarrow \quad \text{Synchrotron radiation} \tag{2.2.51}$$

A more detailed calculations about spectral indices can be found i.e. [12] and in [39].

2.3 Synchrotron Self-Compton (SSC)

The simplest leptonic model observed in astrophysical environment and able to provide VHE γ-rays spectrum is called Synchrotron Self-Compton (SSC) mechanism. The synchroton spectrum is due to the interaction of relativistic electrons with magnetic fields, while the IC spectrum comes from the interaction of relativistic electrons with radiation fields, such as synchrotron, thermal infrared, or CMB radiation.

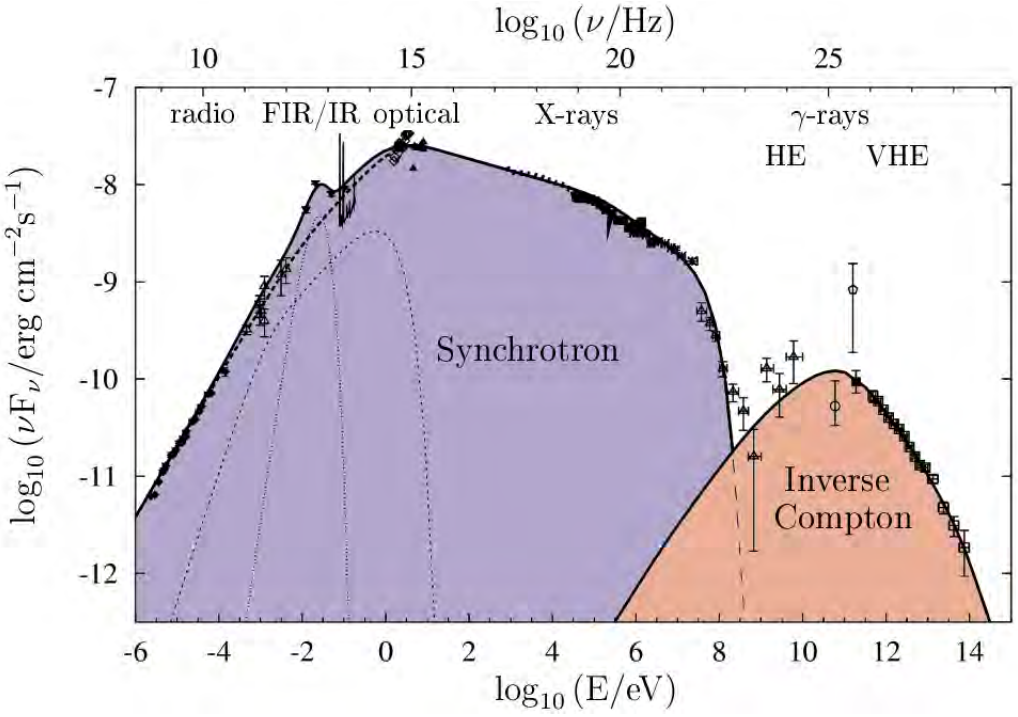

Figure 2.7: Crab Nebula Spectral Energy Distribution and SSC model.

The SSC signature is characterized by a superposition of a synchrotron spectrum, from radio to soft γ-rays, and an IC spectrum, from soft γ-rays to VHE γ-rays. Compton upscattering of synchrotron photons by the electrons themselves preserves the spectral index in the Thomson regime.

[2] It is important not to confuse the spectrum with the spectral energy distribution $E_\gamma \frac{dN_\gamma}{dE_\gamma} \propto \nu F_\nu$.

2.4 Bremsstrahlung

When a high energy electron encounters the Coulomb field of another charge, it emits bremsstrahlung radiation. The word "bremsstrahlung" means braking radiation because the electron rapidly decelerates when the other charge is a massive charged particle or a nucleus.

The derivation can be done classically using the dipole approximation for non-relativistic particles (see i.e. Rybicki & Lightman, 2008 [47]), but we are more interested in relativistic non-thermal bremsstrahlung.

Thus we have to consider a quantum description of this interactions using Weizsaker-Williams approach (see Blumenthal & Gould [12]) whereby the bremsstrahlung process is treated as Compton scattering of the virtual photons of the Coulomb field of the scattering charge.

We only need to consider electron-nucleus bremsstrahlung because it is the main effect, less radiation is emitted for collisions between particles of the same kind. (e.g. electron-electron).

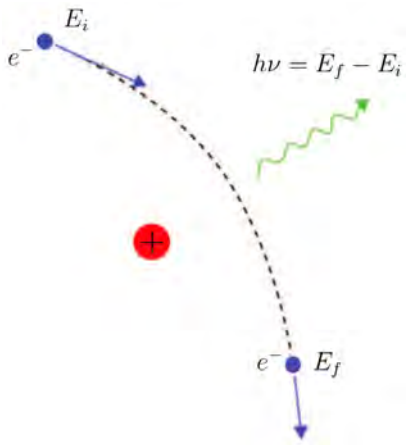

Figure 2.8: Sketch of the bremsstrahlung radiation (semi-classical view).

In electron-nucleus bremsstrahlung, the electrons are the primary emitters because, compared for example with protons, their acceleration is m_p/m_e times greater.

2.4.1 Weizsaker-Williams approach

The basic idea of Weizsaker-Williams approach is that the bremsstrahlung can be considered as Compton scattering, by the incoming electron of the virtual photons of the Coulomb field of a massive charged particle. This approach allows to simplify the calculation of the cross section and the bremsstrahlung spectrum.

A more complete discussion based on quantum electrodynamics was provided by Bethe Heitler in 1934. [11]

The main relation giving the bremsstrahlung cross section is:

$$d\sigma_B = dN d\sigma_C \tag{2.4.1}$$

where $d\sigma_C$ is the differential Compton cross section and dN is the differential number of incident virtual photons in the electron's rest frame.

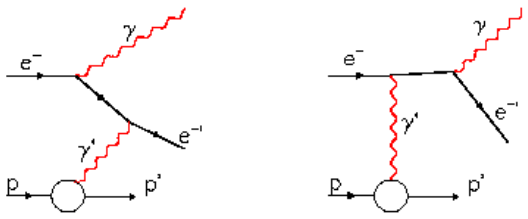

Figure 2.9: Simplified Feynman diagrams for bremsstrahlung.

In order to calculate this quantity dN we consider the transverse component of the electric field in $|E_t(\boldsymbol{r}, t)|$ in the extreme relativistic limit $\beta \approx 1$, as we see in (A.2.3).

$$|\boldsymbol{E}_t(\boldsymbol{r}, t)| = \frac{1}{4\pi\varepsilon_0} \frac{q\gamma b}{(b^2 + \gamma^2 c^2 t^2)^{3/2}} \tag{2.4.2}$$

where $b = R\sin\theta$ is the *impact parameter*. If dN is the differential number of these incident photons and dA is the element of area we obtain as (2.1.15) that:

$$S = \frac{1}{\mu_0 c}|\boldsymbol{E}_t(t)|^2 = \frac{dW}{dtdA} = \frac{\hbar\omega dN}{dtdA} \tag{2.4.3}$$

Using the Fourier transform of the transverse field as (2.1.2) we obtain that

$$E(\omega) = \frac{1}{\sqrt{2\pi}} \int E(t) e^{i\omega t} dt = \frac{q}{\sqrt{2\pi} 4\pi\varepsilon_0 cb} \int_{-\infty}^{+\infty} \frac{\exp\left(i\omega bx/\gamma c\right)}{(1+x^2)^{3/2}} dx \tag{2.4.4}$$

where we had the change variable $x = \gamma ct/b$. The integral solution is the modified Bessel function at first order $2|\omega b/\gamma c|K_1(\omega b/\gamma c)$ that for $\omega \ll \gamma c/b$ is approaches 2. Thus for a given ω: we have that:

$$E_t(\omega) \to \frac{q}{\sqrt{2\pi} 2\pi\varepsilon_0 cb} \qquad b \ll b_{max} = \frac{\gamma c}{\omega} \tag{2.4.5}$$

if the charge is incident at random impact parameters, we can take $dA = 2\pi b db$. Then using (2.1.15) and (2.4.3) we have:

$$\frac{\hbar\omega dN}{dA} = 2c\varepsilon_0 |E_t(\omega)|^2 d\omega \tag{2.4.6}$$

From this relation, rememebering that $\alpha = e^2/(4\pi\varepsilon_0\hbar c)$ we obtain:

$$dN = \frac{2z^2\alpha}{\pi} \left(\frac{db}{b}\right)\left(\frac{d\omega}{\omega}\right) \tag{2.4.7}$$

In order to obtain the differential cross section extreme relativistic limit, we have to consider some kinematic and transformation relations. To be careful about the notation we will indicate the energy with the symbol E. It is convenient to express photon energies in the following units:

$$\begin{aligned} &\text{Observer's reference frame} \to \tilde{E}_\gamma = E_\gamma/\gamma mc^2 \qquad (\text{units of } \gamma mc^2) \\ &\text{Electron rest frame} \qquad\quad \to \tilde{E}_{\gamma,0} = E_{\gamma,0}/mc^2 \qquad (\text{units of } mc^2) \end{aligned} \tag{2.4.8}$$

Thus we have with same meaning of Compton's kinematic:

$$\begin{aligned} \tilde{E}'_{\gamma,0} &= \frac{\tilde{E}_{\gamma,0}}{1 + \tilde{E}_{\gamma,0}(1-\cos\theta_0)} \\ \tilde{E}_\gamma = \tilde{E}'_\gamma &= \tilde{E}_{\gamma,0}(1-\cos\theta_0) \qquad \beta \approx 1 \end{aligned} \tag{2.4.9}$$

From wich we obtain:

$$\tilde{E}_{\gamma,0} = \left(\frac{\tilde{E}_\gamma}{1-\tilde{E}_\gamma}\right) \frac{1}{(1-\cos\theta_0)} = \frac{\tilde{E}'_{\gamma,0}}{1-\tilde{E}_\gamma} \tag{2.4.10}$$

For fixed $\tilde{E}_\gamma$, the minimum photon energy before scattering in electron rest system is:

$$\tilde{E}_{\gamma,0}^{\,min} = \frac{\tilde{E}_\gamma}{2(1-\tilde{E}_\gamma)} \tag{2.4.11}$$

The maximum energy is gotten from $\omega_{max} \sim \gamma c/b_{min} \sim \gamma mc^2/\hbar$ thus $\tilde{E}_{\gamma,0}^{\,max} \sim \gamma \gg \tilde{E}_{\gamma,0}^{\,min}$.
Now with the help of the kinematic relations the Klein Nishina formula (2.2.30) can be written as function of $\tilde{E}_{\gamma,0}$ and $\tilde{E}_\gamma$, with the differential solid angle transformed in terms of $d\tilde{E}_\gamma$.

$$d\Omega'_0 = 2\pi d(1-\cos\theta_0) = \frac{2\pi}{\tilde{E}_{\gamma,0}} \left[\frac{d\tilde{E}_\gamma}{(1-\tilde{E}_\gamma)^2}\right] \tag{2.4.12}$$

where $d\Omega'_0$ is calculated in the rest frame of the electron.

Hence the differential Klein Nishina cross section becomes:

$$d\sigma_{KN} = \pi r_0^2 \frac{1}{\tilde{E}_{\gamma,0}} \left[1 - \tilde{E}_\gamma + \frac{1}{1-\tilde{E}_\gamma} - \frac{2}{\tilde{E}_{\gamma,0}} \frac{\tilde{E}_\gamma}{1-\tilde{E}_\gamma} + \frac{1}{\tilde{E}_{\gamma,0}2} \left(\frac{\tilde{E}_\gamma}{1-\tilde{E}_\gamma} \right)^2 \right] d\tilde{E}_\gamma \tag{2.4.13}$$

Replacing this expression in the main formula (2.4.1), an integration over $\tilde{E}_\gamma$ and b can be performed.

$$d\sigma_{Br} = dN d\sigma_{KN} = 4\alpha z^2 r_0^2 \left[\frac{4}{3}(1-\tilde{E}_\gamma) + \tilde{E}_\gamma^2 \right] \left(\frac{d\tilde{E}_\gamma}{E_\gamma} \right) \int \left(\frac{db}{b} \right) \tag{2.4.14}$$

Now we have that $b_{min} \sim \frac{\hbar}{mc}$ while

$$b_{max} \sim \frac{\hbar}{mc} \frac{\gamma}{\tilde{E}_{\gamma,0}^{min}} = \frac{2(\gamma/mc)(1-\tilde{E}_\gamma)}{\tilde{E}_\gamma} \tag{2.4.15}$$

We have finally obtained the bremsstrahlung differential cross section in extreme relativistic regime:

$$d\sigma_{Br} = 4\alpha z^2 r_0^2 \left[\frac{4}{3}(1-\tilde{E}_\gamma) + \tilde{E}_\gamma^2 \right] \left(\frac{d\tilde{E}_\gamma}{\tilde{E}_\gamma} \right) \ln \left(\frac{2\gamma(1-\tilde{E}_\gamma)}{\tilde{E}_\gamma} \right) \tag{2.4.16}$$

which is essentially the same as the exact expression, in the extreme relativistic limit, obtained through a more rigorous quantum discussion (see [28]).

$$d\sigma_{Br} = 4\alpha z^2 r_0^2 \frac{d\omega}{\omega} \left[E_i^2 + E_f^2 - \frac{2}{3} E_i E_f \right] \left(\ln \frac{2E_i E_f}{mc^2 \hbar \omega} - \frac{1}{2} \right) \tag{2.4.17}$$

2.4.2 Energy loss rate and Spectrum

For an electron moving through a number density n_t of the same type of charged particle, the bremsstrahlung spectrum is:

$$\frac{dN_\gamma}{dt dE'_\gamma} = c n_t \left(\frac{d\sigma_{Br}}{dE'_\gamma} \right) \tag{2.4.18}$$

To calculate the total energy loss we have to integrate the bremsstrahlung spectrum:

$$\frac{dE}{dt} = \int \left(\frac{dN_\gamma}{dt dE'_\gamma} \right) E'_\gamma dE'_\gamma \tag{2.4.19}$$

the only explicit simple expression can be found in the strong shielding and weak shielding limit. The weak shielding or completely ionized case the energy loss is:

$$\frac{dE}{dt} = 4\alpha z^2 r_0^2 c n_t E_e \left[\ln \left(\frac{2E_e}{mc^2} \right) - \frac{1}{3} \right] \tag{2.4.20}$$

while for a strong shielding:

$$\frac{dE}{dt} = 4\alpha z^2 r_0^2 c n_t E_e \left[\ln \left(\frac{183}{Z^{1/3}} \right) - \frac{1}{18} \right] \tag{2.4.21}$$

Thus the total energy emission rate is roughly proportional to E_e, this fact does not mean that the electron energy decreases exponentially with time, but in each bremmstrahlung interactions the electron loses a large fraction of its energy.

2.5 Neutral Pion decay

When relativistic protons or others nuclei interact with the interstellar medium (ISM) or with gaseous environments, they give rise to inelastic collisions. One of the most common interactions occurs between protons, which produce mesons and others hadrons through strong interactions. In the GeV to TeV energy region, the total inelastic cross section σ_{pp} can be approximated by:

$$\sigma_{pp}(E_p) \approx 30[0.95 + 0.06 \ln (E_{kin}/1\text{GeV})] \; mb \tag{2.5.1}$$

where E_p is the energy of the relativistic proton and $E_{kin} = E_p - m_p c^2$ is the kinetic energy.[6] We are interested in the inelastic collisions which produce the meson π^0. Indeed the neutral pion decay provides the main way to convert the kinetic energy of protons into VHE γ-rays.

Among the reactions which have the form:

$$p + p \rightarrow \pi^0 + X \tag{2.5.2}$$

In this kind of processes pions have the larger cross section. One of the most common is:

$$p + p \rightarrow p + p + \pi^+ + \pi^- + \pi^0 \tag{2.5.3}$$

The Pion π is the lightest pseudoscalar meson ($m_{\pi^\pm} = 140$ MeV, $m_{\pi^0} = 135$ MeV).
In this particular reaction the three kinds of pions are produced in equal amounts, thus one third of the produced pions are neutral.

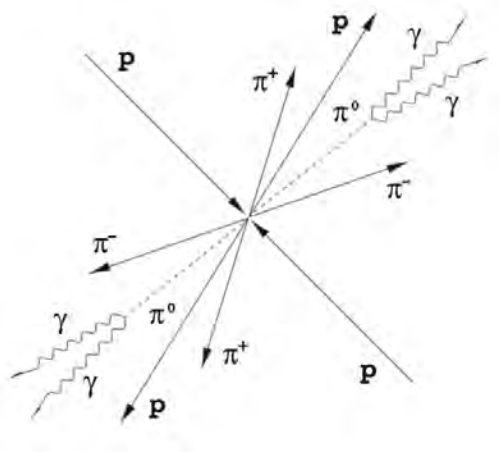

Figure 2.10: A common reaction channel of *pp* inelastic scattering.

Charged pions decay weakly into muons which eventually decay into electron-positron pairs and neutrinos. These secondary pairs may also contribute to the emitted spectrum through bremsstrahlung, synchrotron or IC emission.
The main energy conversion process is due to the neutral pion, who receive cinetical energy from the inelastic collision and then decays electromagnetically in two γ-rays.

$$\begin{array}{ll} \pi^0 \rightarrow \gamma + \gamma & (BR\ 98.8\%) \\ \pi^0 \rightarrow e^+ + e^- + \gamma & (BR\ 1.2\%) \end{array} \tag{2.5.4}$$

The minimum kinetic energy E_{th} necessary for a proton to produce a π^0 is:

$$E_{th} = \frac{2 m_{pi^0} c^2 (1 + m_{pi^0})}{4 m_p} \simeq 280\text{MeV} \tag{2.5.5}$$

The energy of the photons emitted by a π^0 at rest is peaked at $E_{\gamma,0} = m_{\pi^0} c^2/2 \simeq 67.5$ MeV, in the laboratory frame. The energy depends on the emission angle θ_γ and on the initial energy of the meson. Its value is:

$$E_\gamma = \gamma_{\pi^0}(1 + \beta_{\pi^0} \cos\theta_\gamma) E_{\gamma,0} \tag{2.5.6}$$

The final energies of the emitted photons can thus reach the VHE regime. The γ–rays produced by pions are the so-called γ–rays of hadronic origin. They are distinguishable from those of electromagnetic origin because of their spectra, lack of correlation with X-rays, and presence of molecular clouds. They occur together with a flux of neutrinos coming from the charged pion decays, whose spectrum is similar to that of γ–rays from π^0 decay.

The neutral pion decay rate is described through Quantum Chromodynamics (QCD) and in particular it is a remarkable example of a chiral currents anomaly. A detailed study of the interaction and the evaluation of the decay rate is discussed by Peskin & Schroeder, 1995 [41]. The decay rate results in:

$$\begin{aligned}\Gamma(\pi^0 \to \gamma + \gamma)_{theo} &= \frac{\alpha^2}{2\pi}\frac{m_{\pi^0}^3}{f_\pi^2} = 7.75 \text{ eV} \\ \Gamma(\pi^0 \to \gamma + \gamma)_{meas} &= (7.86 \pm 0.54) \text{ eV}\end{aligned} \tag{2.5.7}$$

which corresponds to a life time of $\tau_{\pi^0} = 8.6 \cdot 10^{-17}\ s$ in the particle rest frame, very short compared to the charged pion decay $\tau_{\pi^\pm} = 2.6 \cdot 10^{-8}\ s$.

The spectral features of γ–rays emitted by neutral pions decay produced by pp interactions have been studied by many authors (i.e Mori, 1997; Kelner,Aharonian & Bugayov, 2006 [30]). For a given proton energy distribution density $n_p(E_p)$, the resulting gamma ray emissivity is given by:

$$q_\gamma(E_\gamma) = \frac{N_\gamma}{dtdVdE_\gamma} = 2\int_{E_{min}}^{\infty} \frac{q_{\pi^0}(E_{\pi^0})}{\sqrt{E_{\pi^0}^2 - m_{\pi^0}^2 c^4}} dE_{\pi^0} \tag{2.5.8}$$

where $E_{min} = E_\gamma + m^2c^4/4E_\gamma$. The emissivity of secondary pions q_{π^0} from pp inelastic scattering can be calculated with high accuracy using accelerators measurements.

$$\begin{aligned}q_{\pi^0}(E_{\pi^0}) &= cn_H \int \delta(E_{\pi^0} - \kappa_{\pi^0} E_{kin}) \sigma_{pp} n_p(E_p) dE_p \\ &= \frac{cn_H}{\kappa_{\pi^0}} \sigma_{pp}\Big(m_p c^2 + \frac{E_{\pi^0}}{\kappa_{\pi^0}}\Big) n_p\Big(m_p c^2 + \frac{E_{\pi^0}}{\kappa_{\pi^0}}\Big)\end{aligned} \tag{2.5.9}$$

where n_H is the density of the target nuclei and in the broad region from GeV to TeV energies $\kappa_{\pi^0} \approx 0.17$ (see Gaisser, 1990).

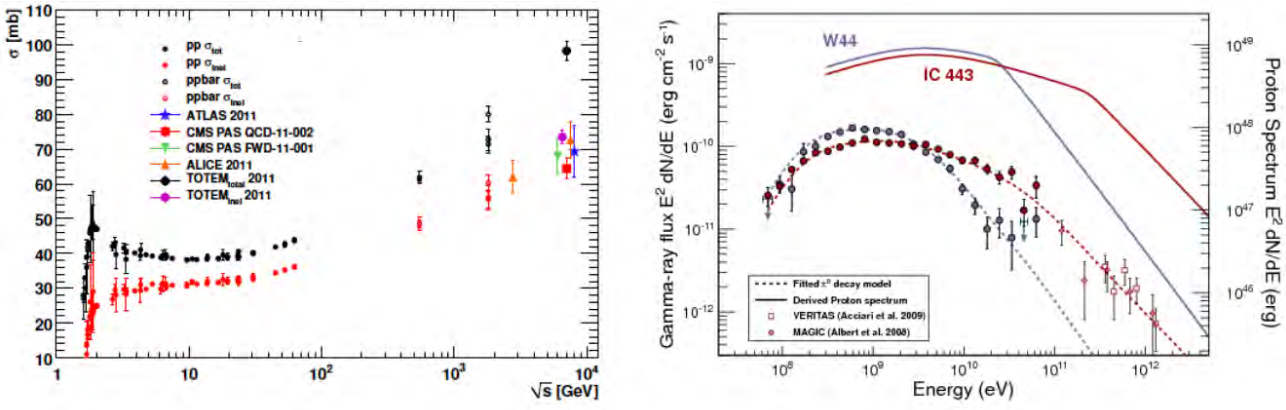

Figure 2.11: (*Left*) Total cross section of proton-proton inelastic scattering (σ_{inel} in red), the measurements were provided by several experiments. (*Right*) Proton and gamma-ray spectra determined for Supernova Remnants IC-443 and W44. Example of fitting with hadronic models.[2]

2.6 Pair production and gamma ray absorption

The discussion about Compton scattering of section 2.2 can be easily generalized to describe the process $\gamma + \gamma \to e^- + e^+$ in which the photons collision have pair production as result.

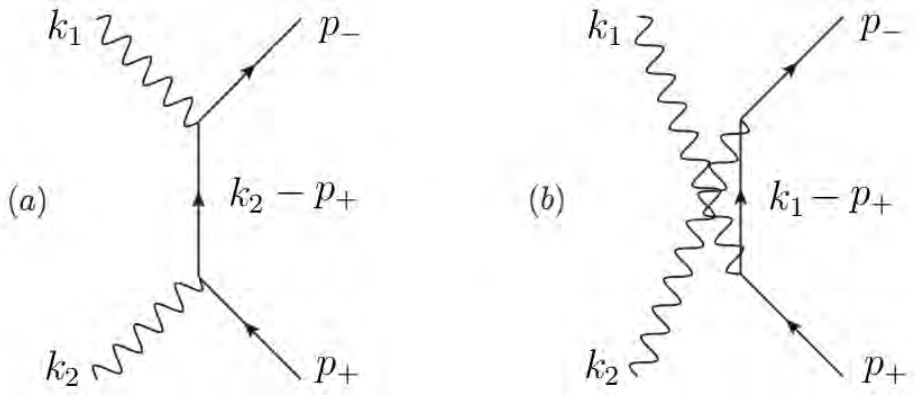

Figure 2.12: Feynman Diagrams for $\gamma + \gamma \to e^- + e^+$.

Comparing Feyman diagrams which describe this process at the same order of the Compton's diagrams, we can see that the only differences consist in the replacements:

$$k \to k_1, \quad k' \to -k_2, \quad p \to -p_-, \quad p' \to p_+ \tag{2.6.1}$$

Following from this substitution we have that the Compton Feynman amplitude $\overline{|\mathcal{M}_a + \mathcal{M}_b|^2}$ written in terms of Mandelstam variables could be used in this case also, to obtain the cross section of the process. Where $k_1 = (\omega_1, \boldsymbol{k}_1)$, $k_2 = (\omega_2, \boldsymbol{k}_2)$,$p_+ = (E_{e^+}, \boldsymbol{k}_+)$ e $p_- = (E_{e^-}, \boldsymbol{k}_-)$ represent the four-momenta of photons and particles in the initial and final state and the Mandelstam variables are:

$$s = (k_1 - p_-)^2 = (p_+ - k_2)^2, \quad t = (p_+ + p_-)^2 = (k_1 + k_2)^2, \quad u = (p_- - k_2)^2 = (k_1 - p_+)^2 \tag{2.6.2}$$

Hence the differential cross section is calculated by eq. (2.2.27).

$$\frac{d\sigma}{ds} = \frac{1}{16\pi}\frac{2q^4}{t^2}\left[4m^4\left(\frac{1}{s-m^2} + \frac{1}{u-m^2}\right)^2 + 4m^2\left(\frac{1}{s-m^2} + \frac{1}{u-m^2}\right) - \left(\frac{u-m^2}{s-m^2} + \frac{s-m^2}{u-m^2}\right)\right] \tag{2.6.3}$$

Thus the total cross section for the Pair production calculated in the CoM frame is:

$$\sigma_{\gamma\gamma} = \frac{\pi r_e^2}{2}(1-\beta^2)\left[2\beta(\beta^2-2) + (3-\beta^4)\ln\left(\frac{1+\beta}{1-\beta}\right)\right] \tag{2.6.4}$$

where $\beta = v/c$ is the velocity of electron (positron) in the center of mass reference frame.
In the high energy limit $\beta \to 1$ we have:

$$\sigma_{\gamma\gamma} \to \frac{3\sigma_T}{16}(1-\beta^2)\left[2\beta(1-2) + (3-1)\ln\left(\frac{(1+\beta)(1+\beta)}{(1-\beta)(1+\beta)}\right)\right] \tag{2.6.5}$$

$$\sigma_{\gamma\gamma} \simeq \frac{3}{8}\frac{\sigma_T}{\gamma}\left[\ln(4\gamma^2) - 1\right] \tag{2.6.6}$$

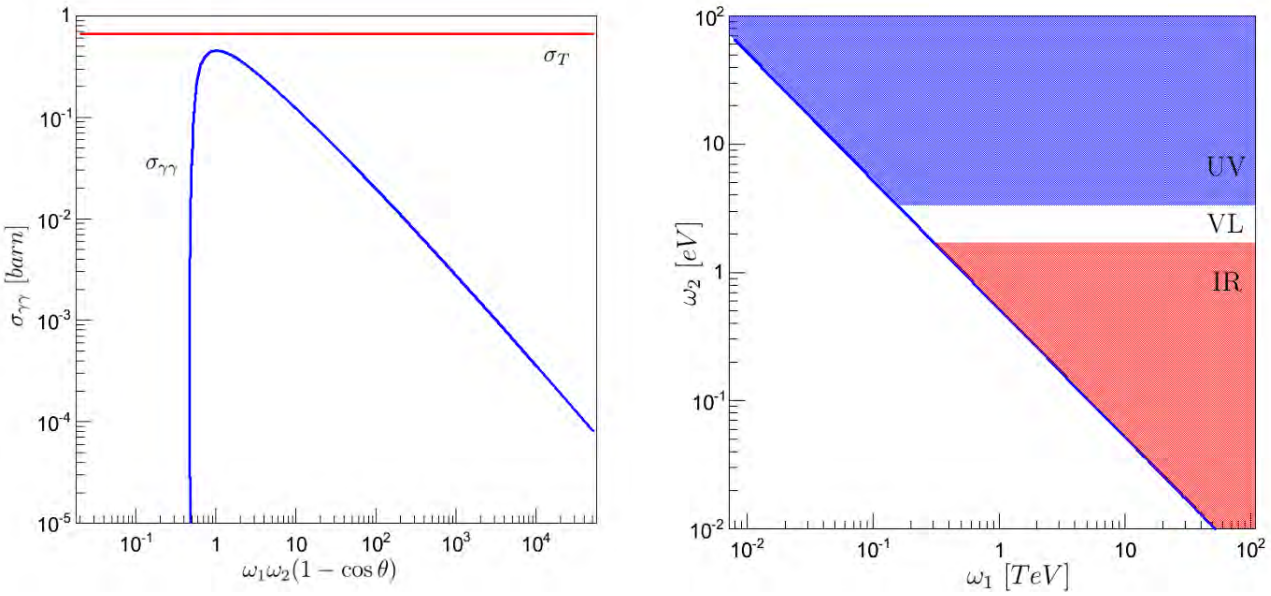

Figure 2.13: (*Left*) Pair Production Cross Section. (*Right*) Absorption energy threshold. A γ-ray of energy ω_1 can interact with all photons above threshold.

It is useful to express $\sigma_{\gamma\gamma}$ in terms of photons energies and collision angle θ. Thus:

$$t/2 = \omega_1\omega_2(1-\cos\theta) = 2E_e^2 \qquad E_e = \gamma mc^2 = mc^2(1-\beta^2)^{-1/2} \tag{2.6.7}$$

where E_e is the total energy of electron (positron) in CoM frame, so:

$$\beta = \sqrt{1 - \frac{2m^2c^4}{\omega_1\omega_2(1-\cos\theta)}} \tag{2.6.8}$$

From which we obtain the condition $\omega_1\omega_2(1-\cos\theta) > 2m^2c^4 \approx 0.522\ MeV$. Therefore if we fixed there is a threshold value of

The cross section $\sigma_{\gamma\gamma}$ have a maximum:

$$\sigma_{\gamma\gamma} \simeq \sigma_T/4 \quad \text{at} \quad t_{max} \simeq 4m^2c^2 \approx 1.04MeV \tag{2.6.9}$$

Thus if we consider an isotropic radiation $\langle\cos\theta\rangle = 0$ we can write that $t = 2\omega_1\omega_2$.
This means for example that TeV photons interact most efficiently with infrared photons (range $1.24meV - 1.7eV$):

$$\omega_1\omega_2 \approx 1MeV \quad \rightarrow \quad \omega_2 \approx 1\left(\frac{1\ TeV}{\omega_1}\right)\ eV \tag{2.6.10}$$

Therefore ω_1 can interact with all photons above threshold (see Figure 2.13 b), but cross-section decreases. When γ-rays travel along cosmological distance can interact with cosmic matter and low energy photon fields.

If we can neglect the interaction between VHE γ-rays and intergalactic or interstellar medium (due to the low matter densities) we have to consider the absorption due to the low energy photons belonging to the extragalactic background light (EBL).
The EBL is the second largest background, in terms of contained energy, after CMB.

There are several different models about the EBL, but it is common accepted that the energy density spectrum is characterized by two main peaks (see Figure 2.14).
The first peak at $\sim 1\mu m$ is known as the stellar term, associated with the light emitted by stars, the second one at $\sim 100\mu m$ comes from the re-processing of starlight by dust and for this reason is called dust term.

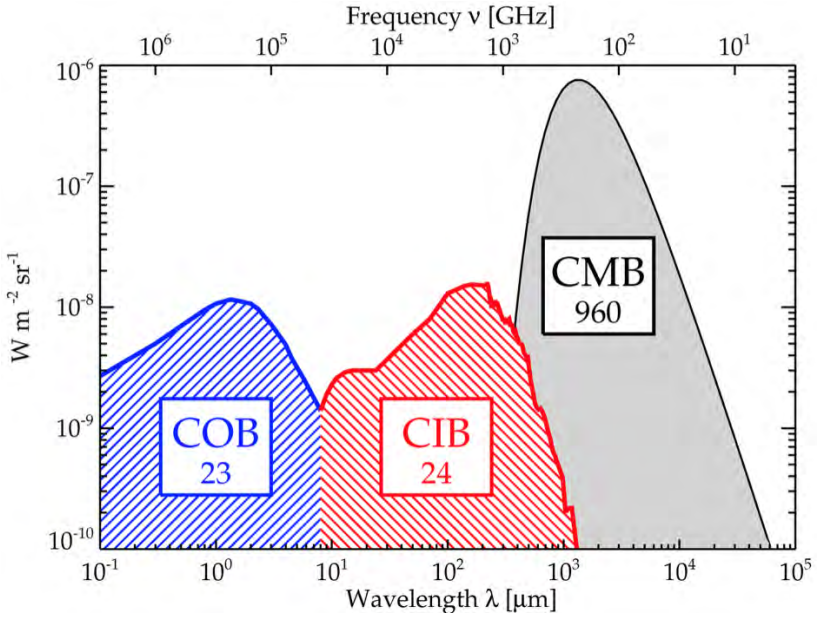

Figure 2.13: Schematic spectral energy distributions of the most relevant backgrounds in the Universe. In the boxes is written the approximate brightness in $nWm^{-2}sr^{-1}$. From right to left: The Cosmic Microwave Background (CMB),the Cosmic Infrared Background (CIB), and he Cosmic Optical Background (COB). Image taken from [19].

VHE γ-rays have high cross section for pair production with EBL, therefore the Universe is not completely transparent to VHE γ-rays, at least above $\sim$ 100 GeV.
This means that far distant source cannot be observe. Hence we can define a *Gamma-Ray Horizon* beyond which we cannot detect far VHE sources.
The γ ray observed flux F_{obs}, for a given energy E and redshift z, can be written as an exponential cutoff:

$$F_{obs}(E,z) = F_{int}(E)e^{-\tau(E,z)} \tag{2.6.11}$$

where F_{int} and τ are respectively the intrinsic flux of the source and the optical depth, function of the energy and the redshift z.

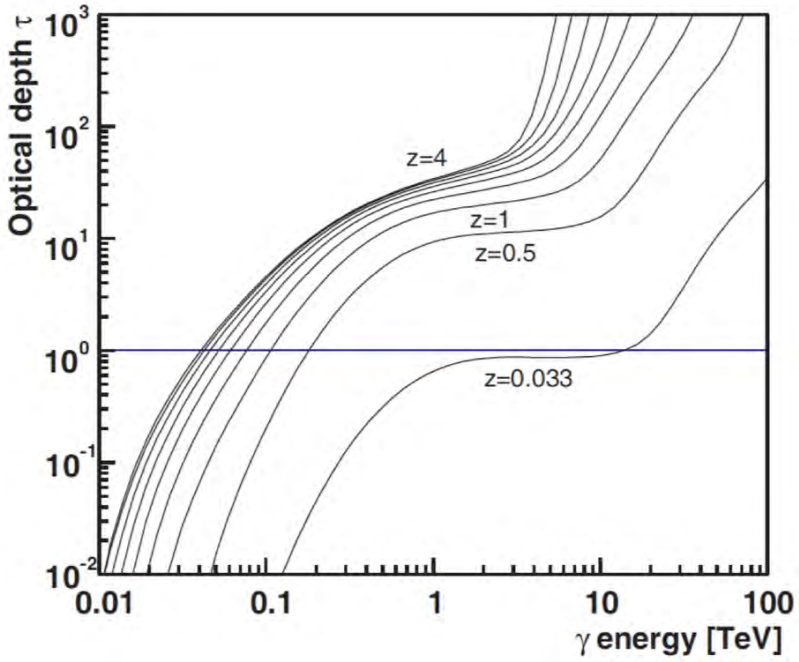

Figure 2.14: A model of the optical depth τ as a function of energy for different redshift z. The horizontal line a $\tau = 1$ represent the *Gamma-Ray Horizon* as calculated from this model, i.e the distance at which the Universe becomes opaque to VHE γ-rays.

Chapter 3

VHE Gamma Ray Astronomy

In this section a brief description of the main classes of known VHE γ-ray sources will be given. These astrophysical emitters are naturally divided in galactic and extragalactic sources.

3.1 Galactic Sources

Due to their vicinity, Galactic objects are of basic interest in γ-ray Astronomy. They can be observed as extended objects in a wide range of wavelengths, and this is a unique opportunity to understand and study the morphology of the emission region. Another of their features is that their γ-ray emission does not suffer absorption due to cosmological background light, but the main absorption is due to the local distribution of matter and gas around the source.

3.1.1 Supernova Remnants (SNRs)

Supernova Remnants are the structures resulting from the explosion of Supernova. When a massive star ($\approx 5 - 10$ $M_\odot$) collapses, it gives rise to a gigantic explosion, which blows out a huge amount of material expanding into the interstellar medium, costituing a shock wave.

It is generally thought that SNRs are probably the main acceleration sites for CRs below the *knee* ($\sim$ 3 PeV). However, while particle acceleration to high energies has now clearly been demonstrated with the current generation of instruments, it is still not proven that supernovae accelerate most of the CRs. The crucial question is the origin of the emission that is observed. Leptonic origin and Hadronic origin are debated. To discriminate, we must compare the predictions of acceleration models with observations.

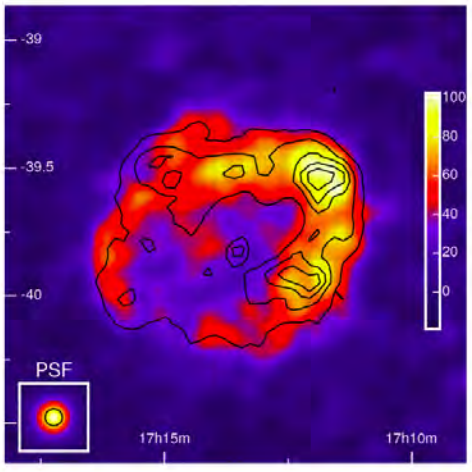

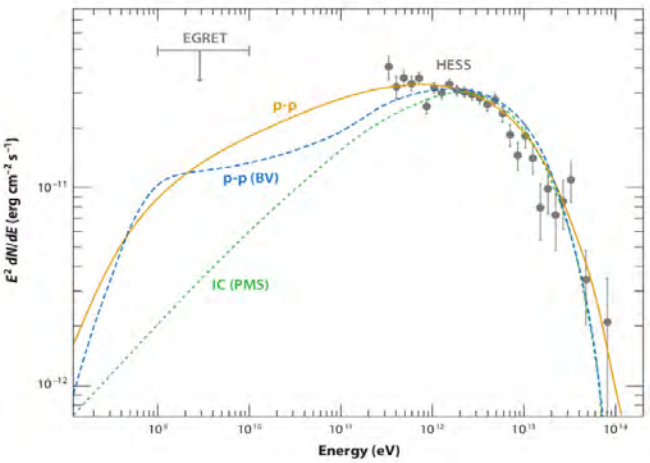

Figure 3.1 : (*Left*) The combined HESS image of the supernova remnant RXJ 1713.7-3946 (Shell type) from data taken in 2004 and 2005. Advanced Satellite for Cosmology and Astrophysics (ASCA) contours are drawn as black lines (1-3 keV) for comparison. (*Right*) The SED of RX J1713.7-3946 at γ-ray energies. Three curves are shown in comparison to the dark gray HESS data (Aharonian et al. 2007e) and EGRET upper limit.[26]

In order to accelerate CRs, strong magnetic fields, $10^2 - 10^3$ times higher than the interstellar medium ones, are required. Such high values of the magnetic fields would lead to exclude a leptonic origin for the observed γ-ray emission, because the expected synchrotron radiation from relativistic electrons would be much greater than the measured X-ray emission.

Theory suggests that such an amplification of the magnetic field might be induced by the CRs themselves, and high resolution X-ray observations of SNR seem to support this scenario. Thus, an accurate determination of the intensity of the magnetic field is of crucial importance to discriminate the origin of the observed γ-ray emission.

3.1.2 Pulsars and Pulsar Wind Nebulae (PWNe)

A Supernova explosion may create a Pulsar, a neutron star with masses of the order of a solar mass and and a few tens of kilometers in radius, which represents the most dense state of stable matter known in the Universe, apart from the Black Holes.

The main feature of the Pulsar is to have the magnetic axis misaligned with respect to the rotation axis. The very short rotational period (down to the order of milliseconds) and the extremely intense magnetic fields (typically in the range $10^8 - 10^{12}G$) cause a very powerful electromagnetic emission, as due to the rotation of a magnetic dipole. The spin-down energy loss is given by:

$$\frac{dE}{dt} \sim 3 \cdot 10^{33} B_{12}^2 T_{ms}^{-4} \text{erg s}^{-1} \tag{3.1.1}$$

where B_{12} is the surface magnetic field in units of $10^{12}G$ and T_{ms} is the period in milliseconds. The SNRs that are powered by the rotational energy of a pulsar is called Pulsar Wind Nebula (PWN) and tend to have a dE/dt around and above 10^{35} erg s^{-1}.

The rotating field creates a voltage drop of order $10^{17} B_{12}/T_{ms}$ V, which accelerates particles forming outflowing jets. VHE γ-ray emission is expected in the *Polar Cap* region of the Pulsar, due to synchroton processes and in the *Outer Gap* regions of the magnetosphere by IC scattering.

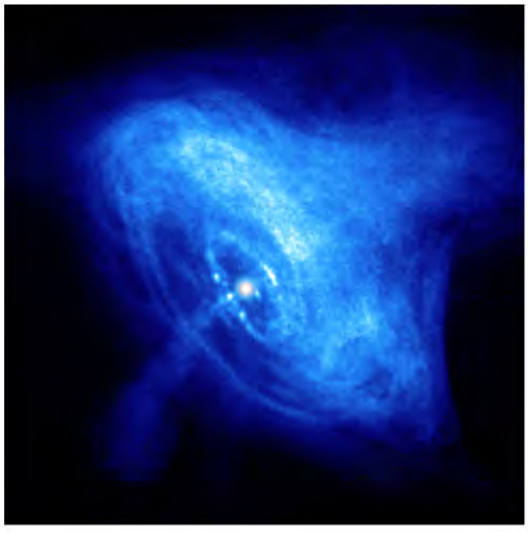

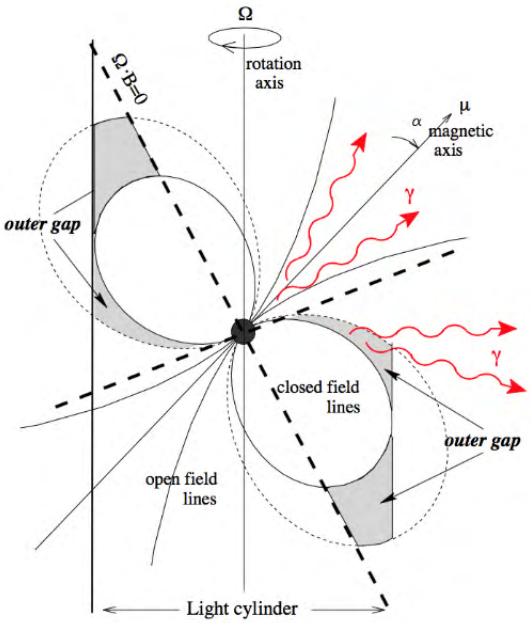

Figure 3.2 : (*Left*) The Chandra X-ray image of Crab Nebula. (*Right*) A Sketch of the *Polar Cap* and the *Outer Gap* models for the VHE emission of pulsars. Image taken from[40]

The strong magnetic field of a young pulsar has the effect of suppressing the γ-ray emission, which is produced from high-energy electrons via the inverse Compton mechanism. Paradoxically, a less powerful pulsar with a weaker magnetic field would result in a higher γ-ray production efficiency.[17]
The best known and studied example of PWN is the Crab Nebula. The first VHE γ-ray source to be detected (Weekes et al. 1989), located at a distance of 2 kpc, results of the remnant of a supernova explosion that occurred in the year 1054. It is generally regarded as the "standard candle" for high energy astrophysics.
As is well known, the Crab Nebula is a very effective accelerator but not an effective IC γ-ray emitter. Indeed, we see γ-rays from Crab because its large spin-down power ($\sim 10^{38}$ erg s^{-1}), although the γ-ray luminosity is much less than spin-down power of its pulsar.

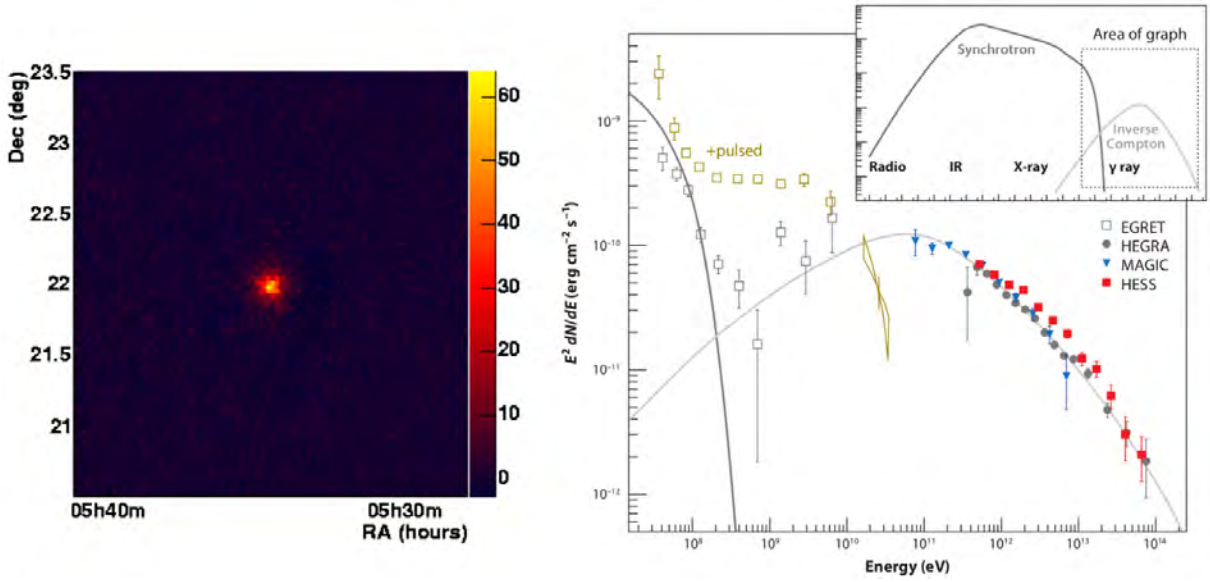

Figure 3.3 : (*Left*) Gamma rays from the Crab Nebula in the H.E.S.S. 3-telescope data . (*Right*) The SED of the Crab Nebula and Pulsar, with focus on VHE γ-ray regime. Adapted from Hinton (2009).[26]

PWNe are the most abundant class among the sources discovered in the HESS survey of the Galactic plane. Nevertheless there are many questions unresolved such as the understanding of the particle acceleration mechanisms, the intensities time evolution of multi-wavelenght synchroton and Inverse Compton (or hadronic) radiation and the magnetohydrodynamic flow in PWNe.

3.1.3 Binary Systems and Microquasar

A Binary Systems (BS) consists of a compact object, such as a neutron star or black hole, orbiting a massive star. The study of BS at VHE is very important because these systems allow us to test models and obtain feedback of important physical processes.
If the matter of the companion star is stripped off forms an accretion disk around the compact object, much a like a miniature AGN and the system is called Microquasar.
Microquasars have many observational and morphological properties similar to AGNs (i.e a strong emission over a wide energy range, a rapid flux variability, and the existence of jets of relativistic plasma along the rotational axis of the black hole [46]) and obviously many differences.
The main difference is the presence of a companion star that interacts with the compact object, causing precession of the jets and hence a periodic variability of the nonthermal emission.

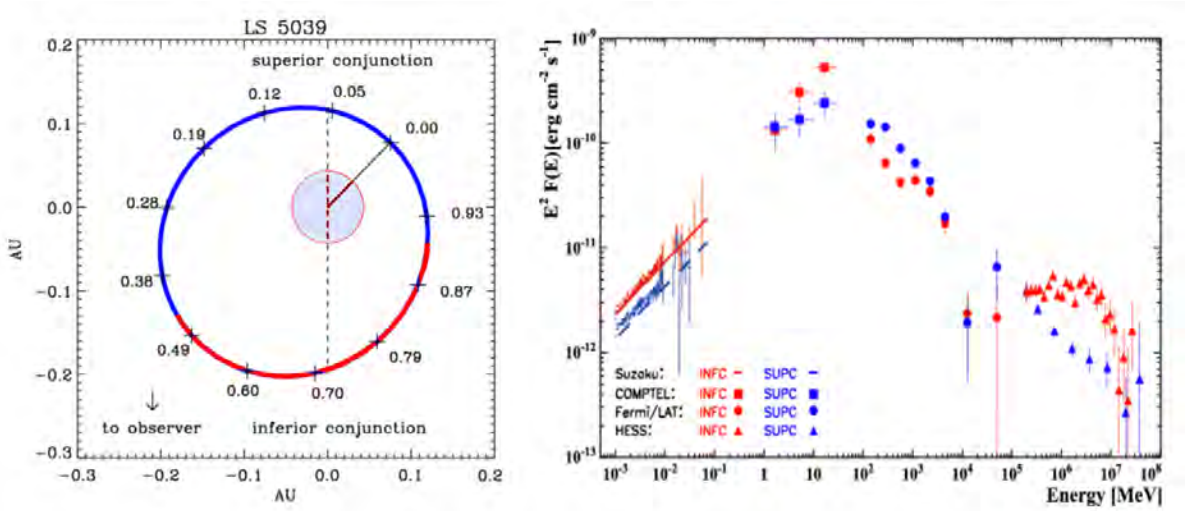

Figure 3.4 : (*Left*) Orbits of $\gamma - ray$ Binary System LS-5039. The star size is to scale. (*Right*) The SED of the Binary System LS-5039 for two broad orbital phase intervals: **INFC** $0.45 < \phi \leq 0.9$ (red circles); **SUPC** $\phi \leq 0.45$ and $\phi > 0.9$ (blue triangles). [5]

For example, γ-ray binaries such as LS I +61 303 and LS 5039 are found to be periodic at GeV and TeV energies, although the emission at the two energies is anti-correlated. A cut-off in the spectrum is observed at a few GeV, which was completely unexpected.[17]
The typical microquasar spectrum is dominated by the emission from the jets. The IC emission peak can reach GeV–TeV energies. Many questions about the γ-ray emission from such systems are still open.

3.1.4 Galactic Centre (GC)

The Galactic Centre region is clearly one of the main targets of γ-ray astrophysics. The GC hosts the nearest super-massive black hole, called Sagittarius A* (Sgr.A*).

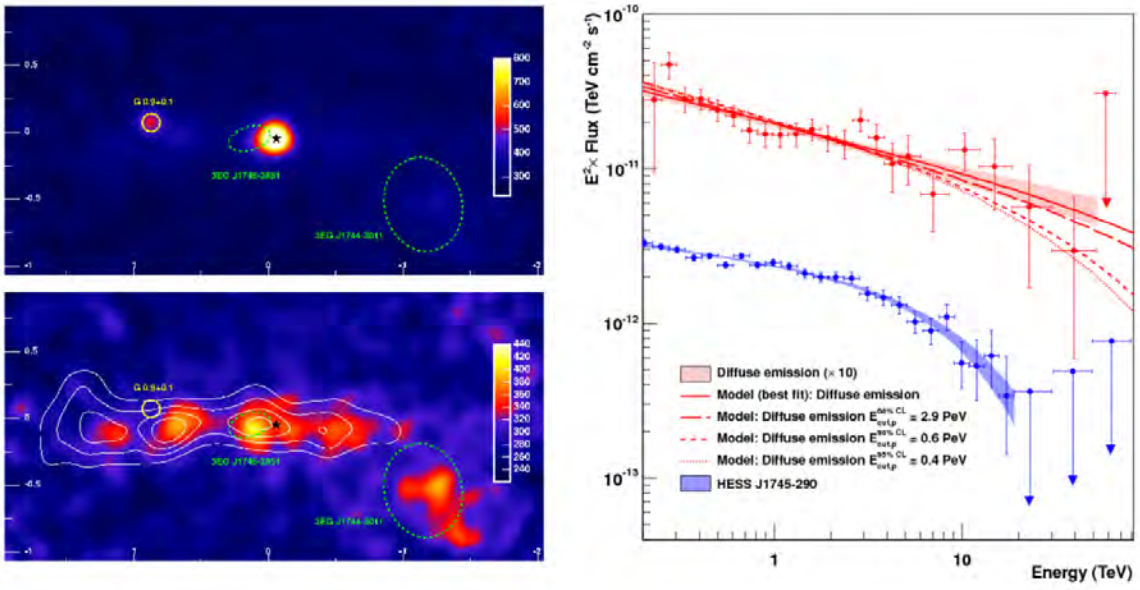

Figure 3.5 : (*Left*) VHE γ-ray images of the GC region. Top: γ-ray map, bottom: the same map after subtraction of the two dominant point sources, showing an extended band of γ-ray emission.[4]
(*Right*) VHE γ-ray spectra of the diffuse emission and HESS J1745-290.
The red lines show the numerical computations assuming that γ-ray result from the decay of neutral pions produced by proton-proton interactions. The fluxes of the diffuse emission spectrum and models are multiplied by 10.[15]

The interpretation of the emission mechanisms is difficult since the region is populated by several potential sources and the current angular resolution doesn't allow to disentangle the exact position of the VHE γ-ray emissions.

Observations of the Galactic Centre are particularly interesting because among the great variety of γ-ray emitters there could be γ-ray sources due to hypothetical Dark-Matter particles annihilation or decay.

3.2 Extragalactic Sources

The Universe is not transparent to VHE γ-rays. For this reason, we cannot observe γ-rays in the VHE domain from objects at high redshifts: roughly greater than $z \approx 1$ for energies above 100 GeV. This fact is due to γ-rays interaction with EBL causing pair production.

3.2.1 Active Galactic Nuclei (AGNs)

The electromagnetic radiation emitted from usual galaxies is almost entirely produced by stellar evolution processes, but in approximately 1% of cases the galaxy core is so bright that it can outshine completely the host galaxy.

This effect is due to the presence of a supermassive black-hole (SMBH) surrounded by an accretion disk of about $10^6 - 10^{10}$ solar masses with an extension of often 1 pc only in diameter. This enormous amount of material in orbital motion around the SMBH releases a large amount of gravitational energy as thermal and non-thermal radiation. For these reasons the nucleus of these galaxies is called active, and so this objects are called Active Galactic Nuclei.

AGNs have been grouped into different subclasses according to their morphology, the mass of SMBH, their evolutionary status, their accretion speed, and the orientation of the galaxy (and the emitting regions) with respect to the line of sight. Nevertheless it is believed that the many different kinds of AGNs belong to the same class of objects seen from different angles (Unified Model).

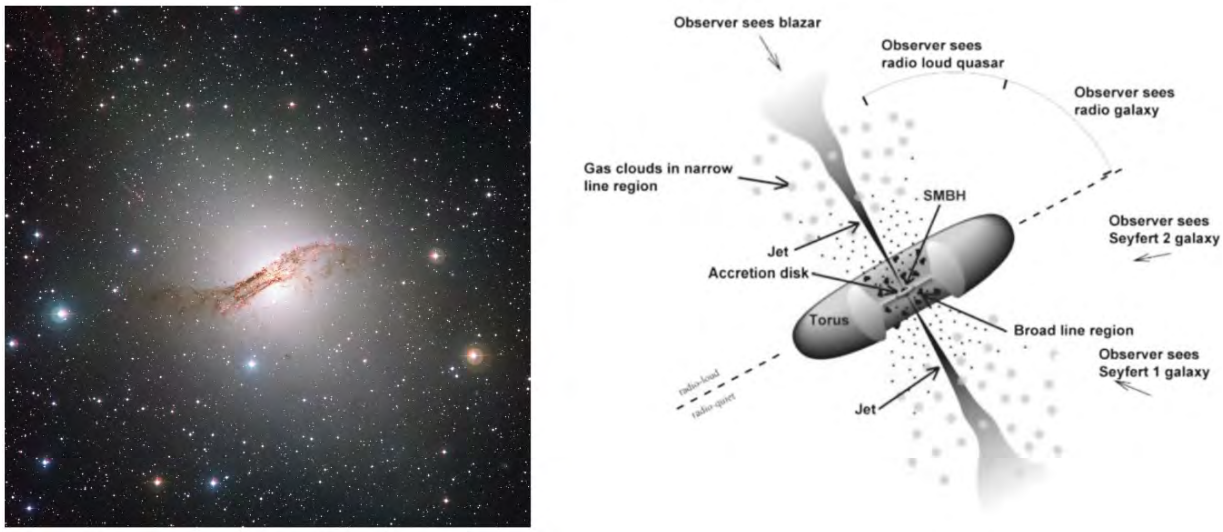

Figure 3.6 :(*Left*) Image of the radio galaxy Centaurus A, also known as NGC 5128 from ESO optical telescope at the La Silla Observatory in Chile. (*Right*) A schematic figure for radio-loud AGN (not to scale). Note the accretion disk surrounding the SMBH and the strong emission of particles and highly collimated radiation (jet). The type AGN observed depends on the angle of view, as suggested by the Unified Model. Image credit: NASA.

It is convenient to divide AGN into two classes, conventionally called *radio-quiet* and *radio-loud*. An AGN is considered radio-loud if the ratio R between the radio flux at 5GHz and the optical flux (B band) is greater than 10 (Kellermann et al. 1989).

$$R = \frac{F_{5GHz}}{F_B} \qquad \text{if } R > 10 \rightarrow \text{radio-loud} \tag{3.2.1}$$

Since VHE emissions have been found only in radio loud AGNs, we will focus our description on these objects. According to the Unified Model, we can divide the radio loud AGNs into the following categories:

Radio Galaxies: are AGNs whose jets lie at a large angle(>30 deg) with respect to the line of sight. The central hole is obscured by the large torus and the light coming from an inner disk and the BLR [1]. The intense radio emission is synchrotron radiation from the jets and the lobes.

Quasars: they are the intermediate case. A quasar (quasi-stellar source) is a galaxy which shows a very luminous, unresolved nucleus. The emission from the central object is directly seen, together with the NLR [2] and BLR, which cause typical emission lines in the spectrum. The spectrum is dominated by a non-thermal radio-optical emission, that is recognized as synchrotron emission due to ultra relativistic charged particles in the jet.

Blazars: When the jet is direct along the observer line of sight, the spectral features change completely and we have a blazar. Jets in blazars are the favored site of GeV–TeV γ-ray emmission. The production process of VHE γ-rays is still under debate: both leptonic and hadronic models seem to be able to well describe the observational data. Depending on the characteristic of the emission, blazars are divided into two classes[18]:

- BL Lacertae objects (BL Lacs): they have no strong broad lines in their optical spectrum. BL Lacs are moreover classified according to the energies of the peaks of their SED: they are called accordingly low-energy peaked BL Lacs (LBLs), intermediate-energy peaked BL Lacs (IBL) and high-energy peaked BL Lacs (HBL).
- Flat Spectrum Radio Quasars (FSRQ): they show broad emission lines in their optical spectrum. Typically FSRQs have a synchrotron peak at lower energies than LBLs.

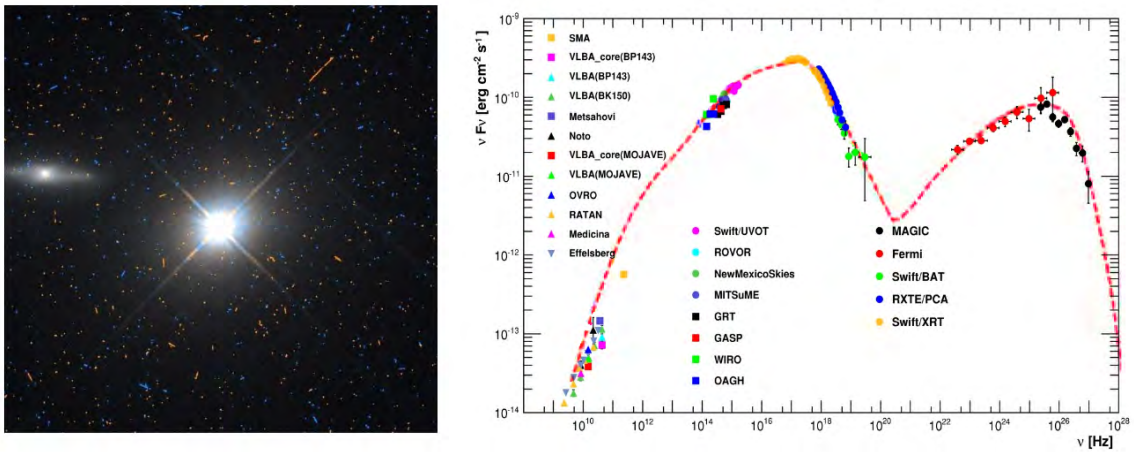

Figure 3.7 :(*Left*) The blazar Markarian 421, observed with WFPC2 of HST in 1999.
(*Right*) SED of Mrk-421 with all the observations taken during a multifrequency campaign in 2009. [1]

[1]Broad Line Region (BLR): A region where dense molecular clouds are responsible of the broad emission lines that could be detected in the optical range.(Fig.??)

[2]Narrow Line Region (NLR): A region where molecular clouds less dense than BRL cause tight emission lines that could be detected in particular in the optical range.(Fig.??)

3.2.2 Gamma-Ray Bursts (GRBs)

Gamma-Ray Bursts are the most energetic phenomena observed in the Universe. Their consists in powerful flashes whose luminosity peak is equivalent to the light emitted by millions of galaxies (typically $10^{51} - 10^{54}$erg s^{-1}). Due to this high brightness they can be detected at high redshifts and so they are messengers from the galaxies formation history.

The highest measured GRB redshift is $z = 8.2$, the mean redshift is $z \sim 2.2$ but some GRBs have been observed down to $z = 0.0085$.[3] This fact means that in most cases the VHE γ-rays are absorbed by the EBL and only HE γ-rays can be detected. This phenomena was studied by BATSE (Burst And Transient Source Experiment) , aboard the CGRO (Compton Gamma Ray Observatory) satellite, which observed about 2700 events (see Figure C.5) discovering that GRBs occur isotropically on the sky and probably were originated by violent explosions in distant galaxies mainly outside the Local Group.

It is widely accepted that GRBs come from asymmetric supernova or hypernova explosions. There are many models describing the phenomenon of GRBs, but none of them is fully satisfactory.

One of the most favoured model is the Fireball Model, in which the emission is separated into two components: the prompt outburst phase (strong gamma-ray and X-ray emission) due to internal shocks in the relativistic blast-wave, followed by the afterglow (strong X-ray, optical and radio emission) which arises from the cooling fireball and its interaction with the surrounding medium.[42]

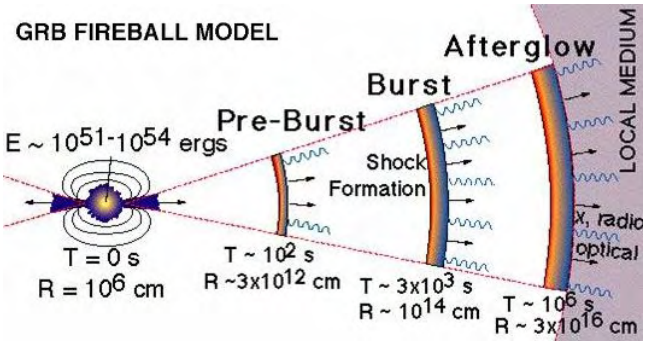

Figure 3.8: Schematic image of the *Fireball Model*

Recent observations by the Swift and Fermi missions have revealed an even more complex behavior than previously observed, featuring significant spectral and temporal evolution. Thanks to their accuracy in determining GRBs directions, it could be established the position of the extragalactic sources that probably gave rise to the observed γ-ray burst.

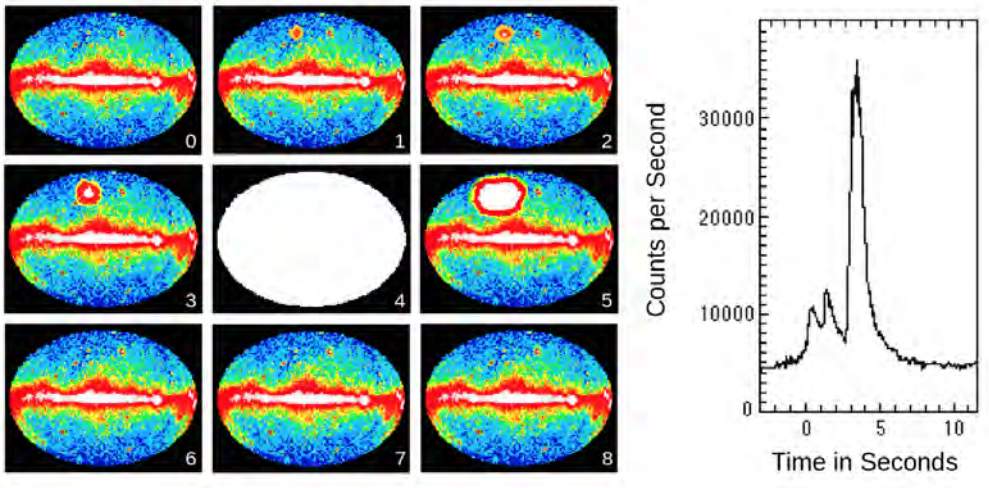

Figure 3.8 :(*Left*) An example of a long GRB. The figure show nine successive instants of a GRB event. (*Right*) Plot of the same event, counts vs time. Image credit: NASA.

Currently no GRB has been detected at energies > 100 GeV but new data from Fermi suggest that a good fraction of the brightest GRBs could be detected by CTA in just a few minutes by quickly re-pointing part of the array. [17]

3.3 Dark Matter (DM)

Nowadays there are several experimental evidences for the presence of a large non-baryonic component of the matter density of the Universe (so-called Dark Matter) at all observed astrophysical scales, such as galaxies, galaxy clusters, and cosmic background radiation. [10]

It is believed that the Dark Matter constitutes about 27% of the energy budget of the Universe. Although DM has not been directly observed, its presence is known through gravitational effects: such as the motions of visible matter, gravitational lensing and its effects in the CMB.

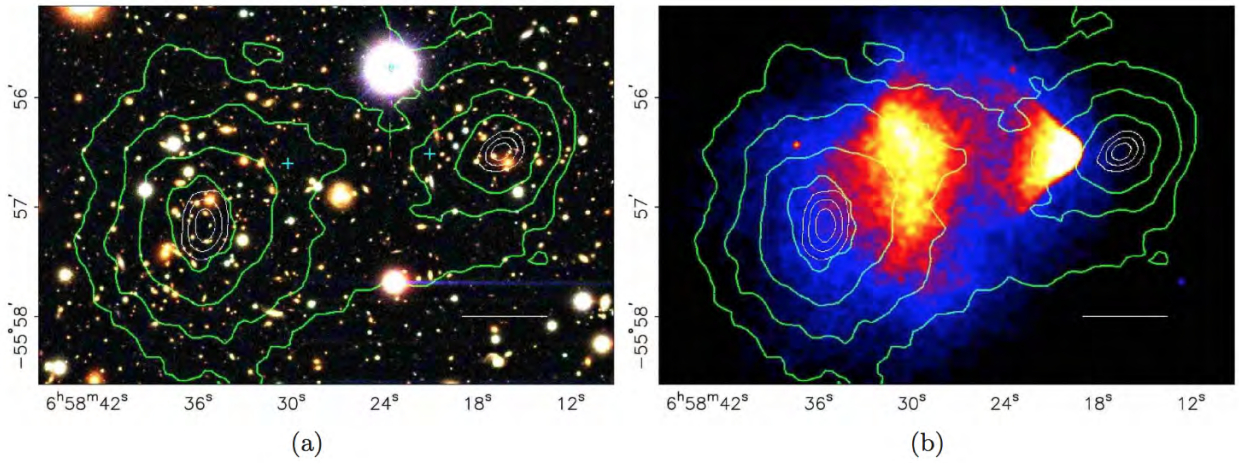

Figure 3.10 : A direct empirical proof of the existence of Dark Matter. *(a)* Color image in the visible range from the Magellan telescope of the 1E0657- 558 cluster. *(b)* Chandra X-ray image (500 ks) of the same cluster. The green contours in the pictures correspond to weak lensing maps marking the gravitational potential. The white contours show the errors on the positions of the peaks of the mass distribution deduced by the weak lensing analysis and correspond to 68.3%, 95.5%, and 99.8% confidence levels. The blue crosses in the left picture locate the mass peaks of the measured baryonic plasma clouds, which are shown in bright colors in the right picture. The white line on the right bottom indicates 200 kpc size scale. [14]

We do not know the DM nature and if it could finally be detected via primary or secondary radiation associated with its annihilation or decay, but there are several models that predict such signatures and so it is worth to adapt our telescopes and detectors to these scenarios.

In the research and study of DM, gamma-ray band is a very privileged one for several reasons:

- The γ-rays are neutral and be traceable to the origin point, so we can survey sky where DM is expected to be particularly concentrated.
- The γ-ray spectrum emerging from DM interactions (either annihilations or decays) is universal. All DM targets are expected to show exactly the same gamma-ray spectrum. The observation of multiple spectra from different targets would therefore constitute an excellent result.
- The γ-ray spectra from DM annihilations or decay typically show several characteristic features, naturally depending on the specific DM model, but in general classifiable in sharp cutoff, bumps, or even line emissions. This makes the DM spectra hardly confusable with typical astrophysical spectra.
- The recent experimental results of the LHC experiments: the quite large Higgs boson mass and the non-evidence for New Physics beyond the Standard Model (until now) are possibly hinting to DM particle being more massive than expected, about the TeV. This region is where ground-based telescopes have highest sensitivity.

One of the best theoretical candidates is the Weakly interacting massive particles (WIMPs) model, which foresees a particle at the GeV–TeV scale. If DM is coupled to the SM with some interactions, in the final products of annihilations or decays one can find either hadrons, leptons and gauge bosons, which can produce gamma-rays. Generally, the DM annihilation and decay flux in gamma rays are expressed as:

$$\frac{d\Phi_\gamma^{ann}}{dE_\gamma}(E_\gamma,\phi,\theta) = \frac{1}{4\pi}\frac{\langle\sigma_{ann}v\rangle}{2m_\chi^2}\sum_f \frac{dN_{\gamma,f}}{dE_\gamma}B_f \int_{\Delta\Omega(\phi,\theta)} d\Omega \int_{l.o.s} \rho^2(l,\phi,\theta,\Omega)dl$$
$$\frac{d\Phi_\gamma^{dec}}{dE_\gamma}(E_\gamma,\phi,\theta) = \frac{1}{4\pi}\frac{\Gamma_\chi}{m_\chi^2}\sum_f \frac{dN_{\gamma,f}}{dE_\gamma}B_f \int_{\Delta\Omega(\phi,\theta)} d\Omega \int_{l.o.s} \rho(l,\phi,\theta,\Omega)dl \quad (3.3.1)$$

where m_χ is the mass of the WIMP, $\langle\sigma_{ann}v\rangle$ is the annihilation rate averaged over the DM velocity distribution and Γ_χ the decay rate. B_f is the branching ratio into the final state f and its yield per reaction $dN_{\gamma,f}/dE_\gamma$. The integral terms are called Astrophysical factors or J-factors, where (ϕ,θ) are the angle with respect to the Galactic centre, Ω is the solid angle and l is the line of sight (l.o.s). ρ is the DM density.

Many observations were conducted from current ground-based IACT instruments in the last decades in order to discover DM signatures (see [20]). The Galactic Centre is one of the most promising regions to look for DM annihilation radiation due to its predicted very high DM density. VHE γ-ray emission has been detected, but the identification of DM in the GC is complicated by the presence of many conventional candidates sources and the diffuse gamma-ray background. The improvement of the angular and energy resolution, together with its enhanced sensitivity planned for CTA will be crucial for disentangling the different contributions to the GC radiation. Others important targets for DM searches are Dwarf Satellite Galaxies (DSGs), which exhibit large mass-to-light ratios, and make DM searches with low astrophysical backgrounds possible. Also Galaxy Cluster and Globular Cluster were observed for their relevance in both cosmological and astrophysical studies, and because it is supposed that DM could be the dominant component of the cluster mass budget, accounting for up to 80% of its mass. [10]

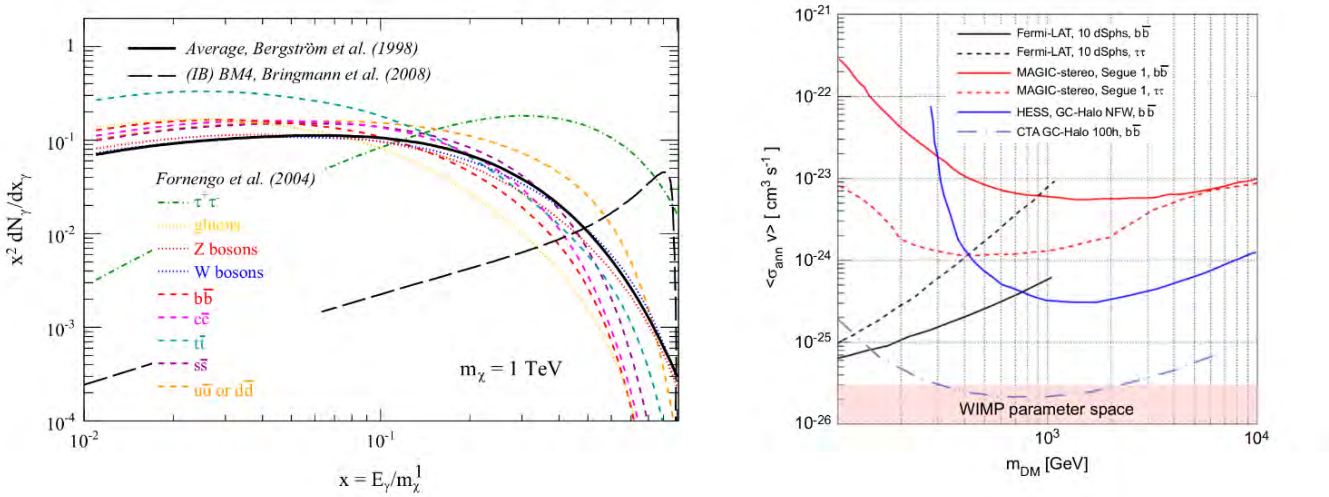

Figure 3.11 : (*Left*) Differential spectra (multiplied by x2) of gamma-rays from several neutralino annihilation products. (*Right*) Comparison of several exclusion lines for the Fermi-LAT observation of 10 combined DSGs for $b\bar{b}$ and $\tau^+\tau^-$ channels, H.E.S.S. observation of the galactic center halo for the NFW for the $b\bar{b}$ channel, MAGIC-stereo observations of the Segue 1 DSG for the $b\bar{b}$ and $\tau^+\tau^-$ channels and for the estimation for 100 h observation at the galactic center halo with CTA. For more details see ref. [20].

Chapter 4

Atmospheric shower and IACT technique

In the first chapter we discuss the main features of atmospheric showers due to primary cosmic ray interaction with Earth's Atmosphere and then we explain how these effect can be very useful to detect VHE γ-ray.

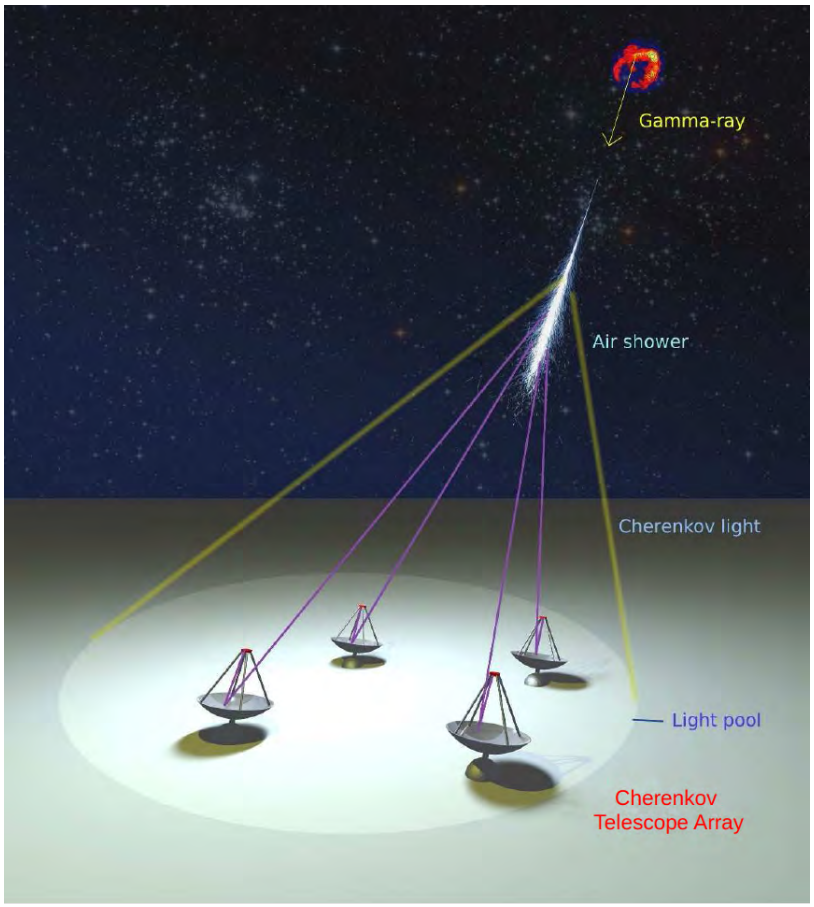

Figure 4.1: Schematic drawing of atmospheric shower due to VHE cosmic ray on Cherenkov Telescope Array. Note the atmospheric shower due to primary γ-ray, the Cherenkov light cone due to ultra-relativistic charged particles which form the shower and the light pool stereoscopically detected by Cherenkov Telescope Array.

We have seen that photons are the main information messengers about astrophysical objects. They cover long distance keeping energy, space and temporal information from the source. Once arrived on the Earth, they may interact with atmosphere according to their range of energy. Indeed, as we can observe from Figure 1.7, Earth's atmosphere is transparent exclusively in the optical range and in high frequency radio bands.

Therefore we cannot detect directly HE or VHE photons with ground-based instruments, for these reason to study X-ray and γ-ray astronomy, instruments are placed on satellite i.e. Chandra for X-ray and Fermi LAT for γ-ray. But the size of satellite instruments is small, their effective area is about the order of m^2 too small to obtain a good statistic and energy resolution to study VHE γ-rays.

Thought γ-rays absorption not allows direct measurements, their own interaction allows a secondary detection. In fact, more generally, when a primary cosmic ray interacts with atmosphere, it produce a cascade of ultra-relativistic charged particles.

These particle cascades are called Atmospheric showers which are essentially of two kinds: Hadronic showers and Electromagnetic showers (better explained in the next sections).

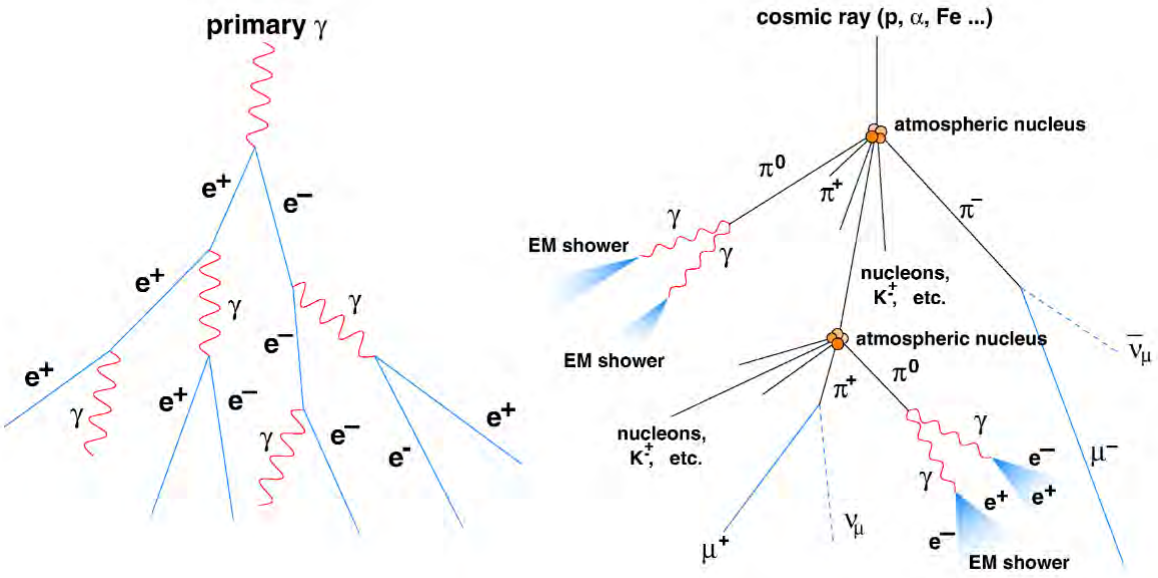

Figure 4.2: Schematic representation of two atmospheric showers initiated by a photon (left) or by a generic cosmic ray (right).

The first experimental evidence for the phenomenon of the atmospheric particle showers is dated back to 1938 and achieved by Auger.
The French scientist who performing experiments at high altitudes with the aid of Geiger counters and observed temporally coincident signals, which could be attributed to bunches of particles belonging to Atmospheric showers.

Atmospheric showers emit Cherenkov radiation at a characteristic angle. Since the first interaction with nuclei of the atmosphere takes place at about $10 - 20$ km above sea level the Cherenkov light footprint on the ground is of the order of 10^5 m^2.

The Cherenkov light can be detected with a particular types of instruments called Imaging Atmospheric Cherenkov Telescope (IACT). This detection method is called IACT technique and provide a way to detect very high energy gamma-ray photons in the 50 GeV - 50 TeV range.

The main idea of this technique is essentially that atmosphere act as a sort of natural calorimeter and so thanks to Cherenkov radiation, allows VHE γ-ray detection with ground-based instruments.

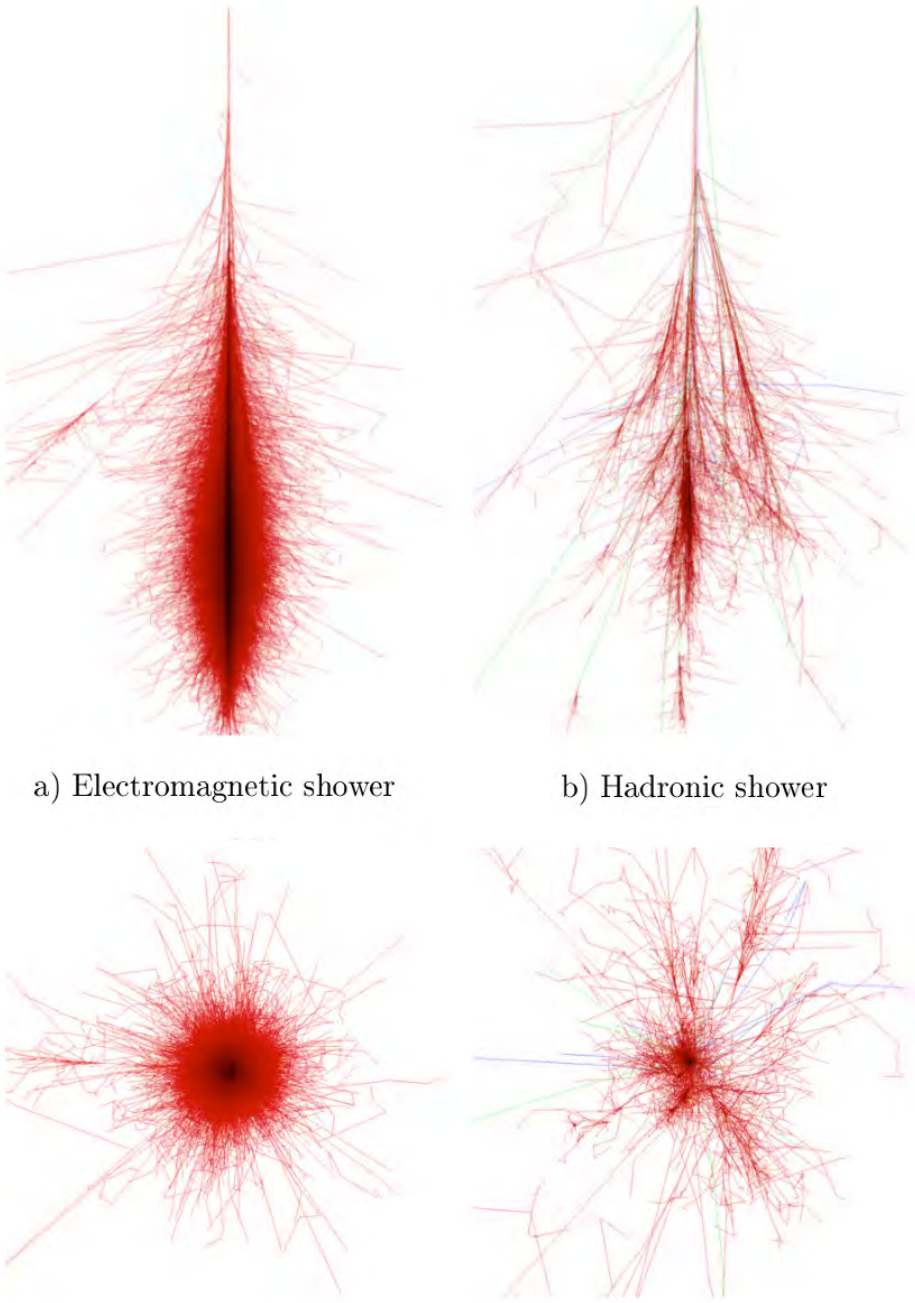

Figure 4.3: Monte Carlo simulations of Atmospheric showers obtained with the MC simulator CORSIKA (COsmic Ray SImulations for KAscade). a) Electromagnetic shower from primary γ-ray of energy 1 TeV. b) Hadronic shower from primary protons of energy 100 GeV. https://www.ikp.kit.edu/corsika/

4.1 Hadronic showers

The vast majority of primary CRs are composed of protons and α particles. The strong interaction of these particles with the nuclei in atmosphere generates mainly pions ($\sim$ 90%), kaons($\sim$ 10%), and light baryons $(p, \bar{p}, n)$. These secondary particles, together with the primary CR, form the Hadronic shower core.

During the initial development of the shower, strong interactions are dominant and hadronic particles are producted while in the final stage, shower ionization and decays become dominant. Hadronic showers are more penetrating and extended than Electromagnetic ones.

The atmospheric showers induced by hadrons are composed mainly of three components:

- Hadronic component: the core of the hadronic shower constituted by high energy nucleons and mesons which decay into muons and neutrinos through this main channels:

$$\begin{array}{ll} \pi^{\pm} \rightarrow \mu^{\pm} + \nu_{\mu}(\bar{\nu}_{\mu}) & BR(\sim 99.98\%) \\ K^{\pm} \rightarrow \mu^{\pm} + \nu_{\mu}(\bar{\nu}_{\mu}) & BR(\sim 63.55\%) \\ K^{\pm} \rightarrow \pi^{\pm} + \pi^{0} & BR(\sim 20.66\%) \end{array} \tag{4.1.1}$$

- Muonic component: the mesons decays products. Their energy loss is essentially ionization, although they can also decay in electrons.

$$\mu^{\pm} \rightarrow e^{\pm} + \nu_{e}(\bar{\nu}_{e}) \qquad BR(\sim 100\%) \tag{4.1.2}$$

  Due to their large lifetime ($2.2 \cdot 10^{-6} s$), muons can travel along a relevant portion of the sky and rarely decay before reaching the ground.

- Electromagnetic component: the consequence of neutral pion decay.

$$\pi^{0} \rightarrow \gamma\gamma \qquad BR(\sim 98.82\%) \tag{4.1.3}$$

  About one third of the produced pion are neutral and so about one third of the energy in hadronic interactions is transfered to electromagnetic component.

4.2 Electromagnetic showers

The Electromagnetic (EM) showers are produced by VHE γ-rays or cosmic electrons or positrons. Two main processes are involved to the shower development:

- Bremsstrahlung, which caused the production of new photons (more details in sect. 2.4).
- Pair production, which caused the creation of a pair $e^{+}\, e^{-}$ (more details in sect. 2.5).

The two processes are very similar: the radiation length of an $e^{\pm}$ for the Bremsstrahlung is $X_0^e = 37 g/cm^2$ in air, and the mean free path of the photon before pair creation which interaction length is $X_0^{\gamma} = 7/9 X_0^e$.

Since the cross section of VHE γ-rays with air is weakly energy dependent, this first interaction occurs for different primary γ-ray energies typically at a height of about 20 km above sea level.

In 1934, Heitler proposed a relatively simple model to describe in first approximation the development of an electromagnetic shower [11].
Assuming that the primary energy is equally split into secondary products, each $e^{\pm}$ produce a photons through Bremsstrahlung and and each photons cause pair production. Another assumption is that the radiation length and the interaction length are equal $X_0^{\gamma} \simeq X_0^e \simeq X_0$ (see Figure 4.4).

According to this simple model, after n radiation length X_0 the amount of particles is $N(n) = 2n$, equally distributed between electrons, positrons and photons, whereas the mean energy per particle is $E(n) = E_0/2n$, where E_0 is the primary γ-ray energy.

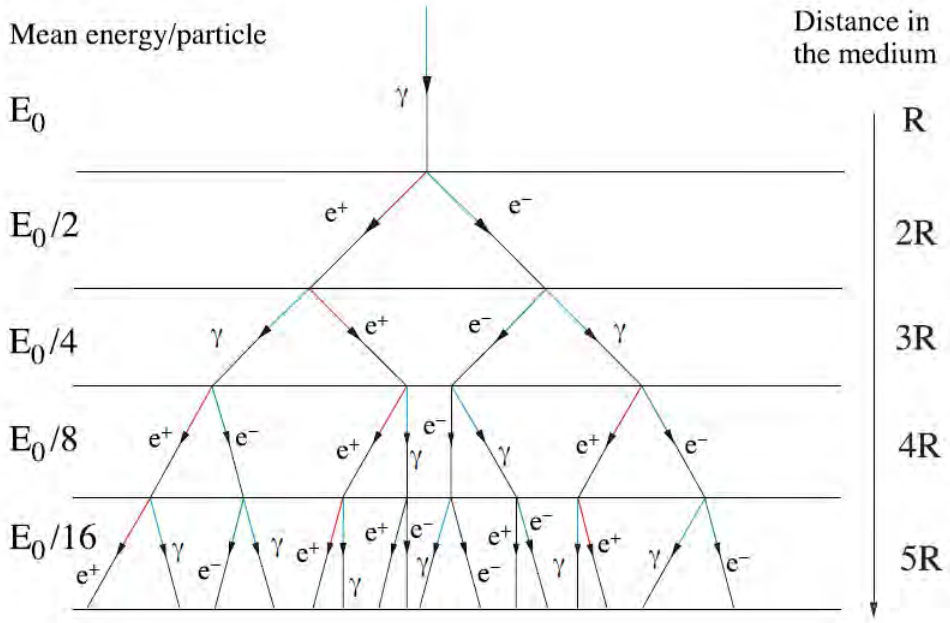

Figure 4.4: The Heitler model for an electromagnetic shower. Every segment corresponds to the mean free path of secondary particles.

The number of radiation length n_{max} at which the maximum of the shower is reached when products have a critical energy E_c and the total number of produced particles at the depth $R_{max} = n_{max} \cdot X_0$ are thus:

$$E_c = \frac{E_0}{2^{n_{max}}} \rightarrow n_{max} = \frac{\ln(E_0/E_c)}{\ln 2} \qquad R_{max} = 2^n_{max} \cdot X_0 \tag{4.2.1}$$

The number of particles with energy greater than E is:

$$N(>E) = \int^n (E)_0 N dn = \int^n (E)_0 2^n dn = \frac{E_0/E}{ln2} \tag{4.2.2}$$

where $n(E)$ is the depth, in radiation length units, at which the mean energy of the particles is E. From this relation it is possible to infer the the differential energy spectrum of the particles decreases as:

$$\frac{dN}{dE} \propto \frac{1}{E^2} \tag{4.2.3}$$

More complicated analytic models were developed by Rossi and Greisen in 1940s.
The result obtained by Heitler model are confirmed by detailed studied based on Monte Carlo (MC) simulations. Today with development of computational tools analytic models are less relevant than MC simulations.
For example, CORSIKA (COsmic Ray SImulations for KAscade) is a useful program for detailed simulation of extensive air showers (EAS) initiated by high energy cosmic ray particles or γ-rays.

4.3 Cherenkov Radiation

When a charged particle moves through a dielectric medium at a speed greater than the local phase velocity of light in that medium, it emits a characteristic electromagnetic radiation.

This radiation was observed for the first time by soviet scientist P.A. Cherenkov in 1934 and theoretically interpreted and calculated by I.M. Frank and I.E. Tamm in 1937.

We underline that this radiation is different from Bremsstrahlung radiation wich is almost always emitted by the moving charged particle itself when it collides with atoms. The Cherenkov effect, instead, involves radiation emitted by the medium under the action of the field of the particle moving in it. The distinction between the two kinds of radiation appears with particulary clarity when the particle has a very large mass: the Bremsstrahlung disappears, but the Cherenkov radiation is unaffected.

The explanation of this phenomenon is based on Maxwell's equations in a dielectric medium, which provide macroscopic dynamic description of the electromagnetic field.

Since a particle in uniform rectilinear motion does not give rise to any radiation field, at the microscopic level the Cerenkov radiation must therefore be originated from polarization charges.

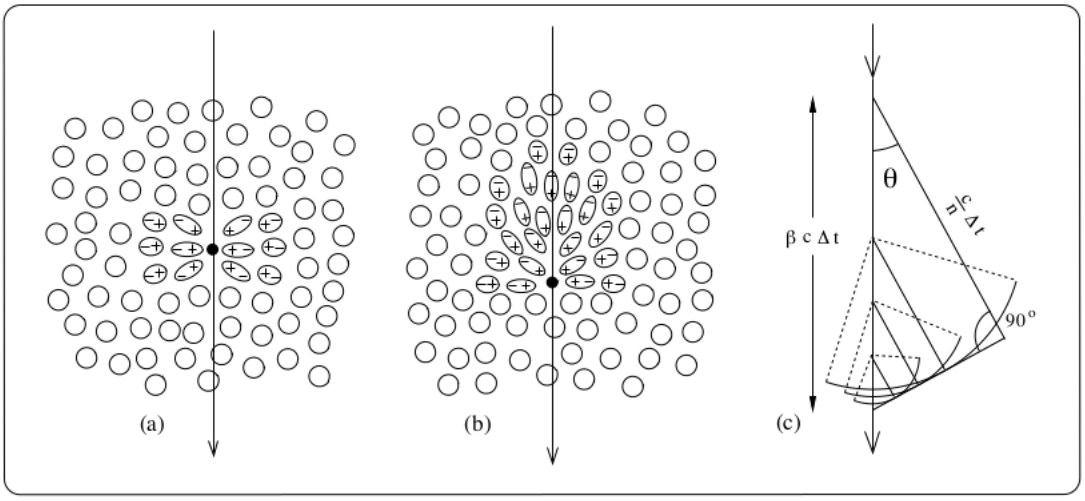

Figure 4.5: Schematic representation of the Cherenkov radiation. *(a)* Symmetric polarizatione produce by a particle moving with speed $v < c/n$. *(b)* The net polarization due to a charge moving at $v > c/n$ creates a wave of radiation. *(c)* Geometrica description of the Cherenkov emission.

In fact, what happens at the microscopic level is that the charged particle during its passage deforms the molecules of the medium doing their purchase an electric dipole moment, which disappears immediately after the charged particle passage. The charges of the dipole moments are so subjected to instantaneous acceleration, and thus become impulsive sources of elementary electromagnetic waves, which manifest as Cherenkov radiation.

The wave number and frequency of an electromagnetic wave propagated in a trasparent medium are related by $k = n\omega/c$, where $n = \sqrt{\varepsilon_r}$ is the refractive index, which is real and ϵ_r is the relative permittivity. In a trasparent medium the phase velocity of electromagnetic waves is $c_m := \dfrac{c}{n} = \dfrac{c}{\sqrt{\varepsilon_r}}$ and for $n > 1$ results $c_m < c$.

Now we consider a particle of charged ze moving at speed $\vec{v} = \vec{\beta}c$. It gives rise to a charge distribution $\rho(\vec{r}, t) = ze\delta^3(\vec{r} - \vec{v}t)$ and a current density $j(\vec{r}, t) = ze\vec{v}\delta^3(\vec{r} - \vec{v}t)$.

We suppose the medium isotropic and non-magnetic, $\vec{B} = \mu_0 \vec{H}$ and which it is represented by a generic operator $\hat{\varepsilon}$ such that $\vec{D} = \hat{\varepsilon}\vec{E}$. To greatly simplify the discussion, assume that $\hat{\varepsilon}$ is linear (and therefore continuous).

Linearity is typically satisfied with good approximation at optical frequencies in the most common transparent mediums, excluding at most restricted resonance bands. The salient features of Cherenkov radiation, however, is also preserved by relaxing the hypothesis of linearity, but the mathematical treatment becomes very complex, not being permitted commutation of $\hat{\varepsilon}$ with differential operators.

We impose the following physical (mathematical) conditions at dielectric medium:

- The properties of the medium remains unchanged during the entire observation period. ($\rightarrow$ $\hat{\varepsilon}$ commute with $\partial/\partial t$).
- The medium is homogeneous ($\rightarrow$ $\hat{\varepsilon}$ commute with ∇).
- The medium is isotropic ($\rightarrow$ $\hat{\varepsilon}$ commute with div:= $\nabla\cdot$ and with rot:= $\nabla\times$).

From homogeneous Maxwell's equations we introduce scalar and vector potentials, with usual definitions:

$$\begin{aligned} \nabla \cdot \vec{B} = 0 \qquad &\rightarrow \qquad \vec{B} = \nabla \times \vec{A} \\ \nabla \times \vec{E} = -\frac{\partial \vec{B}}{\partial t} \qquad &\rightarrow \qquad \vec{E} = -\frac{\partial \vec{A}}{\partial t} - \nabla\phi \end{aligned} \tag{4.3.1}$$

with the additional Lorentz gauge condition.

$$\nabla \cdot \vec{A} + \mu_0 \hat{\varepsilon} \frac{\partial \phi}{\partial t} = 0 \tag{4.3.2}$$

From homogeneous Maxwell's equations and current and density definitions we obtain:

$$\begin{aligned} \nabla \cdot \vec{D} = \rho \qquad &\rightarrow \qquad \left(\hat{\varepsilon}\nabla \cdot \vec{E}\right)(\vec{r}) = ze\delta^3(\vec{r} - \vec{v}t) \\ \nabla \times \vec{H} = \vec{j} + \frac{\partial \vec{D}}{\partial t} \qquad &\rightarrow \qquad \left(\nabla \times \vec{B} - \mu_0 \hat{\varepsilon} \frac{\partial \vec{E}}{\partial t}\right)(\vec{r}) = \mu_0 ze\vec{v}\delta^3(\vec{r} - \vec{v}t) \end{aligned} \tag{4.3.3}$$

Then substituing (4.3.1) in (4.3.3) with condition (4.3.2), we obtain the following equations for the potentials:

$$\begin{aligned} \hat{\varepsilon}\left(\cancel{-\frac{\partial \nabla \cdot \vec{A}}{\partial t}} - \nabla^2\phi + \mu_0\hat{\varepsilon}\frac{\partial^2\phi}{\partial t^2} - \cancel{\mu_0\hat{\varepsilon}\frac{\partial^2\phi}{\partial t^2}}\right)(\vec{r}) \;&=\; ze\delta^3(\vec{r} - \vec{v}t) \\ \rightarrow \qquad \hat{\varepsilon}\left(\nabla^2 - \mu_0\hat{\varepsilon}\frac{\partial^2}{\partial t^2}\right)\phi(\vec{r}) \;&=\; -ze\delta^3(\vec{r} - \vec{v}t) \\ \cancel{\nabla(\nabla \times \vec{A})} - \nabla^2\vec{A} + \mu_0\hat{\varepsilon}\frac{\partial^2\vec{A}}{\partial t^2} + \cancel{\mu_0\hat{\varepsilon}\frac{\partial^2\phi}{\partial t^2}} \;&=\; \mu_0 ze\vec{v}\delta^3(\vec{r} - \vec{v}t) \\ \rightarrow \qquad \left(\nabla^2 - \mu_0\hat{\varepsilon}\frac{\partial^2}{\partial t^2}\right)\vec{A}(\vec{r}) \;&= -\mu_0 ze\vec{v}\delta^3(\vec{r} - \vec{v}t) \end{aligned} \tag{4.3.4}$$

We can observe that scalar and vector potentials expressions can be grouped as a single four vector relation.

Now we expand $\vec{A}$ and ϕ as Fourier space integrals in the wave vector domain. Where we have $f(\vec{r}) = \int d^3k\ e^{i\vec{k}\cdot\vec{r}} f(\vec{k})$, the operator ∇ begin $i\vec{k}$ and $\partial/\partial t$ can be soluted thanks to the terms $\delta^3(\vec{r}-\vec{v}t) = \int d^3k\ e^{i\vec{k}\cdot\vec{r}} e^{-i\vec{k}\cdot\vec{v}t}$, imposing $\omega := \vec{k}\cdot\vec{v}$ we obtain that $\partial/\partial t$ begin $i\omega$, because $i\vec{k}\cdot\vec{r} = i\vec{k}\cdot\vec{v}t = i\omega t$.

So in the wave vector domain we have:

$$\begin{aligned}
\frac{1}{(2\pi)^3}\int d^3k\hat{\varepsilon}\left(\nabla^2 - \mu_0\hat{\varepsilon}\frac{\partial^2}{\partial t^2}\right)\left[e^{i\vec{k}\cdot\vec{r}}\phi(\vec{k})\right] &= \frac{-ze}{(2\pi)^3}\int d^3k\ e^{i\vec{k}\cdot\vec{r}}e^{-i\omega t} \\
\int d^3k\hat{\varepsilon}\left(-\nabla^2 e^{i\vec{k}\cdot\vec{r}} + \mu_0\hat{\varepsilon}\frac{\partial^2 e^{i\omega t}}{\partial t^2}\right)\phi(\vec{k}) &= ze\int d^3k\ e^{i\vec{k}\cdot\vec{r}}e^{-i\omega t} \\
\int d^3k\varepsilon(\omega)\left(k^2 - \mu_0\varepsilon(\omega)\omega^2\right)\phi(\vec{k}) &= ze\int d^3k\ e^{i\vec{k}\cdot\vec{r}}e^{-i\omega t} \\
\rightarrow \qquad \phi(\vec{k}) &= \frac{ze}{\varepsilon(\omega)}\frac{e^{-i\omega t}}{k^2 - \mu_0\varepsilon(\omega)\omega^2}
\end{aligned} \tag{4.3.5}$$

and similarly for the vector potential $\vec{A}$:

$$\begin{aligned}
\frac{1}{(2\pi)^3}\int d^3k\left(\nabla^2 - \mu_0\hat{\varepsilon}\frac{\partial^2}{\partial t^2}\right)\left[e^{i\vec{k}\cdot\vec{r}}\vec{A}(\vec{k})\right] &= \frac{-\mu_0 ze\vec{v}}{(2\pi)^3}\int d^3k\ e^{i\vec{k}\cdot\vec{r}}e^{-i\omega t} \\
\int d^3k\left(-\nabla^2 e^{i\vec{k}\cdot\vec{r}} + \mu_0\hat{\varepsilon}\frac{\partial^2 e^{i\omega t}}{\partial t^2}\right)\vec{A}(\vec{k}) &= \mu_0 ze\vec{v}\int d^3k\ e^{i\vec{k}\cdot\vec{r}}e^{-i\omega t} \\
\int d^3k\left(k^2 - \mu_0\varepsilon(\omega)\omega^2\right)\vec{A}(\vec{k}) &= \mu_0 ze\vec{v}\int d^3k\ e^{i\vec{k}\cdot\vec{r}}e^{-i\omega t} \\
\rightarrow \qquad \vec{A}(\vec{k}) &= \mu_0 ze\vec{v}\frac{e^{-i\omega t}}{k^2 - \mu_0\varepsilon(\omega)\omega^2}
\end{aligned} \tag{4.3.6}$$

And now a few considerations:

1. $\hat{\varepsilon} \rightarrow \varepsilon(\omega)$ this is a consequence of the assumptions made about the nature of the dielectric. In addition the local causality conditions require that $\varepsilon(\omega)$ is analytic in all complex semi-plane $\Im > 0$. Since we are considering a dieletric medium we can expand the condition in $\Im \geq 0$. At this point, since $\varepsilon(\omega)$ is regular, we can replace $\mu_0\varepsilon(\omega) = 1/c_m^2$, where c_m is the electromagnetic wave velocity.

2. We can note that $\vec{A}$ is parallel to $\vec{v}$. Therefore $B = \nabla \times \vec{A}$ is parallel to $\vec{k}\times\vec{v}$. Fixed the direction of $\vec{B}$ along the axis of $\vec{k}$ and $\vec{v}$ plane, the Poynting vector tells us that $\vec{B}$ and $\vec{E}$ are polarized as in (FIG).

3. $\omega = \vec{k}\cdot\vec{v}$ is for now only a mathematical equality: to consider ω as the angular frequency of the electromagnetic wave has to occur $|\omega| = kc_m$. If this is true, Bessel's inequality (the projection of a vector is less than or equal to the norm of vector) tells us that $kc_m = \omega = \vec{k}\cdot\vec{v} \leq kv \rightarrow v \geq c_m$, so the Cherenkov emission can only occur if $v \geq c_m$.

In this case, we are able to calculate the emission angle between the radiation emitted along $\vec{k}$ and the charged particle moving along $\vec{v}$. From $kc_m = \omega = \vec{k} \cdot \vec{v} = kv \cos\theta_c$ we obtain:

$$\cos\theta_c = \frac{c_m}{v} = \frac{1}{\beta n} \tag{4.3.7}$$

The emission angle can be explained by the Huygens contruction about the superposition of spherical electromagnetic waves generated by passing of the charged particle (see Figure 4.6).

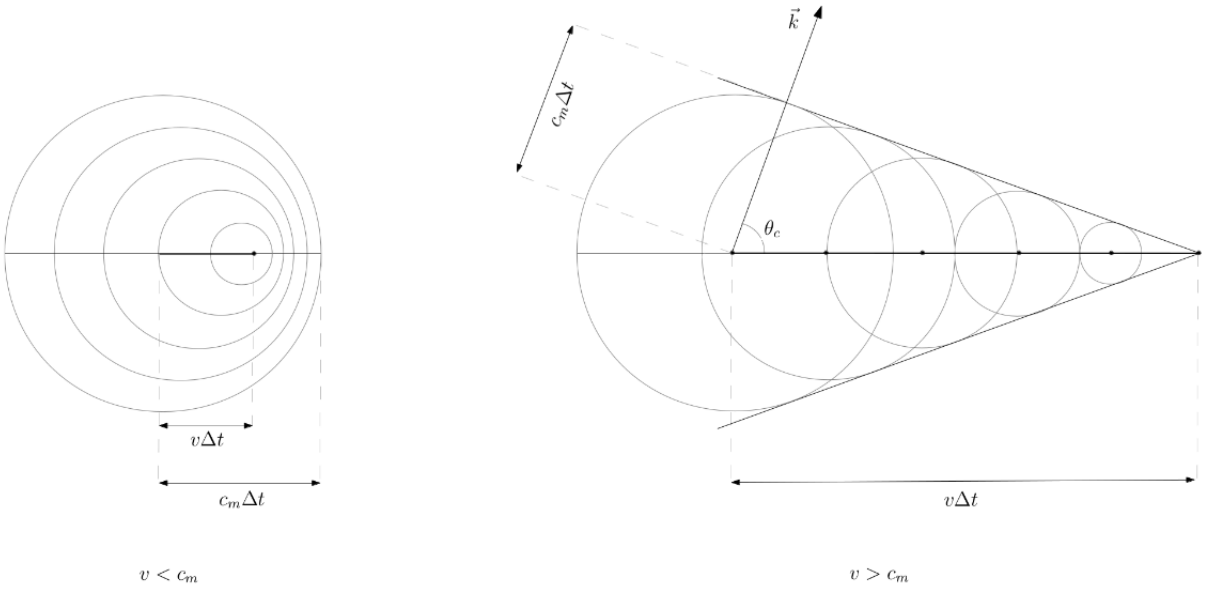

Figure 4.6: Simple sketch of the Cherenkov effect. (*Left*) When a cherged particle moves slower than the speed of light in the medium, the electromagnetic waves, initiated along its trajectory, are not superimposed. (*Right*) When its speed exceeds the local speed of light, a surface of costructive interference appears.

Hence we still have to prove only that $|\omega| = kc_m$. We can show this by calculating the expression of the force $\vec{F}(\vec{r}) = ze\vec{E}(\vec{r})$ acting on the particle.

$$\begin{aligned}\vec{F}(\vec{r}) &= \frac{ze}{(2\pi)^3}\int d^3k\,\left(-\frac{\partial\vec{A}(\vec{k})}{\partial t} - \nabla\phi(\vec{k})\right)e^{i\vec{k}\cdot\vec{r}} \\ &= \frac{-z^2e^2\mu_0}{8\pi^3}\int\frac{d^3k}{k^2-\mu_0\varepsilon(\omega)\omega^2}\left(\vec{v}\;e^{i\vec{k}\cdot\vec{r}}\frac{\partial e^{-i\omega t}}{\partial t} + \frac{e^{-i\omega t}\;\nabla e^{i\vec{k}\cdot\vec{r}}}{\mu_0\varepsilon(\omega)}\right)\end{aligned} \tag{4.3.8}$$

Simplifying and substituing in (4.3.8) the following relations $\mu_0\varepsilon_0 = 1/c^2$, $\mu_0\varepsilon(\omega) = 1/c_m^2$ and the fine structure constant is $\alpha = \dfrac{e^2}{4\pi\varepsilon_0 c\hbar}$ we have:

$$\begin{aligned}&= \frac{iz^2}{2\pi^2}\left(\frac{e^2}{4\pi\varepsilon_0 c\hbar}\right)\frac{\hbar}{c}\int\frac{d^3k}{k^2-\mu_0\varepsilon(\omega)\omega^2}\left(\omega\vec{v} - \frac{\vec{k}}{\mu_0\varepsilon(\omega)}\right)\cancel{e^{i\vec{k}\cdot\vec{r}}}\,\cancel{e^{-i\omega t}} \\ \vec{F}(\vec{r}) &= \frac{iz^2\alpha\hbar}{2\pi^2 c}\int\frac{d^3k}{k^2-\frac{\omega^2}{c_m}}\left(\omega\vec{v} - c_m^2\vec{k}\right)\end{aligned} \tag{4.3.9}$$

The component orthogonal to $\vec{v}$ is odd. Hence the force is parallel to $\vec{v}$: $F(\vec{r}) = \frac{\vec{F}\cdot\vec{v}}{v}$.

Since there is a cylindrical symmetry we consider $k_{/\!/} = \frac{\vec{k}\cdot\vec{v}}{v} = \frac{\omega}{v}$ and $k_\perp$ and we substitute $d^3k = 2\pi k_\perp dk_\perp dk_{/\!/} = 2\pi k_\perp dk_\perp d\omega/v$ and therefore:

$$\begin{aligned} F(\vec{r}) = \frac{\vec{F}\cdot\vec{v}}{v} &= \frac{iz^2\alpha\hbar}{2\pi\not{c}} \iint \frac{2\not{\pi}k_\perp dk_\perp}{k^2 - \frac{\omega^2}{c_m}} \frac{d\omega}{v}\left(\frac{\omega\vec{v}\cdot\vec{v}}{v} - \frac{c_m^2\vec{k}\cdot\vec{v}}{v}\right) \\ &= \frac{iz^2\alpha\hbar}{2\pi c}\int d\omega \int \omega\frac{d\xi}{\xi}\left(1 - \frac{c_m^2}{v^2}\right) \end{aligned} \tag{4.3.10}$$

where $\xi = k^2 - \frac{\omega^2}{c_m}$ and $d\xi = 2k_\perp dk_\perp$.
The second integral $\int \omega\frac{d\xi}{\xi}$ is a Cauchy's integral, easily computable in complex analysis. The function $\varepsilon(\omega)$ has no singularity and no zero in half-plane $\Im > 0$ and so the required poles can only be the zeros of the expression $\xi = k^2 - \omega^2/c_m^2$. It imply that $\rightarrow |\omega| = kc_m$. Using the Residue theorem we obtain:

$$\oint_\gamma f(z)dz = 2\pi i\sum_k \mathrm{Res}(f_\gamma, c_k)$$

where $\quad \mathrm{Res}(f,c) = \lim_{z\to c}(z-c)f(z)$

$$\oint_\gamma \omega\frac{d\xi}{\xi} = 2\pi i\omega$$

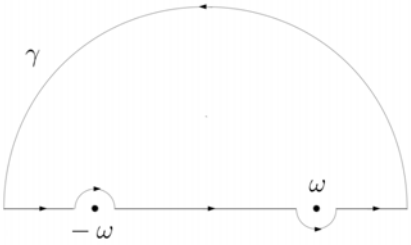

Figure 4.7: Contour γ for the calculation of the Cauchy's integral.

Hence the expression of the force results:

$$F(\vec{r}) = \frac{-z^2\alpha\hbar}{c}\int d\omega\ \omega\left(1 - \frac{c_m^2}{v^2}\right) \tag{4.3.11}$$

The differential expression of the force in in a frequency interval $d\omega$ results:

$$\frac{dF}{d\omega} = \frac{-z^2\alpha}{c}(\hbar\omega)\left(1 - \frac{c_m^2}{v^2}\right) \tag{4.3.12}$$

The energy loss by the moving particles is just the work done by the force F exerted on the particle by the field wich it produces. Therefore knowing that $F = -\frac{dW}{dx}$ we can write the Frank-Tamm formula:

$$\frac{d^2W}{dxd\omega} = \frac{z^2\alpha}{c}(\hbar\omega)\left(1 - \frac{c_m^2}{v^2}\right) \tag{4.3.13}$$

which gives the intensity of the radiation emitted on a given frequency.
Remembering that the Cherenkov radiation is composed by photons of energy $\hbar\omega$, we can determine the number of photons produced per unit path lenght of a particle with charge ze and per unit in a frequency interval $d\omega$:

$$\frac{d^2N}{dxd\omega} = \frac{z^2\alpha}{c}\left(1 - \frac{c_m^2}{v^2}\right) = \frac{z^2\alpha}{c}\sin^2\theta_c \tag{4.3.14}$$

while the total number of photons per unit path-lenght is given by:

$$\frac{dN}{dx} = \frac{z^2\alpha}{c}\int\left(1 - \frac{c_m^2}{v^2}\right)d\omega \tag{4.3.15}$$

4.3.1 Propagation of Cherenkov radiation through the Atmosphere

In this section we discuss Cherenkov photons propagation. The Cherekov cone is described by the angle $\theta_c = acos(1/\beta n)$, at the sea level, the refractive index of air is $n \approx 1.00029$, this imply that $\theta_{max} \simeq 1.3°$.
The minimum speed to have Cherenkov radiation is:

$$E_{th} = \frac{m_e c^2}{\sqrt{1-\beta_{min}^2}} = \frac{m_e c^2}{\sqrt{1-1/n^2}} \tag{4.3.16}$$

Since the refractive index changed with height we hve to consider the following relation:

$$n = 1 + \eta_h = 1 + \eta_0 e^{-h/h_0} \approx 1 + 2.9 \cdot 10^{-}4 e^{-h/h_0} \tag{4.3.17}$$

where $h_0 \approx 7.1\, km$, thus if $\eta_h \ll 1$ the energy threshold is:

$$E_{th} \simeq \frac{m_e c^2}{\sqrt{2\eta_h}} \tag{4.3.18}$$

Therefore we find i.e. for electrons at height of $10\, km$ an energy threshold of $E_{th} \sim 42 MeV$. that is less than critical energy $E_c \approx 83\, MeV$, so once an EM showers dies out most of the electrons still emit Cherenkov light.

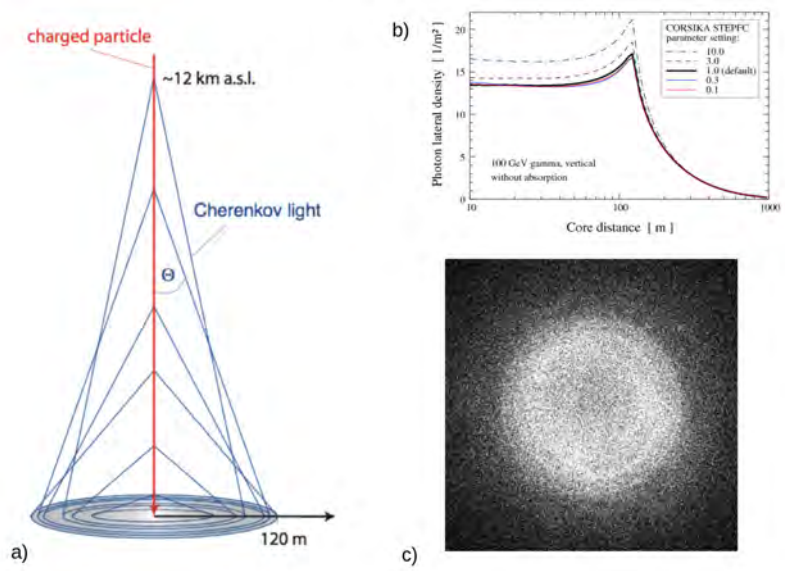

Figure 4.8: In this figures we want emphasize the lateral Cherenkov photons distribution. a) Sketch of the Cherenkov cone. b) Plot of photon lateral density in function of core distance. c) Photon density due to a VHE electron.

For EM showers, the number of electrons with energy greater than E_{th} as a function of the number N_e of electrons present in the shower maximum is given by

$$N(E > E_t h) \approx \frac{N_e}{1 + E_{th}/30} \tag{4.3.19}$$

with energies expressed in MeV. Therefore, about half of the electrons at the shower maximum has energy greater than the minimum one necessary for emitting Cherenkov light. The maximum angle θ_{max} for particles with $\beta \simeq 1$ can be obtained from the expression

$$\cos\theta_{max} \simeq \frac{1}{1 + \eta_0 e^{-h/h_0}} \simeq 1 - \eta_0 e^{-h/h_0} \tag{4.3.20}$$

and has an averaged over altitude value of about 1.2°. By knowing θ_{max}, the distance from the emitted Cherenkov photons to the axis of the emitting charged particle at a given height h_{obs} can be derived:

$$R_c = (h - h_{obs}) \cdot tan\theta_{max} \tag{4.3.21}$$

The Cherenkov radiation of an Atmospheric shower consists of the cumulative Cherenkov light emitted by the charged shower particles. The light from the shower tail is emitted with larger angles, but its distance to the shower axis can be smaller just because of its lower height (see Figure 4.8.a).
From Frank-Tamm formula we obtain that the number of emitted Cherenkov photons per unit path-lenght and wavelenght for a particle with charge $q = ze$ is:

$$\frac{d^2N}{dxd\lambda} = \frac{2\pi z^2 \alpha}{\lambda^2}\left(1 - \frac{1}{\beta^2 n^2(\lambda)}\right) \tag{4.3.22}$$

The $1/\lambda^2$ dependency of the spectrum indicates that most of the Cherenkov photons are emitted at short wavelengths, in the ultraviolet range, and that it decreases along the visible region. However, due to the interactions of the Cherenkov photons with the air molecules in their path through the atmosphere, the spectrum observed at ground level is quite different from the emitted one (see Fig. 4.9), and it peaks at around 330 nm.

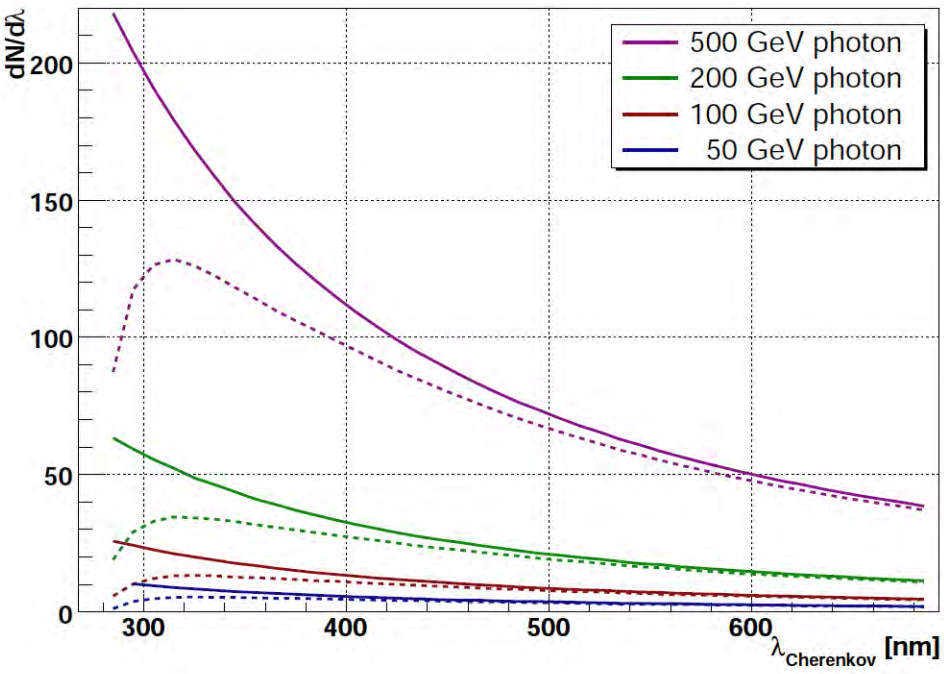

Figure 4.9: Spectra of Cherenkov light by vertical γ–ray showers of different primary energies at 10 km height (solid lines) and the corresponding spectra at 2200 m a.s.l. (dashed curves), affected by absorption, Rayleigh and Mie scattering, as discussed in the text.

Cherenkov photons suffer the following attenuation processes in the atmosphere:

- Rayleigh scattering, in which light wave is diffused by particles smaller than the same wavelenght($\sim$ 100 nm). The absorption coefficient is $\propto \lambda^{-4}$, thus photons with lower wavelenght are more diffused.
- Mie scattering, is strictly connected with the previous phenomenon, but in this case the distributing points may have upon any dimension (dust, drops of water,ect)
- ozone absorption, in which the reaction $O_3 + \gamma \rightarrow O_2 + O$ absorbes photons with $\lambda < 290\, nm$

Chapter 5

The Cherenkov Telescope Array

The CTA Consortium is building a new observatory for very high-energy (VHE) gamma rays. Supported by a wide international collaboration, its project consists into the realization of two arrays of the latest generation of Imaging Atmospheric Cherenkov telescopes (IACTs), one located in the northern hemisphere (Canary Islands), with an emphasis on the study of extragalactic objects, and one in southern hemisphere (Chile) dedicated to the galactic sources. Beside a wealth of high-energy astrophysics results, CTA will have a large discovery potential in key areas of astronomy and fundamental physics research.

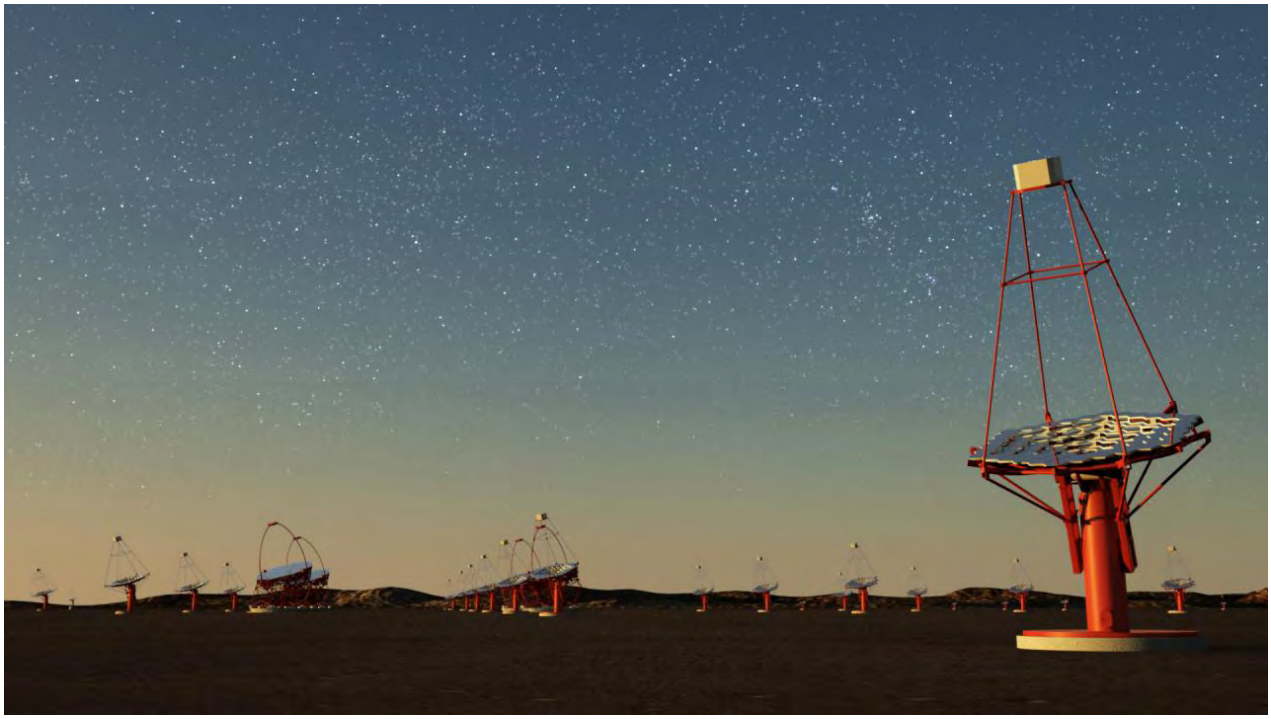

Figure 5.1: Artistic drawing of a CTA site. G.Pérez

These include the study of the origin of cosmic rays and their role in the Universe, the investigation of the nature and varieties of black hole particle accelerators and the search for signals from dark matter and physics beyond the Standard Model.
The CTA project has ambitious science goals, for which it is necessary to achieve full-sky coverage, to improve sensitivity by about an order of magnitude in a wide range of energy, from a few GeV to above 100 TeV with enhanced angular and energy resolutions over the existing VHE gamma ray observatories with the same detection technique, such as H.E.S.S, MAGIC and VERITAS.

5.1 CTA concept

The current generation of ground-based γ-ray instruments have produced a large amount of results, giving rise to a new branch of astronomy, through the discovery, imaging and spectroscopy of VHE γ-ray sources. But many of these results have raised new questions and require more and better data for a deeper understanding of the observed phenomena.

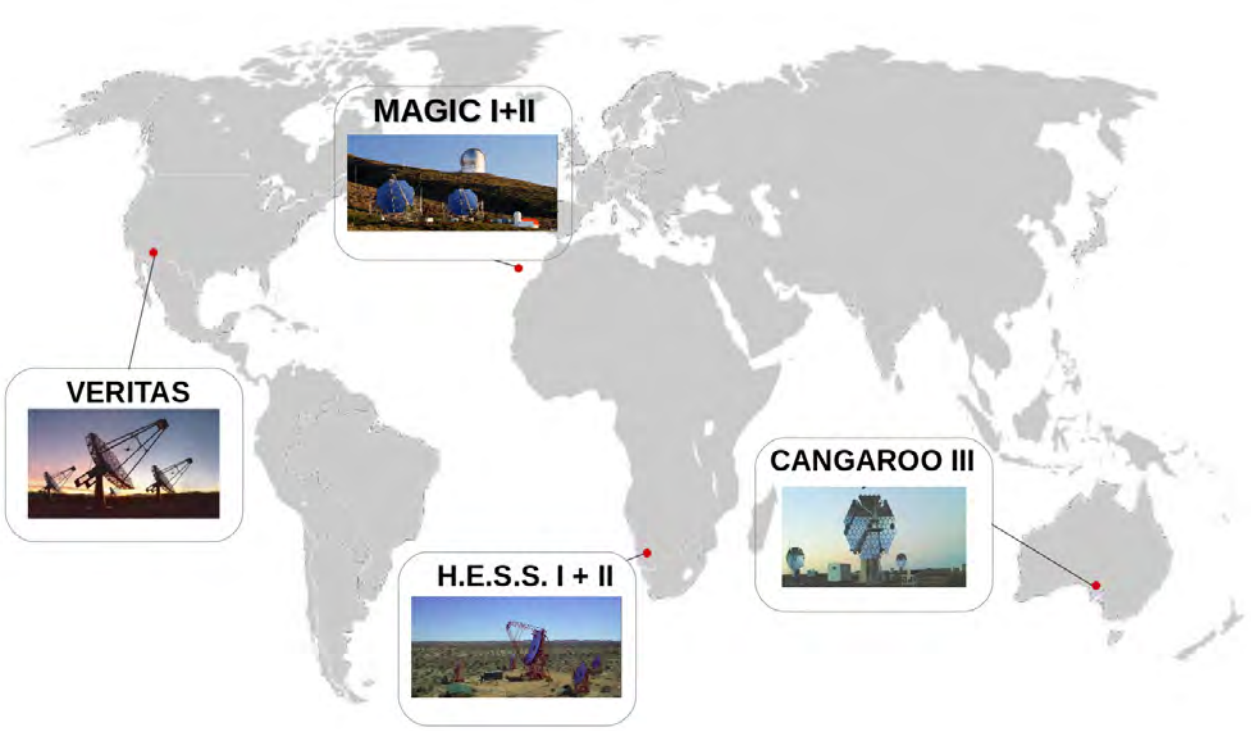

Instrument	Lat (°)	Long (°)	Alt (m)	Telescopes	Area (m^2)	Pixels per camera	FoV (°)	Threshold (TeV)	Sensitivity (% Crab) > 1 TeV
H.E.S.S.	−23	16	1800	4	107	960	5	0.1	0.7
H.E.S.S. II	−23	16	1800	1	614	2048	3.2	tbd	tbd
VERITAS	32	−111	1275	4	106	499	3.5	0.07	0.7
MAGIC I+II	29	−18	2225	2	234	1039	3.5	0.03	0.8
CANGAROO-III	−31	137	160	3	57.3	427	4	0.4	15

Fig 5.2: Map and properties of the main current air-Cherenkov instruments. Adapted from [16]. Significances relate to a point-like source detectable at the 5σ significance level in a 50 h observation.

The current telescope arrays consist of 2–5 Cherenkov telescopes.
They reach sensitivities of about 1% of the Crab flux at energies in the $0.1 - 1$ TeV range. Sensitivity degrades towards lower energies, due to insufficient background rejection, and towards higher energies, due to the limited number of gamma rays.

A typical angular resolution is 0.1° or slightly better for a single gamma ray, but sufficiently intense point sources can be located with a precision of $10 - 20$ arc seconds.

All these instruments are almost exclusively used by the groups who built them, with only limited access for external observers and, initially, with no provision for open data access.

However, a different approach is essential for CTA, due to the expected large increase in the number of detectable objects and the required collaboration with scientists working in other wavelength ranges.

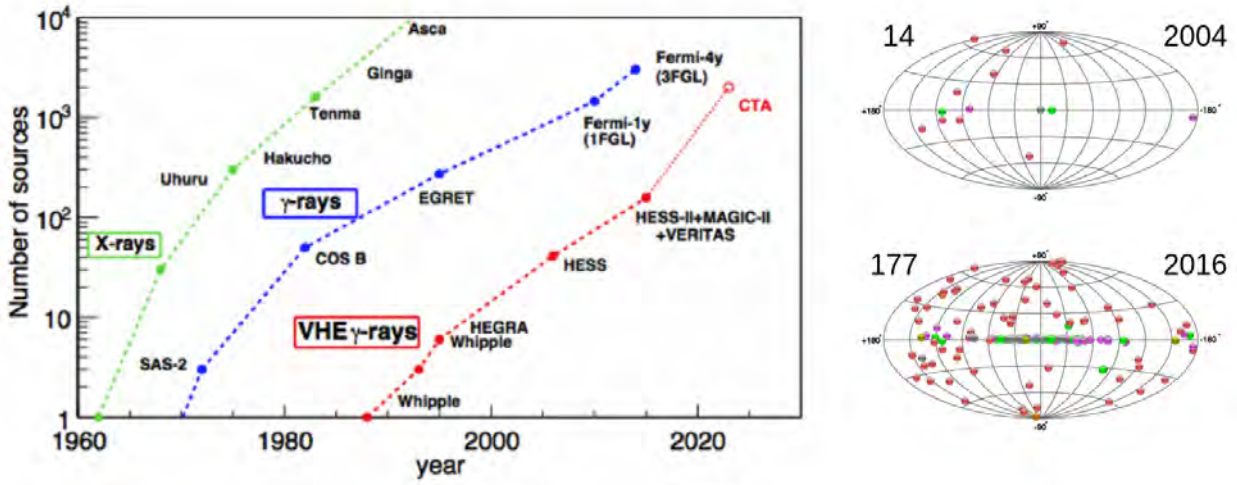

Figure 5.3: (*left*) Kifune plot showing the number of sources detected over time for various waveband.[35] (*Right*) VHE γ-ray sources detected from 2004 (14 sources) to 2016 (177 sources). Images from TeVCat.

The number of the VHE gamma-ray sources has grown over the past decade from about twenty to over 170 sources. This is the result of a better sensitivity and accuracy of the instruments. Due to the low flux of VHE photons the telescopes need a large detection area and long data taking time, to reach the required sensitivity.

Current instruments has conducted successfull survey, in particular H.E.S.S of the Milky Way, but to cover the full visible sky with the same sensitivity of H.E.S.S would be needed at least ten years, and is therefore unrealistic. Hence in the 20 GeV- 100 TeV region, how to do better?

Tab. 5.4: The CTA consortium states members and the two location of the northern site (Las Palmas, Canary Islands) and southern site (Paranal Chile).

5.2 CTA technologies

The CTA solution is give rise a large international collaborations to build a gamma ray observatory in two sites with high performance. This can be possible thanks to solutions to optimize the instrumentation for three adjacent energy ranges (without strong overlap).

- **The low-energy range** ≤ 100 **GeV**: To detect showers down to a few tens of GeV, the Cherenkov light needs to be sampled efficiently, with the fraction of area covered by light collectors being of the order of 10%.

  Since event rates are high and systematic uncertainties of the background limit the achievable sensitivity, the area of this part of the array can be relatively small, of the order of a few 10^4 m^2.

  The CTA design assumes a small number of closely placed large-size telescopes (LSTs), with a mirror diameter of about 23 m, to collect as many Cherenkov photons as possible from the low energy showers. These tele scopes require the short repointing time quoted to allow quick follow-ups of GRB alerts.

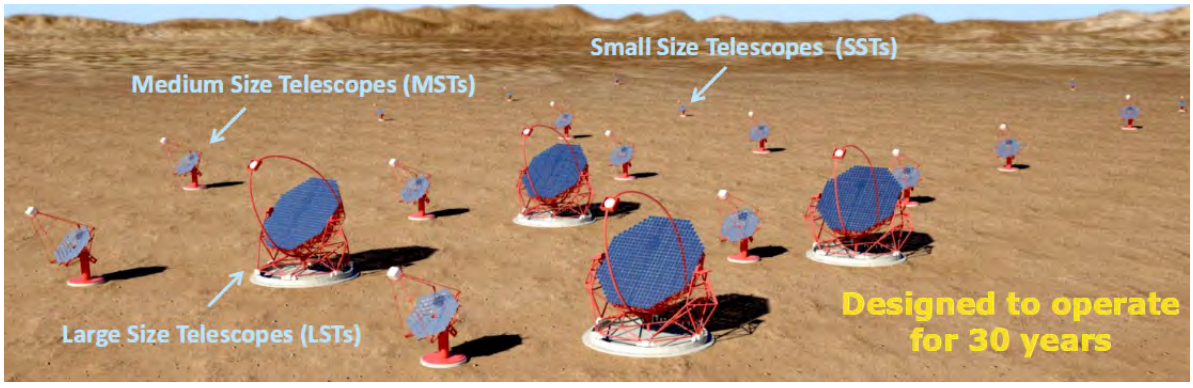

Figure 5.5: A solution with different size of telescopes, focused of a specific energy range. Large-Size Telescopes (LST) for the lower energy range from fews GeV to 100 GeV. Medium-Size Telescopes (MST) for the core energy range from 100 GeV to 10 TeV. Small-Size Telescopes (SST) for the higher energy range above 10 TeV.

- **The core energy range 0.1–10 TeV**: Shower detection and reconstruction in this energy range are well understood from current instruments. The appropriate step for improved performance is an array of mid-sized telescopes (MSTs) with mirrors of about 12 m diameter and a spacing of about 100 m.

  Improved sensitivity compared to existing instruments will be obtained both by the increased area covered by the array and by the higher quality of shower reconstruction, since individual showers will typically be stereoscopically imaged by a larger number of telescopes than in current few-telescope arrays.

  For the first time, array sizes will become much larger than the Cherenkov light pool of a shower, ensuring that images will be uniformly sampled across the light pool and that a number of images are recorded close to the optimum distance from the shower axis (about 70–150 m), where the light intensity is large and intensity fluctuations are small.

  Also, the shower axis is viewed under a sufficiently large angle for efficient reconstruction of its direction. At H.E.S.S. or VERITAS, for example, events which are seen and triggered by all four telescopes provide significantly improved resolution and strongly reduced backgrounds, but they represent only a relatively small fraction of events.

For CTA almost all events will be recorded at high quality. A further advantage of CTA is that an extended telescope grid operated with a two-telescope trigger condition will have a lower threshold than a small array, since there are always telescopes sufficiently close to the shower core.

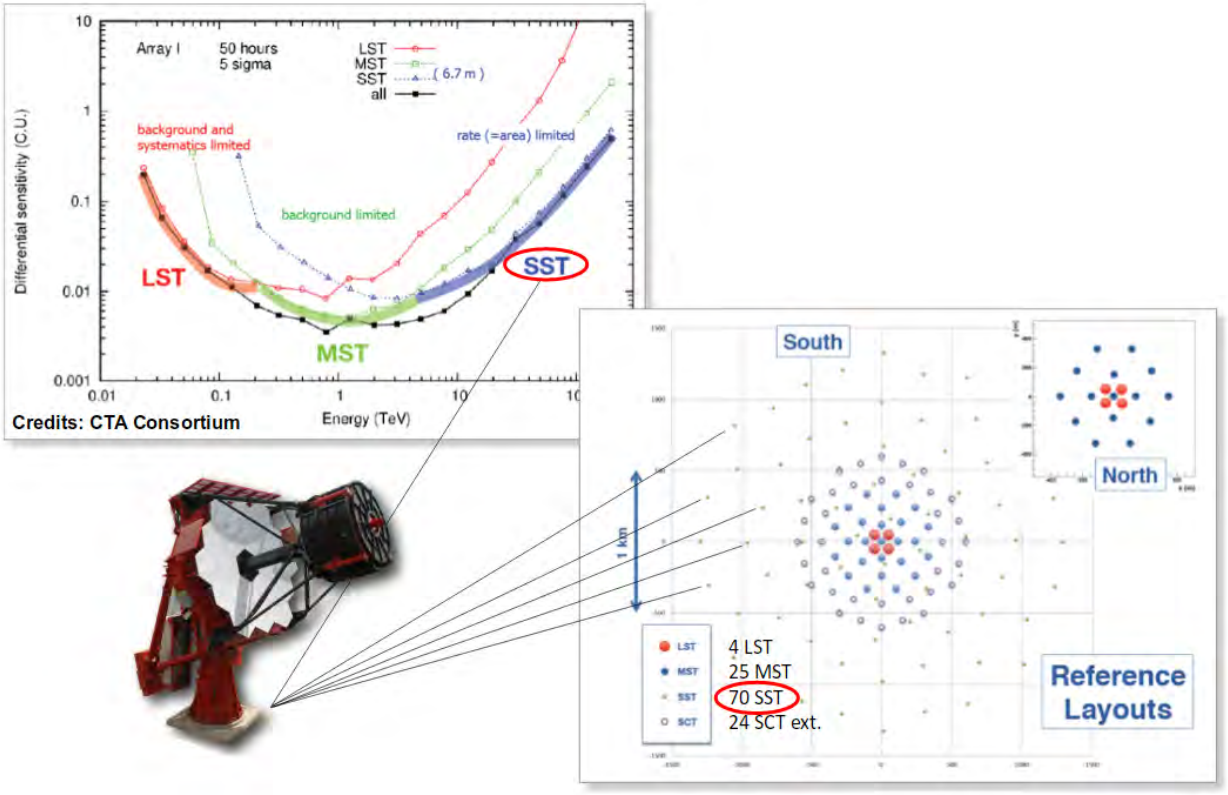

Tab. 5.6: The ASTRI SST-2M is proposed to be placed at the CTA southern site.
The Image show also the differential sensitivity (in units of the energy-dependent flux of the Crab nebula) for array E (50 h, 5r, 5% background, 10 events, $\alpha = 0.2$, i.e. intervals of the decimal exponent of 0.2 meaning 5 logarithmic bins per energy decade).[16]

- **The high-energy range >10 TeV**: Here, the main limitation is the number of detected gamma-ray showers. Consequently, to achieve large improvement the array needs to cover an area of several square kilometers.

  At high energies the light yield of a shower is large, so that showers can be detected well beyond the 150 m radius of a typical Cherenkov light pool. Two options can be considered: either a large number of small telescopes with mirror areas of a few m^2 and spacing matched to the size of the light pool (100-200 m), or a smaller number of larger telescopes with 10 -20 m^2 area which can see showers out to core distances of > 500 m, and can hence be either deployed with a spacing of several 100 m, or in widely separated sub-clusters consisting of a few telescopes. Both implementations are called Small Size Telescopes (SSTs).

  While it is not immediately obvious which option offers the best cost/performance ratio at high energies, the sub-cluster concept with larger telescopes has the advantage of providing additional high-quality shower images towards lower energies, for impact positions near the sub-cluster.

5.3 CTA performance

The aim of CTA is to make significant progress over the existing experiments in every fields. They include in particular:

- **Sensitivity**: CTA will be about an order of magnitude more sensitive than any existing instrument in its energy range. As a consequence it will, for the first time, allow detection and in-depth study of large samples of known source types, it will explore a wide range of classes of suspected gamma-ray emitters and be sensitive to possible new phenomena that lie beyond the sensitivity of current instruments.

  In its core energy range, from about 100 GeV to several TeV, CTA will have milli-Crab (mCrab) sensitivity, i.e. a factor of 10^3 below the flux of the strongest steady source of VHE gamma rays (the Crab nebula), and a factor of 10^4 below the highest fluxes measured so far in bursts from transient sources.

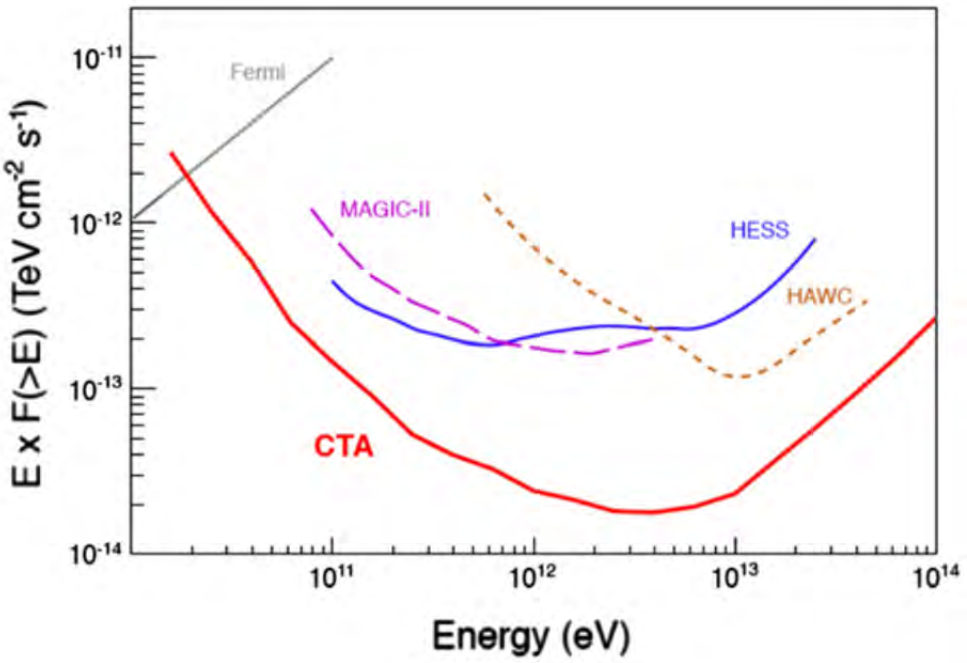

Figure 5.7: Integral sensitivity for CTA from MC simulations, together with the sensitivities in comparable conditions (50 h for IACTs, 1 year for Fermi-LAT and HAWC) for some gamma-ray observatories.[16]

- **Energy range**: Large coverage of the electromagnetic spectrum is crucial for understanding the physical processes occurring in VHE sources. With a single facility, CTA is aiming to cover four orders of magnitude in energy, from a few tens of GeV to a few hundred TeV, again a factor of 10 more than any existing instrument.

  Together with the much improved precision and lower statistical errors, this will enable astrophysicists to distinguish between key hypotheses such as the leptonic or hadronic origin of gamma rays from SNR. Moreover, the energy range and the improved resolution are important for the detection of line emission from dark matter clusters.

Diff. sensitivity (erg cm^{-2} s^{-1})	at 50 GeV	8×10^{-12}
	at 1 TeV	2×10^{-13}
	at 50 TeV	3×10^{-13} (S) / 10^{-12} (N)
Collection area (m^2)	at 1 TeV	$> 10^4$
	at 10 TeV	$> 10^6$ (S)/$> 5 \times 10^5$ (N)
Angular resolution	at 0.1 TeV	0.1°
	>1 TeV	0.05°
Energy resolution	at 50 GeV	$\leqslant$ 25%
	>1 TeV	$\leqslant$ 10%
Field of view	at 0.1 TeV	5°
	at 1 TeV	8°
	>10 TeV	10°
Sensitivity in FoV	at 1 TeV flat out to	$> 2.5°$
Source localisation	at 1 TeV	5″ per axis
Repointing time	<0.1 TeV	20 s (goal), 50 s (max)
	0.1–10 TeV	60 s (goal), 90 s (max)

Figure 5.8: Performance goals for the CTA observatories. The sensitivity is given for 5 bins per decade. For the sensitivity and collection area at high energies, separate values for southern (S) and northern (N) arrays are given. [16]

- **Angular resolution**: Current instruments are able to resolve extended sources, but they cannot probe the fine structures vis- ible in other wavebands. In SNRs, for example, the measure- ment of the width of the gamma-ray emitting shell would provide sensitive constraints on the acceleration mechanism.

  By selecting a subset of gamma-ray induced cascades detected simultaneously by many of its telescopes, CTA can reach angu- lar resolutions of better than 2 arc minutes for energies above 1 TeV, a factor of 5 better than the typical values for current instruments.

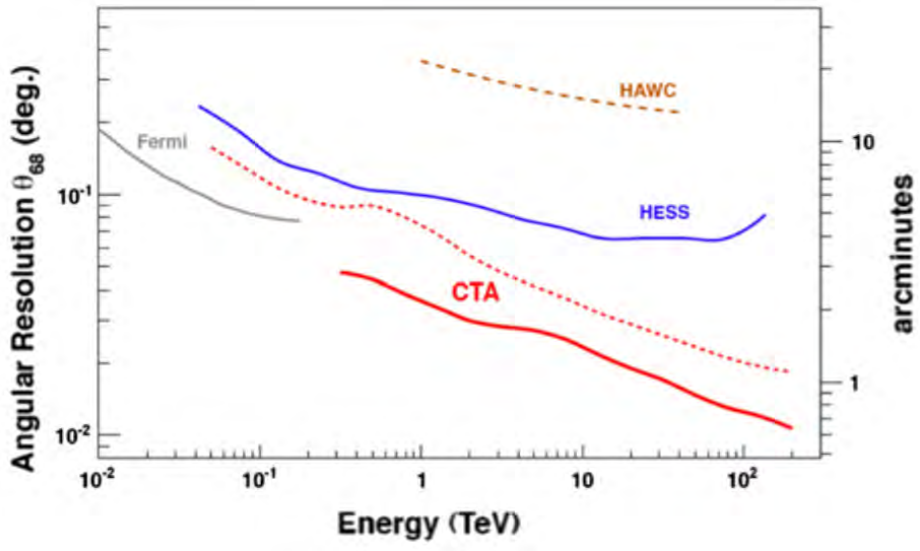

Figure 5.9: Angular resolution for CTA, compared with some existing and future VHE gamma-ray observatories. The solid line provides the angular resolution of CTA obtained from events with ten or more images, the dashed line shows the angular resolution for events with only two images.[16]

- **Temporal resolution**: With its large detection area, CTA can resolve flaring and time-variable emission on sub-minute time scales, which is currently out of reach. In gamma-ray emission from active galaxies, variability time scales probe the size of the emitting region.

Chapter 6

Simulation data using a Toy Monte Carlo

In the previous chapter we described the CTA project, its technical characteristics and goals. A key aspect that distinguishes these new observatories compared to the existing ones is the large number of telescopes.

The increase of the detection surface and the number of telescopes definitely implies a considerable improvement in terms of sensitivity and angular resolution but at the same time gives rise to a great computational challenge: the processing of the data.

In order to study the filtering of the events, we implemented a very flexible Toy-MC simulator able to reproduce the timing-detection of Cherenkov's light on a telescopes array with settled layout.

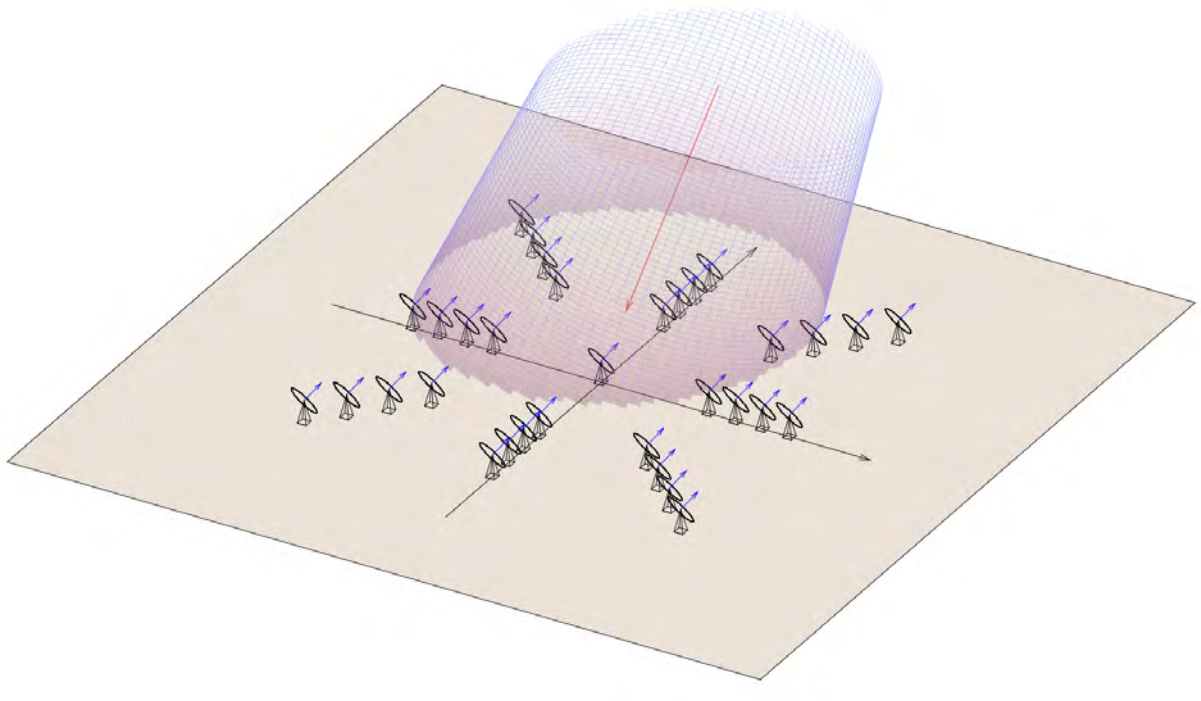

Figure 6.1: Image of a simulated event from Toy-MC simulator on a 33 telescopes array layout.

In this chapter we describe the main assumptions of this model, the use of the random generators and in particular the timing-process of simulated events. In the later chapters we compare our results with new Official MC simulation provided by ASTRI to ease the comparison we focused our study on the same telescopes array layouts.

6.1 Random generator algorithms

In order to implement a solid MC simulator we have to choose the best random number generators which satisfy our needs. A very good choice for our purpose is **ran3** generator described in Numerical Recipes (NR).[44]

The **ran3** generator is a Lagged Fibonacci generator based on subtractive method:

$$X_i = (X_{i-55} - X_{i-24}) \bmod m \tag{6.1.1}$$

where in the NR implementation $m = 10^9$ is used. The period length of this specific generators is known to be $2^{55} - 1 \approx 3.60 \cdot 10^{16}$. Its main characteristic is a very good speed with good period length. Through this generators we obtain random numbers with uniform distribution in range 0 to 1.0 for floating-point numbers.

```
const long k_big = 1000000000;
const long k_seed = 161803398;
const float k_fac = (1./k_big);

using namespace std;
long Random::init(long seed)
{   m_seed = seed<=0 ? clock() : seed;
    m_seed=seed;
    m_array[0] = (k_seed-m_seed)%k_big;
    if (m_array[0]<0) m_array[0]=-m_array[0];
    m_array[55]=m_array[0];
    long mk=1;
    for (int i=1; i<=54; i++)
    {   int ii = (21*i)%55;
        m_array[ii]=mk;
        mk=m_array[0]-mk; if (mk<0) mk+=k_big;
        m_array[0]=m_array[ii]; }
    for (int i=0; i<4; i++)
        for (int j=1; j<=55; j++)
        {   m_array[j] -= m_array[1+(j+30) % 55];
            if (m_array[j]<0) m_array[j] += k_big;}
    return m_seed;
}   /* end of Random::init */

float Random::ran3()
{   if (++m_next == 56) m_next=1;
    if (++m_nextp == 56) m_nextp=1;
    m_array[0] = m_array[m_next]-m_array[m_nextp];
    if (m_array[0]<0) m_array[0]+=k_big;
    m_array[m_next]=m_array[0];
    return m_array[0]*k_fac;
}   /* end of Random::ran3 */
```

In order to insert a statistical uncertainty we implemented also a Box-Muller algorithm to obtain random numbers normal distributed.

```
float Random::gauss()
{   float gret=m_gauss;
    if ((gset=!gset))
    {   float fac, rsq, v1, v2;
        do { v1 = 2.*ran3()-1.;
             v2 = 2.*ran3()-1.,
            rsq = v1*v1+v2*v2; }
        while (rsq>=1. || rsq==0.);
        fac = sqrt(-2.*log(rsq)/rsq);
        m_gauss = v1*fac;
        gret = v2*fac; }
    return gret;
}   /*  end of Random::gauss */
```

6.2 Toy-MC general assumptions

The main assumptions of our Toy-MC simulator are essentially about space and time.

We consider all telescopes as equals, with the same technical characteristics (height, Field of View, etc.). All of them have the same pointing direction expressed by a pair of coordinates: altitude and azimuth (Alt, Azi)$|_{Tel}$. Thus the array has one direction and one Field of View (FoV) in which the events are simulated with isotropic distribution.

Figure 6.2: Image of 150 simulated events into Field of View of telescope array (not to scale).

The FoV is considered unique for the whole array, it is a portion of a sphere centered in the pointing direction of the array and with angular aperture of about $\sim 10°$, in our simulations we set FoV at the ASTRI telescopes value ($\pm 5.5°$).

The primary cosmic rays distribution at ground level is considered uniform in a surface more large than the array area to allow the detections of border events.

Every cosmic rays simulated gives rise to an atmospheric shower which produces a Cherenkov light pool. The Cherenkov light pool on the ground has the shape of an ellipse centered in the point where the ground plane intercepts the cosmic ray direction. Position and dimension of the ellipse depend on the average radius $\langle R \rangle$ and the direction of the event (Alt, Azi)$|_{Evt}$.

In our MC model we established that a telescope detects an event if the following conditions are satisfied: the primary CRs direction is inside the FoV of array and the position (x,y) of the telescope is inside the ellipse of the Cherenkov light pool, we will better explain this point in the section about relative timing assumption.

6.3 Array layouts and Delays Matrix

The layout of the array is easily settable with any geometry, but as we have already mentioned we focused our study in particular on the setup of ASTRI, to compare our result with Official ASTRI MC simulation.

Throughout generality, given an array layout and a pointing direction (Alt, Azi)$|_{Tel}$ we are able to compute geometrically the relative delays due to a plane wavefront coming from the pointing direction between each telescope belonging to the array.

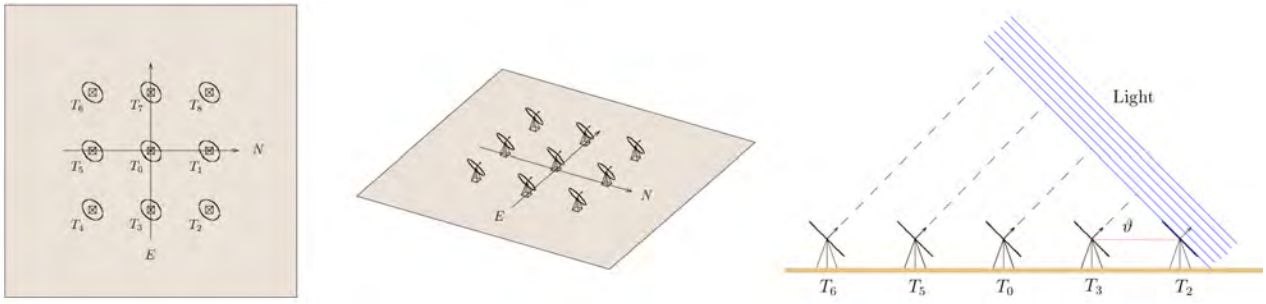

Figure 6.3: (*Left*) Image of ASTRI-CTA 9 layout. (*Right*) Relative geometrical delay due to a plane wavefront.

Assuming the speed of light in air being $c_n = c/n$, we can describe mathematically the array layout as a Delays Matrix $\mathcal{D}_T$ where an element $\mathcal{D}_{ij}$ is the theoretical delay Δt_{ij} between the telescope T_i and telescope T_j.

$$\mathcal{D}_T = \begin{pmatrix} 0 & \Delta t_{01} & \Delta t_{02} & \cdots & \Delta t_{0n} \\ \Delta t_{10} & 0 & \Delta t_{12} & \cdots & \Delta t_{1n} \\ \Delta t_{20} & \Delta t_{21} & 0 & \cdots & \vdots \\ \vdots & \vdots & \vdots & \ddots & \vdots \\ \Delta t_{n0} & \Delta t_{n1} & \cdots & \cdots & 0 \end{pmatrix} \qquad \Delta t_{ij} = -\Delta t_{ji} \tag{6.3.1}$$

To calculate Δt_{ij} is useful to first consider Δt_{i0} and then obtain $\Delta t_{ij} = \Delta t_{i0} - \Delta t_{j0}$. For a generic array (in this case an ASTRI-CTA 9 layout), if we have ϑ = Alt and φ = Azi and d_{ij} the distance between telescope we have:

$$\begin{aligned} d_{i0} &= \sqrt{(x_i - x_0)^2 + (y_i - y_0)^2} & i &= 1,2,3,4,5,6,7,8 \\ \tilde{d}_{i0} &= -d_{i0}\cos(\alpha_i - \varphi) & \alpha_i &= \frac{\pi}{4}(i-1) \\ \Delta t_{i0} &= \frac{\tilde{d}_{i0}}{c_n}\cos(\vartheta) & c_n &= c/n \end{aligned} \tag{6.3.2}$$

Thus $\mathcal{D}_T(d_{ij}, \vartheta, \varphi)$ contains all the information about the CTA layout. At first sight you could move the correct objection that all the information is contained, for example, in the first row of the Delays Matrix. This is true but this redundancy is useful for computational reasons and above all for the meaning of another matrix that we define in the next chapter.

To understand how the relative delays change in function of (Alt,Azi)$|_{Tel}$, we can observe Figure 6.4, it is instructive to understand the filtering algorithm performance.

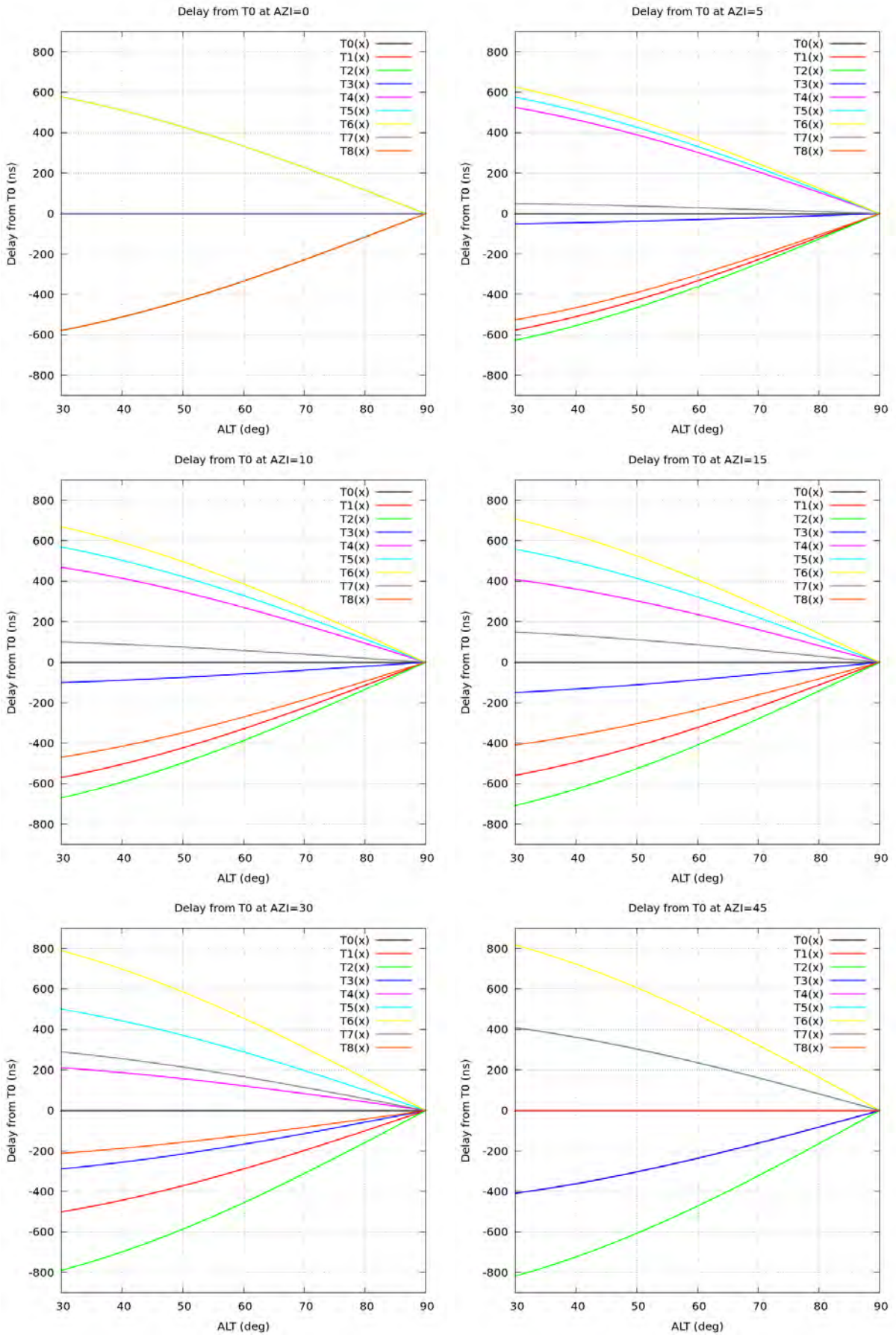

Figure 6.4: Delays plots of CTA_9_200. In these plots, we can observe how change the relative delay D_{ij} changes between telescopes in function of Alt= $[30:90]$ and Azi= $\{0, 5, 10, 15, 30, 45\}$. The telescopes belong to a squared array of 9 Tel. with distance $d_{10} = 200m$.

When the Cherenkov light intercepts a telescope we record a timing information. In the real data acquisition this timing information represent an absolute time in GPS format (date, seconds and nanoseconds). When the photoelectrons detected by a camera exceed a threshold value a timing information is recorded.

In our MC simulations we try to obtain a time sequence of events the most similar as possible to real experimental data, to do this we consider two aspect about timing of events: the *relative timing* of the same event recorded by different telescopes and the *absolute timing* elapsed between different events.

6.4 Relative timing assumptions

We assume, as first approximation, the Cherenkov light due to atmospheric showers to be a plane wavefront directed along (Alt, Azi)$|_{Evt}$ inside a Cherenkov cone. In order to assign a time value to each telescope which intercepts the light wavefront, we consider the set of telescope inside the ellipse. Whose semi minor axis is set at a constant value called $\langle R \rangle$ average radius.

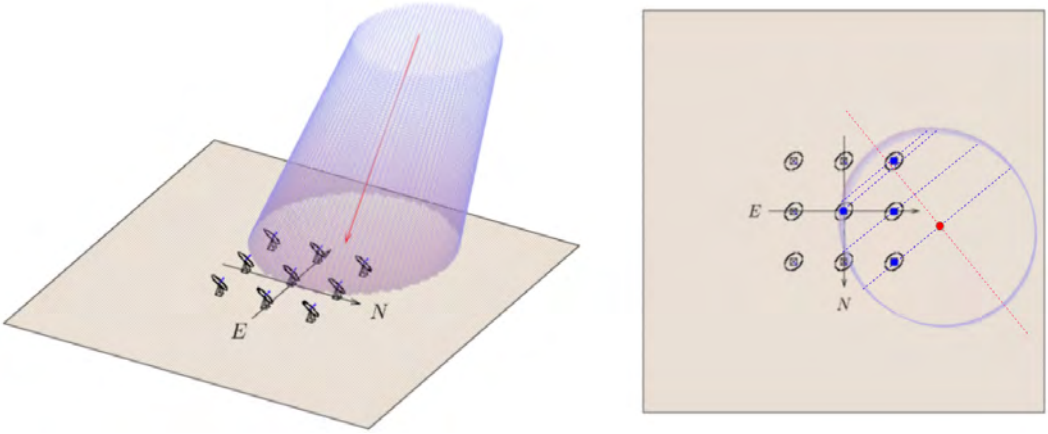

Figure 6.6: (*Left*) Event simulation on 9 telescope array. (*Right*) The same event in xy-plane and relative timing assignment.

The semi major axis is function of $\langle R \rangle$ and altitude and the direction of the ellipse depends by azimuth of the event. The center of the ellipse is set at relative time $t_{Evt} = 0$ of the event and for each telescope inside ellipse we compute the relative time geometrically in the way explained in the previous section, but with two differences: 1) in this case we use (Alt, Azi)$|_{Evt}$ instead of (Alt, Azi)$|_{Tel}$, 2) we sum a random terms τ normal distributed (mean 0, sigma 5 ns) to consider second order effects (i.e. curvature) or fluctuations/noise.

$$\Delta\tilde{t}_{ij} = \Delta t_{ij}|_{Evt} + \tau \qquad \tau := N(0,5)\ ns \tag{6.4.1}$$

Therefore we can describe mathematically every event as a Delays Matrix $\mathcal{D}_{EVT}$ where an element $\mathcal{D}_{ij}$ is the simulated delay $\Delta\tilde{t}_{ij}$ between the telescopes.

$$\mathcal{D}_{EVT} = \begin{pmatrix} 0 & \Delta\tilde{t}_{01} & \Delta\tilde{t}_{02} & \cdots & \Delta\tilde{t}_{0m} \\ \Delta\tilde{t}_{10} & 0 & \Delta\tilde{t}_{12} & \cdots & \Delta\tilde{t}_{1m} \\ \Delta\tilde{t}_{20} & \Delta\tilde{t}_{21} & 0 & \cdots & \vdots \\ \vdots & \vdots & \vdots & \ddots & \vdots \\ \Delta\tilde{t}_{m0} & \Delta\tilde{t}_{m1} & \cdots & \cdots & 0 \end{pmatrix} \qquad \Delta\tilde{t}_{ij} = -\Delta\tilde{t}_{ji} \qquad m \leq n \tag{6.4.2}$$

We want to emphasize two relevant observations:

- $\mathcal{D}_{EVT}$ is always well defined, especially in a real experiment, where $\mathcal{D}_{ij}$ will be the time differences of the trigger time between telescopes.
- $\mathcal{D}_{EVT}$ contains the whole timing information of the event without redundancy, because it contains also informations about event directions, second order effects and fluctuations.

From the comparison of $\mathcal{D}_T$ and $\mathcal{D}_{EVT}$ we have found a way to fast discriminate which telescopes are triggering the same event. We will describe accurately this procedure in the next chapter.

6.5 Absolute timing assumptions

The absolute timing of events is a crucial point of our simulations and this thesis. We know from existing IACT experiments that hadronic events are about three magnitude order more frequent than γ-ray events.
Thus we have to consider an average Rate $\lambda \sim 1kHz$ detected from a single telescope.
We assume that the IACT detections of cosmic rays can be treated as a independent Poisson-random events. This assumption can be expressed starting from Poisson distribution formula:

$$P(k;\Delta t) = \frac{(\lambda\Delta t)^k e^{-\lambda\Delta t}}{k!} \tag{6.5.1}$$

$P(k;\Delta t)$ is the probability of detecting k events in Δt. If we consider the probability to have zero events in Δt we obtain:

$$P(0;\Delta t) = e^{-\lambda\Delta t} \tag{6.5.2}$$

We know that $P \in [0:1]$ so if we consider a uniform distributed random variable $u \in [0:1]$ we obtain a distribution for Δt:

$$\Delta t = -\frac{\log(u)}{\lambda} \tag{6.5.3}$$

Therefore we obtain a Poisson distribution of the events if the waiting time elapsed between two events is exponentially distributed. In order to obtain this timing distribution of the events we implemented the following algorithm.

```
float Random::expdev()
{   float u;
    do u=ran3(); while (u==0.);
    return -log(u);
}   /* end of Random::expdev */
```

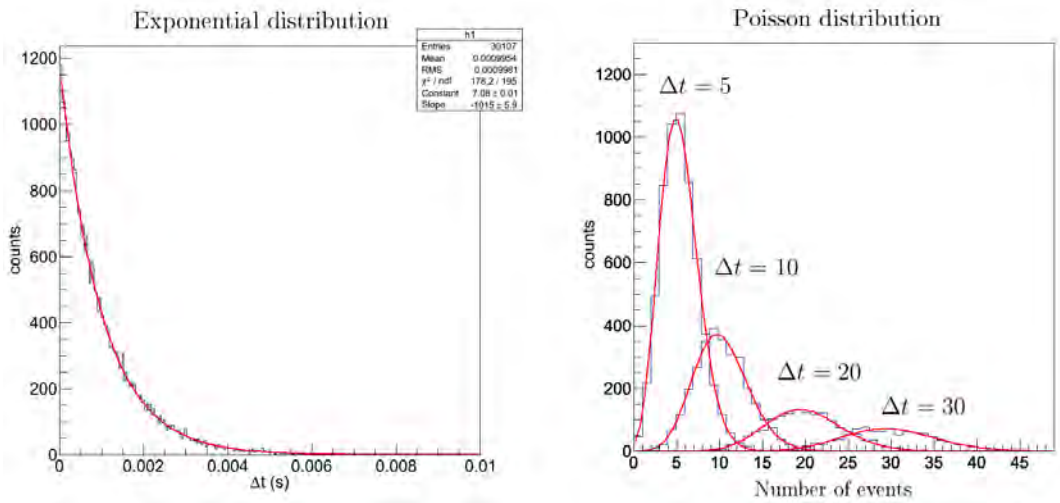

Figure 6.6: (*Left*) Test of exponential distribution of waiting time elapsed between two successive events; with Rate $\lambda = 1kHz$ and about $3.0 \cdot 10^4$ events. (*Right*) The same events into different range of time $\Delta t = \{5, 10, 20, 30\}$ that are Poisson distributed.

6.6 Toy-MC Output data

In this section we show and describe an example of Toy-MC simulator output. Fixed the telescope array layout and a list of parameters: (Alt,Azi)$|_{Tel}$, FoV, Rate, $D/\langle R\rangle$ and the time of simulation, we obtain the following output:

#ENTRY	EVT_ID	RUN_ID	TEL_ID	SEC	NSEC	ALT	AZI
0	1	1	4	0	43749	73.466	352.676
1	2	2	6	0	195748	65.747	14.471
2	2	2	9	0	196012	65.747	14.471
3	3	1	4	0	462275	71.731	11.404
4	4	1	7	0	538880	69.717	10.812
5	5	2	3	0	582097	71.288	350.945
6	5	2	2	0	582130	71.288	350.945
7	6	3	6	0	1211099	64.926	10.678
8	6	3	8	0	1211316	64.926	10.678
9	6	3	9	0	1211365	64.926	10.678
10	7	4	1	0	1384152	66.868	4.019
11	7	4	6	0	1384166	66.868	4.019
12	7	4	8	0	1384403	66.868	4.019
13	7	4	9	0	1384424	66.868	4.019
14	8	3	3	0	1750235	69.308	352.599
15	8	3	2	0	1750268	69.308	352.599
16	8	3	5	0	1750501	69.308	352.599
17	9	1	2	0	1761987	76.185	345.153
18	10	3	1	0	1858386	66.793	3.232
19	10	3	6	0	1858398	66.793	3.232
20	10	3	9	0	1858664	66.793	3.232
21	11	4	1	0	2072861	72.499	352.806
22	11	4	5	0	2072885	72.499	352.806
23	11	4	8	0	2073054	72.499	352.806
24	11	4	7	0	2073082	72.499	352.806
25	12	1	6	0	2265650	67.786	359.134

In this little portion of output file (which normally contains thousands of triggered events) are shown for example 12 events, each of them is triggered by at least one telescope and so we obtain 25 entries. Each entry corresponds to a telescope, whose identification number is printed in TEL_ID column and the absolute time of detection is expressed in SEC and NSEC columns.

Therefore if we consider the event number 7 in the example, we can observe that it was detected from 4 telescopes {1,6,8,9} in this chronological order, specified by absolute timing information (sec, nsec).

For the filtering procedure only the columns ENTRY, TEL_ID, SEC and NSEC are "visible" the others columns are used for the comparison after the filtering process to evaluate the filtering performance. In particular the column RUN_ID which contains the multiplicity of triggered telescope is used for this purpose.

Chapter 7

Filtering Events

All measurements made with CTA should undergo a rapid data analysis, in particular the filtering of events has to be rapid and efficient to allow a real-time analysis and make the observation of transient phenomena possible.
As we have already mentioned, the vast majority of events detected (about three order of magnitude) are background events due to hadronic showers and only a little fraction are due to electromagnetic showers originated by a VHE γ-rays. Therefore it will be necessary to reduce a huge volume of raw data (typically $10 - 20$ TB per night) to a few MB of high-level data, with great accuracy to maximize the efficiency of γ-ray detection.

In this chapter we explain the importance of filtering events, which critical issues can be found and finally we describe a way to discriminate events, which allowed us to implement a first-level trigger.

7.1 Near events and Overlapping events

The first-level trigger must be able to recognize from the whole telescope array which signals belong to the same physical event stereoscopically detected. But, is it always possible ?

When we assigned the absolute time to the events, we assumed Poisson distribution, therefore we know that there might be some events very near in time and even overlapping.
Hence if we fix t_0 as absolute time of an event we are able to estimate the probability to have another event in a range of time Δt:

$$P(1, \Delta t) = (\lambda_T \Delta t)\, e^{-\lambda_T \Delta t} \tag{7.1.1}$$

where λ_T is the rate of the whole telescope array.
In general for any array of N telescope we can say that:

$$\lambda < \lambda_T < N\lambda \quad \rightarrow \quad \lambda_T = C_A \lambda \tag{7.1.2}$$

where λ is the single telescope rate and C_A is a factor which considers the geometrical distribution of the telescopes that we consider as:

$$C_A = \frac{A_{eff}}{A_{evt}} \tag{7.1.3}$$

where A_{evt} is the elliptic area of the Cherenkov light pool, function of $\langle R \rangle$ and A_{eff} is the effective detection area of the array. C_A may represent a measure of the "compactness" of the array.

The effective area of the array A_{eff} is not simple to calculate analytically, therefore we can use an easy geometrical MC to evaluate C_A considering the overlapping of the detection area of each telescope (see Figure 7.1).

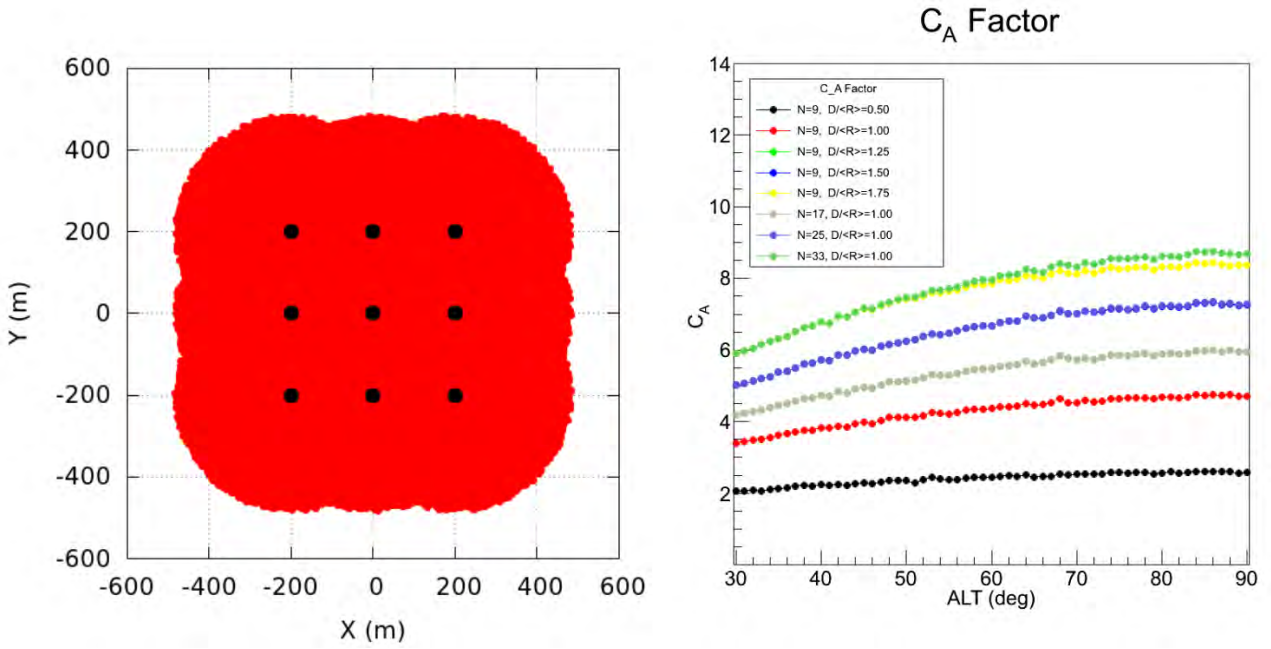

Figure 7.1: (*Left*) The effective area estimated with MC. (*Right*) The C_A factor in function of number of telescopes N and $D/\langle R\rangle$.

Now we are able to define a time relationship between two events: a) *Far Events* if $\Delta t > \Delta t_c$, b) *Near Events* if $\Delta t \simeq \Delta t_c$ and c) *Overlapping Events* if $\Delta t < \Delta t_c$.

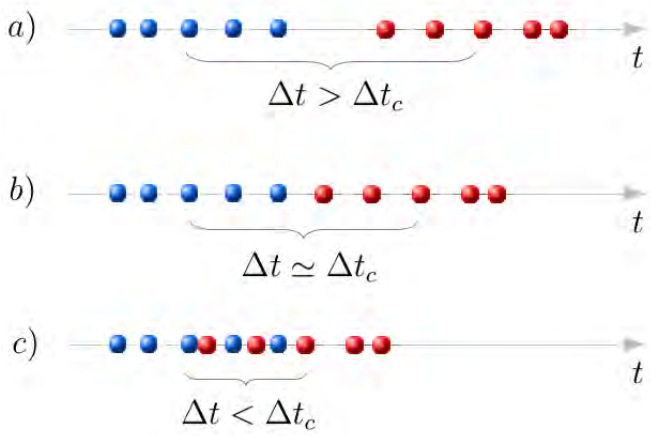

Where Δt_c is a critical time value not well defined and so we arbitrarily fixed it to be:

$$\Delta t_c = \mathcal{D}_{ij}^{Max} + \Delta t_{th} \tag{7.1.4}$$

where $\mathcal{D}_{ij}^{Max}$ is the maximum time range of the event and Δt_{th} is the time that c_n takes to arrive at more distant nearest-neighbor telescopes. We explain better the meaning of Δt_{th} in the next section.

Now we have all the elements to give an estimation of the event number hard to discriminate, hence the Near events and the Overlapping events.

$$N_{hd} = N_{Near} + N_{Overlap} = 2P(1, \Delta t_c)$$
$$P(1, \Delta t_c) = (\lambda_T \Delta t_c)\, e^{-\lambda_T \Delta t_c} \tag{7.1.5}$$

Below we can see the plot of N_{hd} in function of Alt, for the different layouts studied in this thesis.

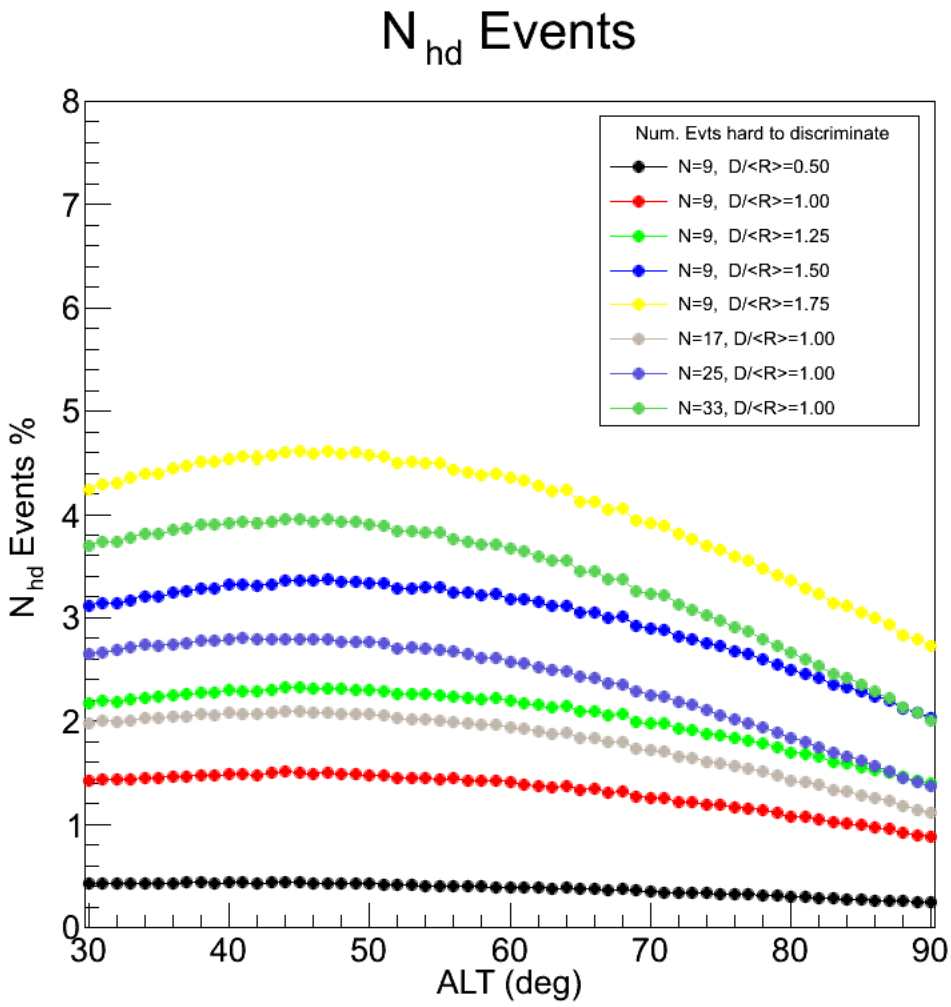

Figure 7.2: Plot of the hard to discriminate event number expressed in %, in function of ALT, for several layout and different values of $D/\langle R \rangle$.

If we consider our assumptions as acceptable, from this estimations some relevant data emerge: there is a remarkable fraction of the events ($1 \div 4\,\%$) which is hard to discriminate through a rapid analysis. It depends essentially from the rate λ and C_A, therefore increase with the size of the array. Moreover this fraction of events is difficult to recognize and it may compromise some of the measurements, reducing the efficiency or slowing down the analysis.
Therefore the goal of this thesis is to develop a fast filter able to discriminate not only Far Events but also Near and Overlapping events, where it is possible.
To do this we implement two algorithms: The first one is FCTA-R a raw filter able to separate the events in time-blocks, to isolate groups of events without dividing any events between blocks. The second one is FCTA-N, a Network filter algorithm combined with the first one and able to discriminate a very good fraction of events thanks to compatibility between $\mathcal{D}_T$ and $\mathcal{D}_{EVT}$.
In the next sections we describe this two algorithms and the ideas on which they rely on.

7.2 Minimum Large Threshold (MLT)

The vast majority of the events ($\sim 90\%$) are well temporally isolated and it is quite simple to understand that they are different events. But as we have seen in the previous section, sometimes we are not able to understand if a group of entries which usually identifies an event is a single event, two near events, two overlapping events or three, etc.

Hence we need a criteria which "cut" our absolute time-line, in which are contained the events in intervals of time (we call them *time-boxes*), each of them containing at least one ore more events but with the strong condition that no event is divided into different time-box. This criteria exists and never wrongs (in theory), if we adjust correctly Δt_{th}.

In the previous section to define near and overlapping events we consider the elapsed time between two events, because the time separations is physically correlated to the rate of events. But that is not a good choice if we want separate the events, a better choice is find a good threshold between the entries.

Indeed if we compare each i-th entries with $(i+1)$-th, we can find that there is a strong difference in their $\Delta t_{i,i+1}$ distribution respect to the events. (compare with Figure 6.6.a)

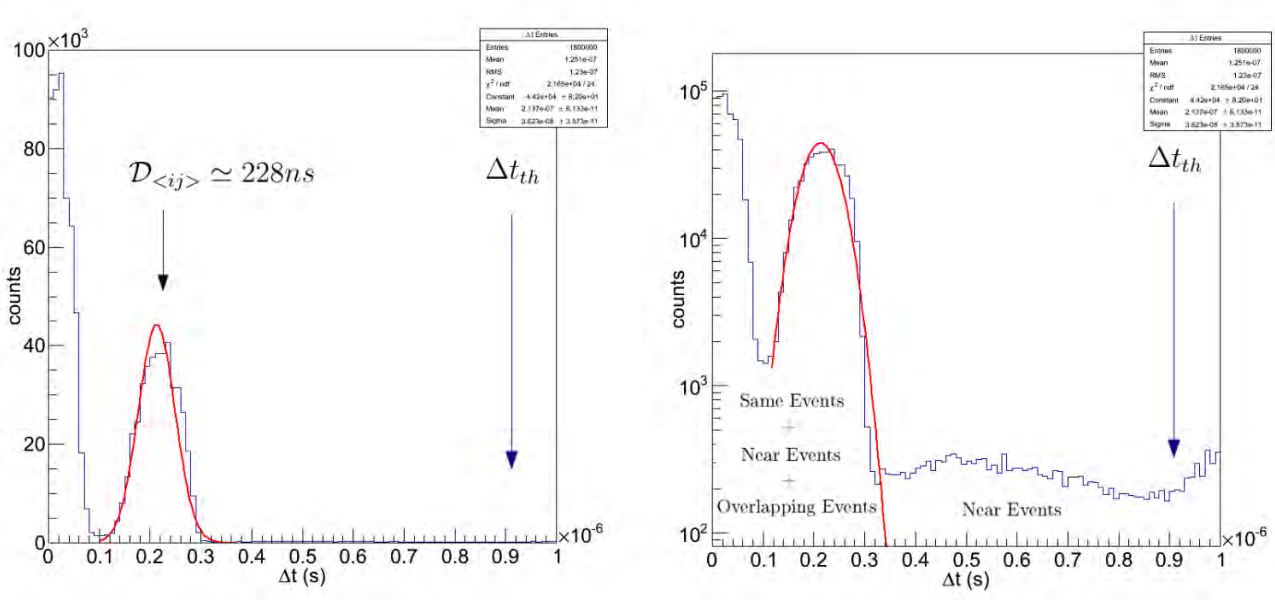

Figure 7.3: (*Left*) Distribution of Entries elapsed times $\Delta t_{i,i+1}$.(*Right*) The same plot in log-scale, it is possible discriminate some entries which reveal us a Near Events relationship. But there is a time-zone where we cannot distinguish the relationship between events.

Thus the algorithm consists in a simple condition and it is enough to have a raw filter whose name is FCTA-R.

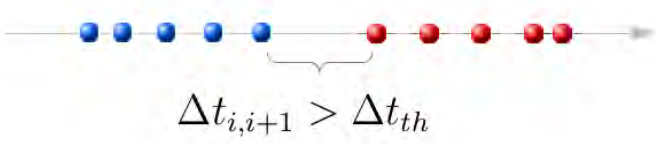

If this condition is satisfied the algorithm separates the entries, otherwise it keeps them together in a time box. If the threshold is large enough this algorithm never separates a single event, but at the same times we want minimize Δt_{th} to speed up the second step of the filter.

A good compromise is to choose as threshold Δt_{th} the time spent from the light to cover the distance from the hit telescope to its farthest first neighbor.

$$\Delta t_{th} \approx \frac{d^{Max}_{<ij>}}{c_n} \tag{7.2.1}$$

In example in a square layout of side d , like ASTRI, the $d^{Max}_{<ij>}$ is $d\sqrt{2}$.
We want anticipate that the speed of the next algorithm depends on the size of the time-box, which have to contain less events as possible. The time-box may contain: a) single events, b) two near events, c)three or more event.

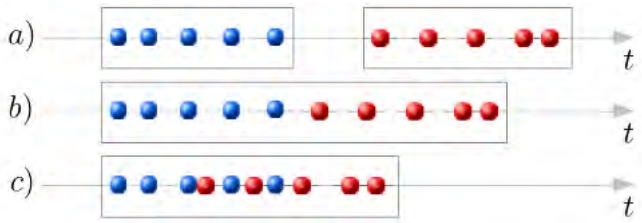

Another good point of this algorithm is that: separating correctly the events, a huge flow of data may be divided and processed from different processor units at the same time, so we are thinking about a parallel computing solution as GPU.
We remember that the validity of this method is based on two assumptions: the list of entries must be chronologically ordered and the threshold must be much greater than fluctuations $\Delta t_{th} \gg \tau_{evt}$. Both assumptions are experimentally acceptable.

7.3 Compatibility Matrix

The previous algorithm FCTA-R separates correctly all Far events and a good quantity of Near events, but its purity, as we discuss in the next chapter, remains in the order of $1 \div 3\%$. Is there a way to recognize and distinguish two overlapping events ?
A useful tool to observe the time-box and to split overlapping events is the *Delay Diagram*. The Delay Diagram is simply a plot in which along the x-axis are set the expected delays, for example with respect to telescope T_0 and along y-axis the detected time of each entry. If both axis are chronologically ordered and x-axis is adjusted with an offset, the diagram shows the correlation between data and expected values. In the figure below we show a real example of simulated time-box plotted in Delay Diagram.

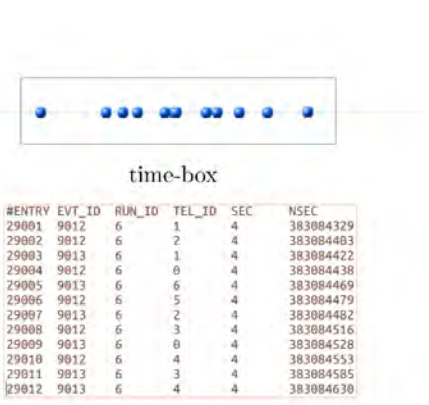

time-box

#ENTRY	EVT_ID	RUN_ID	TEL_ID	SEC	NSEC
29001	9012	6	1	4	383084329
29002	9012	6	2	4	383084403
29003	9013	6	1	4	383084422
29004	9012	6	0	4	383084438
29005	9013	6	6	4	383084469
29006	9012	6	5	4	383084479
29007	9013	6	2	4	383084482
29008	9012	6	3	4	383084516
29009	9013	6	0	4	383084528
29010	9012	6	4	4	383084553
29011	9013	6	3	4	383084585
29012	9013	6	4	4	383084630

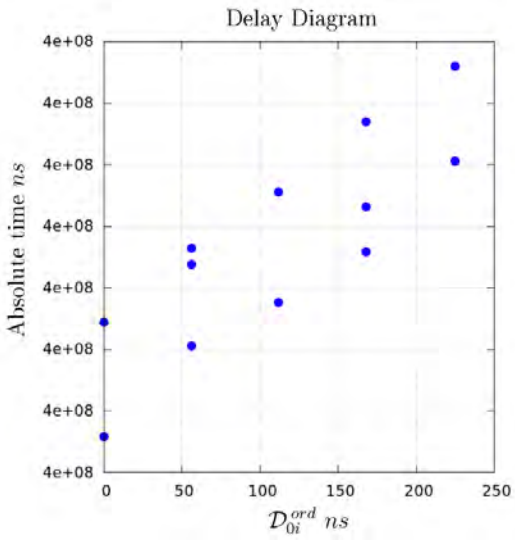

Figure 7.4: (*Left*) A time-box with two overlapping events. (*Right*) The same events in a Delay Diagram. It is possible to observe how the diagram splits the overlapping events.

This method is interesting because it reveals us if there is overlapping. Moreover if the same telescope was detected more than one time gives us a good estimations of the Δt_{evt}. This method has two limits: is too sensitive with respect to the fluctuations and it expresses the time-delay correlation in one dimension only (in example with respect to T_0).

To overcome this limits we define a new matrix using the delays matrices $\mathcal{D}_T$ and $\mathcal{D}_{EVT}$ defined in the previous chapter. To estimate the fluctuations we identify two components that contribute to the uncertainty: a term σ_{FoV} due to the Field of View and a term σ_{stat} due to secondary order effects and random fluctuations.

We define a Compatibility Matrix using all these quantities as:

$$\Lambda = \frac{|\mathcal{D}_{EVT} - \mathcal{D}_T|}{\sqrt{\sigma^2_{FoV} + \sigma^2_{stat}}} \tag{7.3.1}$$

This matrix is well defined and very rich of information. It can be generalized in more dimensions using entries as indices (i, j) and so its size may be $N \times N$ where N is the entries number which belong to an event or more generally, a time-box.

To obtain a "true" Compatibility matrix Λ it is very important correctly estimate the statistical fluctuations. The FoV term σ_{FoV} can be estimated using a uniform distribution inside a box $(a, b)_{ij}$, which is another matrix $(a, b)_{ij} = \mathcal{D}_{ij}(Alt \pm FoV, Azi \pm FoV)$:

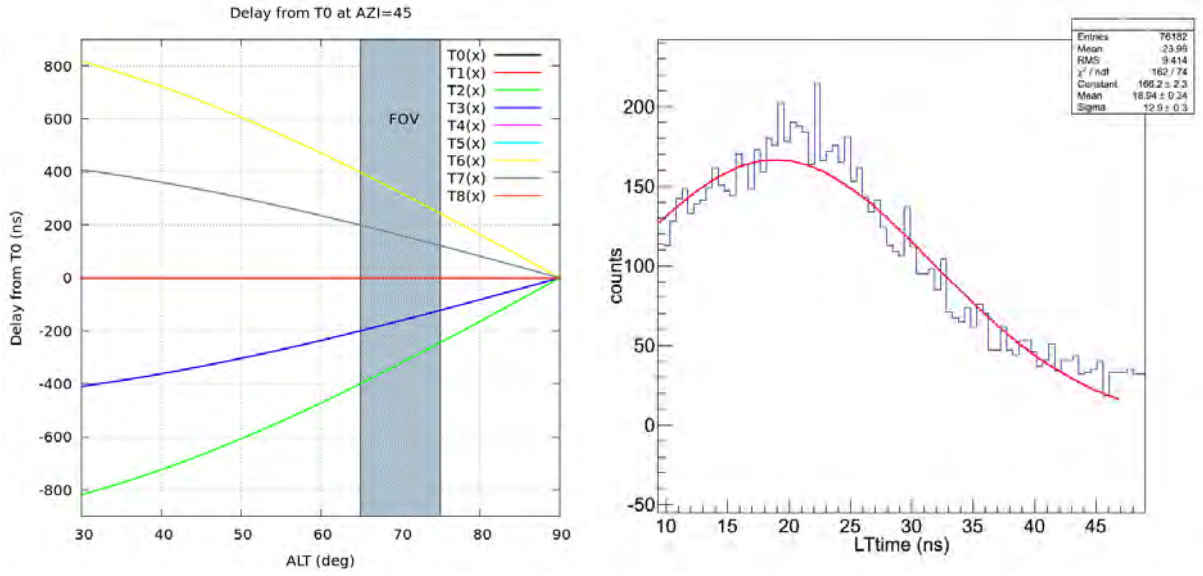

Figure 7.5: (*Left*) The Field of View interval in which we assume uniform distribution. (*Right*) Fluctuations of secondary order effects. Taken from ASTRI data about point-like source, (no FoV effects).

Hence the formula used to evaluate the FoV uncertainty is:

$$\sigma^2_{FoV} = \frac{(b-a)^2_{ij}}{12} \tag{7.3.2}$$

and for the σ_{stat} we expect a value of $\sigma_{stat} \approx 20\, ns$ but we found through simulations that $\sigma_{stat} \approx 40\, ns$ is a better value, and for each filtering process we used this value. Parameters Δt_{th} and σ_{stat} can in fact, be optimized in a calibration phase, to obtain the best result.

7.4 Network Filter Algorithm

The Λ-matrix contains the whole information about the process, except the absolute timing information which is only a constant value. The elements λ_{ij} are not independent but correlated among themselves. The fluctuations can compromise a single element of the matrix but the others elements can reveal how the entries are bounded with others entries.

Therefore the basic idea is to use the collective information contained into the compatibility Λ-matrix to distinguish near events or overlapping events.

7.4.1 Network theory

The Network theory is the study of graphs as representation of relations between discrete objects. A network can be defined as a graph in which nodes and/or edges have attributes.

In our case each entry (a telescope which detected an event and produced a timestamp) can be considered as a node and λ_{ij} is the edge which connects the i-th entry with j-th entry. Hence a Λ-matrix can be thought as network, a complete network with each node connected to each other.

$$\Lambda = \begin{pmatrix} 0 & \lambda_{01} & \lambda_{02} & \cdots & \lambda_{0N} \\ \lambda_{10} & 0 & \lambda_{12} & \cdots & \lambda_{1N} \\ \lambda_{20} & \lambda_{21} & 0 & \cdots & \vdots \\ \vdots & \vdots & \vdots & \ddots & \vdots \\ \lambda_{N0} & \lambda_{N1} & \cdots & \cdots & 0 \end{pmatrix} \longrightarrow$$

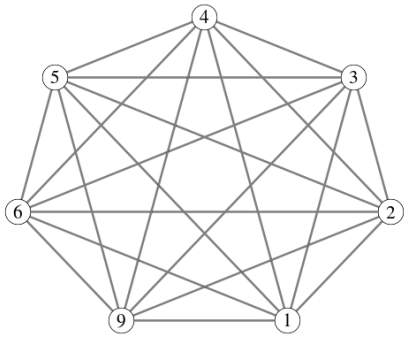

The Λ-matrix is symmetric and can be considered as a weights-matrix, which describe the compatibility among nodes. The whole information is contained in the upper triangular matrix, but for graphical and computational reasons we prefer keep the previous definition.

This structure is not only a descriptive way to represent the relationship between our events, but can suggests an operative way to distinguish the events.

The originality of this approach consists in fact in having identified a map from experimental data to networks.

The use of networks allows to visualize the emerging of sub-data structures, clusters in the networks, which represent different physical events.

Indeed already the Λ-matrix shows a structure like a block diagonal matrix which represent the events, but fluctuations can make impossible or misleading the events recognition.

The advantage of a network with respect to the block diagonal matrix, is that we can evolve the network, by adjusting the dynamic and so priming the clustering process.

Following this idea we developed a filter based on the network clustering to recognize the physical events detected from Cherenkov Telescope Array and we call this filter FCTA-N. In the next section we describe our clustering algorithm and show how to obtain this fragmentation effect which allows us to separate our events.

7.4.2 Clustering Algorithm

It is well known that it is not possible to represent geometrically in $n < N$ dimension a generic weights matrix $N \times N$ mapping weight as lenght, but we can think of the Λ-matrix as a matrix of coefficients of interaction potential or in this case coefficients of a velocity fields.
We can set a threshold $\lambda_{th} = 3$ thus for $\lambda_{ij} > \lambda_{th}$ the nodes are repelled and if $\lambda_{ij} < \lambda_{th}$ the nodes are attracted.

$$\Lambda = \begin{pmatrix} 0 & \lambda_{01} & \lambda_{02} & \cdots & \lambda_{0N} \\ \lambda_{10} & 0 & \lambda_{12} & \cdots & \lambda_{1N} \\ \lambda_{20} & \lambda_{21} & 0 & \cdots & \vdots \\ \vdots & \vdots & \vdots & \ddots & \vdots \\ \lambda_{N0} & \lambda_{N1} & \cdots & \cdots & 0 \end{pmatrix} \longrightarrow$$

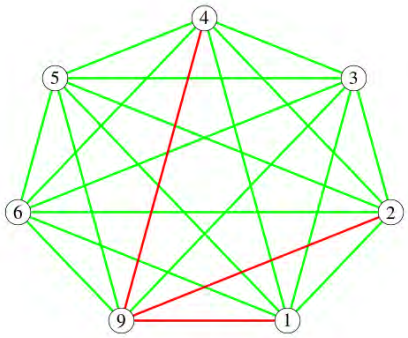

The speed is proportional to $|\lambda_{ij} - \lambda_{th}|$, with a maximum value threshold $\lambda_{ij} \leq 5$, which means high incompatibility. Thus the speed spectrum is $-3 \leq |\lambda_{ij} - \lambda_{th}| \leq 2$ and we assigned speed value $+3$ only if $Tel_i = Tel_j$. If we evolve the system we may obtain a clustering effect due to the displacement of the nodes. Finally we report the clustering algorithm.

```
for(int k=0;k<3*N;k++)
     {

     for(int i=0; i<N;i++)
          {
           x=vertex[i].x;
           y=vertex[i].y;

           for(int j=i+1; j<N;j++)
                {
                 dist_x=(x-vertex[j].x);
                 dist_y=(y-vertex[j].y);
                 dist=sqrt(dist_x*dist_x+dist_y*dist_y);

                 V=L[i][j]-lambda_th;

                 dx=h*V*(dist_x/dist);
                 dy=h*V*(dist_y/dist);

                 if(dx*dx>=dist_x*dist_x)
                           {
                            dx=0.5*dist_x+0.01;
                           }

                 if(dy*dy>=dist_y*dist_y)
                           {
                            dy=0.5*dist_y+0.01;
                           }

                 vertex[i].x+=dx;
                 vertex[i].y+=dy;
                 vertex[j].x+=-dx;
                 vertex[j].y+=-dy;
                }
           }
}
```

Figure 7.5: The Network Filter Algorithm written in C++. It is the core of our filter FCTA-N.

The clustering algorithm has a complexity is $\mathcal{O}(N^3)$ where N is the dimension of the time-boxes. Thus if FCTA-R is optimized, we have that $4 \leq N \lesssim 2N_{Tel}$, indeed we set the condition that FCTA-N runs only if $N > 4$, otherwise is possible to evaluate in an unique way the if entries are correlated using Λ-matrix.

To better understand how the algorithm works it is possible to graphically show the clustering process in different steps in a real example. Thus we consider a Λ-matrix extracted by MC-data with size $N = 10$ containing overlapping events.

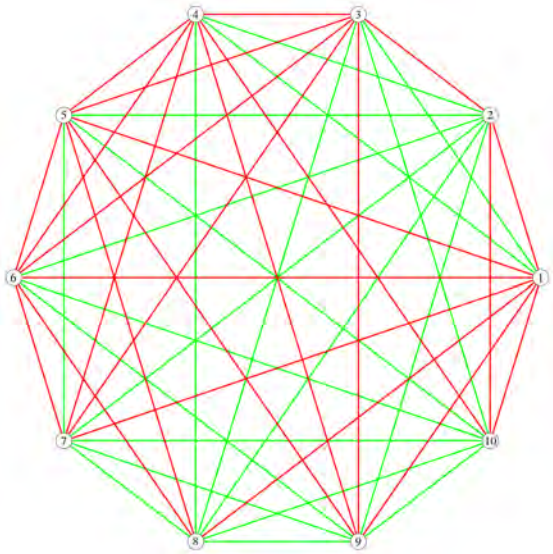

1)

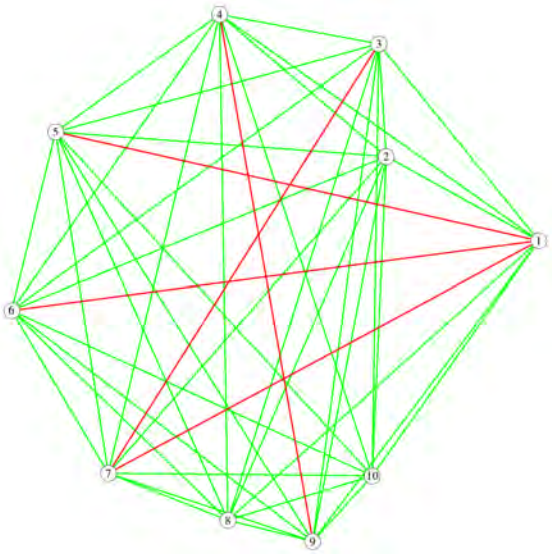

2)

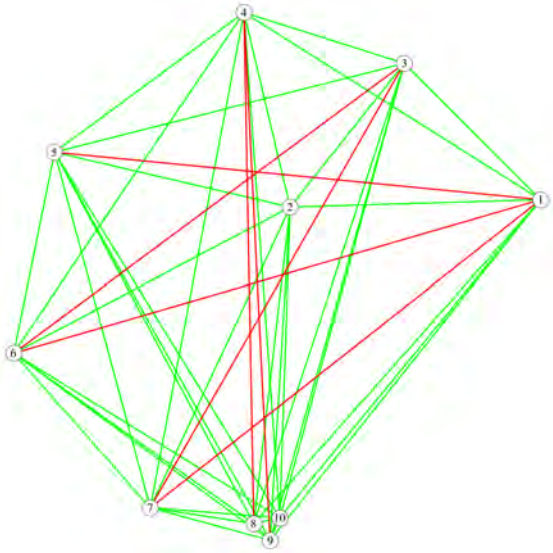

3)

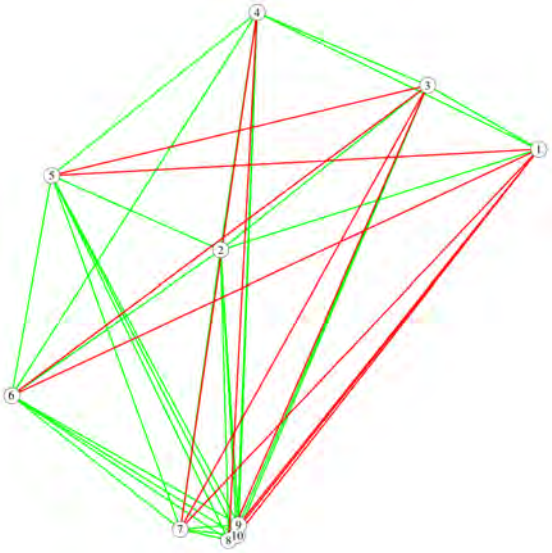

4)

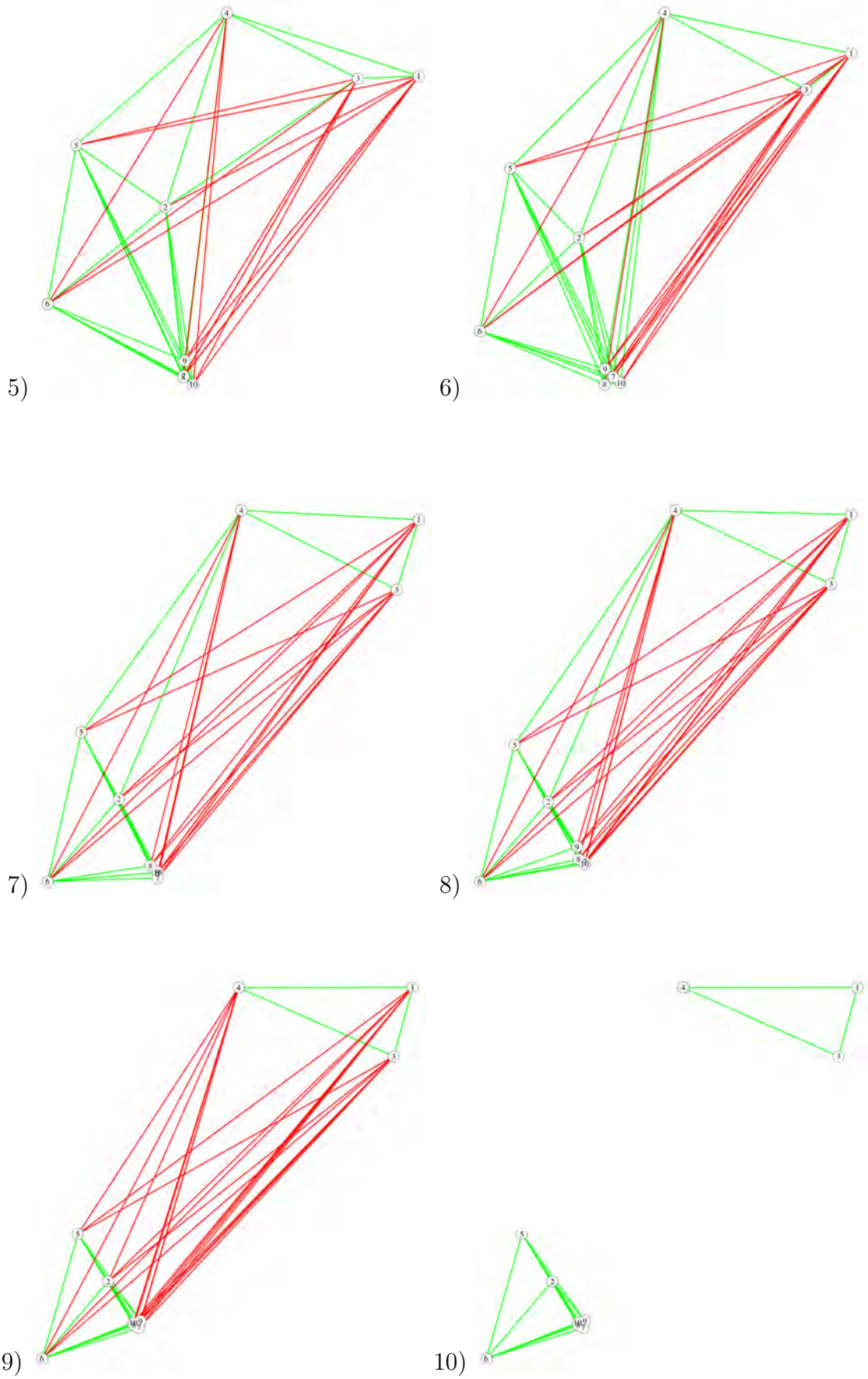

Figure 7.6: Images of a clustering process obtained with FCTA-N. Starting from compatibility Λ-matrix we obtain the first graph, then evolving the system through our filter algorithm we obtain a clustering effect. From undefined time-box containing ten entries we obtain clearly the separation of two overlapping events: $\mathrm{Evt}_1 := \{1, 3, 4\}$ and $\mathrm{Evt}_2 := \{2, 5, 6, 7, 8, 9, 10\}$.

Chapter 8

Data Analysis and Filter Perfomance

In this chapter we report the analysis done both on our Toy-MC data and on data provided by ASTRI collaboration. The analysis consists essentially to test our Filter for Cherenkov Telescope Array (FCTA) in different situations. In fact, we considered several different layouts in function of pair coordinates (Alt, Azi), with different parameter $D/\langle R \rangle$ whit the change of the number of telescopes N_{Tel} and single telescope rate λ.
The result of these tests showed a good agreement with ASTRI-MC simulations, therefore allowing a deeper knowledge of the problem that we set out to solve.

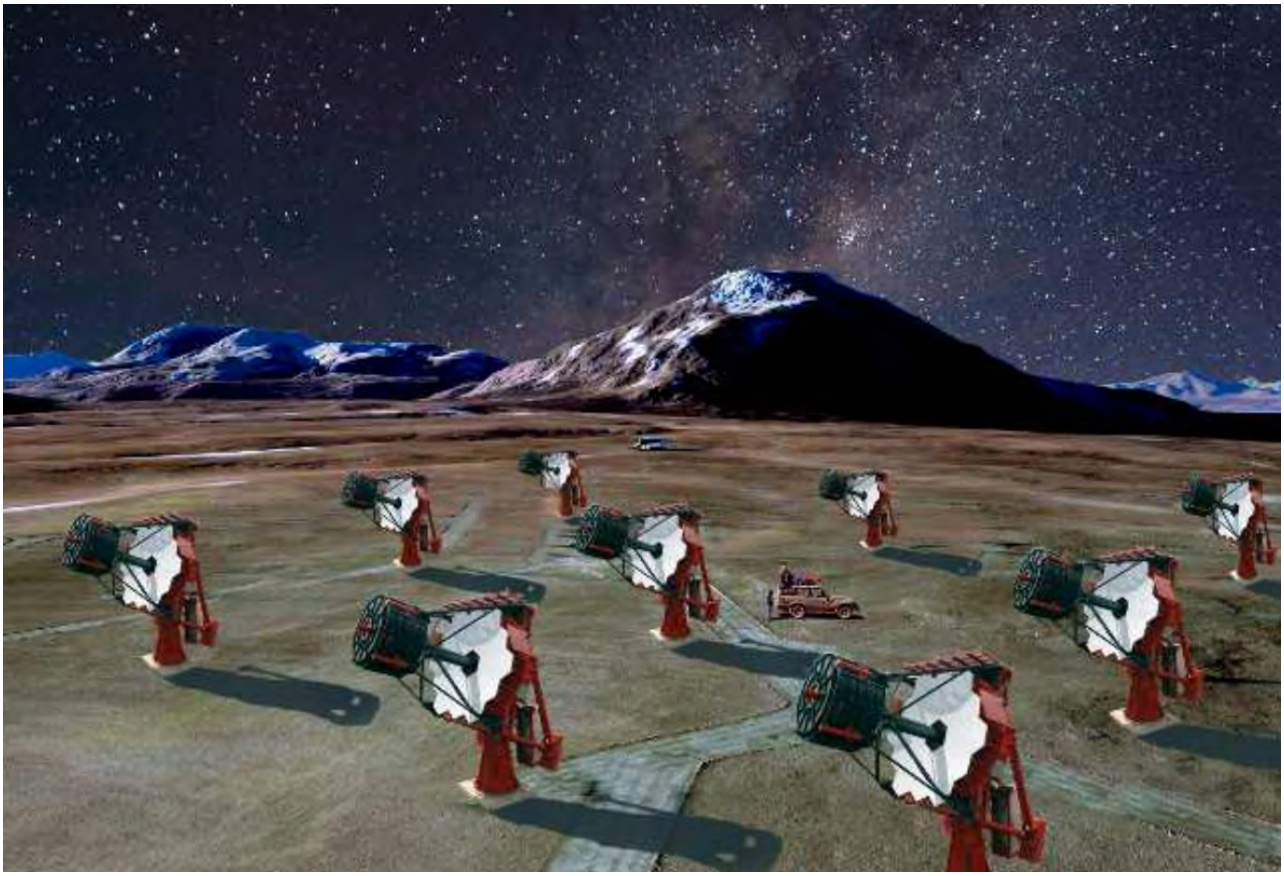

Figure 8.1: Artistic concept (not to scale) of the ASTRI mini-array. [49]

8.1 ASTRI-MC Simulations

In the framework of the international Cherenkov Telescope Array (CTA) gamma-ray observatory, a mini-array of nine small-sized, dual-mirror (SST-2M) telescopes developed by the ASTRI Collaboration has been proposed to be installed at the future CTA southern site.

To perform the mini-array and analysis tools, the collaboration made several MC simulations using CORSIKA as standard package to simulate showers development in the atmosphere and **sim_telarray**[9] a tools which allows to simulated also the telescope array.

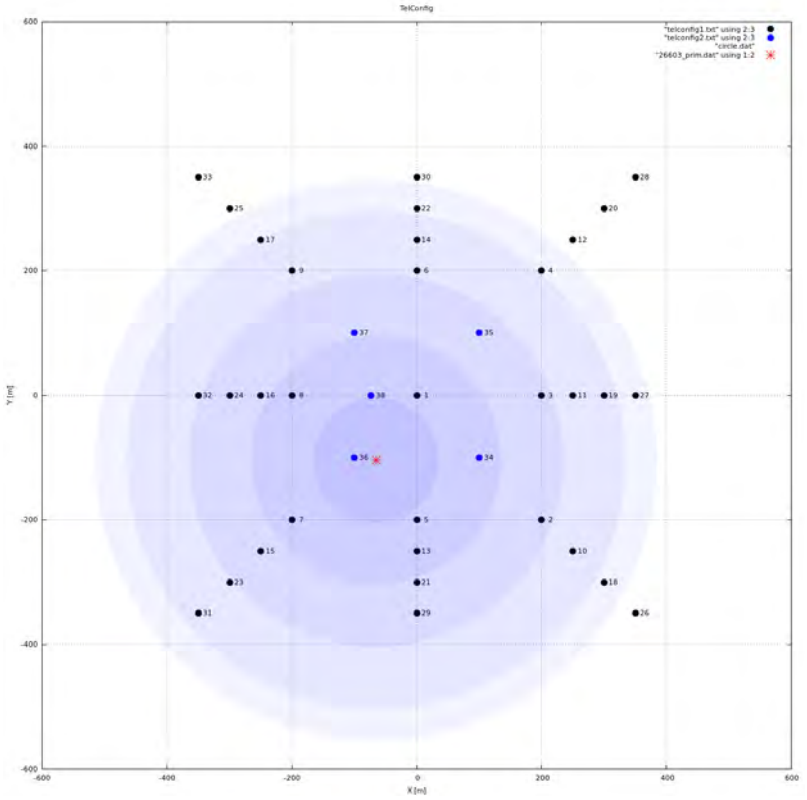

Figure 8.2: The ASTRI-MC layout and an example of γ-ray event $n_{evt} := 26603$. Note the ASTRI-MC layout and two kinds of telescopes with their TEL_ID, the blue ones LST and black ones SST. The red cross is the centre of light pool. Blue circles denote approximately the dimension of the light pool.

The data levels (DL) of the ASTRI SST-2M prototype and mini-array have been defined in compliance with the CTA data model , and they are: raw data (DL0); telescope-wise reconstructed data (DL1); array-wise reconstructed data (DL2); reduced data (DL3); science data (DL4); observatory data (DL5).[36]

The MC simulation used are DL2 where our filter allows to reconstruct all the events, the next step is data reduction based on gammaness analysis. The original raw format is *simtel* while the format adopted by ASTRI Collaboration is mainly FITS [1] data format, using the CFITSIO and CFITS libraries for reading, processing, and writing FITS data.

To handle raw data and extract the timing information about MC events, we developed a code using **pyhessio**[2] library, the CTA Python wrapper for event format that is used in output of sim_telarray.
This is an advantage because we will could access at the newest CTA simulations CTA_Prod3 with the same code.

[1]Flexible Image Transport System (FITS) http://fits.gsfc.nasa.gov/
[2]https://github.com/cta-observatory/pyhessio

The ASTRI collaboration provided us:

- 20 runs (the official runs coded as: 1001-1020) containing raw MC data of EM showers initiated by VHE γ-rays.
- 100 runs (the official runs coded as: 10000-10099) containing raw MC data of hadronic showers initiated by VHE protons.

Each γ-ray run has some thousands of triggered events, while each proton run has some hundreds of triggered events. All these data were processed to have the statistics required. The most important parameter that has been extracted from these data is *teltrg_time*.
The *teltrg_time* is defined as the relative time in nanoseconds elapsed from the first event detection by a telescope and the others detections by remaining telescopes, after subtractions of nominal delay due to pointing directions of array. Using our formulation previously defined in chapters 6 and 7, we can write:

$$Teltrg\_time = |\mathcal{D}_{EVT} - \mathcal{D}_T| \tag{8.1.1}$$

where in this case $\mathcal{D}_{EVT}$ is not obtained only with geometrical with simply assumptions as our Toy-MC, but contains a physical meaning due to particle interactions simulated by CORSIKA.
Each run of ASTRI-MC data is simulated in a unique configuration: (Alt, Azi)$|_{Tel}$=(70, 0).
This is a little limit, because we cannot tested our Filter with official MC data on others (Alt, Azi)$|_{Tel}$ configurations.
In the figure below we show in example a γ-ray event of ASTRI-MC simulations $n_{evt} := 26603$, which belongs at run_1001. This event has a primary cosmic energy of $\sim 16TeV$ and (MCxcore, MCycore)=$(-65, 104)$ with primary γ-ray direction (Alt, Azi)$|_{Evt}$=(70, 0).

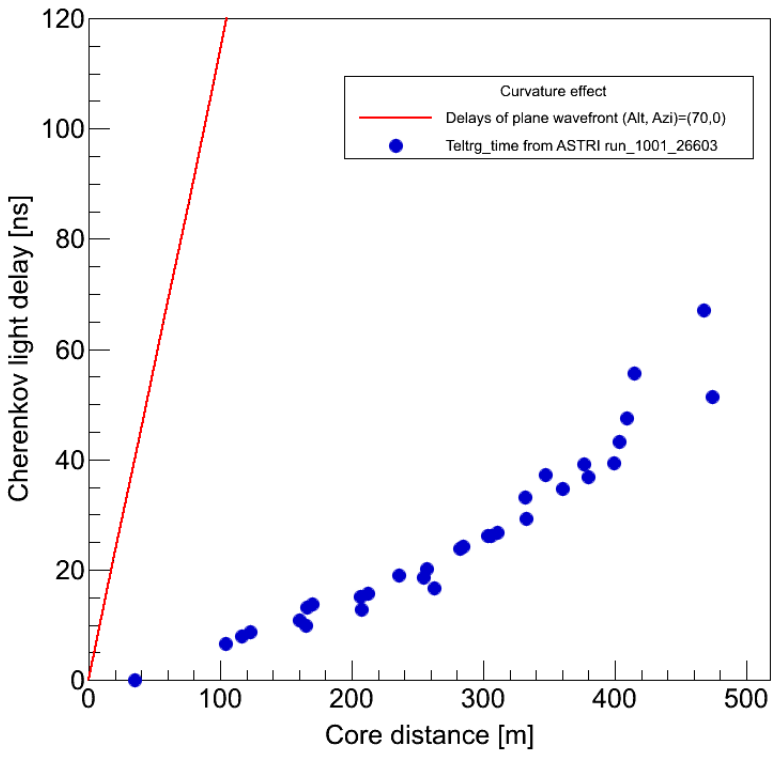

Figure 8.3: This plot shows the different components of relative delay in a γ-ray event $n_{evt} := 26603$. The (Alt, Azi)$|_{Evt}$ dependence red line, and the curvature effect due to shower development in atmosphere. The curvature effect can be observed through teltrg_time. Note that curvature effect can be neglect with respect to (Alt, Azi)$|_{Evt}$ component.

In the plot above (Figure 8.3) we can see the different components of relative delay in a γ-ray event $n_{evt} := 26603$, which is a good representative example of all γ-ray data.
The γ-ray data are simulated as coming by a point-like source, thus we have that (Alt, Azi)$|_{Tel}$=(Alt, Azi)$|_{Evt}$, thus we haven't effects due to FoV uncertainty.

The curvature effect can be observed through teltrg_time in function of core distance. We can note that curvature effect can be neglected with respect to (Alt, Azi)$|_{Evt}$ component.

Therefore it is probably the main reason to explain the very good agreement among Toy-MC data and ASTRI-MC data.

8.2 Purity and Efficiency

In algorithm analysis, besides the complexity, there are two features which describes the algorithm performance: purity and efficiency. The definition of purity:

$$p = \frac{N_{rec} - N_{disc}}{N_{tot} - N_{disc}}$$

were N_{rec} are the number of events "strictly correctly reconstructed" by the filter, N_{disc} the number of events discarded and N_{tot} the number of total events detected.
We are assuming that an event is "strictly correctly reconstructed" if all the entries which belong to the event are grouped in the correctly way. If an entry which not belongs to the events or in the opposite case if a valid entry is discarded, it represent to us an incorrectly reconstruction.

Indeed the definition of efficiency is:

$$\varepsilon = \frac{N_{rec} - N_{disc}}{N_{tot}}$$

Knowing very well the purity it is possible estimate correctly the uncertain of a measurements, and knowing very well the efficiency it is possible to obtain precision measurements without systematic errors.

Purity and efficiency, in this thesis, are evaluated with MC simulation, but in a real experiment, they will evaluated again with real data. This procedure is possible and required, and can be performed analyzing in depth a great data sample, knowing, as well as possible, the identity of events and then running again the filter on data sample. In this way purity and efficiency can be confirmed, previous values obtained with MC events.

Given a CTA layout, the main goal is maximize purity and efficiency. In general there are many factors that have to be considered, for example we have to maximize the effective area minimizing the number of telescopes.

A relevant parameter for this studies about the filtering of the events is the ratio $D/\langle R \rangle$.
Indeed we observed a dependence of the algorithm performance due to the scalability between D and $\langle R \rangle$ which have geometrical reasons.

In the next sections we report the purity and the efficiency of our main filtering algorithms FCTA-R and FCTA-N.

8.3 CTA_9

In this section we considered four different layouts of the ASTRI mini-array with nine telescopes with the change of distance D on the array. We studied each layout in function of pair coordinates (Alt, Azi) for Toy-MC data, ASTRI-MC data have a fixed configuration (Alt, Azi)=(70,0).

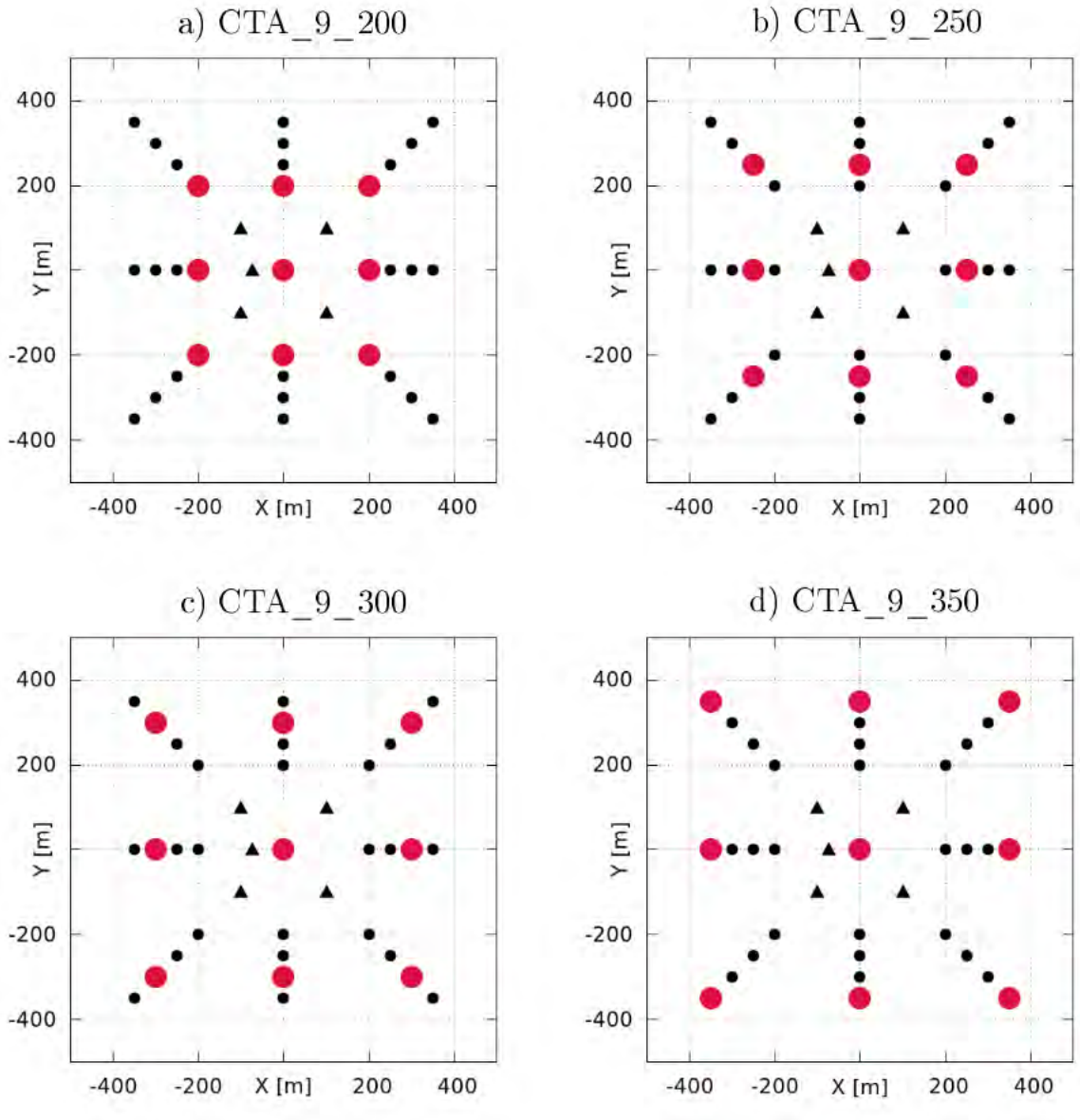

Figure 8.4: From the same ASTRI-MC data, we considered different sub-array, to show dependence of algorithm performance changing D.

In the Layouts: CTA_9_200, CTA_9_250, CTA_9_300, and CTA_9_350 we have chosen to maintain fixed the parameter $D/\langle R\rangle = 1$. These choice leads different values in the efficiency between ASTRI-MC data and Toy-MC data, but it is essentially a scale effect.
Indeed in Toy-MC simulator $\langle R\rangle$ is a free parameter and if we tune it we obtain the same efficiency of ASTRI-MC data.
There are two others factors that we have to consider: 1) In our Toy-MC $\langle R\rangle$ is fixed without fluctuations, instead in ASTRI-MC data $\Delta R \neq 0$. 2) In our Toy-MC we detect also single events, instead ASTRI-MC data containing only events triggered by at least two telescopes. This second factors is not a problem if $D < 350\,m$ because we can have the approximately true number of single events, triggered by the external telescopes

8.3.1 CTA_9_200

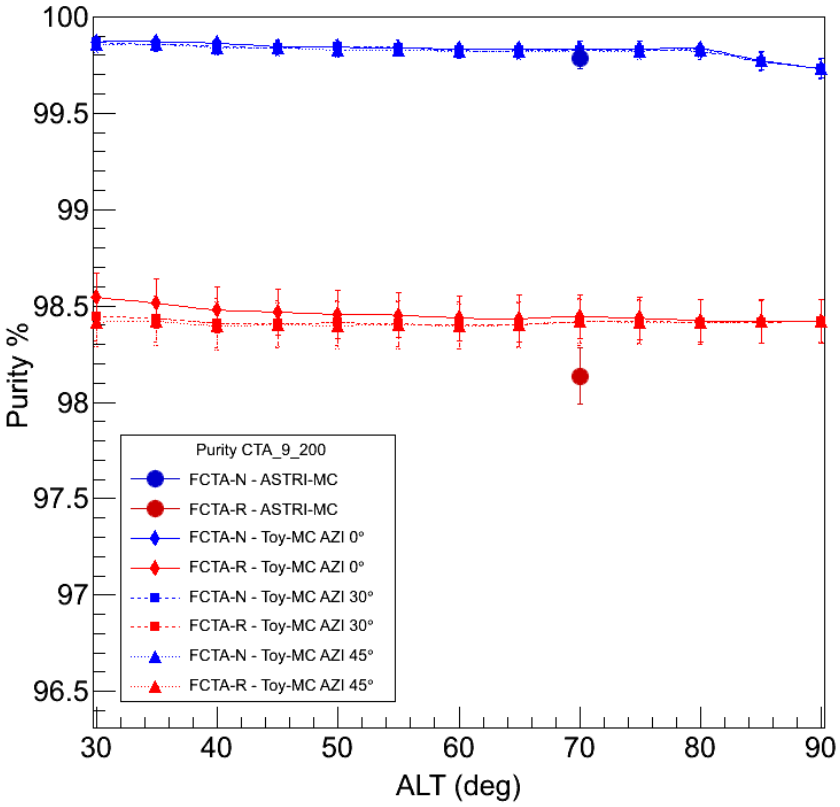

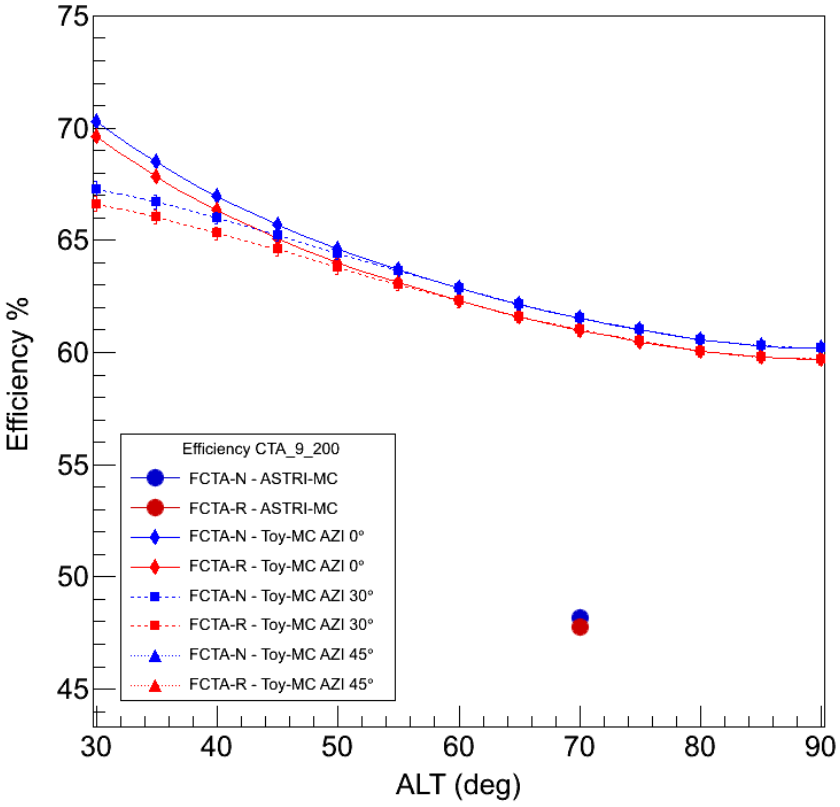

Figure 8.5: Purity and Efficiency of FCTA-R and FCTA-N. Others parameters are $D/\langle R\rangle = 1$ and $\lambda = 1\,kHz$. The deslocation of the telescopes is shown in Figure 8.4.a.

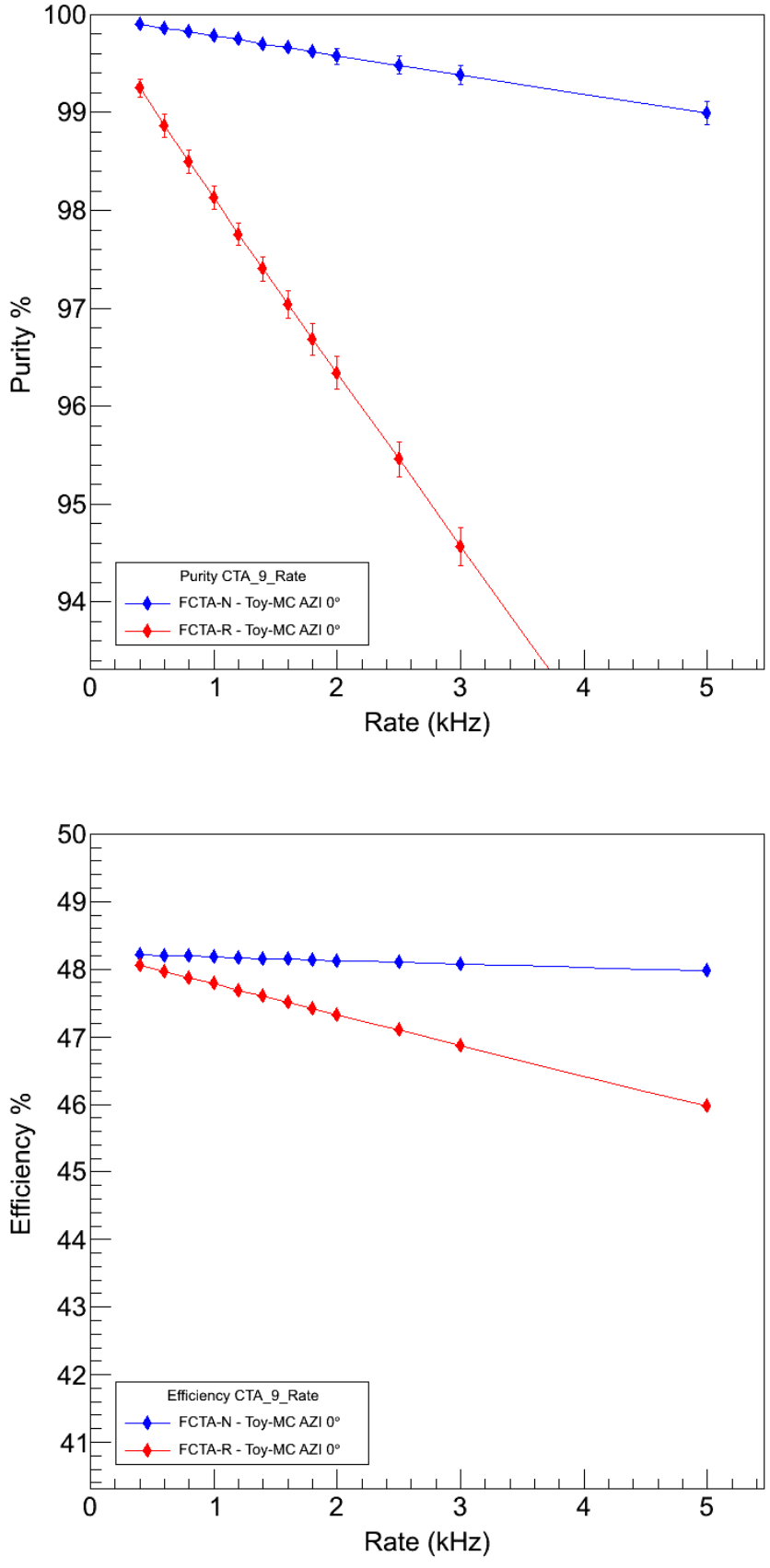

Figure 8.6: Purity and Efficiency of FCTA-R and FCTA-N with changing of the single telescope rate λ. The dislocation of the telescopes is shown in Figure 8.4.a. Others parameters are (Alt,Azi)=(70,0) and $D/\langle R\rangle = 1$.

8.3.2 CTA_9_250

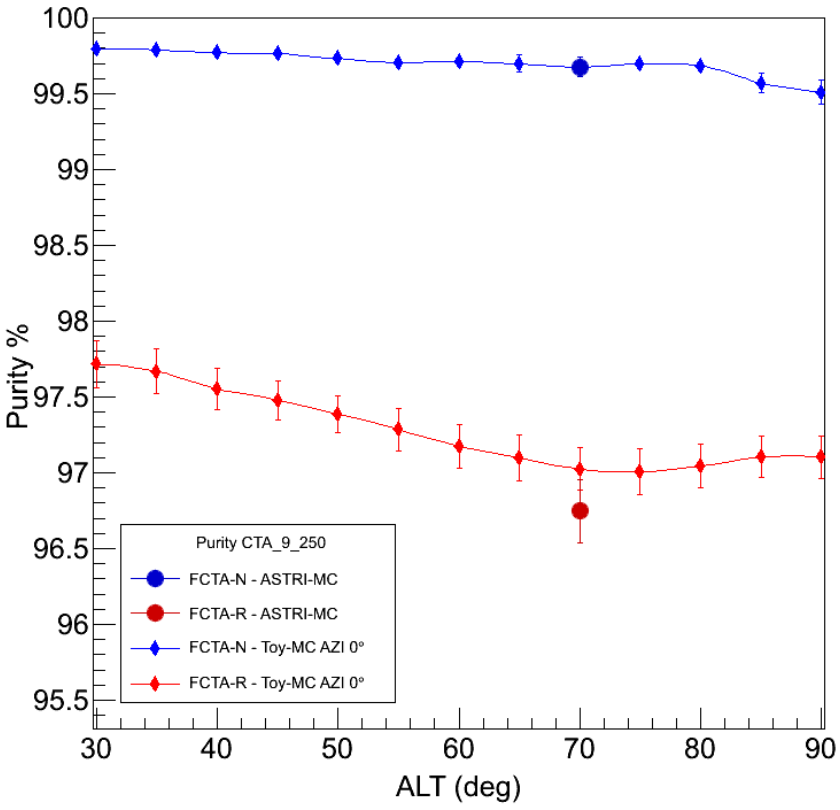

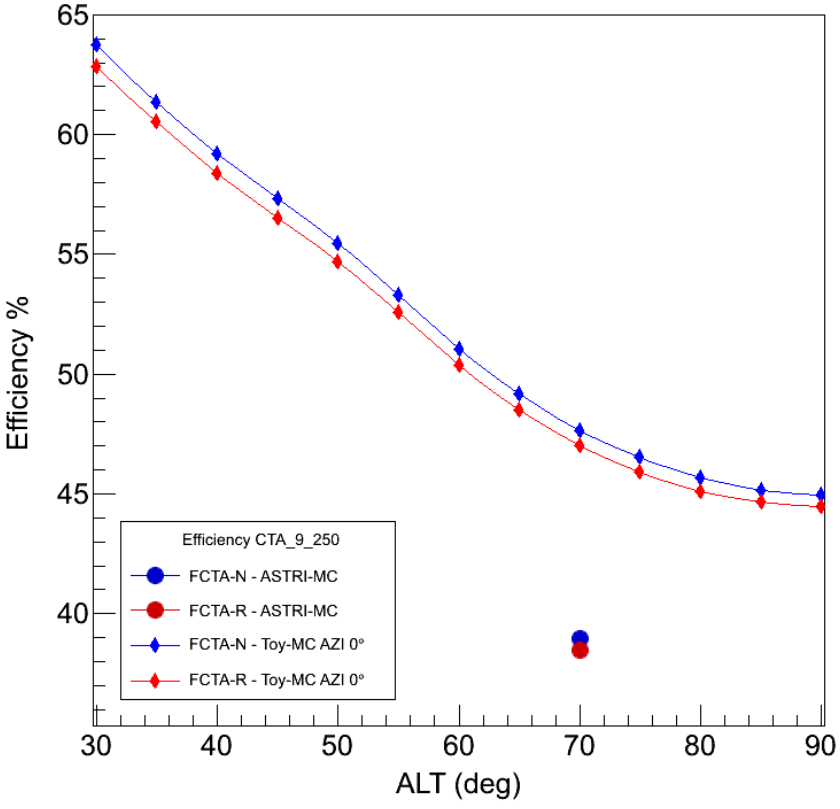

Figure 8.7: Purity and Efficiency of FCTA-R and FCTA-N. Others parameters are $D/\langle R\rangle = 1$ and $\lambda = 1\,kHz$. The dislocation of the telescopes is shown in Figure 8.4.b.

8.3.3 CTA_9_300

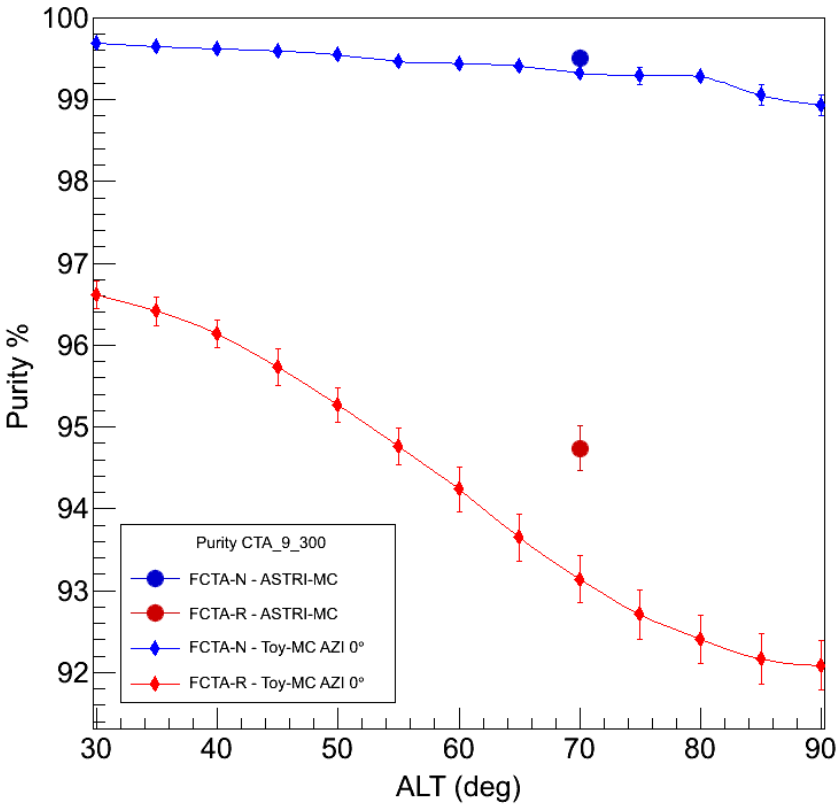

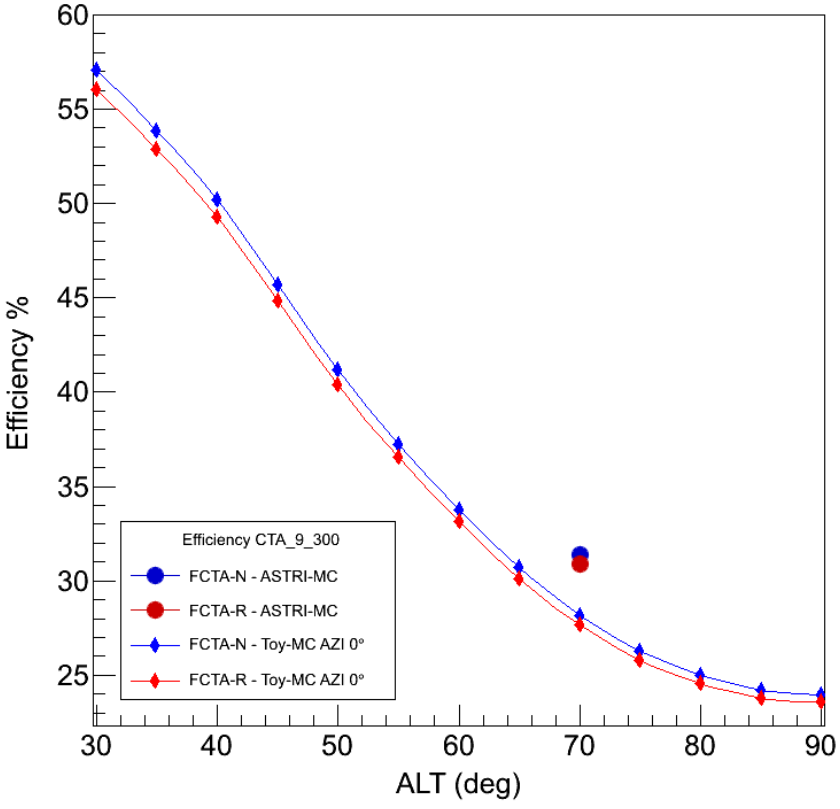

Figure 8.8: Purity and Efficiency of FCTA-R and FCTA-N. Others parameters are $D/\langle R\rangle = 1$ and $\lambda = 1\,kHz$. The dislocation of the telescopes is shown in Figure 8.4.c.

8.3.4 CTA_9_350

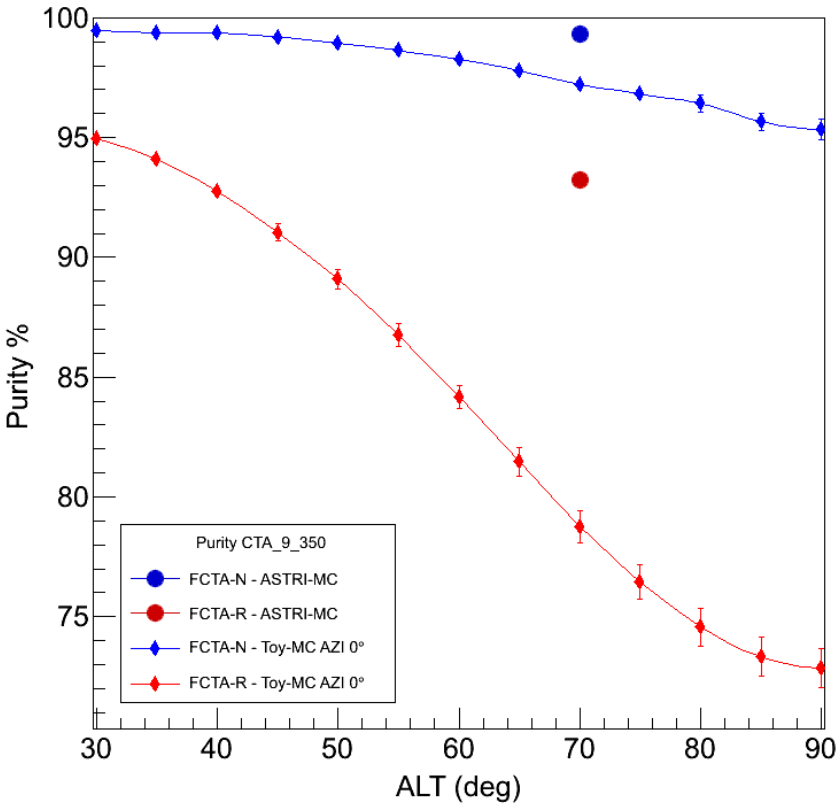

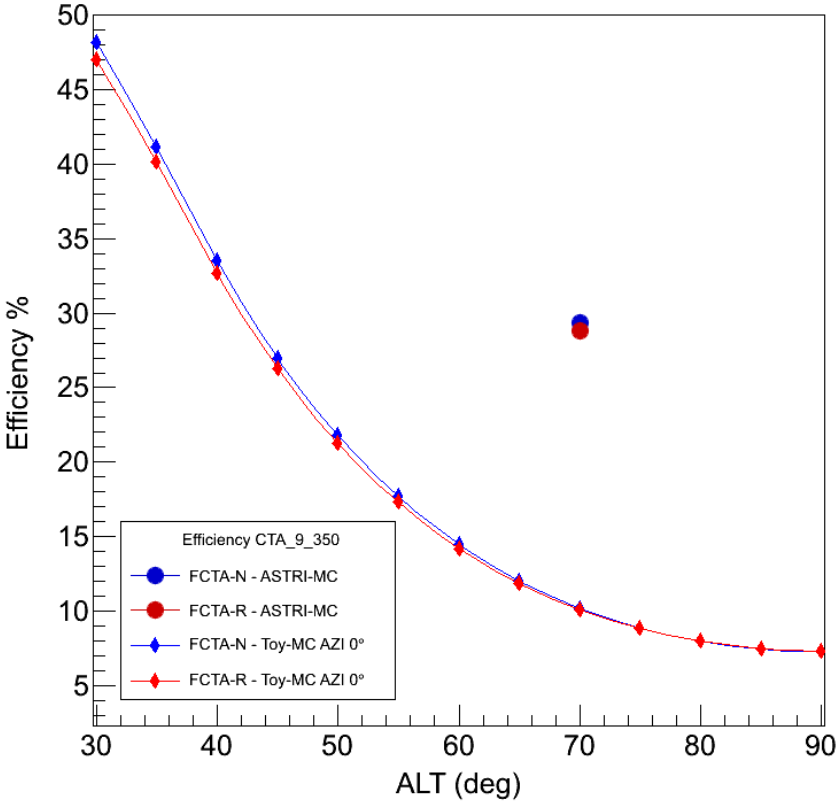

Figure 8.9: Purity and Efficiency of FCTA-R and FCTA-N. Others parameters are $D/\langle R\rangle = 1$ and $\lambda = 1\,kHz$. The dislocation of the telescopes is shown in Figure 8.4.d.

8.3.5 CTA_9 Comparison

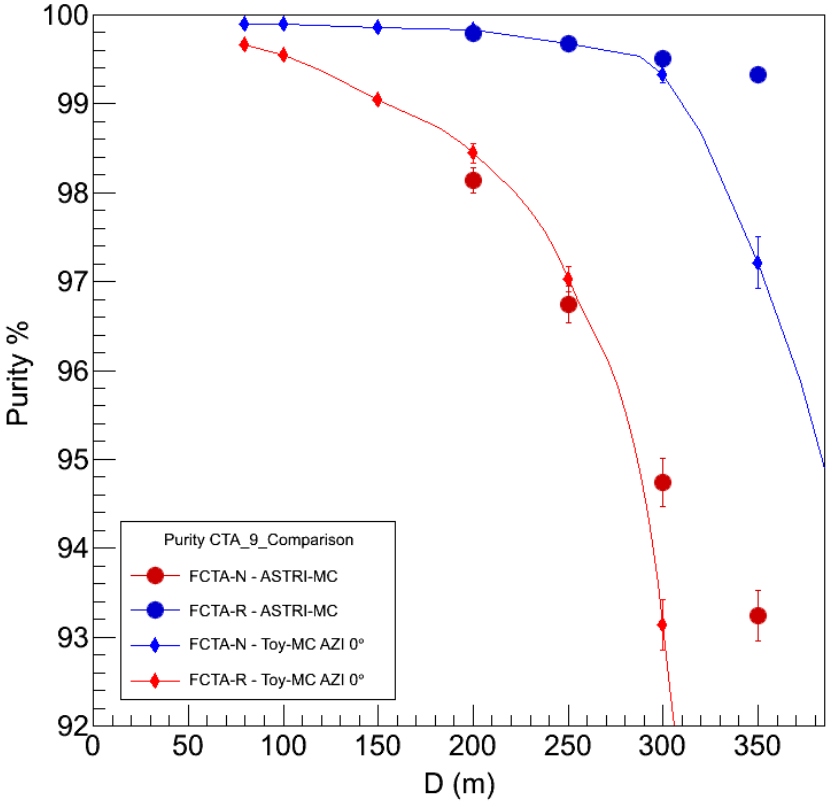

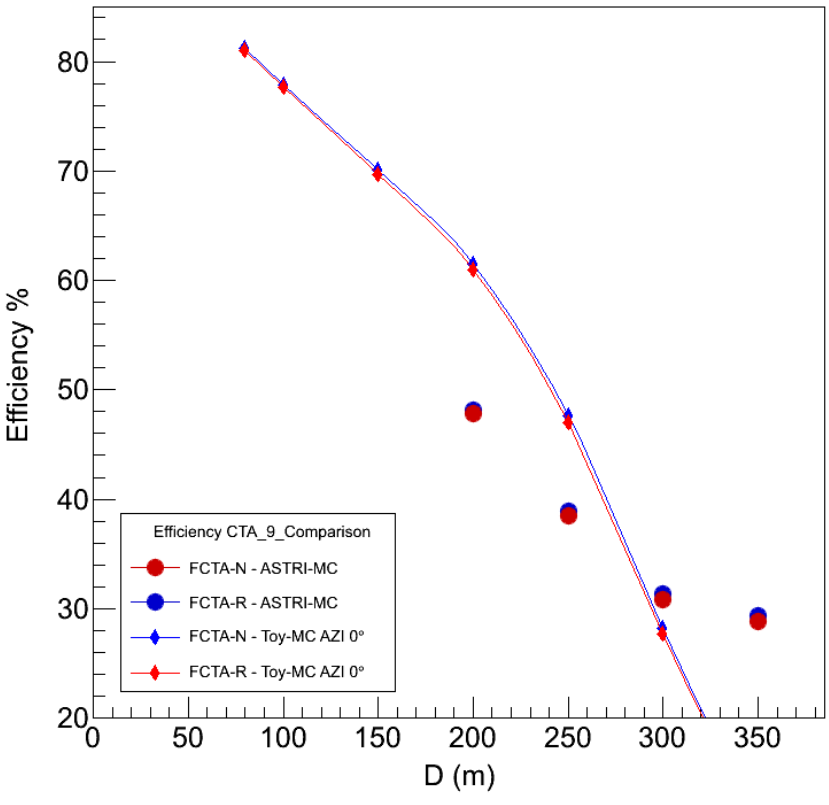

Figure 8.10: Purity and Efficiency of FCTA-R and FCTA-N. Others parameters are $D/\langle R\rangle = 1$ and $\lambda = 1\,kHz$. Comparison between the all telescopes dislocated as shown in Figure 8.4.

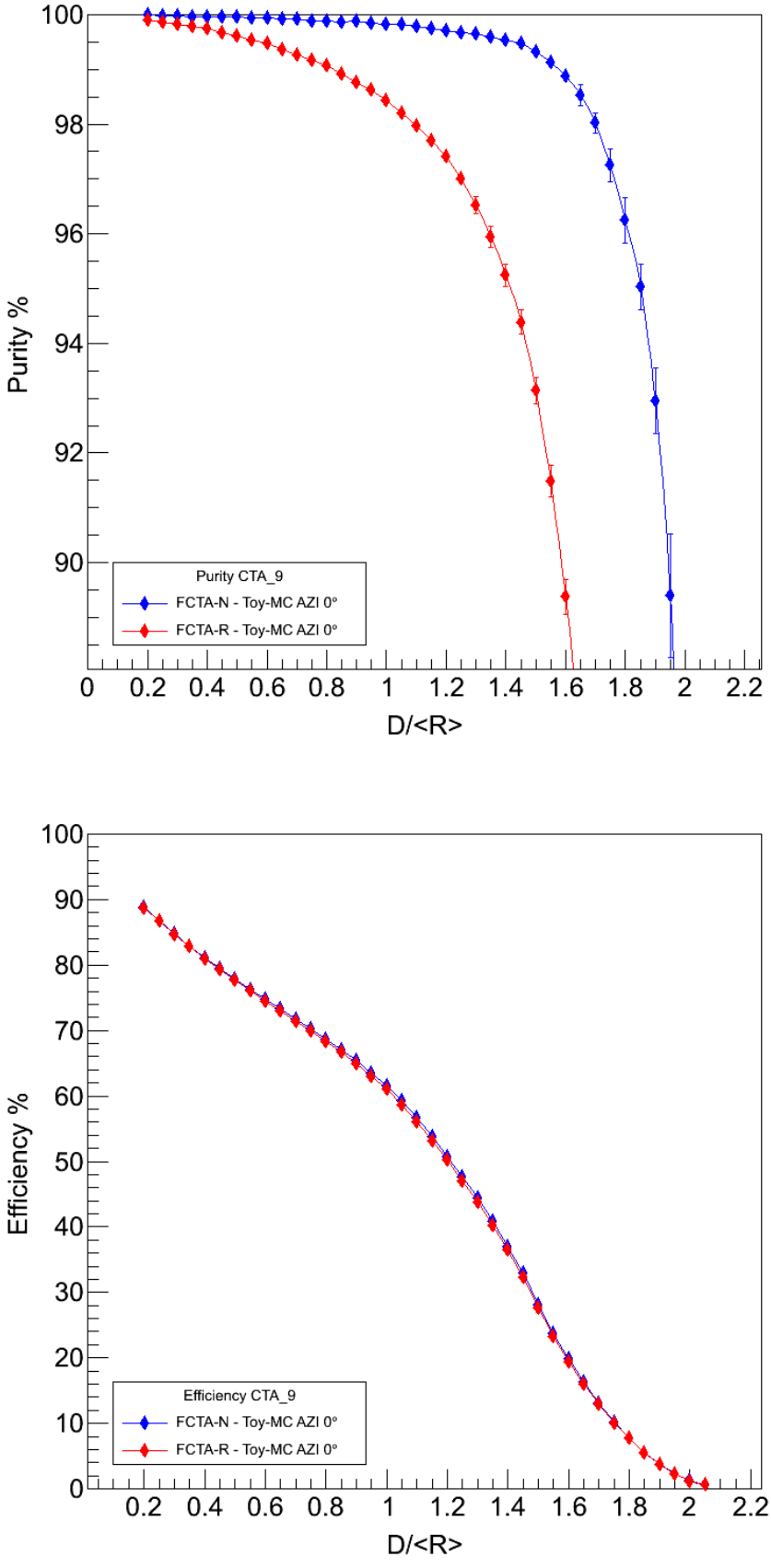

Figure 8.11: Purity and Efficiency of FCTA-R and FCTA-N. Others parameters are (Alt,Azi)=(70,0) and $\lambda = 1\,kHz$. Dependence between $D/\langle R \rangle$. Scaling effect.

8.4 CTA_N

In this section we considered four different layouts of the ASTRI mini-array with cumulative telescopes: $N_{Tel} = 17$, $N_{Tel} = 25$, $N_{Tel} = 33$. We studied each layout in function of pair coordinates (Alt, Azi) for Toy-MC data, ASTRI-MC data have a fixed configuration (Alt, Azi)=(70,0).

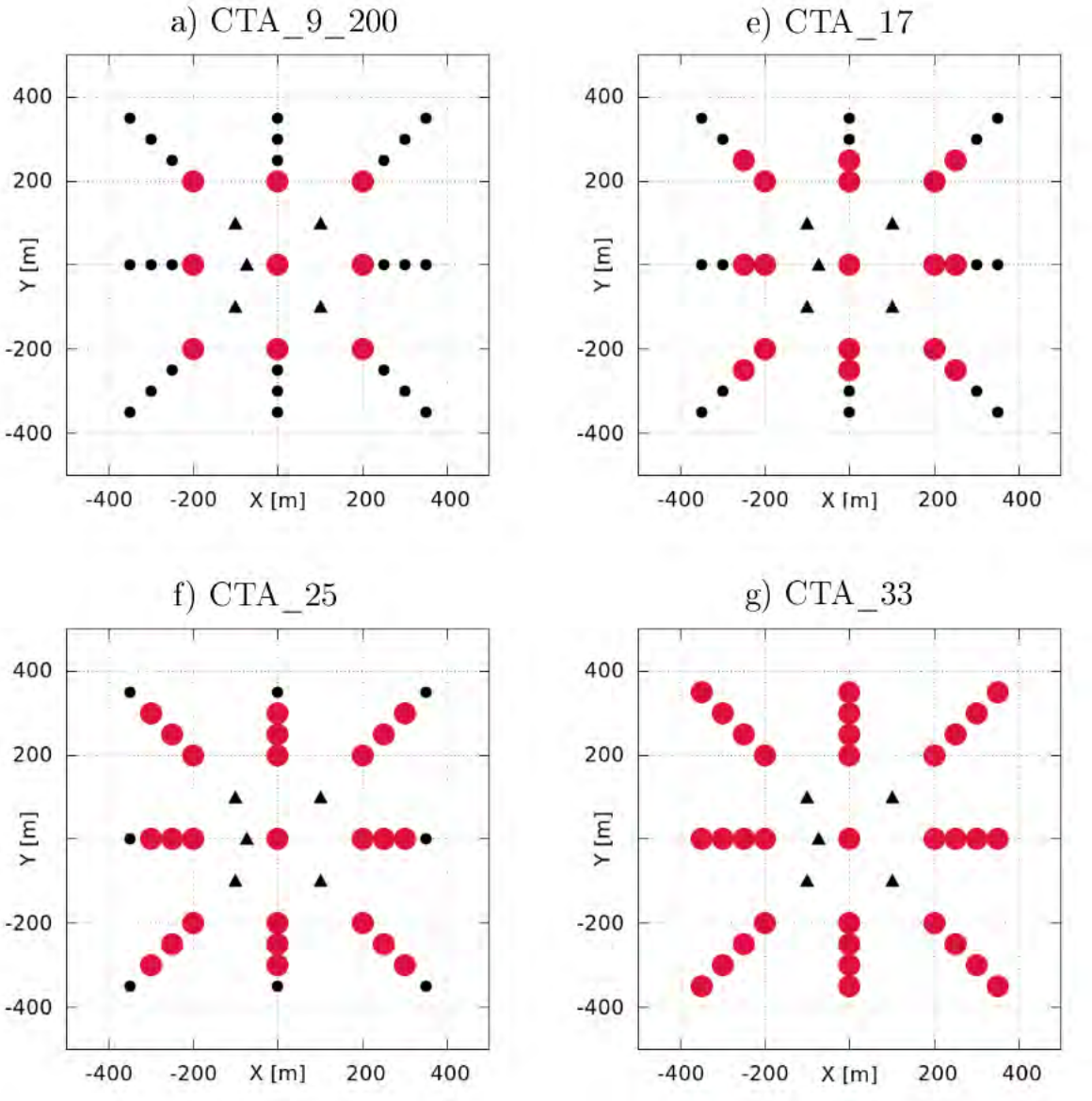

In the Layouts: CTA_17, CTA_25, CTA_33, we have chosen to keep fixed the parameter $\langle R \rangle = 200$. We note that the increasing of the number of telescope N_{Tel}, increase the performance of FCTA-N.
Indeed in Figure 8.16 we can see that purity remain more and less at the constant value of $p \sim 99.8\%$, instead the FCTA-R much worse. It is a very good point in favor of Network filter algorithm FCTA-N.
Because more telescopes were triggered, more information is available, so a collective method to discriminate the events becomes a winning solution.

In Figure 8.16 we can note also that efficiency at CTA_33 of ASTRI-MC data is too high, it is as we have already mentioned that ASTRI-MC data containing only events triggered by at least two telescopes.

8.4.1 CTA_17

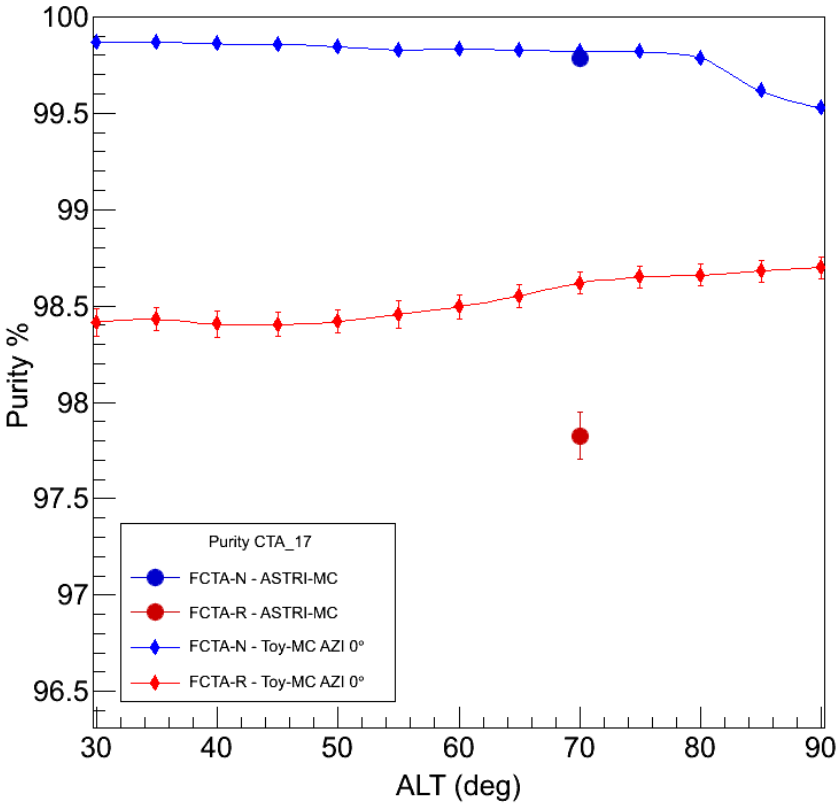

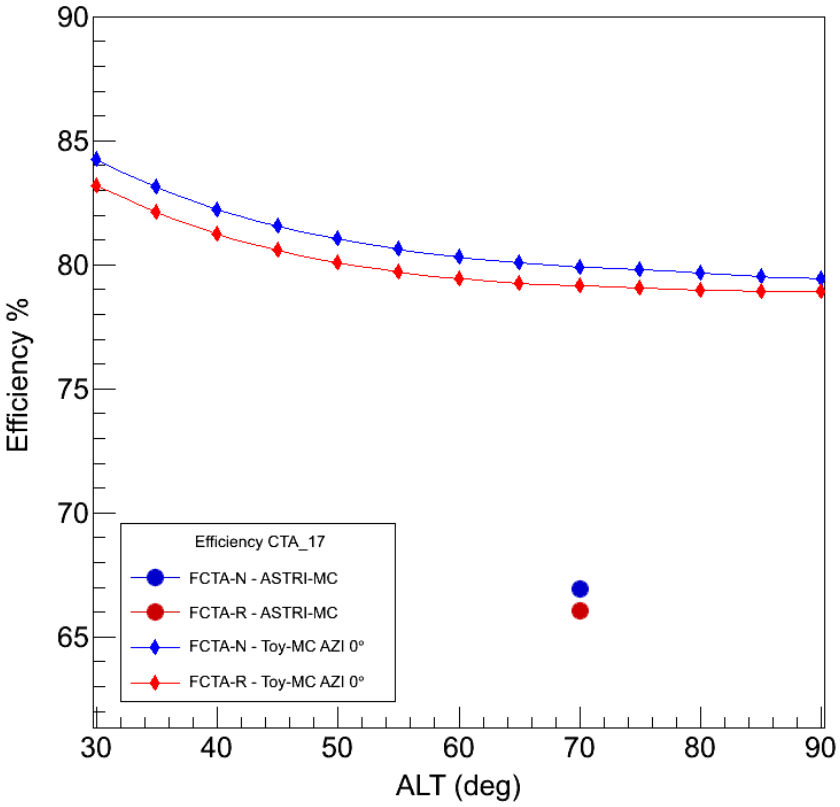

Figure 8.13: Purity and Efficiency of FCTA-R and FCTA-N. Others parameters are $\langle R \rangle = 200$ and $\lambda = 1\,kHz$. The dislocation of the telescopes is shown in Figure 8.12.e.

8.4.2 CTA_25

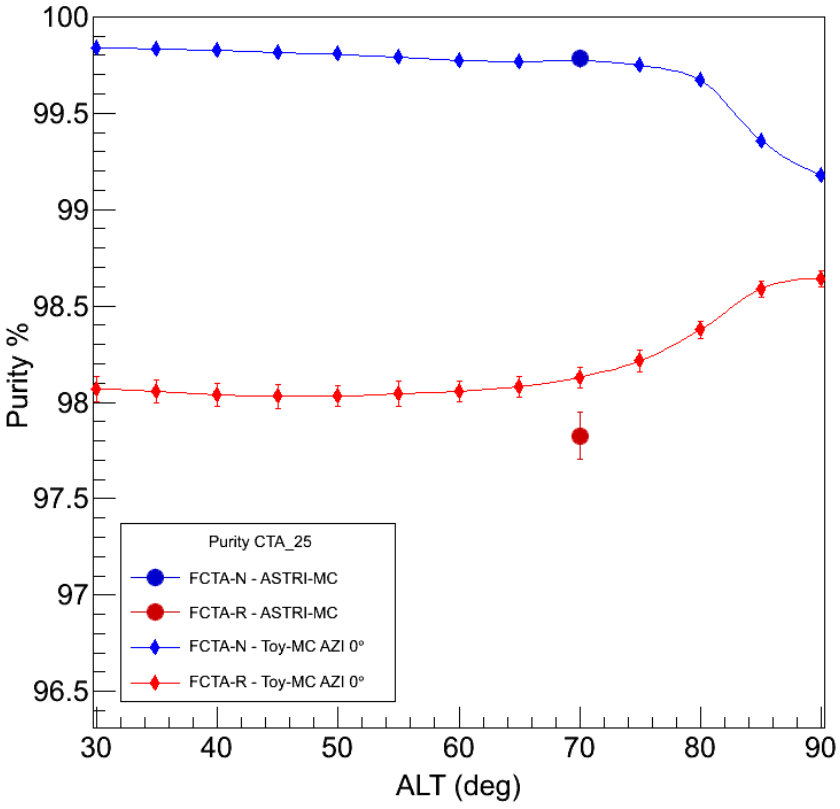

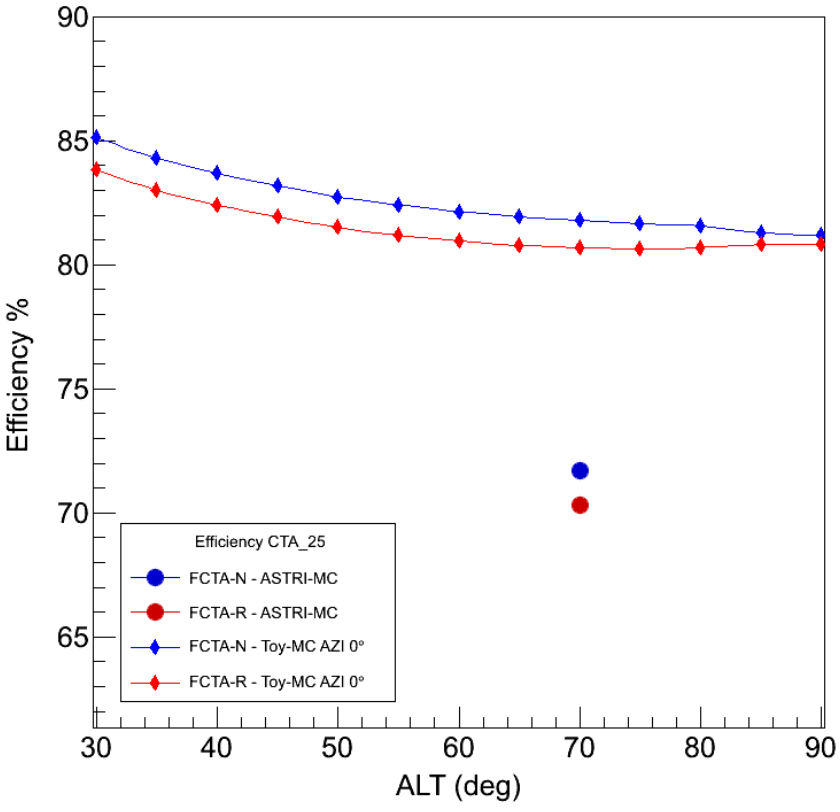

Figure 8.14: Purity and Efficiency of FCTA-R and FCTA-N. Others parameters are $\langle R \rangle = 200$ and $\lambda = 1\,kHz$. The dislocation of the telescopes is shown in Figure 8.12.f.

8.4.3 CTA_33

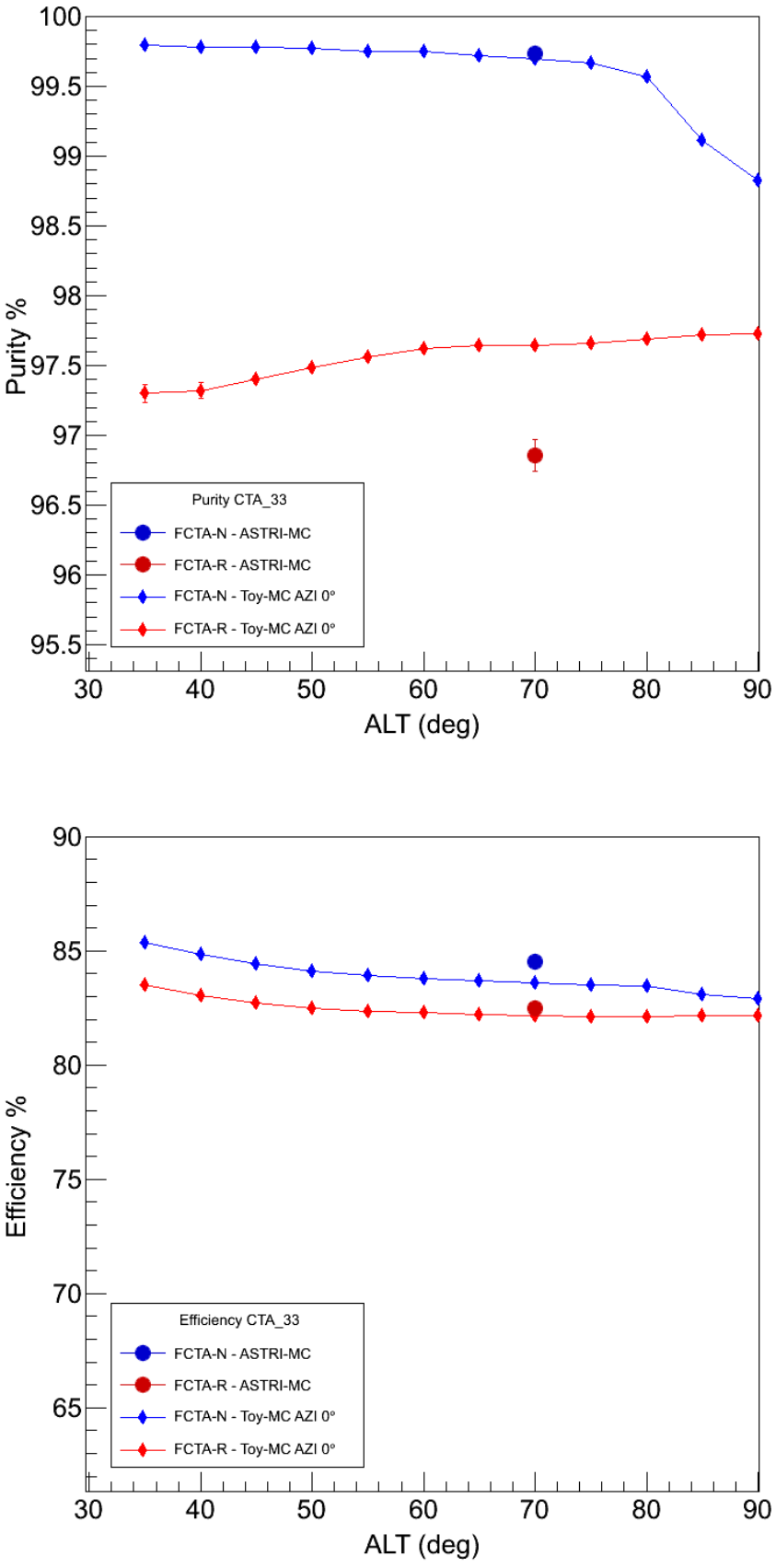

Figure 8.15: Purity and Efficiency of FCTA-R and FCTA-N. Others parameters are $\langle R \rangle = 200$ and $\lambda = 1\,kHz$. The dislocation of the telescopes is shown in Figure 8.12.g.

8.4.4 CTA_N Comparison

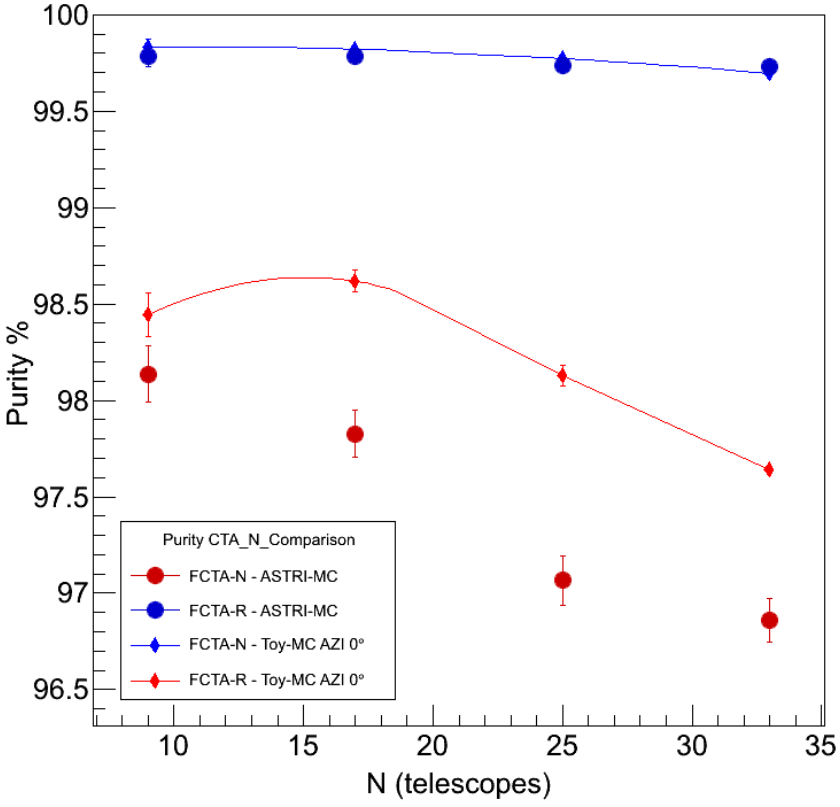

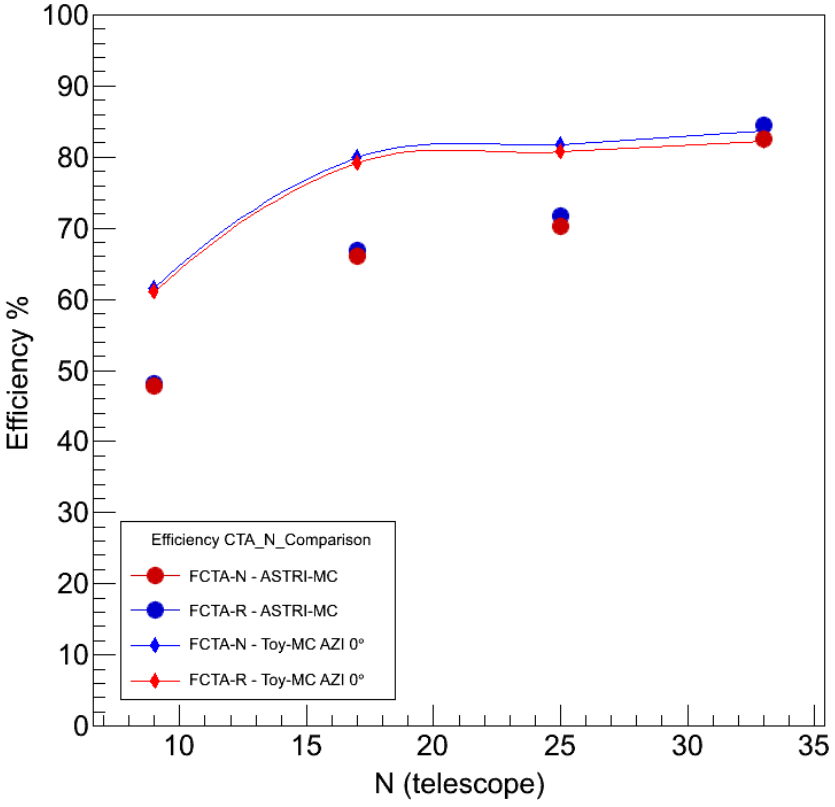

Figure 8.16: Purity and Efficiency of FCTA-R and FCTA-N. Others parameters are $\langle R \rangle = 200$ and $\lambda = 1\,kHz$. Comparison between the all telescopes dislocated as shown in Figure 8.12.

8.5 Concluding remarks and future work

The main goals of this thesis work are:

1. the in-depth study of VHE gamma ray astronomy and the CTA project,
2. the development of a first-level trigger for the CTA,
3. testing its efficiency through a Toy-MC simulations of several different setup and with MC simulations provided by the ASTRI collaboration,
4. finally to deploy the algorithm on a GPU system in order to obtain the required performance.

Hence in chapters 1-5 we offer, without claim for completeness, a full and self-consistent presentation of many aspects and topics of VHE gamma ray astronomy, which allows the reader to appreciate the main results, understanding how they were obtained. It is the result of hard work and passion to the subject.

The most relevant work is the development of a first-level trigger to fast filtering the events for the CTA. It was a challenge, many attempts were made until to find some simply but efficient ideas. After an in-depth study of the discrimination events problem, which allowed to develop a filter working with two original algorithms called FCTA-R and FCTA-N.

The first one, FCTA-R, is simple but not trivial, it never wrongs. It consists essentially in a criteria to "cut" the absolute time-line, in intervals of time (we call them *time-boxes*), each of them containing at least one ore more events but with the strong condition that no event is divided into different time-box.

The second one, FCTA-N, is a original Network Filter Algorithm, which transforms a compatibility matrix, well defined through the delays matrices in a graph and than evolves the systems obtaining a clustering effect. The cluster corresponds at the simulated physical events. All this procedure is innovative and probably never used before in CTA data analysis.

Finally we tested our filter onto Official ASTRI-MC data. Obtaining a very good performance with a purity of about $\sim 99.8\%$ and the highest efficiency obtainable with the same purity.

The implementation of the algorithm on a GPU system, made possible by the FCTA-R condition, is the next step and, I hope, my future work.

Appendices

Appendix A

Classical Electrodynamics

Classical Electrodynamics is a branch of Physics that studies the interactions between charges and electromagnetic fields, whenever the length scales and field strengths are large enough to neglect quantum mechanical effects.
The description of the electromagnetic phenomena is based on the Maxwell's equations and the Lorentz Force. The Maxwell's equations in S.I. units are:

$$\begin{aligned} \nabla \cdot \boldsymbol{D} &= \rho_f \qquad & \nabla \cdot \boldsymbol{B} &= 0 \\ \nabla \times \boldsymbol{E} &= -\frac{\partial \boldsymbol{B}}{\partial t} \qquad & \nabla \times \boldsymbol{H} &= \boldsymbol{j}_f + \frac{\partial \boldsymbol{D}}{\partial t} \end{aligned} \tag{A.0.1}$$

In vacuum $\boldsymbol{D} = \varepsilon_0 \boldsymbol{E}$ and $\boldsymbol{H} = \boldsymbol{B}/\mu_0$ where $\mu_0 \varepsilon_0 = 1/c^2$. In general, into a dielectric medium the auxiliary fields are: $\boldsymbol{D} = \varepsilon_0 \boldsymbol{E} + \boldsymbol{P}$ and $\boldsymbol{H} = \boldsymbol{B}/\mu_0 - \boldsymbol{M}$ where $\boldsymbol{P}$ is the polarization field and $\boldsymbol{M}$ the magnetization field defined by:

$$\rho_b = -\nabla \cdot \boldsymbol{P} \qquad \boldsymbol{j}_b = \nabla \times \boldsymbol{M} + \frac{\partial \boldsymbol{P}}{\partial t} \tag{A.0.2}$$

where footer f means $free$ and b means *bound*:

$$q = q_f + q_b = \int_V (\rho_f + \rho_b) dV \qquad j = j_f + j_b = \int_V (j_f + j_b) dV \tag{A.0.3}$$

Implicit in the Maxwell's equations is the continuity equation for charge density ρ and current density æ. Also essential for consideration of charge particle motion is the Lorentz Force:

$$\boldsymbol{F} = q\big(\boldsymbol{E} + \boldsymbol{v} \times \boldsymbol{B}\big) \tag{A.0.4}$$

The energy density of the electromagnetic field and the energy flux (Pointing vector) are:

$$u = \frac{1}{2}\big(\boldsymbol{E} \cdot \boldsymbol{D} + \boldsymbol{B} \cdot \boldsymbol{H}\big) \qquad \boldsymbol{S} = \boldsymbol{E} \times \boldsymbol{H} \tag{A.0.5}$$

Maxwell's equations could be also written in covariant form, consistent with Special Relativity.

$$\epsilon^{\mu\nu\rho\sigma} \partial_\nu F_{\rho\sigma} = 0 \qquad \partial_\mu F^{\mu\nu} = j^\nu \tag{A.0.6}$$

where $F^{\mu\nu}$ is the electromagnetic tensor and $j^\mu = (\rho, \boldsymbol{j})$ is the four-current.

A.1 Liénard-Wiechert potentials

Consider a particle of charged $q = ze$ moving along the trajectory $r_q(\tau)$ at speed $\boldsymbol{v} = \boldsymbol{\beta}c$. Suppose we wish to measure the radiation field at point P at time t, located at $\boldsymbol{r}(t)$.

The radiation measured at P, at time t, was emitted by the particle when it was at point S', at an earlier time t', where $\overline{S'P} = \boldsymbol{R}(t') = \boldsymbol{r}(t) - \boldsymbol{r}_q(t')$. This is because an electromagnetic wave has a finite travel time $\Delta t = |\boldsymbol{R}(t')|/c$ before arriving at point P. Thus, the radiation field at P needs to be specified in terms of the time emission t', called *retarded time*:

$$t' = t - \frac{|\boldsymbol{r} - \boldsymbol{r}\,'|}{c} = t - \frac{|\boldsymbol{R}(t')|}{c} \qquad \text{(A.1.1)}$$

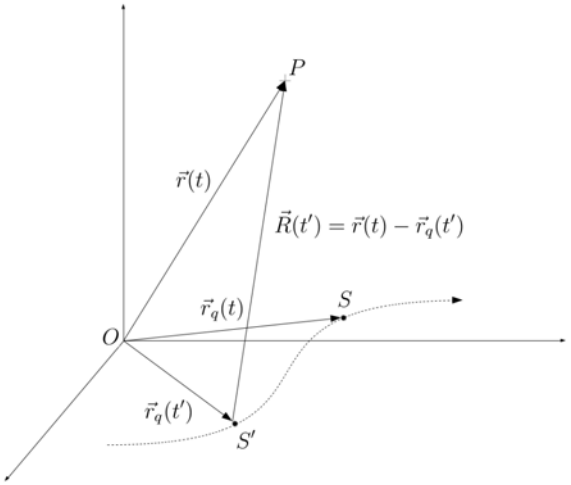

To evaluated the radiation field at P at time t is useful introduce the scalar and vector potentials $\phi(\boldsymbol{r}, t)$ and $\boldsymbol{A}(\boldsymbol{r}, t)$.

From homogeneous Maxwell's equations, we obtain the following usual definitions:

$$\nabla \cdot \boldsymbol{B} = 0 \quad \rightarrow \quad \boldsymbol{B} = \nabla \times \boldsymbol{A} \qquad\qquad \nabla \times \boldsymbol{E} = -\frac{\partial \boldsymbol{B}}{\partial t} \quad \rightarrow \quad \boldsymbol{E} = -\frac{\partial \boldsymbol{A}}{\partial t} - \nabla\phi \qquad \text{(A.1.2)}$$

where we used the property of B to be a solenoidal vector field and that $E - \partial \boldsymbol{A}/\partial t$ is an irrotational vector. Electromagnetic potentials are not uniquely defined, it is possible prove that following transformations leave $\boldsymbol{E}$ and $\boldsymbol{B}$ unchanged.

$$\boldsymbol{A}\,' = \boldsymbol{A} + \nabla\chi \qquad\qquad \phi' = \phi - \frac{\partial \chi}{\partial t} \qquad \text{(A.1.3)}$$

The choice of any scalar field χ determines the gauge, but no physical result depends upon the choice. Replacing these results into the others two Maxwell's equations we obtain:

$$\begin{aligned} &\nabla \cdot \boldsymbol{E} = \frac{\rho}{\varepsilon_0} \quad \rightarrow \quad \nabla^2\phi + \frac{\partial(\nabla \cdot \boldsymbol{A})}{\partial t} = -\frac{\rho}{\varepsilon_0} \\ &\nabla \times \boldsymbol{B} = \mu_0 \boldsymbol{j} + \mu_0\varepsilon_0 \frac{\partial \boldsymbol{E}}{\partial t} \quad \rightarrow \quad \nabla^2 \boldsymbol{A} - \mu_0\varepsilon_0 \frac{\partial^2 \boldsymbol{A}}{\partial t^2} - \nabla\big(\nabla \cdot \boldsymbol{A} + \mu_0\varepsilon_0 \frac{\partial \phi}{\partial t}\big) = -\mu_0 \boldsymbol{j} \end{aligned} \qquad \text{(A.1.4)}$$

where in the second equations we used a vector identity [1], with the appropriate gauge choice $\nabla \cdot \boldsymbol{A} = -\mu_0\varepsilon_0 \dfrac{\partial \phi}{\partial t}$, called Lorentz gauge condition, we obtain the same differential equation for each potential.

$$\nabla^2\phi - \mu_0\varepsilon_0 \frac{\partial^2 \phi}{\partial t^2} = -\frac{\rho}{\varepsilon_0} \qquad\qquad \nabla^2 \boldsymbol{A} - \mu_0\varepsilon_0 \frac{\partial^2 \boldsymbol{A}}{\partial t^2} = -\mu_0 \boldsymbol{j} \qquad \text{(A.1.5)}$$

To find a solution we consider the associated homogeneous differential equation, replacing $\mu_0\varepsilon_0 = 1/c^2$.

$$\nabla^2\phi - \frac{1}{c^2}\frac{\partial^2 \phi}{\partial t^2} = 0 \qquad \text{(A.1.6)}$$

[1] $\nabla \times (\nabla \times \boldsymbol{A}) = \nabla(\nabla \cdot \boldsymbol{A}) - \nabla^2 \boldsymbol{A}$

It is clear that in this case ϕ has a central symmetry (ϕ is a function only of R). Therefore if we write the Laplace operator in spherical coordinates (A.1.6) reduces to:

$$\frac{1}{R^2}\frac{\partial}{\partial R}\left(R^2\frac{\partial\phi}{\partial R}\right)-\frac{1}{c^2}\frac{\partial^2\phi}{\partial t^2}=0 \qquad \longrightarrow \qquad \frac{\partial^2\varphi}{\partial R^2}-\frac{1}{c^2}\frac{\partial^2\varphi}{\partial t^2}=0 \tag{A.1.7}$$

where we made the substitution $\phi=\varphi(R,t)/R$, with $R=|\boldsymbol{r}-\boldsymbol{r}_q|$. Then we find for φ the equation of plane waves, whose the general solution has the form:

$$\varphi=\varphi_1\big(t-\frac{R}{c}\big)+\varphi_2\big(t+\frac{R}{c}\big) \tag{A.1.8}$$

Since we only want a particular solution of the equation, with physical meaning, we take $\varphi_2=0$. Then everywhere except at the origin, ϕ has the form:

$$\phi=\frac{\varphi\big(t-\frac{R}{c}\big)}{R} \tag{A.1.9}$$

The function φ in this moment is arbitrary, we now choose it so that we obtain the correct value at the origin. It is easy to see that if $R\to 0$, the potential increase to infinity, and therefore in the limit of $R\to 0$ we can neglect the time derivative term respect $\nabla^2\phi$. Therefore remembering the solution of the *Poisson equation* we obtain that the *retarded potentials* are:

$$\phi(\boldsymbol{r},t)=\frac{1}{4\pi\varepsilon_0}\int\frac{\rho(\boldsymbol{r}\,',t')}{|\boldsymbol{r}-\boldsymbol{r}\,'|}d^3r\,' \qquad \boldsymbol{A}(\boldsymbol{r},t)=\frac{\mu_0}{4\pi}\int\frac{\boldsymbol{j}(\boldsymbol{r}\,',t')}{|\boldsymbol{r}-\boldsymbol{r}\,'|}d^3r\,' \tag{A.1.10}$$

For a moving point charge along $r_q(\tau)$ formally we define: the charge distribution $\rho(\boldsymbol{r}\,',t')=q\,\delta^3(\boldsymbol{r}\,'-\boldsymbol{r}_q(t'))\,\delta(t'-t+|\boldsymbol{R}(t')|/c)$ and current $\boldsymbol{j}(\boldsymbol{r}\,',t')=q\boldsymbol{v}\,\delta^3(\boldsymbol{r}\,'-\boldsymbol{r}_q(t'))\,\delta(t'-t+|\boldsymbol{R}(t')|/c)$. Thus we have:

$$\begin{aligned}\phi(\boldsymbol{r},t)&=\frac{1}{4\pi\varepsilon_0}\iint\frac{q\,\delta(t'-t+|\boldsymbol{R}(t')|/c)}{|\boldsymbol{r}-\boldsymbol{r}\,'|}\delta^3(\boldsymbol{r}\,'-\boldsymbol{r}_q(t'))\,d^3r\,'dt'\\ \boldsymbol{A}(\boldsymbol{r},t)&=\frac{\mu_0}{4\pi}\iint\frac{q\boldsymbol{v}\,\delta(t'-t+|\boldsymbol{R}(t')|/c)}{|\boldsymbol{r}-\boldsymbol{r}\,'|}\delta^3(\boldsymbol{r}\,'-\boldsymbol{r}_q(t'))\,d^3r\,'dt'\end{aligned} \tag{A.1.11}$$

To evaluate this integral, therefore, we need the identity: $\delta(f(t'))=\sum_j\dfrac{\delta(t'-t_j)}{|f'(t_j)|}$ so we have:

$$\delta(t'-t+|\boldsymbol{R}(t')|/c)=\frac{\delta(t'-t+|\boldsymbol{R}(t')|/c)}{\frac{\partial}{\partial t'}(t'-t+|\boldsymbol{R}(t')|/c)}=\frac{\delta(t'-t+|\boldsymbol{R}(t')|/c)}{1+\frac{1}{c}\frac{\boldsymbol{R}(t')}{|\boldsymbol{R}(t')|}(-\boldsymbol{v}_q(t'))}= \tag{A.1.12}$$

Replacing (A.1.12) into (A.1.11) and simpliyfing the notation with $\hat{\boldsymbol{n}}=\boldsymbol{R}(t')/|\boldsymbol{R}(t')|$ and $\boldsymbol{\beta}=\boldsymbol{v}_q/c=\dot{\boldsymbol{r}}_q/c$ we obtain :

$$\begin{aligned}\phi(\boldsymbol{r},t)&=\frac{1}{4\pi\varepsilon_0}\left(\frac{q}{(1-\hat{\boldsymbol{n}}\cdot\boldsymbol{\beta})R}\right)\\ \boldsymbol{A}(\boldsymbol{r},t)&=\frac{\mu_0 c}{4\pi}\left(\frac{q\boldsymbol{\beta}}{(1-\hat{\boldsymbol{n}}\cdot\boldsymbol{\beta})R}\right)\end{aligned} \tag{A.1.13}$$

These are the famous *Liénard-Wiechert potentials* for a moving point charge.

A.2 The Radiation Field

The differentiation of Liénard-Wiechert potentials through the definitions (A.1.2) provides the electromagnetic fields generated by a point charge moving along $r_q(\tau)$. The calculation is not trivial (see Jackson [27] for details):

$$\begin{aligned} \boldsymbol{E}(\boldsymbol{r},t) &= \frac{1}{4\pi\varepsilon_0}\left[\frac{q(\hat{\boldsymbol{n}}-\boldsymbol{\beta})}{\gamma^2(1-\hat{\boldsymbol{n}}\cdot\boldsymbol{\beta})^3R^2}+\frac{q\,\hat{\boldsymbol{n}}\times\left((\hat{\boldsymbol{n}}-\boldsymbol{\beta})\times\dot{\boldsymbol{\beta}}\right)}{c(1-\hat{\boldsymbol{n}}\cdot\boldsymbol{\beta})^3R}\right] \\ \boldsymbol{B}(\boldsymbol{r},t) &= \frac{1}{c}\left[\hat{\boldsymbol{n}}\times\boldsymbol{E}(\boldsymbol{r},t)\right] \end{aligned} \tag{A.2.1}$$

The first term of the electric field, $\propto R^{-2}$, is the *velocity field* and represent the generalization of the Coulomb law for moving point charge (indeed for $\beta \ll 1$ it becomes exactly the Coulomb law). The second term $\propto R^{-1}$ is called *acceleration field* and is always perpendicular to $\hat{\boldsymbol{n}}$.

Hence the radiation field of a moving charge is defined by:

$$\begin{aligned} \boldsymbol{E}_{rad}(\boldsymbol{r},t) &= \frac{q}{4\pi\varepsilon_0 c}\left[\frac{\hat{\boldsymbol{n}}\times\left((\hat{\boldsymbol{n}}-\boldsymbol{\beta})\times\dot{\boldsymbol{\beta}}\right)}{(1-\hat{\boldsymbol{n}}\cdot\boldsymbol{\beta})^3R}\right] \\ \boldsymbol{B}_{rad}(\boldsymbol{r},t) &= \frac{1}{c}\left[\hat{\boldsymbol{n}}\times\boldsymbol{E}_{rad}(\boldsymbol{r},t)\right] \end{aligned} \tag{A.2.2}$$

In the special cases in which the particle moves with uniform motion, the second term in (A.2.1) is absent. The first term have to be the same of what we can obtain with a Lorentz transformaion of the static Coulomb field.

Observing the Fig.?? we can note that:

$$P'Q = \beta R\cos\theta = \boldsymbol{\beta}\cdot\hat{\boldsymbol{n}}R$$

so we have :

$$OQ = (1-\boldsymbol{\beta}\cdot\hat{\boldsymbol{n}})R \quad \text{and} \quad b = R\sin\theta$$

where b is the impact parameter. Hence:

$$[(1-\boldsymbol{\beta}\cdot\hat{\boldsymbol{n}})R]^2 = b^2+v^2t^2-\beta^2b^2 = \frac{1}{\gamma^2}(b^2+\gamma^2v^2t^2)$$

Thus the transverse component of the field, calculated from (A.2.1) results:

$$|\boldsymbol{E}_t(\boldsymbol{r},t)| = \frac{1}{4\pi\varepsilon_0}\frac{q\gamma b}{(b^2+\gamma^2v^2t^2)^{3/2}} \tag{A.2.3}$$

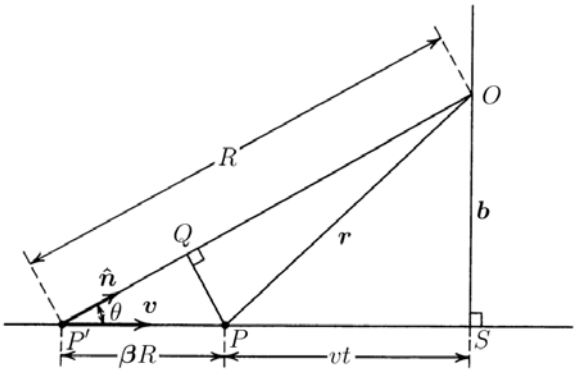

Figure 2.3: Present and retarded positions of a charge in uniform motion.

The other components of $\boldsymbol{E}$ and $\boldsymbol{B}$ come out similarly. This result is the starting point of Weizsaker-Williams approach used to describe bremsstrahlung radiation.

A.3 Larmor's Formula and its relativistic generalization

To calculated the Total emitted power by a moving charge along $r_q(\tau)$, we consider before the non-relativistic case. If $\beta \ll 1$, the radiation fields simplified are:

$$\begin{aligned} \boldsymbol{E}_{rad}(\boldsymbol{r},t) &= \frac{q}{4\pi\varepsilon_0 Rc}\Big[\hat{\boldsymbol{n}} \times (\hat{\boldsymbol{n}} \times \boldsymbol{\beta})\Big] \\ \boldsymbol{B}_{rad}(\boldsymbol{r},t) &= \frac{1}{c}\Big[\hat{\boldsymbol{n}} \times \boldsymbol{E}_{rad}(\boldsymbol{r},t)\Big] \end{aligned} \tag{A.3.1}$$

Note that $\boldsymbol{E}_{rad}$ remains in the plane containing $\hat{\boldsymbol{n}}$ and $\dot{\beta}$ and $\boldsymbol{B}_{rad}$ is orthogonal to this plane. If we define the angle between $\hat{\boldsymbol{n}}$ and $\boldsymbol{\beta}$ as θ, we have:

$$|\boldsymbol{E}_{rad}| = c|\boldsymbol{B}_{rad}| = \frac{q}{4\pi\varepsilon_0}\frac{\dot{v}}{Rc^2}\sin\theta \tag{A.3.2}$$

The Pointing vector is directed as $\hat{\boldsymbol{n}}$ and its magnitude is:

$$S = \frac{1}{\mu_0}\boldsymbol{E} \times \boldsymbol{B} = \frac{1}{\mu_0 c}|\boldsymbol{E}^{\boldsymbol{2}}_{rad}| = \frac{1}{16\pi^2\varepsilon_0 c^3}\frac{q^2\dot{v}^2}{R^2}\sin^2\theta \tag{A.3.3}$$

Since S is the flux of the emitted power ($S = dW/(dtd\Sigma)$), we can write $d\Sigma = R^2 d\Omega$, where $d\Omega$ is the solid angle. Thus the emitted power per solid angle is:

$$\frac{dW}{dtd\Omega} = \frac{1}{16\pi^2\varepsilon_0 c^3}q^2\dot{v}^2\sin^2\theta \tag{A.3.4}$$

Note the characteristic dipole pattern $\propto \sin^2\theta$. The maximum emitted power is perpendicular to the acceleration and indeed there is no emission along the acceleration direction.

The total emitted power is obtained integrating in the whole solid angle.

$$P = \frac{dW}{dt} = \frac{1}{16\pi^2\varepsilon_0 c^3}q^2\dot{v}^2\int_0^{2\pi}\int_0^{\pi}\sin^2\theta\sin\theta d\theta d\phi \;\cancel{\;\;\;\;}\; \tfrac{8}{3}\pi \tag{A.3.5}$$

The result is the *Larmor's formula*: the total emitted power by an accelerating charge (non-relativistic):

$$P = \frac{q^2\dot{v}^2}{6\pi\varepsilon_0 c^3} \tag{A.3.6}$$

The relativistic generalization of the Larmor's formula is obtained knowing that the power P have to be Lorentz invariant. Therefore we relate P with the first derivative of the four-momenta, knowing that $a^\mu = dv^\mu/d\tau$ is the four-acceleration and $v^\mu = \gamma(c,\boldsymbol{v})$ the four-velocity:

$$P = \frac{q^2}{6\pi\varepsilon_0 m^2 c^3}\left(\frac{dp^\mu}{d\tau}\frac{dp_\mu}{d\tau}\right) = \frac{q^2}{6\pi\varepsilon_0 c^3}(a^\mu a_\mu) \tag{A.3.7}$$

Where $\frac{1}{m^2}(\frac{dp^\mu}{d\tau}\frac{dp_\mu}{d\tau}) = (a^\mu a_\mu) = -a^0 a_0 + |\boldsymbol{a}|^2$. Note that in all reference frames the four-velocity and four-acceleration are orthogonal: $a^\mu v_\mu = (dv^\mu/d\tau)v_\mu = \frac{1}{2}d(\cancel{v^\mu v_\nu}^{-c^2})/d\tau = 0$.

But since exists a reference frame K' where the particle is at the rest $v^\mu = (c,\boldsymbol{0})$ this imply that $a'^0 = 0$. Hence we can write that: $a^\mu a_\mu = a'^\mu a'_\mu| = |\boldsymbol{a}'|^2$. Therefore we can write:

$$P = \frac{q^2}{6\pi\varepsilon_0 c^3}|\boldsymbol{a}'|^2 \tag{A.3.8}$$

Expliciting the acceleration's components parallel $a_{/\!/}$ and perpendicular $a_\perp$ to the particle's velocity and considering the transformation properties of these components: $a'_{/\!/} = \gamma^3 a_{/\!/}$ and $a'_\perp = \gamma^3 a_\perp$, we obtain:

$$P = \frac{q^2}{6\pi\varepsilon_0 c^3}(a'^2_{/\!/} + a'^2_\perp) = \frac{q^2}{6\pi\varepsilon_0 c^3}\gamma^4(\gamma^2 a^2_{/\!/} + a^2_\perp) \tag{A.3.9}$$

Clearly, the emitted power P increase drastically in the relativistic regime. This expression can be written in a compact form as:

$$P = \frac{q^2}{6\pi\varepsilon_0 c^3}\gamma^6(a^2 - |\boldsymbol{\beta} \times \boldsymbol{a}|^2) \tag{A.3.10}$$

A.4 The Radiation Spectrum

For astrophysical studies, we want to specify the Radiation Spectrum of an accelerating charge. This specifies how the power is distributed over frequency. First we introduce the Fourier transform of the particle's acceleration :

$$\begin{aligned} \dot{\boldsymbol{v}}(t) &= \frac{1}{\sqrt{2\pi}}\int_{-\infty}^{+\infty} \dot{\boldsymbol{v}}(\omega)\exp(-i\omega t)d\omega \\ \dot{\boldsymbol{v}}(\omega) &= \frac{1}{\sqrt{2\pi}}\int_{-\infty}^{+\infty} \dot{\boldsymbol{v}}(t)\exp(i\omega t)dt \end{aligned} \tag{A.4.1}$$

Then we use Parseval's theorem, which relates these as follows:

$$\int_{-\infty}^{+\infty} |\dot{\boldsymbol{v}}(\omega)|^2 d\omega = \int_{-\infty}^{+\infty} |\dot{\boldsymbol{v}}(t)|^2 dt \tag{A.4.2}$$

Another useful relation is:

$$\int_{0}^{+\infty} |\dot{\boldsymbol{v}}(\omega)|^2 d\omega = \int_{-\infty}^{0} |\dot{\boldsymbol{v}}(\omega)|^2 d\omega \tag{A.4.3}$$

which is valid if $\dot{\boldsymbol{v}}(\omega)$ is real. Applying these relations to the Larmor's formula (A.3.6) or its relativistic generalization(A.3.10) we have the integral relation:

$$\int_{-\infty}^{+\infty} P dt = \int_{-\infty}^{+\infty} \frac{q^2}{6\pi\varepsilon_0 c^3}|\dot{\boldsymbol{v}}(t)|^2 dt = \frac{q^2}{3\pi\varepsilon_0 c^3}\int_{0}^{+\infty} |\dot{\boldsymbol{v}}(\omega)|^2 d\omega \tag{A.4.4}$$

Since the total emitted energy is also equal to $\int_0^\infty (dW/d\omega)d\omega$, then the energy emitted on a given frequency is:

$$\frac{dW}{d\omega} = \frac{q^2}{3\pi\varepsilon_0 c^3}|\dot{\boldsymbol{v}}(\omega)|^2 \tag{A.4.5}$$

This is the *Radiation Spectrum* of an accelerating charge particle.

Appendix B

Quantum Electrodynamics

Quantum Electrodynamics (QED) is a quantum field theory of interacting fermionic matter and photons. As a field theory, it can receive a description both in Lagrangian and Hamiltonian formalism.

$$\mathcal{L}_{QED} = \bar{\psi}(i\not{\partial} - m)\psi - \frac{1}{4}F^{\rho\sigma}F_{\rho\sigma} - q\bar{\psi}\not{A}\psi \tag{B.0.1}$$

where:

- $\mathcal{L}_D = \bar{\psi}(i\not{\partial} - m)\psi$ is the fermionic free Lagrangian
- $\mathcal{L}_{EM} = -\frac{1}{4}F^{\rho\sigma}F_{\rho\sigma}$ is the electromagnetic Lagrangian, where $F^{\rho\sigma} = \partial^\rho A^\sigma - \partial^\sigma A^\rho$
- $\mathcal{L}_I = -q\bar{\psi}\not{A}\psi$ is the interaction term of Lagrangian.

The hamiltonian density associated to $\mathcal{L}_{QED}$ is defined to be:

$$\mathcal{H}_{QED} = \sum_\alpha \frac{\partial \mathcal{L}_{QED}}{\partial \partial_0 \phi_\alpha}\, \partial_0\phi_\alpha - \mathcal{L}_{QED} \tag{B.0.2}$$

But the only useful component for our purpose to study the interactions is:

$$\mathcal{H}_I = \cancel{\dot{\bar{\psi}}\frac{\partial \mathcal{L}_I}{\partial \dot{\bar{\psi}}}} + \cancel{\frac{\partial \mathcal{L}_I}{\partial \psi}\dot{\psi}} + \cancel{\frac{\partial \mathcal{L}_I}{\partial \dot{A}_\mu}\dot{A}_\mu} - \mathcal{L}_I \quad \rightarrow \quad \mathcal{H}_I = -\mathcal{L}_I \tag{B.0.3}$$

B.1 The S-Matrix

The S-matrix operator relates the initial state and final state of a physical system undergoing a scattering process. Is implicit in this discussion that we switched to an *interaction picture* (I.P) description of our quantized system where states and operators follow different time evolution:

- The operators evolve with the Interaction hamiltonian $\mathcal{H}_I$
- The states evolve with free hamiltonian

$$\begin{array}{ll} |i\rangle & : \text{initial states } \rightarrow |\psi(t=-\infty)\rangle = |\psi_{in}\rangle \\ |f\rangle & : \text{final states } \rightarrow |\psi(t=\infty)\rangle = |\psi_{fin}\rangle \end{array} \tag{B.1.1}$$

The transition from $|i\rangle$ to $|f\rangle$ is:

$$\begin{aligned} &\langle\psi_{fin}|\, S\, |\psi_{in}\rangle = S_{fi} \qquad |\langle\psi_{fin}|\, S\, |\psi_{in}\rangle|^2 = |S_{fi}|^2 \\ &\textstyle\sum_f |S_{fi}|^2 = \langle\psi_{in}|\, S^+\, |\psi_{fin}\rangle \langle\psi_{fin}|\, S\, |\psi_{in}\rangle = \langle\psi_{in}|\, S^+ S\, |\psi_{in}\rangle = 1 \end{aligned} \tag{B.1.2}$$

B.2 The Cross Section

Consider a beam of particles of type 1 and mass m_1 colliding with a target made of particles of type 2 and mass m_2. The target is at rest in the *Lab* frame.
Let $n_1^{(0)}$ and $n_2^{(0)}$ the number density of beam and of the target and $v_1^{(0)}$ the speed of the type 1 particles in the beam.

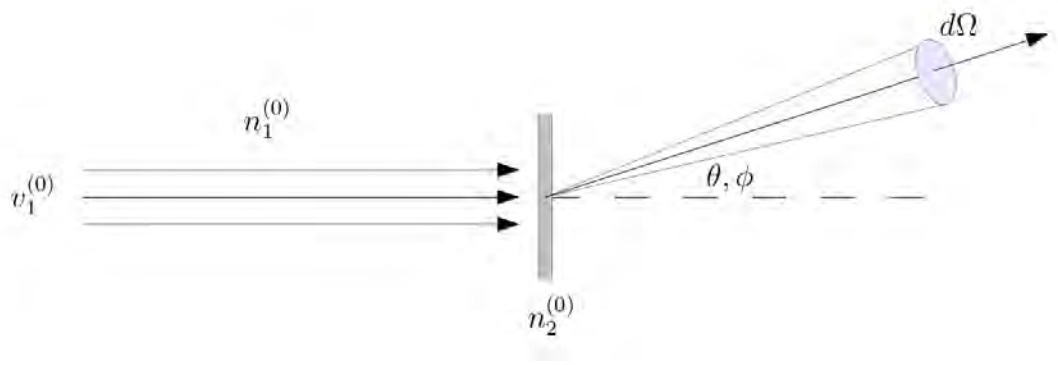

Figure 1.4: Cross section geometry, showing incident beam, target and outgoing beam into solid angle $d\Omega$.

The Rate of scattering R_s is defined by the number of scattering events N_s per unit of time T and volume V. It is proportional to the target and beam density and the speed $v_1^{(0)}$ by σ.

$$R_s = \frac{N_s}{VT} = \sigma(n_1^{(0)} v_1^{(0)}) n_2^{(0)} \tag{B.2.1}$$

where σ is the cross section of the process.
The cross section has dimension of area $[\sigma] = L^2$ and a specific unit of area called barn $1\ b = 100\ fm^2$. The quantity $d\sigma/d\Omega$ is called differential cross section, and give us relevant information about angular distribution of the scattering products. The cross section σ can be found by integrating $d\sigma/d\Omega$ over all angle.

$$\sigma = \int \frac{d\sigma}{d\Omega} = \int_0^{\pi} d\theta\ \sin\theta \int_0^{2\pi} d\phi\ \frac{d\sigma}{d\Omega} \tag{B.2.2}$$

We want now made a connection between cross section σ and the S-matrix element S_{fi} at given order of perturbation.

$$S_{fi} = \langle f|\, S\, |i\rangle = (2\pi)^4 \delta^4(P_{IN} - P_{FIN}) \mathcal{M}_{fi} \qquad i \neq f \tag{B.2.3}$$

If the states are canonically normalized $\langle i|\, |i\rangle = 1 \quad \sum_f \langle f|\, |f\rangle = 1$ we can give a probabilistic interpretation of S_{fi} as transition amplitude from the unitarity of S-matrix.

$$\sum_f |S_{fi}|^2 = \sum_f \langle i|\, S^+\, |f\rangle \langle f|\, S\, |i\rangle = \langle i|\, S^+ S\, |i\rangle = 1 \tag{B.2.4}$$

But when we calculate Feynman amplitude $\mathcal{M}$ from Feynman diagrams using Feynman rules in momentum space we are using covariant normalization.

$$\langle 1(\boldsymbol{p})|\, |1(\boldsymbol{p})\rangle = (2\pi)^3 2E_p \delta^3(0) \to (2E_p)V \tag{B.2.5}$$

So the canonically normalized[1] state is given by $|1(\boldsymbol{p})\rangle_{CN} = \left(\frac{1}{2E_p V}\right)^{\frac{1}{2}} |1(\boldsymbol{p})\rangle$.

[1]N.B.There is another common normalization used for leptons states $|1(\boldsymbol{p})\rangle'_{CN} = \sqrt{2m_l}\, |1(\boldsymbol{p})\rangle$.

The quantity S_{fi}^{CN} can now be correctly interpreted with a "probabilistic" meaning.

$$S_{fi}^{CN} = \langle f| S |i\rangle_{CN} = \prod_{i=1}^{n_i}\left(\frac{1}{2E_iV}\right)^{\frac{1}{2}} \prod_{f=1}^{n_f}\left(\frac{1}{2E_fV}\right)^{\frac{1}{2}} S_{fi} \tag{B.2.6}$$

$$= (2\pi)^4\delta^4(P_{IN} - P_{FIN}) \prod_{i=1}^{n_i}\left(\frac{1}{2E_iV}\right)^{\frac{1}{2}} \prod_{f=1}^{n_f}\left(\frac{1}{2E_fV}\right)^{\frac{1}{2}} \mathcal{M}_{fi} \tag{B.2.7}$$

where $\mathcal{M}_{fi}$ is the Feynman amplitude that we can calculate from Feynman diagrams.
To obtain a meaningful result we have to require to consider final states with $p \in (p_f, p_f + dp_f)$ so the number of states is:

$$d^3n = \prod_{f=1}^{n_f}\left(\frac{Vd^3p_f}{(2\pi)^3}\right) \qquad p \in (p_f, p_f + dp_f) \tag{B.2.8}$$

We have all elements to define the transition probability between $|i\rangle$ to $|f\rangle$ with $p \in (p_f, p_f+dp_f)$ in two relevant processes:

$$dW_{fi} = |S_{fi}^{CN}|^2 \prod_{f=1}^{n_f}\left(\frac{Vd^3p_f}{(2\pi)^3}\right) \tag{B.2.9}$$

• Decay process $1 \to n_f$:

$$dW_{1\to n_f} = (2\pi)^4\delta^4(P_{IN} - P_{FIN})(VT)\frac{1}{2E_1V} \prod_{f=1}^{n_f}\left(\frac{d^3p_f}{(2\pi)^3 2E_f}\right)|\mathcal{M}_{fi}|^2 \tag{B.2.10}$$

• Scattering process $1 + 2 \to n_f$:

$$dW_{1+2\to n_f} = (2\pi)^4\delta^4(P_{IN} - P_{FIN})(VT)\left(\frac{1}{2E_1V}\right)\left(\frac{1}{2E_2V}\right)\prod_{f=1}^{n_f}\left(\frac{d^3p_f}{(2\pi)^3 2E_f}\right)|\mathcal{M}_{fi}|^2 \tag{B.2.11}$$

where we used this passage $\left((2\pi)^4\delta^4(P_{IN} - P_{FIN})\right)^2 = (2\pi)^4\delta^4(P_{IN} - P_{FIN})\cancel{(2\pi)^4\delta^4(0)}^{(VT)}$.
With this definition of transition probability we can made a connection between cross section σ previously defined with experimental observables and Feynman amplitude $|\mathcal{M}_{fi}|^2$ which rappresent the interaction of perturbative theory.
In the *Lab* frame previously described we can write:

$$d\sigma = \frac{dW_{fi}}{VT}\frac{1}{(n_1^{(0)}v_1^{(0)})n_2^{(0)}} = \frac{(2\pi)^4\delta^4(P_{IN} - P_{FIN})}{4m_2E_1^{(0)}v_1^{(0)}} \prod_{f=1}^{n_f}\left(\frac{d^3p_f}{(2\pi)^3 2E_f}\right)|\mathcal{M}_{fi}|^2_{Lab} \tag{B.2.12}$$

when we used the fact that our states are normalized in such a way to have one particle per unit of volume and so $n_1^{(0)} = n_2^{(0)} = 1/V$.
Most of the object in this formula are invariant under a proper Lorentz transformation.
Let's define the flux factor as:

$$I = \left[(p_1p_2)^2 - (m_1^2m_2^2)\right]^{\frac{1}{2}} \tag{B.2.13}$$

this is an invariant quantity. That in the *Lab* frame is $I_{Lab} = m_2|p_1|_{Lab} = m_2E_1^{(0)}v_1^{(0)}$.
Thus $d\sigma$ can be written in a Lorentz invariant way as:

$$d\sigma = \frac{|\mathcal{M}_{fi}|^2}{4I}d\phi_{(n)} \qquad d\phi_{(n)} = (2\pi)^4\delta^4(P_{IN} - P_{FIN}) \prod_{f=1}^{n_f}\left(\frac{d^3p_f}{(2\pi)^3 2E_f}\right) \tag{B.2.14}$$

where $d\phi_{(n)}$ is the Lorentz invariant phase space of n_f body.

B.2.1 Cross Section in Scattering process $1+2 \to 1'+2'$

Let's start being general and assuming all particles different and in generic reference frame.

$$\begin{array}{ll} p_1 = (E_1, \boldsymbol{p}_1) & p_{1'} = (E_{1'}, \boldsymbol{p}_{1'}) \\ p_2 = (E_2, \boldsymbol{p}_2) & p_{2'} = (E_{2'}, \boldsymbol{p}_{2'}) \end{array} \tag{B.2.15}$$

The differential of cross section can be written as:

$$d\sigma = \frac{|\mathcal{M}_{fi}|^2}{4I}(2\pi)^4\delta^4(p_1 + p_2 - p_{1'} - p_{2'})\frac{d^3p_{1'}}{(2\pi)^3 2E_{1'}}\frac{d^3p_{2'}}{(2\pi)^3 2E_{2'}} \tag{B.2.16}$$

In this formula there are six integration variable and four deltas. So we can integrate in order to write $d\sigma$ in terms of the only two independent variables. The others variables can be eliminated:

• by integrating the phase space over $d^3p_{2'}$ with condition $\boldsymbol{p}_{2'} = \boldsymbol{p}_1 + \boldsymbol{p}_2 - \boldsymbol{p}_{1'}$.

$$d\phi'_{(2)} = \int d\phi_{(2)} = \frac{1}{(4\pi)^2 E_{1'}E_{2'}}\delta(E_1 + E_2 - E_{1'} - E_{2'})d^3p_{1'} \tag{B.2.17}$$

• by integrating the phase space over $d|\boldsymbol{p}_{1'}|$, knowing that $d^3p_{1'} = |\boldsymbol{p}_{1'}|^2 d|\boldsymbol{p}_{1'}|d\Omega_{1'}$.

$$d\phi''_{(2)} = \int d\phi'_{(2)} = \frac{d\Omega_{1'}}{(4\pi)^2 E_{1'}E_{2'}}\int d|\boldsymbol{p}_{1'}|\delta(E_1 + E_2 - E_{1'} - E_{2'})|\boldsymbol{p}_{1'}|^2 \tag{B.2.18}$$

using this general relation :

$$\int f(x,y)\delta[g(x,y)]dx = \int f(x,y)\delta[g(x,y)]\left(\frac{\partial x}{\partial g}\right)_y dg = \left[\frac{f(x,y)}{\partial x/\partial g}\right]_{g=0} \tag{B.2.19}$$

we obtain the differential cross section for scattering process $1+2 \to 1'+2'$ in a generic reference frame.

$$\frac{d\sigma}{d\Omega_{1'}} = \frac{|\mathcal{M}_{fi}|^2}{64\pi^2 I}\frac{|\boldsymbol{p}_{1'}|^2}{E_{1'}E_{2'}}\left[\frac{\partial E_{1'} + \partial E_{2'}}{\partial|\boldsymbol{p}_{1'}|}\right]^{-1} \tag{B.2.20}$$

To go further we have to choose the reference frame.

$\boxed{CoM}$

$$s = (p_1 + p_2)^2 = (p_{1'} + p_{2'})^2$$

$$p_{1'} + p_{2'} = (E_{1'} + E_{1'}, \boldsymbol{p}_{1'} + \boldsymbol{p}_{2'}) = (\sqrt{s}, 0)$$

$$I_{CM} = |\boldsymbol{p}_1|\sqrt{s}$$

$$\frac{\partial E_{1'} + \partial E_{2'}}{\partial|\boldsymbol{p}_{1'}|} = |\boldsymbol{p}_{1'}|\frac{E_{1'} + E_{2'}}{E_{1'}E_{2'}} = |\boldsymbol{p}_{1'}|\frac{\sqrt{s}}{E_{1'}E_{2'}}$$

$$|\boldsymbol{p}_{1'}| = \frac{1}{2\sqrt{s}}\left[s^2 + (m_{1'}^2 - m_{2'}^2)^2 - 2s(m_{1'}^2 + m_{2'}^2)\right]^{1/2} \tag{B.2.21}$$

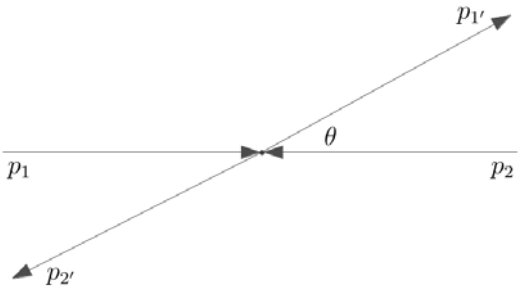

Scattering $1+2 \to 1'+2'$ in CoM frame.

With these quantities evaluated in the center of mass reference frame we obtain the master equation for $1+2 \to 1'+2'$ in CoM frame:

$$\left(\frac{d\sigma}{d\Omega_{1'}}\right)_{CoM} = \frac{1}{64\pi^2}\frac{|\boldsymbol{p}_{1'}|}{|\boldsymbol{p}_1|}\frac{|\mathcal{M}_{fi}|^2}{s} \tag{B.2.22}$$

In many cases this formula can be simplified:

• $m_1 = m_{1'}$ and $m_2 = m_{2'}$

In this case $|\boldsymbol{p}_{1'}| = |\boldsymbol{p}_1|$, $(E_{1'} = E_1)$the cross section in the reference frame is:

$$\left(\frac{d\sigma}{d\Omega_{1'}}\right)_{CoM} = \frac{1}{64\pi^2}\frac{|\mathcal{M}_{fi}|^2}{s} \tag{B.2.23}$$

• $m_1 = m_2 = 0$ and $m_{1'} = m_{2'} = M$

In this case $|\boldsymbol{p}_1| = E_1 = \frac{\sqrt{s}}{2}$ and $|\boldsymbol{p}_{1'}| = \frac{\sqrt{s}}{2}\left(1 - \frac{4M^2}{s}\right)^{1/2}$ the cross section in the reference frame is:

$$\left(\frac{d\sigma}{d\Omega_{1'}}\right)_{CoM} = \frac{1}{64\pi^2}\left(1 - \frac{4M^2}{s}\right)^{\frac{1}{2}}\frac{|\mathcal{M}_{fi}|^2}{s} \tag{B.2.24}$$

$\boxed{RF - Lab}$

$$|\boldsymbol{p}_2| = 0$$

$$I_{RF} = |\boldsymbol{p}_1| m_2$$

$$|\boldsymbol{p}_{2'}|^2 = |\boldsymbol{p}_1|^2 + |\boldsymbol{p}_{1'}|^2 - 2|\boldsymbol{p}_{1'}||\boldsymbol{p}_{1'}|\cos\theta$$

$$\frac{\partial E_{1'} + \partial E_{2'}}{\partial |\boldsymbol{p}_{1'}|} = \frac{\partial E_{1'}}{\partial |\boldsymbol{p}_{1'}|} + \frac{\partial E_{1'}}{\partial |\boldsymbol{p}_{2'}|^2}\frac{\partial |\boldsymbol{p}_{2'}|^2}{\partial |\boldsymbol{p}_{1'}|} =$$

$$\frac{|\boldsymbol{p}_1|}{E_{1'}} + \frac{|\boldsymbol{p}_{1'}| - |\boldsymbol{p}_1|\cos\theta}{E_{2'}} = \frac{|\boldsymbol{p}_{1'}|(E_1 + m_2) - E_{1'}|\boldsymbol{p}_1|\cos\theta}{E_{1'}E_{2'}} \tag{B.2.25}$$

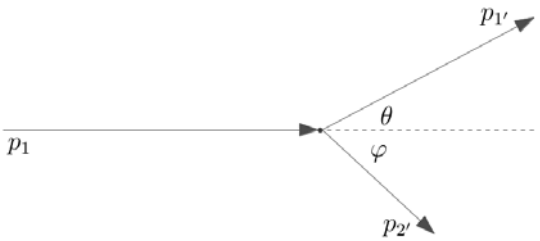

Scattering $1 + 2 \to 1' + 2'$ in rest frame.

With these quantities evaluated in the rest reference frame we obtain the master equation for $1 + 2 \to 1' + 2'$ in the RF frame:

$$\left(\frac{d\sigma}{d\Omega_{1'}}\right)_{RF} = \frac{1}{64\pi^2}\frac{1}{|\boldsymbol{p}_1| m_2}\frac{|\boldsymbol{p}_{1'}|^2}{|\boldsymbol{p}_{1'}|(E_1 + m_2) - E_{1'}|\boldsymbol{p}_1|\cos\theta}|\mathcal{M}_{fi}|^2 \tag{B.2.26}$$

This formula can be simplified when:

• $m_1 = m_{1'} = 0$ and $m_2 = m_{2'} = M$

In this case $|\boldsymbol{p}_1| = E_1$ and $|\boldsymbol{p}_{1'}| = E_{1'}$. Using t variable and conservation of energy we obtain a relation for $E_{1'}$.

$$E_{1'} = \frac{ME_1}{M + E_1(1 - \cos\theta)} \tag{B.2.27}$$

$$\begin{aligned} t &= (p_1 - p_{1'})^2 = -2E_1E_{1'}(1 - \cos\theta) \\ t &= (p_2 - p_{2'})^2 = 2M^2 - 2ME_{2'} \\ E_{2'} &= E_1 + M - E_{1'} \end{aligned} \tag{B.2.28}$$

In these conditions the cross section results:

$$\left(\frac{d\sigma}{d\Omega_{1'}}\right)_{RF} = \frac{1}{64\pi^2}\left(\frac{E_{1'}}{E_1}\right)^2\frac{|\mathcal{M}_{fi}|^2}{M^2} \tag{B.2.29}$$

B.3 Calculations of γ-matrix Traces

In this section we calculate the γ-matrix trace of the Compton Scattering unpolarized Feynman Amplitude (2.2.22).

$$\mathbb{T} = Tr\Big[\gamma_\mu(\not{p}' + m)\gamma^\mu(\not{p} + \not{k} + m)\gamma_\nu(\not{p} + m)\gamma^\nu(\not{p} + \not{k} + m)\Big] \tag{B.3.1}$$

The trace $\mathbb{T}$ have to be evaluated using γ-matrix properties and Clifford algebra.
Using $\gamma^\mu\gamma_\mu = 4$ and $\gamma^\mu\gamma^\rho\gamma_\mu = -2\gamma^\rho$ we obtain:

$$\mathbb{T} = Tr\Big[(4m - 2\not{p}')(\not{p} + \not{k} + m)(4m - 2\not{p})(\not{p} + \not{k} + m)\Big] = \mathbb{T}_1 + \mathbb{T}_2 + \mathbb{T}_3 + \mathbb{T}_4 \tag{B.3.2}$$

with

$$\begin{aligned}
\mathbb{T}_1 &= 16m^2 Tr\big[(\not{p} + \not{k} + m)(\not{p} + \not{k} + m)\big] = 16m^2(4(p+k)^2 + 4m^2) = 64m^2(s + m^2) \\
\mathbb{T}_3 &= -8m^2 Tr\big[\not{p}'(\not{p} + \not{k} + m)\not{p}(\not{p} + \not{k} + m)\big] = -64m^2 p'(p+k) = -32m^2(s + m^2) \\
\mathbb{T}_4 &= -8m^2 Tr\big[(\not{p} + \not{k} + m)\not{p}(\not{p} + \not{k} + m)\big] = -64m^2 p(p+k) = -32m^2(s + m^2)
\end{aligned} \tag{B.3.3}$$

where we used the following relations obtained from Mandelstam variables (2.2.23):

$$\begin{aligned}
p'(p+k) &= p'(p'+k') = m^2 + p'k' = m^2 + (s - m^2)/2 = (s + m^2)/2 \\
p(p+k) &= m^2 + pk = m^2 + (s - m^2)/2 = (s + m^2)/2
\end{aligned} \tag{B.3.4}$$

Additioning all terms we note that $\mathbb{T}_1 + \mathbb{T}_3 + \mathbb{T}_4 = 0$ so the result depends only by trace $\mathbb{T}_2$. The evaluation of $\mathbb{T}_2$ is less immediately.

$$\mathbb{T}_2 = 4Tr\big[\not{p}'(\not{p} + \not{k} + m)\not{p}(\not{p} + \not{k} + m)\big] = 4\big\{Tr\big[p'(\not{p} + \not{k})\not{p}(\not{p} + \not{k})\big] + Tr\big[\not{p}\not{p}'\big]m^2\big\} = \tag{B.3.5}$$

Now we use the relation $Tr[\not{a}\not{b}\not{c}\not{d}] = 4[(ab)(cd) - (ac)(bd) + (ad)(bc)]$ for several times:

$$\begin{aligned}
Tr[\not{p}'\not{p}\not{p}\not{p}] &= 4[(p'p)(pp) \cancel{-(p'p)(pp)} \cancel{+(p'p)(pp)}] \\
Tr[\not{p}'\not{p}\not{p}\not{k}] &= 4[\cancel{(p'p)(pk)} \cancel{-(p'p)(pk)} + (p'k)(pp)] \\
Tr[\not{p}'\not{k}\not{p}\not{p}] &= 4[(p'k)(pp) \cancel{-(p'p)(kp)} \cancel{+(p'p)(kp)}] \\
Tr[\not{p}'\not{k}\not{p}\not{k}] &= 4[(p'k)(pk) \cancel{-(p'p)(kk)} + (p'k)(kp)]
\end{aligned} \tag{B.3.6}$$

summing all traces we finally obtain:

$$\begin{aligned}
\mathbb{T}_2 &= 16\big\{2(p'p)m^2 + 2(p'k)m^2 + 2(p'k)(pk)\big\} = 32\big\{(p'(p+k)m^2 + (p'k)(pk)\big\} \\
\mathbb{T}_2 &= 8\big\{4m^4 - (s - m^2)(u - m^2) + 2m^2(s - m^2)\big\}
\end{aligned} \tag{B.3.7}$$

Bibliography

[1] Aous A Abdo, M Ackermann, Marco Ajello, L Baldini, J Ballet, G Barbiellini, D Bastieri, K Bechtol, R Bellazzini, B Berenji, et al. Fermi large area telescope observations of markarian 421: The missing piece of its spectral energy distribution. *The Astrophysical Journal*, 736(2):131, 2011.

[2] Markus Ackermann, Marco Ajello, A Allafort, L Baldini, J Ballet, G Barbiellini, MG Baring, D Bastieri, K Bechtol, R Bellazzini, et al. Detection of the characteristic pion-decay signature in supernova remnants. *Science*, 339(6121):807–811, 2013.

[3] M Actis, G Agnetta, F Aharonian, A Akhperjanian, J Aleksić, E Aliu, D Allan, I Allekotte, F Antico, LA Antonelli, et al. Design concepts for the cherenkov telescope array cta: an advanced facility for ground-based high-energy gamma-ray astronomy. *Experimental Astronomy*, 32(3):193–316, 2011.

[4] F Aharonian, AG Akhperjanian, AR Bazer-Bachi, M Beilicke, Wystan Benbow, David Berge, K Bernlöhr, C Boisson, O Bolz, V Borrel, et al. Discovery of very-high-energy γ-rays from the galactic centre ridge. *Nature*, 439(7077):695–698, 2006.

[5] Felix Aharonian, AG Akhperjanian, AR Bazer-Bachi, M Beilicke, Wystan Benbow, David Berge, K Bernlöhr, C Boisson, Oliver Bolz, V Borrel, et al. 3.9 day orbital modulation in the tev γ-ray flux and spectrum from the x-ray binary ls 5039. *Astronomy & Astrophysics*, 460(3):743–749, 2006.

[6] Felix A Aharonian. *Very high energy cosmic gamma radiation: a crucial window on the extreme Universe*. World Scientific, 2004.

[7] Felix A Aharonian. Gamma rays from supernova remnants. *Astroparticle Physics*, 43:71–80, 2013.

[8] Vladimir Borisovich Berestetskii, Evgenii Mikhailovich Lifshitz, and Lev Petrovich Pitaevskii. *Quantum electrodynamics*, volume 4. Butterworth-Heinemann, 1982.

[9] K Bernlöhr, A Barnacka, Yvonne Becherini, O Blanch Bigas, E Carmona, P Colin, G Decerprit, F Di Pierro, F Dubois, Christian Farnier, et al. Monte carlo design studies for the cherenkov telescope array. *Astroparticle Physics*, 43:171–188, 2013.

[10] Gianfranco Bertone, Dan Hooper, and Joseph Silk. Particle dark matter: Evidence, candidates and constraints. *Physics Reports*, 405(5):279–390, 2005.

[11] Hans Bethe and Walter Heitler. On the stopping of fast particles and on the creation of positive electrons. *Proceedings of the Royal Society of London A: Mathematical, Physical and Engineering Sciences*, 146(856):83–112, 1934.

[12] George R Blumenthal and Robert J Gould. Bremsstrahlung, synchrotron radiation, and compton scattering of high-energy electrons traversing dilute gases. *Reviews of Modern Physics*, 42(2):237, 1970.

[13] Torsten Bringmann and Christoph Weniger. Gamma ray signals from dark matter: Concepts, status and prospects. *Physics of the Dark Universe*, 1(1):194–217, 2012.

[14] Douglas Clowe, Maruša Bradač, Anthony H Gonzalez, Maxim Markevitch, Scott W Randall, Christine Jones, and Dennis Zaritsky. A direct empirical proof of the existence of dark matter. *The Astrophysical Journal Letters*, 648(2):L109, 2006.

[15] HESS collaboration et al. Acceleration of petaelectronvolt protons in the galactic centre. *Nature*, 531(7595):476–479, 2016.

[16] CTA Consortium. Introducing the {CTA} concept. *Astroparticle Physics*, 43:3 – 18, 2013.

[17] CTA-Science. https://portal.cta-observatory.org/Pages/CTA-Science.aspx, 2013.

[18] Alessandro De Angelis and Mário João Martins Pimenta. *Introduction to Particle and Astroparticle Physics: Questions to the Universe*. Springer, 2015.

[19] Herve Dole, Guilaine Lagache, J-L Puget, Karina I Caputi, Nestor Fernandez-Conde, E Le Floc'h, Casey Papovich, Pablo G Pérez-González, George H Rieke, and Myra Blaylock. The cosmic infrared background resolved by spitzer-contributions of mid-infrared galaxies to the far-infrared background. *Astronomy & Astrophysics*, 451(2):417–429, 2006.

[20] Michele Doro. A decade of dark matter searches with ground-based cherenkov telescopes. *Nuclear Instruments and Methods in Physics Research Section A: Accelerators, Spectrometers, Detectors and Associated Equipment*, 742:99–106, 2014.

[21] F. Aharonian et al. The crab nebula and pulsar between 500 gev and 80 tev: Observations with the hegra stereoscopic air cerenkov telescopes. *The Astrophysical Journal*, 614(2):897, 2004.

[22] Richard P Feynman, Robert B Leighton, and Matthew Sands. *The Feynman Lectures on Physics, mainly electromagnetism and matter, The Definitive Edition, vol. II*. Zanichelli, 2013.

[23] Bryan M Gaensler and Patrick O Slane. The evolution and structure of pulsar wind nebulae. *arXiv preprint astro-ph/0601081*, 2006.

[24] Gabriele Ghisellini. Gamma ray bursts: basic facts and ideas. *Proceedings of the International Astronomical Union*, 6(S275):335–343, 2010.

[25] Gabriele Ghisellini. *Radiative processes in high energy astrophysics*, volume 873. Springer, 2013.

[26] JA Hinton and W Hofmann. Teraelectronvolt astronomy. *Annu.Rev.Astro.Astrophys.*, 47:523–565, 2009.

[27] John David Jackson. *Classical electrodynamics*. Wiley, 1999.

[28] Josef M Jauch and Fritz Rohrlich. *The Theory of Photons and Electrons: The relativistic quantum field theory of charged particles with spin one-half*. Springer Science & Business Media, 2012.

[29] Ervin Kafexhiu, Felix Aharonian, Andrew M Taylor, and Gabriela S Vila. Parametrization of gamma-ray production cross sections for p p interactions in a broad proton energy range from the kinematic threshold to pev energies. *Physical Review D*, 90(12):123014, 2014.

[30] SR Kelner, Felex A Aharonian, and VV Bugayov. Energy spectra of gamma rays, electrons, and neutrinos produced at proton-proton interactions in the very high energy regime. *Physical Review D*, 74(3):034018, 2006.

[31] Henric Krawczynski and Ezequiel Treister. Active galactic nuclei—the physics of individual sources and the cosmic history of formation and evolution. *Frontiers of Physics*, 8(6):609–629, 2013.

[32] EA Kuraev, ES Kokoulina, and E Tomasi-Gustafsson. Light meson emission in (anti) proton induced reactions. *arXiv preprint arXiv:1503.02167*, 2015.

[33] Lev D Landau and Evgeny M Lifshitz. *The classical theory of fields*, volume 2. Elsevier, 2013.

[34] Lev D Landau and Evgeny M Lifshitz. *Electrodynamics of continuous media*, volume 8. Elsevier, 2013.

[35] Marianne Lemoine-Goumard. Status of ground-based gamma-ray astronomy. *arXiv preprint arXiv:1510.01373*, 2015.

[36] S Lombardi. Astri sst-2m prototype and astri mini-array data analysis and scientific prospects in the framework of the cherenkov telescope array. In *Proceedings of the 28th Texas Symposium on Relativistic Astrophysics*, 2015.

[37] Luciano Maiani and Omar Benhar. *Meccanica quantistica relativistica*. Riuniti Univ. Press, 2012.

[38] Franz Mandl and Graham Shaw. *Quantum field theory*. John Wiley & Sons, 2010.

[39] Rafal Moderski, Marek Sikora, Paolo S Coppi, and Felix Aharonian. Klein—nishina effects in the spectra of non-thermal sources immersed in external radiation fields. *Monthly Notices of the Royal Astronomical Society*, 363(3):954–966, 2005.

[40] M. Lopez Moya. Observaciones de la nebulosa y pulsar del cangrejo. Ph.D. thesis, 2006.

[41] Michael Peskin and Dan Schroeder. An introduction to quantum field theory. 1995.

[42] Tsvi Piran. Gamma-ray bursts and the fireball model. *Physics Reports*, 314(6):575–667, 1999.

[43] Tsvi Piran. The physics of gamma-ray bursts. *Reviews of Modern Physics*, 76(4):1143, 2005.

[44] William H Press. *Numerical recipes 3rd edition: The art of scientific computing*. Cambridge university press, 2007.

[45] Frank M Rieger, Emma de Oña-Wilhelmi, and Felix A Aharonian. Tev astronomy. *Frontiers of Physics*, 8(6):714–747, 2013.

[46] GE Romero, IA Grenier, MM Bernado, IF Mirabel, and DF Torres. Unidentified gamma-ray sources and microquasars. *arXiv preprint astro-ph/0402285*, 2004.

[47] George B Rybicki and Alan P Lightman. *Radiative processes in astrophysics*. John Wiley & Sons, 2008.

[48] M. S. Longair. *High Energy Astrophysics*. Cambridge University Press, 1992.

[49] Stefano Vercellone, G Agnetta, LA Antonelli, D Bastieri, G Bellassai, M Belluso, C Bigongiari, S Billotta, B Biondo, G Bonanno, et al. The astri mini-array science case. *arXiv preprint arXiv:1307.5671*, 2013.

[50] CF v Weizsäcker. Ausstrahlung bei stößen sehr schneller elektronen. *Zeitschrift für Physik A Hadrons and Nuclei*, 88(9):612–625, 1934.

[51] KC Westfold. The polarization of synchrotron radiation. *The Astrophysical Journal*, 130:241, 1959.

Acknowledgments